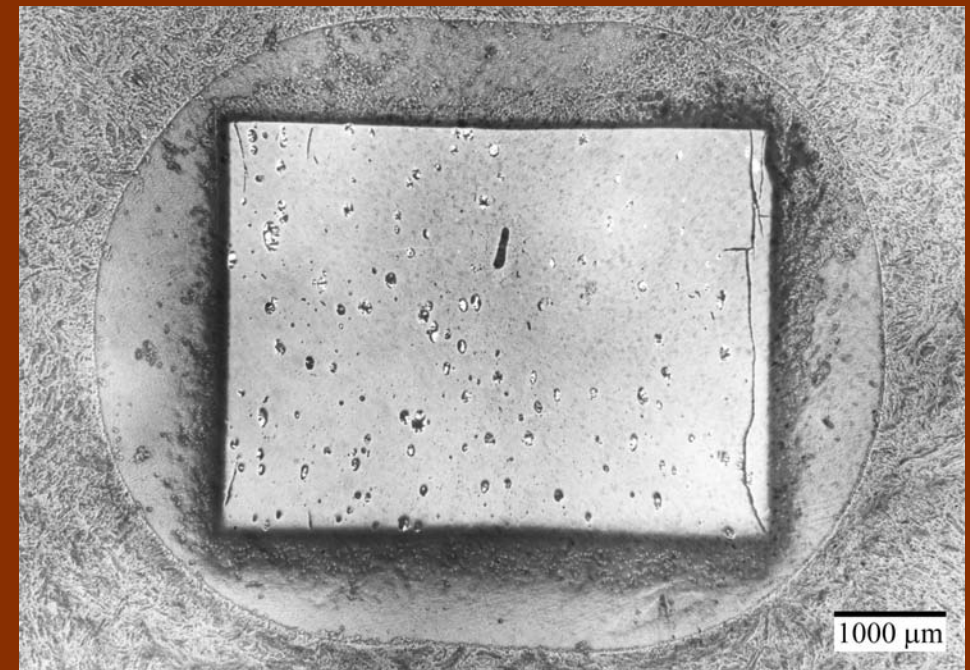
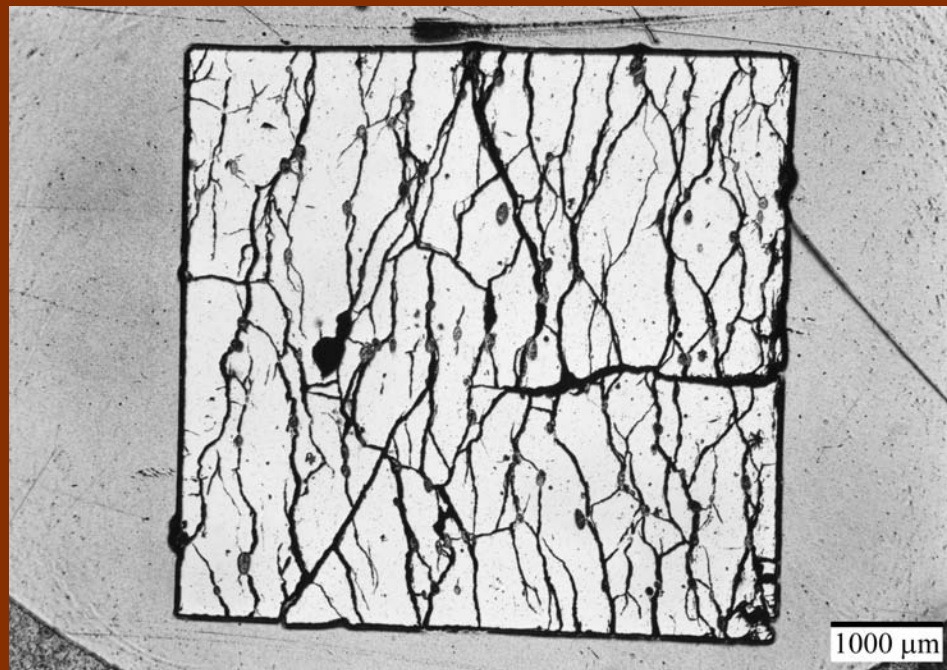


Mechanical behaviour and diffusion of gas during neutron irradiation of actinides in ceramic inert matrices



Mechanical behaviour and diffusion of gas during neutron irradiation of actinides in ceramic inert matrices

E.A.C. Neeft

— 3 —

E.A.C. Neeft

Mechanical behaviour and diffusion of gas during
neutron irradiation of actinides in ceramic inert matrices

Picture on front: Macro-dispersed fuel containing about 2.5 vol% UO_2 inclusions in MgAl_2O_4 before neutron irradiation. Fabrication and ceramography performed by H.Hein and W.J. Tams, respectively.

Picture on back: Macro-dispersed fuel containing about 2.0 vol% actinide-oxides, 20% of the initial amount of uranium atoms was fissioned after neutron irradiation in HFR. Ceramography performed by W.J. Tams.

Part of the research in this thesis was performed at Nuclear Research and consultancy Group (NRG), P.O. Box 25, 1755 ZG Petten.

Part of the research in this thesis was performed at the Department of Defects in Materials of the Interfaculty Reactor Institute, Delft University of Technology, Mekelweg 15, 2629 JB Delft.

The author of this thesis would like to thank NRG for the financial support.

Mechanical behaviour and diffusion of gas during neutron irradiation of actinides in ceramic inert matrices

Proefschrift

ter verkrijging van de graad van doctor
aan de Technische Universiteit Delft,
op gezag van de Rector Magnificus prof. dr. ir. J.T. Fokkema,
voorzitter van het College Promoties,
in the openbaar te verdedigen op maandag 29 maart 2004 om 13.00
door Erika Anna Cornelia NEEFT
doctorandus in de Geochemie
geboren te Beverwijk

Dit proefschrift is goedgekeurd door de promotoren:

Prof. dr. A. van Veen †

Prof. dr. A.H.M. Verkooijen

Samenstelling promotiecommissie

Rector Magnificus,	voorzitter
Prof. dr. A. van Veen, †	promotor
Prof. dr. A.H.M. Verkooijen,	promotor
Prof. dr. T. Hibma,	Rijksuniversiteit Groningen
Prof. dr. C.W.E. van Eijk,	Technische Universiteit Delft
Prof. dr. B.J. Thijsse,	Technische Universiteit Delft
Prof. dr. R.W. Grimes,	Imperial College, Engeland
Dr. K. Bakker,	Nuclear research and consultancy Group, Petten
Dr. R.P.C. Schram,	Nuclear research and consultancy Group, Petten

Published and distributed by: DUP Science

DUP Science is an imprint of

Delft University Press

P.O. Box 98

2600 MG Delft

The Netherlands

Telephone: +31 15 2785678

Telefax: +31 15 2785706

Email: info@library.tudelft.nl

ISBN 90-407-2475-X

Keywords: actinide transmutation, diffusion, mechanical behaviour

Copyright ©2004 by E.A.C. Neeft

All rights reserved. No part of the material protected by this copyright notice may be reproduced or utilised in any form or any means, electronic or mechanical, including photocopying, recording or by any information system and retrieval system, without permission from the publisher: Delft University Press.

Printed in The Netherlands.

 Contents

1	Introduction	1
2	Experimental methods	7
2.1	Implantation of helium in materials	8
2.1.1	α -emission from americium	8
2.1.2	Electrostatic accelerator	8
2.2	Examination of thermal behaviour of helium implanted samples	9
2.2.1	Neutron Depth Profiling	9
2.2.2	Thermal Helium Desorption Spectroscopy	12
2.3	Pre -and post irradiation examination of fuels	15
2.3.1	Gammaspectrometry	15
2.3.2	Pressure and volume of plenum	15
2.3.3	Dimensional measurements	18
2.3.4	Ceramography	19
2.3.5	α -and β,γ autoradiography	19
2.3.6	Electron Probe Micro Analysis	19
2.3.7	Indentation	19
3	Modelling of helium in MgAl_2O_4	21
3.1	Structure of MgAl_2O_4	22
3.2	Mott-Littleton methodology	23
3.2.1	Theory	23
3.2.2	Calculated properties of MgAl_2O_4	25
3.2.3	Calculated helium interactions in the lattice of MgAl_2O_4	33
3.2.4	Conclusions of atomistic calculations and outlook	37
3.3	Rate diffusion theory	38
3.3.1	Overview impact of implantation on transport of helium in different matrices	38
3.3.2	Diffusion in single crystal semi-infinite media	40
3.3.3	Diffusion in polycrystal semi-infinite media	41
3.3.4	Effect of diffusion mechanisms on the concentration profiles	44
3.3.5	Impact of diffusion mechanism on the helium release rate	49
3.4	Conclusion of rate diffusion theory	54
4	Diffusion of helium in helium implanted sampled of MgAl_2O_4	55
4.1	Preparation and characterisation of samples	56
4.2	Identification of diffusion mechanisms using NDP	57
4.3	THDS	66
4.3.1	^3He and background	66
4.3.2	Difference between temperature of sampleholder and sample	67
4.3.3	Results	68
4.4	Comparison of calculated energies and empirically determined energies	74
4.4.1	Single crystals	74
4.4.2	Polycrystalline samples	78

4.5	Relation between results of implanted samples and irradiation	81
4.5.1	Summary of fabricated fuel and irradiation of EFTTRA-T4	81
4.5.2	Diffusion of helium during neutron irradiation conditions	82
4.6	Relation between helium implantations and irradiation	84
4.7	Americium in spinel	88
4.8	Conclusion	90
5	Inert matrix fuels	91
5.1	Characterisation of UO ₂ used for macro-dispersed fuel	92
5.2	Fabrication of pellets	93
5.3	Characterisation of IMF pellets prior to irradiation	95
5.3.1	X-ray diffraction	96
5.3.2	Ceramography prior to irradiation	97
5.3.2.1	Macro-dispersed fuels	97
5.3.2.2	Micro-dispersed fuel	98
5.4	Microstructure of pellets without fissile phase	98
5.5	Irradiation pins	99
5.6	Neutron irradiation	99
5.7	Post irradiation examination of pins and wires	101
5.7.1	Gamma spectrometry of wires	101
5.7.2	Gamma spectrometry of pins	102
5.7.3	Profilometry	107
5.7.4	Fission-gas release	107
5.8	Post irradiation examination of pellets without uranium	110
5.9	Post-irradiation examination of IMF-pellets	111
5.9.1	Dimensional measurements	111
5.9.2	Ceramography and α - and β, γ autoradiography of IMF	112
5.9.2.1	Matrix in macro-dispersed fuels	113
5.9.2.2	Fissile phase in macro-dispersed fuels	113
5.9.2.3	Micro-dispersed fuel	125
5.9.3	EPMA	125
5.9.3.1	Macro-dispersed fuel	125
5.9.3.2	Micro-dispersed fuel	132
5.9.4	Calculated fission product distribution in macro-dispersed UO ₂ fuel	132
5.9.5	Mechanical properties	133
5.9.5.1	Indentations in ceramic matrices	133
5.9.5.2	Literature data of ceramic matrices	136
5.10	Discussion	138
5.10.1	Swelling of UO ₂	138
5.10.2	Swelling of uranium-free matrices	140
5.10.2.1	Micro-dispersed fuel	140
5.10.2.2	Macro-dispersed fuel	141
5.10.3	Formation of cracks in matrices	141
5.10.4	Steady state creep of ceramics	143
5.10.5	Radial thermally induced stress gradient	144
5.10.6	Impact of fission induced creep of matrix	144
5.10.7	Solid solution with fissile phase	145

5.10.8	Use of ellipsoidal fissile inclusions instead of spherical inclusions	146
5.10.9	Fission-gas release	146
5.10.9.1	Determination of fission gases in UO ₂ inclusions	146
5.10.9.2	Fission-gas release from UO ₂	148
5.10.10	The origin of CO ₂	149
5.11	Conclusions	150
5.12	Final remarks	152
	Appendix	154
	References	156
	Summary	161
	Samenvatting	165
	List of publications	170
	Acknowledgements	172
	Curriculum vitae	174

1 Introduction

Ordinary reactor fuel for commercial nuclear reactors is UO_2 . The uranium is a mixture of the fissile isotope ^{235}U and the fertile isotope ^{238}U . The disadvantage of ^{238}U is that other actinides are generated during neutron irradiation. Some of these actinides have very long half-lives. Consequently, the time that spent fuel is more radiotoxic than uranium ore is about 200.000 years. Spent fuel is composed of actinides and fission products. Figure 1.1 shows that fission products are more radiotoxic than uranium ore for a period of about 300 years and actinides for a period of about 200.000 years.

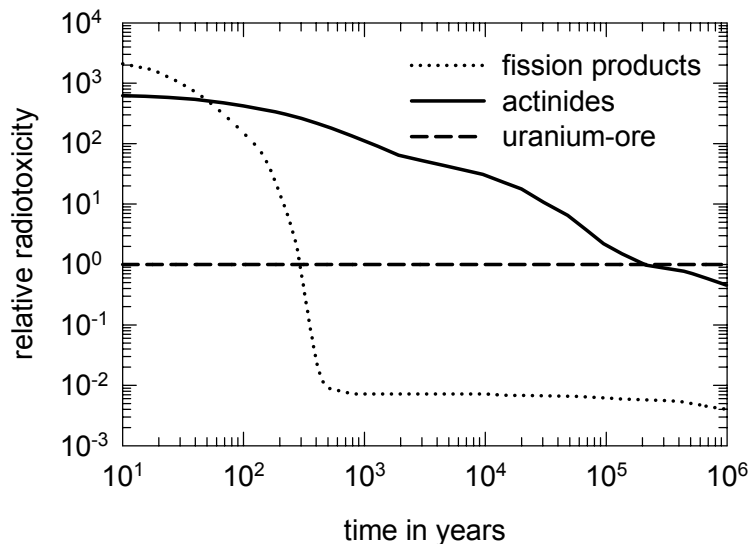


Figure 1.1 Radiotoxicity of actinides and fission products in spent fuel relative to that of uranium ore needed to manufacture the fuel [Gruppelaar et al. 1998]^a.

The actinides, causing nuclear waste to be more radiotoxic than uranium ore for such a long time, are mainly plutonium and americium. The number of actinides is reduced when these actinides are

fissioned in a matrix without uranium. Theoretically, the time that nuclear waste is more radiotoxic than uranium ore can be reduced from 200.000 years to 300 years. Fuels with actinides and uranium-free matrices are called inert matrix fuels. Atoms in the matrices are inert to generation of actinides such as plutonium and americium during neutron irradiation. Another benefit of inert matrix fuels is the burn-up of actinides within the pellet. Neutron irradiation of UO_2 fuel results in a locally high burn-up in the periphery of the pellet. Irradiation of inert matrix fuels is expected to have a more uniform burn-up of actinides within the pellet when the atoms in the inert matrices have low neutron absorption cross sections.

The conditions in a nuclear power plant require materials to remain relatively stable (chemically, dimensionally, mechanically) during irradiation. UO_2 has empirically proven to show acceptably small material degradation during these irradiation conditions. This thesis describes the research on some ceramics to test whether they are suitable inert matrices.

^a Probably ICRP-68 is used as a reference of uranium ore to obtain the value of 200.000 years. Using ICRP-72 [WISE] as a reference of uranium ore reduces this period till 130.000 years [Magill et al. 2003].

Neutron irradiation, implantation of products produced during decay and fission cause displacement of atoms from the lattice sites of the crystal structure of inert matrices. The rate of displacements per atom (dpa) depends on the flux, energy and mass of the implanted particle. The kinetic energy for fission products for a fission of ^{235}U is about 165 MeV [Freudenreich 1996]. Assuming two fission products created during one fission, the energy of the fission products are for example 94 MeV (^{100}Zr) and 71 MeV (^{140}Sn). Decay of ^{241}Am results in the emission of α (5.483 MeV) and ^{237}Np (93 keV). These products lose their energy during their travel in materials by collisions with the atoms in the crystal structure. The distance that a particle covers until it has lost its energy is called the implantation range. The implantation range in materials of these reaction products is fixed.

The amount of reaction products implanted in the inert matrix depends on the geometry of fissile phase and matrix in the pellet [White et al. 1956]. Figure 1.2 shows the implantation volume of reaction products^b in the inert matrix for macro-dispersed fuel (A) and micro-dispersed fuel (B). These reaction products are produced during fission and decay of actinides. Typical implantation ranges are 8-10 μm for fission products (f.p) and 13-18 μm for alpha's.

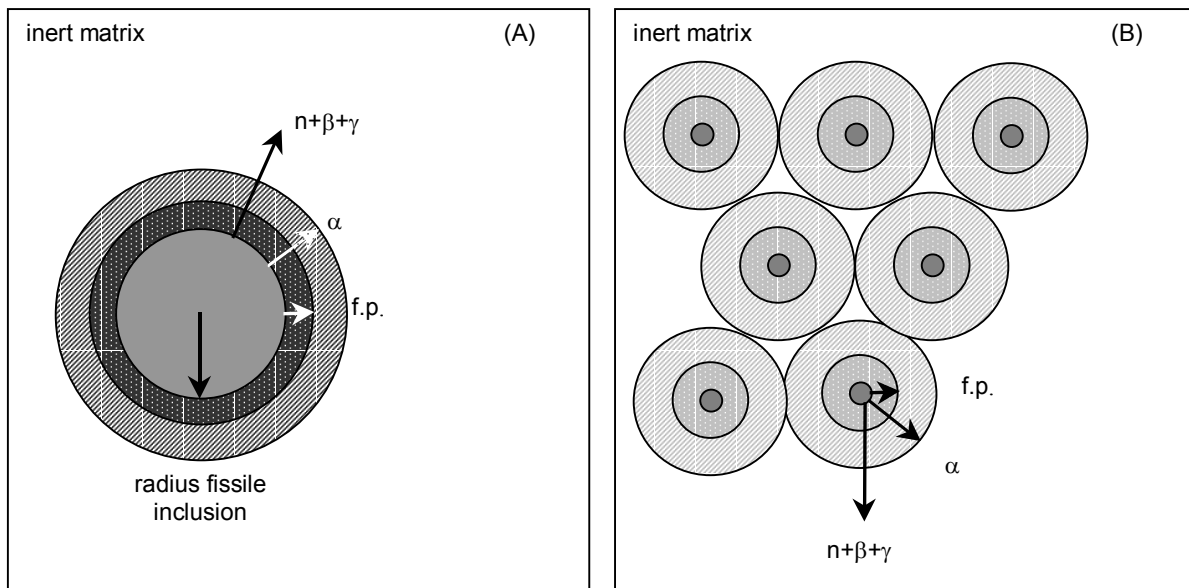


Figure 1.2 Implantation volume of reaction products, from the fissile phase, in the inert matrix for macro-dispersed fuel (A) and micro-dispersed fuel (B). Implantation ranges are fixed.

For macro-dispersed fuels, defects and/or other material degradation characteristics can be caused by the emission of neutrons (n), beta's (β) and gamma's (γ) in the majority of the volume of the inert matrix. Figure 1.2 shows that alpha's are implanted in the vicinity of the fissile inclusion. Consequently, the volume fraction of inert matrix for macro-dispersed fuels in

^b implantation range of ^{237}Np is not drawn in the figure because of its small size of about 30 nm

which alpha's (α) are implanted is smaller than the volume fraction of inert matrix where neutrons, beta's and gamma's are implanted. Also, the implantation of alpha's results in a larger dpa-rate in the implantation zone of alpha's in the inert matrix than in the region where solely neutrons, beta's and gamma's are implanted. Fission products (f.p.) have to be accommodated in an even smaller volume fraction of inert matrix than where alpha's are implanted. The largest dpa-rate occurs in the region of inert matrix in which fission products are implanted.

In order to have the same amount of fissile atoms per pellet, more fissile inclusions are required when the radius of the fissile phase is smaller. Since the implantation range of alpha's and fission products is fixed, the volume of inert matrix implanted with fission products and alpha's is larger for micro-dispersed fuels than for macro-dispersed fuels. The relative volume of the implantation zones of inert matrix per fissile inclusion is smaller for macro-dispersed fuels than for micro-dispersed fuel. Therefore, the dpa-rate in the implantation zones of the inert matrix by implantation of fission products and alpha's is larger for macro-dispersed fuel than for micro-dispersed fuel. This is indicated in Figure 1.2 using a darker filling colour for the implantation zones of the macro-dispersed fuel than for the implantation zones of the micro-dispersed fuel. The concentration of fission products is larger in the implantation zones of macro-dispersed fuel than in the implantation zones of micro-dispersed fuel [White et al. 1956] if no diffusion of fission products occurs. Ceramic inert matrices tested up till now and known to the author, show significant larger swelling than UO_2 by implantation of fission products. For macro-dispersed fuels localised swelling, in and near the fissile phase, is expected. For micro-dispersed fuels, a more uniform swelling in the pellet is expected.

The formation of a solid solution between fissile phase and inert matrix may result in:

- 1) fissile atoms diffusing into the inert matrix without change in crystal structures;
- 2) an increase in the uranium concentration of locations with fissile atoms;
- 3) formation of a new phase with a different crystal structure than the individual phases: fissile phase and inert matrix phase.

New phases can also be created by the formation of a solid solution between the fission products/transmutation products and fissile phase/inert matrix.

The empty location on the lattice site that remains after displacement of an atom by implantation is called a vacancy and the displaced atom a self-interstitial. These self-interstitials and vacancies are called extrinsic defects. These extrinsic defects can cluster. Defect-clusters can be dislocation loops (1-D), platelets and stacking faults (2-D), voids and bubbles (3-D). They can be generated and annihilated by implantation.

There are roughly four temperature stages for indicating the thermal impact on defects in materials.

In the first temperature stage, self-interstitials and vacancies are immobile and amorphisation of the material occurs during continuous displacement of atoms.

In the second stage at a higher temperature, self-interstitials are mobile. The self-interstitial can recombine with a vacancy resulting in annihilation of both extrinsic defects and clustering of self-interstitials can occur. Vacancy-clusters generated by implantation till large concentrations of vacancies can be reduced in size by trapping of self-interstitials. Amorphisation is less likely in this second temperature stage than in the first one.

In the third temperature stage, vacancies are mobile by migration of a self-interstitial from a lattice site to an empty vacancy. Besides the three effects described in the second temperature stage, also thermal clustering of vacancies can occur in this third temperature stage.

In the fourth and highest temperature stage, self-diffusion of the constituents in materials takes place by generation of intrinsic defects. The extra source of vacancies and self-interstitials can be used to form larger clusters of defects. But size reduction of clusters can occur by trapping of self-interstitials in vacancy-clusters and dissociation of self-interstitials from self-interstitial-clusters. The annihilation of self-interstitial-clusters is only in the fourth temperature stage not limited to implantation.

The above four stages can occur in metals and ionics (=ceramics). There are a few differences between these two groups. Vacancies in ionics can be charged resulting in polarisation of ions surrounding the vacancy. Due to charged states of vacancies and interstitials, besides elastic interaction between vacancies, self-interstitials and defect clusters also electrostatic interaction occurs. In ionics, the electroneutrality must be fulfilled and therefore only stoichiometric defect clusters are formed. Stoichiometric vacancy clusters are Schottky clusters and stoichiometric interstitial clusters are anti-Schottky clusters. A Frenkel pair is a vacancy plus an interstitial [van Bueren 1961]. The energy to displace cations and anions from their lattice sites may be different in ceramics resulting in a non-stoichiometric ratio of vacancies. For some ionics, Frenkel pairs are only created by implantation. For these ionics, thermal formation of intrinsic defects is energetically more favourable by formation of Schottky defects than Frenkel pairs. Schottky defects are non-interacting vacancies in a stoichiometric ratio.

Fission gases, xenon and krypton, are generated during neutron irradiation of actinides. During neutron irradiation of americium also helium is generated. The generated noble gases can be stored in the perfect lattice as an interstitial or at an interstitial site. "Stored as an interstitial" means that the gas atom is located between rows of atoms; "stored at an interstitial site" means that the gas atom is located in an empty volume present in the crystal structure. For example, in MgO noble gas atoms can only be stored as an interstitial since all cation and anion sites are occupied in the crystal structure. In MgAl_2O_4 , $\frac{5}{8}$ of the cation sites is empty and noble gas can occupy such an interstitial site.

Migration of gas can result in release of gas but when a vacancy is present, the gas atom becomes trapped in a vacancy and migration of gas is stopped. When a gas atom occupies a vacancy then annihilation of this vacancy by recombination with a self-interstitial may not occur. At low temperatures, the gas atom can only be removed from the vacancy by implantation. When more gas atoms are trapped in a vacancy or if the temperature of the sample is raised, the pressure of the vacancy increases and this pressure may exert stress on the

surroundings of the vacancy. Relaxation can occur by creation of a larger room for noble gas or by dissociation of noble gas atoms from the vacancy.

How a larger room than a vacancy for noble gas is created depends primarily on the diffusion coefficient for migration of noble gas, the diffusion coefficient for migration of vacancies and concentration of defects. For example, the migration of helium in metals occurs at room-temperature but vacancies are not mobile at room temperature. Trap-mutation, in which an interstitial is created generating a vacancy next to a helium-filled vacancy, results in a cluster with two vacancies. This process continues when more helium is trapped until a platelet is formed [Evans et al. 1983]. This process of trap-mutation requires the formation of a Frenkel pair. As has been described above, Frenkel pairs in some ionics are only created by implantation. For ionics with a low concentration of vacancies, it is unclear how the pressure of a helium-filled vacancy is reduced. At high concentration of vacancies, the helium-filled vacancy can agglomerate with a nearby empty vacancy at low temperatures. At higher temperatures (migration of vacancy stage) and high concentration of vacancies, an empty vacancy next to the helium-filled vacancy can be generated by migration of an interstitial from a lattice site to an empty vacancy.

When reduction of the pressure of gas in the vacancy by creating a larger space is dominant, swelling of the fuel occurs. When dissociation is dominant, release of gas occurs.

The creation of defects during irradiation also results in reduction of the thermal conductivity causing steeper thermal gradients and therefore a higher temperature of the pellet. The originally thermal gradient is in the order of 100-200 degrees per mm during ordinary reactor conditions. Release of the fission gases, xenon and krypton, reduces the thermal conductivity of the helium-filled gap resulting in a higher temperature of the pellet. Increasing irradiation temperature may result in more release of gas but may also result in generation of (larger fission) gas bubbles or even melting of the pellet.

The cladding may fail when the fuel swells during irradiation causing contamination of the cooling medium by radioactive nuclides which can lead to an increase of the radiation dose for reactor employees. The porosity in pellets can be reduced by radiation induced sintering. Then pellets shrink resulting in a larger gap. This gap decreases the heat transfer between the pellet and the cladding. The gap between the surrounding of the pellet and cladding must be less than 300 μm in order to limit the temperature of the fuel. Pellets should therefore remain stable in volume during irradiation.

Most of the experimental methods that were used to obtain the results in chapter 4 and 5 are described in chapter 2.

Parameters to simulate diffusion of helium in a fuel with MgAl_2O_4 as an inert matrix were obtained by atomistic calculations and experiments. The atomistic calculations of He in MgAl_2O_4 are described in Chapter 3. They comprised: migration energies of He and vacancies, permeation energy of He, dissociation energy of helium from vacancies and vacancy clusters

and swelling. The measured helium release and thermal evolution of concentration profiles in single crystals and polycrystalline samples were used to deduce the empirical activation energies of diffusion of He in MgAl_2O_4 and mechanisms of diffusion. The experiments on single crystals are performed to simulate diffusion processes taking place in the grains of fuel. In polycrystalline materials like fuel, two main groups of defects are present before irradiation; these are grain boundaries (2-D) and inter-and intragranular pores (3-D). Which diffusion processes, those taking place within the grain or those taking place between the grains, may be dominant for diffusion of helium is discussed in Chapter 4. Literature data about helium implantations in MgAl_2O_4 , is also described in Chapter 4 in order to obtain a qualitative judgement on the potential of MgAl_2O_4 as an inert matrix for neutron irradiation with americium.

The inert matrices for macro-dispersed fuels in chapter 5 are: MgAl_2O_4 , MgO , Y_2O_3 , $\text{Y}_3\text{Al}_5\text{O}_{12}$ and CeO_{2-x} . These inert matrices have proven to have negligible swelling during neutron irradiation. They are tested for fission product implantation in this thesis. UO_2 is used as a fissile phase to simulate the fission product implantation that would also be generated by americium and plutonium. Fissile phases in the tested macro-dispersed fuels are pure uranium-oxide inclusions and inclusions diluted in uranium: $\text{UY}_{5.94}\text{O}_x$. Also, one micro-dispersed fuel of UO_2 and MgAl_2O_4 is tested.

The irradiation temperature of the inert matrix fuels discussed in chapter 5 was relatively low: 700-1000 K. As ceramics have a relatively high Young's modulus at these temperatures, the building up of stress, by a slight deformation of the inert matrix to accommodate the swelling fissile phase, is large. This impact, caused by low irradiation temperatures and the geometry of fissile phase and inert matrix, on the degradation of inert matrix fuel is discussed in chapter 5. The impact of the formation of a solid solution between fissile phase and matrix is discussed in chapter 4 and 5.

2 Experimental methods

The experimental methods to obtain results for simulation of diffusion of helium in fuel with MgAl_2O_4 as an inert matrix are described in this chapter. Implantation of helium in MgAl_2O_4 was performed using electrostatic accelerators and by decay of ^{241}Am . The concentration profiles after isothermal stages were measured using Neutron Depth Profiling (NDP). The helium release was monitored using Thermal Helium Desorption Spectrometry (THDS). The kinetics of helium diffusion in MgAl_2O_4 can be determined using NDP and THDS. These results, for implanted single crystals and polycrystalline samples, are described in chapter 4.

A variety of techniques was used to assess the material degradation of Inert Matrix Fuels (IMF) and actinide- and fission product distribution after neutron irradiation. With gammaspectrometry of the capsule, the release of cesium can be assessed and the length of the fuel stack was determined. Fission-gas release of these fuels was determined by measurement of the volume and pressure of the plenum, mass-spectrometry of gas from the plenum and calculation of the generated fission gases. Dimensional measurements, in order to obtain the dimensional change of the pellets, were performed using a micrometer. Micro-observations of the inside of the pellets could be obtained by ceramography. Actinide- and fission product distribution in the pellet was qualitatively determined from α - and β,γ emitting nuclides by α - and β,γ -autoradiography and quantitatively by Electron Probe Micro Analysis (EPMA). The mechanical properties: hardness and fracture toughness of the materials, were deduced from indentation measurements. The results obtained of IMF using these techniques are described in chapter 5.

2.1 Implantation of helium in materials

2.1.1 α -emission from americium

α -particles emitted during decay of ^{241}Am were implanted in a single crystal. The ^{241}Am -source (ISO 233 33), obtained from Czech Metrological Institute, contained $^{241}\text{AmO}_2$ mixed with silver powder. This mixture was deposited on a 0.25 mm silver foil covered with 2 μm gold. The active diameter of the source was 11 mm. The amount of radioactive impurities was less than 0.1%. About four years before start of this implantation, the activity of the ^{241}Am was measured to be 409.6 kBq with a measured flux of emitted α -particles from the source of $2.042 \times 10^5 \text{ s}^{-1}$. The energy of the emitted α -particles was measured to be $4.52 \pm 0.166 \text{ MeV}$. The energy loss of the initially emitted 5.483 MeV α -particle is due to the covering of silver and gold. At start of the implantation, the activity was reduced to 406.7 kBq. The single crystal was irradiated for about 4 months and the variation in flux of α -particles between start and end of implantation was 0.04%.

2.1.2 Electrostatic accelerator

The 30 keV helium implanted samples presented in this thesis were produced with the 30 kV electrostatic accelerator DANFYSIK at the Interfaculty Research Institute (IRI) in Delft. ^3He was used for implantation. From a storage bottle ^3He flowed into an ionisation chamber at pressure of $3\text{-}6 \times 10^{-3} \text{ Pa}$. Figure 2.1 shows the ion beam transport.

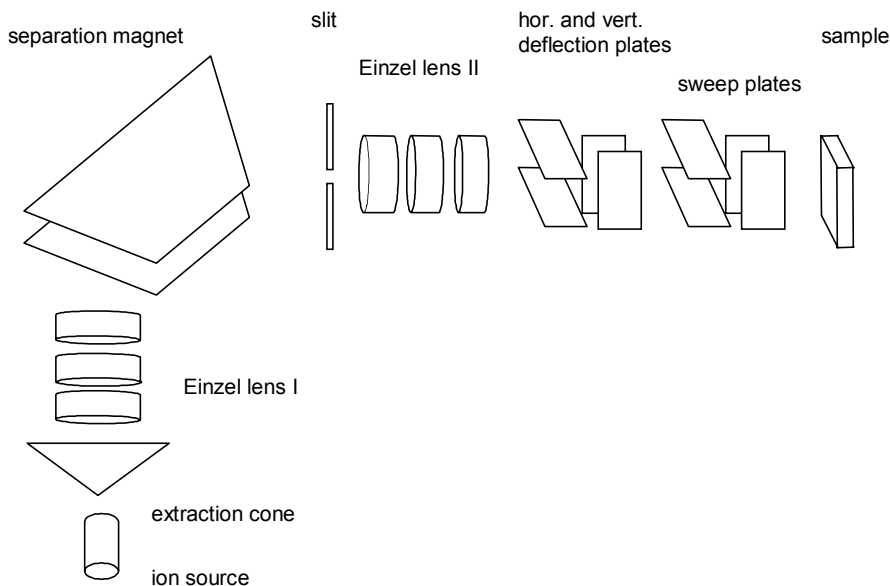


Figure 2.1 Geometry of ion beam transport, picture drawn by Fedorov [Fedorov 2000].

The ionisation chamber (ion source in Figure 2.1) was composed of an anode and a tungsten filament; the hollow cathode. The electrons emitted from this filament stripped one electron from the neutral ^3He atoms by applying a current of about 20-25 A. The bundle of

emitted electrons from the filament was compressed by magnetic coils in order to increase the electron density. The positive charged helium ions were transported to the cathode by applying a charge on the anode of about 60-90 V. A bundle of these ions was created by an extraction cone at ground potential, the ionisation chamber at high voltage (30 kV) and electrostatic lenses (Einzel, set I) that focussed the ion beam in front of a separation magnet.

The 30 keV ${}^3\text{He}^+$ ions were separated from other ions present in the ion beam, like charged hydrogen, using this magnet. The energy of the ion E is equal to the charge of the ion times the accelerator voltage ($q \times U$) from which the velocity of the ${}^3\text{He}$ -ion can be calculated ($E = \frac{1}{2}mv^2$). The force on the ion by the magnetic field is:

$$F = qvB \quad (2.1)$$

where q is the charge of the ion, v is the velocity of the charged helium ion ($v = \sqrt{2qU/m}$) and B is the magnetic field. The centripetal force is equal to:

$$F = \frac{mv^2}{R} \quad (2.2)$$

where m is the mass of the ion and R is the radius of magnet (40 cm). Only ions that match $R = \frac{1}{B} \sqrt{\frac{2mU}{q}}$ passed the magnet to electrostatic lenses (Einzel, set II). The focused beam was guided by deflection plates. Sweep generators were used to have the whole area of the sample (1 cm²) implanted with ions. The current for the separation magnet was electronically controlled as was the implanted dose; the dose was calculated using a nano-ampere meter [Fedorov 2000].

The quantity of implanted ${}^3\text{He}^+$ ions is related to the current measured with a nano-ampere meter. The surface was biased in order to prevent escape of secondary electrons from the surface generated during implantation, these secondary electrons would be counted as implanted ions. For metals it is easy to understand that the excess of positive charge, generated by implantation of ${}^3\text{He}^+$ ions, can be compensated by flow of electrons because of their high electrical conductivity. But MgAl_2O_4 is an insulator and therefore has a band gap. However, during implantation, the sample emits light. This light may be composed of photons that are emitted when electrons from the conduction band fall into the ground state (valence band). The presence of electrons in the conduction band, for the necessary electrical conductivity, was caused by implantation.

The current during implantation was about 1–2 μA for the 30 keV implanted samples. The 900 keV implanted samples were implanted with a current of 700-800 nA using a van de Graaf accelerator at CERI in Orleans.

2.2 Examination of thermal behaviour of helium implanted samples

2.2.1 Neutron Depth Profiling

The distribution of helium in samples can be determined using NDP. The implanted ${}^3\text{He}$

atoms fission into reaction products during irradiation with thermal neutrons. The energy of the reaction products is used to determine the depth of helium in the sample. This paragraph describes briefly how a pure thermal neutron beam was generated and the experimental set-up with which the energy of the reaction products was measured.

A purely thermal neutron beam was generated using a Stacked Neutron Guide (SNG). The onset of the SNG is at 1 meter from reactor core of the HOR¹ at IRI. The SNG consists of a parallel stack of slightly curved glass plates coated with ⁵⁸Ni. Thermal neutrons are reflected between the coated glass plates. Fast neutrons and gamma's are scattered and absorbed in the shielding surrounding the SNG. Thus at the exit of SNG nearly only thermal neutrons are emitted. The thermal neutron flux at the exit of the SNG used for NDP-measurements was about 3×10^7 neutrons $\text{cm}^{-2}\text{s}^{-1}$ [van Well 1992].

Figure 2.2 shows the experimental set-up of NDP.

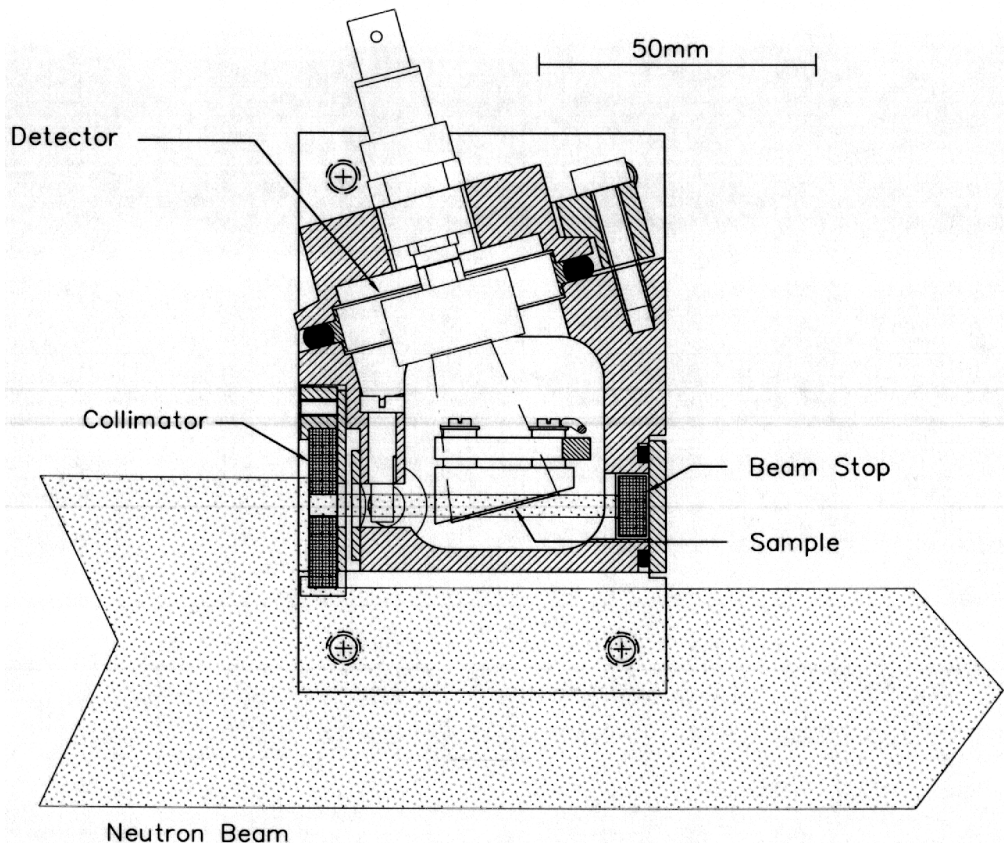


Figure 2.2 Experimental set-up of NDP, picture drawn by F. Labohm.

The collimator and beam stop in Figure 2.2 are made of ⁶Li₂CO₃. ⁶Li absorbs thermal neutrons without the generation of gamma's. The Si-detector had an energy resolution of 12.5 keV FWHM (Full Width at Half Maximum). The MCA (multi-channel analyser) channel width was 3.1 keV. The detection limit was about 10^{14} ³He cm^{-2} [van Veen et al. 1999]. The

¹ Hoger Onderwijs Reactor (Reactor for research at Higher Education level)

implanted surface of the sample was facing the detector. A rough vacuum was attained by a backing pump to prevent straggling and energy loss of the emitted reaction products from the surface of the sample during their travel to the detector.

Sites with ^3He are isotropic sources of protons and tritons during neutron irradiation. The following reaction takes place during neutron irradiation:



Some of these reaction products are emitted to the surface of the sample. The energy of these reaction products is reduced by numerous interactions with the electrons of the matrix. The energy loss with respect to the initial energy of the proton is determined by the distance through which the proton had to travel to reach the surface of the sample. The depth of the ^3He is determined by the density of the sample and calculated data about the energy loss per unit length (stopping power) of this sample using SRIM [Ziegler et al. 2002]. Figure 2.3 shows the data processing, derived from Fink [Fink 1996].

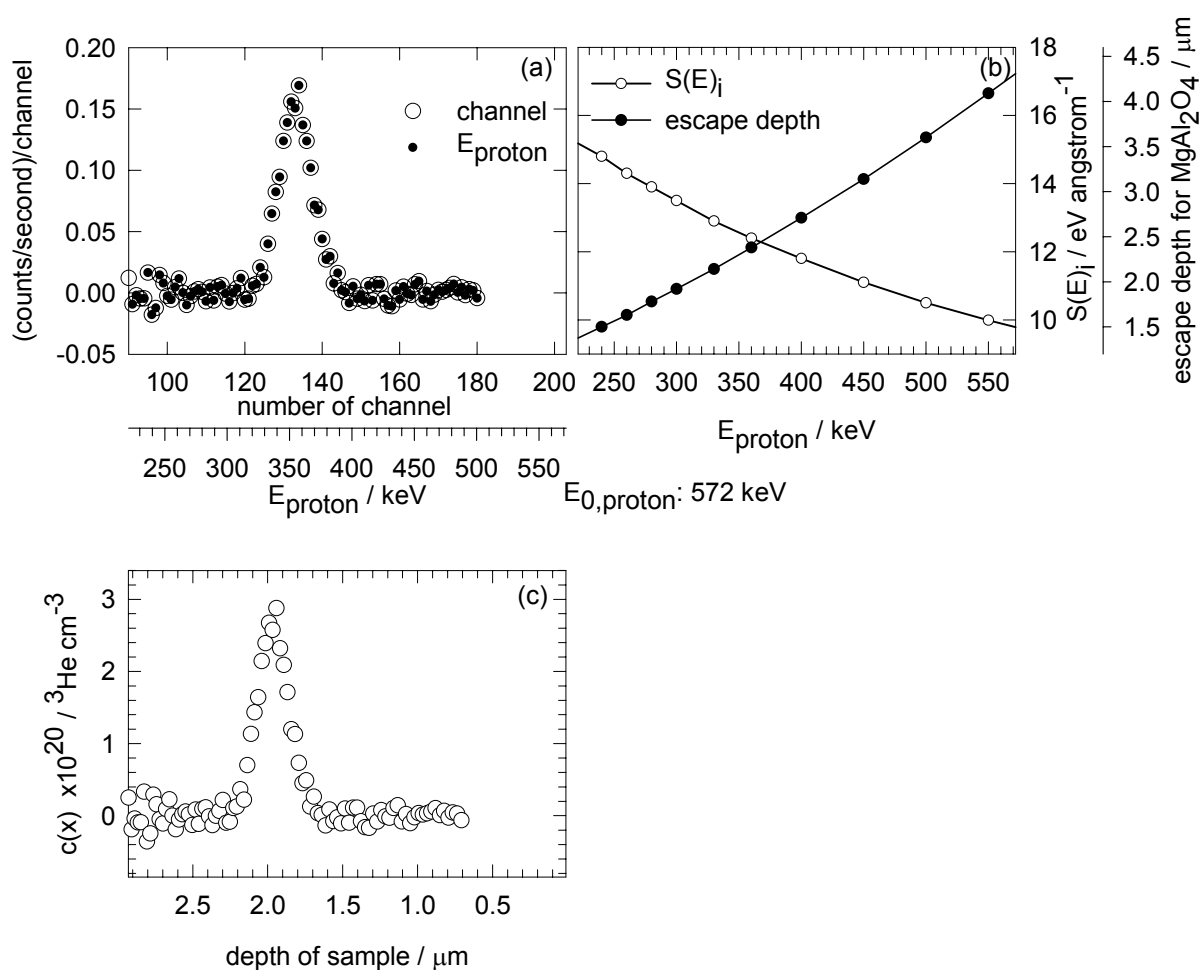


Figure 2.3 (a) NDP measurement, (b) calculated stopping power and escape depth and (c) NDP result.

The concentration at a specific position in depth was determined by:

$$[{}^3\text{He}]_i = \frac{N_i}{f\sigma \frac{\Delta E/\text{channel}}{S(E)_i}} \quad (2.4)$$

where N_i is the actual measurement in (counts/second)/channel, f is the calibration factor, σ is the absorption cross section for thermal neutrons for ${}^3\text{He}$ (5333 barn) [Downing et al. 1993], $\Delta E/\text{channel}$ is the energy step per channel (channel width) and $S(E)_i$ is the stopping power for that specific energy of a reaction product. The calibration factor is measured about every 3 months and has the unit (counts/second)/(at/cm²)/barn. The concentration of helium in the 900 keV implanted samples was calibrated using the standard reference material SRM 2137 from NIST (National Institute of Standards and Technology), a 50 keV ${}^{10}\text{B}$ implanted sample of silicon.

Only the energy spectrum of the protons was measured for the results described in this thesis. The background for the triton was too large to be able to measure its energy and the triton cannot reach the detector at all at implantation depths of ${}^3\text{He}$ larger than about one μm for MgAl_2O_4 .

Stopping power depends on the density of the sample and energy of the proton. The escape depth for a proton with a specific energy is larger for polycrystalline samples than for single crystals since fewer electrons per unit volume are present in these samples due to the presence of pores. For the results described in chapter 4, it is assumed that the density in the sample is uniform.

2.2.2 Thermal Helium Desorption Spectroscopy

THDS can be a useful tool for identification of defects and defect-clusters. Usually, helium implantations in samples are performed in the THDS equipment. This implanted gas is released during heating of the sample. Defects generated during implantation may have clustered and the sample is again implanted with helium, below the threshold energy of displacement of atoms from their lattice sites, in order to fill the defect clusters with gas. Again the sample is heated and the gas release is monitored from the defect clusters [van Veen et al. 1979, van Veen 1991].

In the present study, helium was not implanted in the THDS equipment but elsewhere. The THDS equipment, used for the performance of results described in this thesis, comprised: furnace volume, pumps to attain Ultra High Vacuum (UHV), direct calibration system and a quadrupole mass spectrometer. Figure 2.4 shows the furnace volume and scheme of the entire system to attain vacuum.

The furnace volume consisted of a tungsten crucible, filament (W) surrounded by a metal grid; a Mo shield, thermocouples and a cooling shield. The crucible is attached to a platform. This platform can be detached from the system.

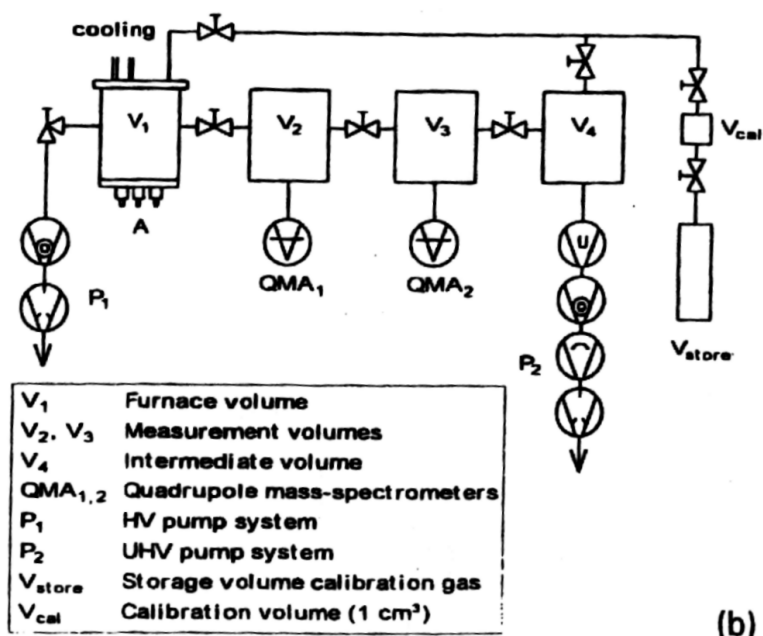
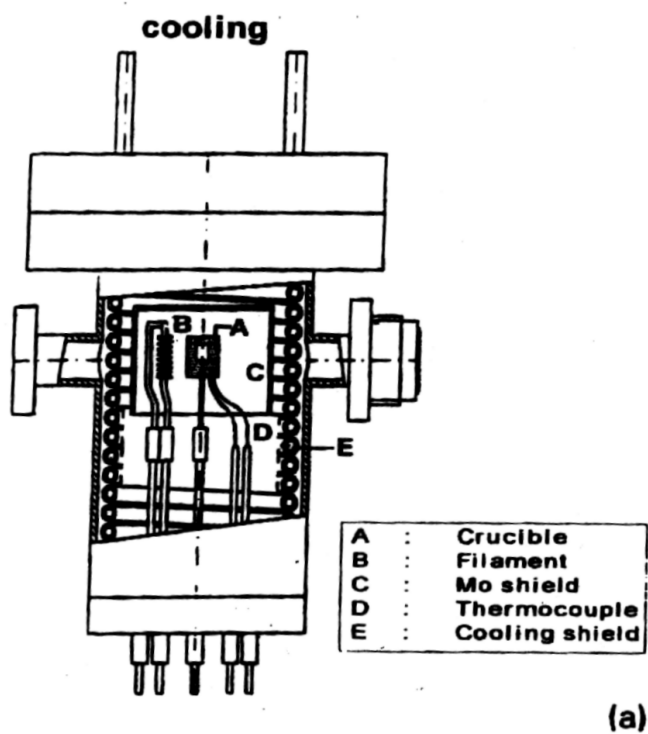


Figure 2.4 Furnace volume (a) and scheme of the entire system to attain vacuum [van Veen et al. 1999]

The helium implanted sample was put in the crucible and the platform was made gas tight with the furnace volume from the atmosphere using Cu rings that are replaced each time a new sample is put in the crucible. Air is incorporated during placement of the sample in the furnace volume. The furnace volume is first heated by an external heat source at about 473-523 K and air is pumped away (P_1 in Figure 2.4) for at least 15 hours in order to limit the background (hydrogen) during measurement. Initially, after heating by the external source, the pressure in the crucible was about 10^{-6} Pa.

Usually, samples are heated by emission of infra-red radiation from the crucible. This is performed by applying a voltage on the filament that results in bombardment of electrons on the crucible. The negatively charged metal grid surrounding the filament direct the electrons to the positively charged crucible. Electromagnetic radiation in the near-infrared region results from excitation of the electrons in the crucible. The radiation by tungsten (W) is as a black body; a continuous spectrum depending on the temperature of W. The temperature of the crucible is controlled by voltage (0-2.5 kV) and current (0.8-2 μ A) on the filament and monitored by thermocouples (Pt/Pt-10%Rh). A Mo shield reflects the radiation. The cooling shield consists of a metal tubes spiral with flowing liquid nitrogen surrounding the crucible. During heating of the sample, the pressure in the crucible was about 10^{-3} - 10^{-4} Pa.

A very low pressure is required to use quadrupoles to measure the helium released from the sample (about $(3-10)\times 10^{14}$ atoms) in the heated crucible. This was performed by, installed in series, fore pump, oil diffusion pump, turbomolecular pump and titanium getter pump. The fore pump can attain pressures near the vapor pressure of lubricating oil (~ 0.5 Pa), the oil diffusion pump attains pressures near the vapor pressure of the used oil ($\sim 2\times 10^{-4}$ Pa). The turbomolecular pump, in which large molecules like oil are eliminated, has a compression ratio of about 10^4 . In the titanium getter pump, titanium is sublimised and precipitated on the wall that is cooled with water. Gases like CO_2 , O_2 are buried during precipitation of titanium. UHV conditions (P_2 in Figure 2.4) achieved with the THDS equipment results in a total pressure $< 2\times 10^{-8}$ Pa.

The direct calibration system consists of two calibrated volumes; 1000 cc and 1 cc, helium flask, tubes, valves and a baratron. Helium is flowing from the flask into the volume with 1000 cc till a known pressure using the baratron that contains membranes with which the pressure can be measured. 1% Of the helium is transported into the 1 cc volume and tubes by opening the valve between the 1 cc volume and 1000 cc volume. Tubes and 1 cc volume amount a calibrated volume of 10 cc. After closing this valve, the amount of helium is transported to the furnace volume and then to the quadrupole (Balzers QMG 111B analyser) with which the number of helium atoms per count per second can be obtained. The measured signal of the quadrupole is proportional to the partial pressure of gas in the 1 cc volume. The measured variation in the calibration factor (number of He atoms per count per second) was 6.1% between two calibration procedures with a time interval of 18 months.

The quadrupole is calibrated with ^4He . The relation between the partial pressure of gas $P(t)$ and desorption rate $L(t)$ are related as follows [Fedorov 2000]:

$$L(t) = \frac{dP(t)}{dt} + \frac{S}{V} P(t) = \frac{dP(t)}{dt} + \frac{P(t)}{\tau_{res}} \quad (2.5)$$

where S is the pumping speed, V is the volume of the desorption chamber and τ_{res} is the average residence time of gas in the desorption chamber. The rate of escape of gas from a container through a hole into vacuum depends on the collision frequency. The collision frequency of ^3He is $\sqrt{4/3}$ times larger than ^4He due to the $\sqrt{4/3}$ times larger velocity and therefore the rate of effusion of ^3He will be faster than ^4He . The calibration factor is multiplied by $\sqrt{4/3}$ to adjust the smaller time in flight in the system of ^3He compared to ^4He . The data acquisition was performed as described by Veen et al. [van Veen et al. 1979] and Fedorov [Fedorov 2000].

2.3 Pre and post irradiation examination of fuels

2.3.1 Gammaspectrometry

The pins contained steel plugs, pellets with and without UO_2 and a spring. After neutron irradiation, the locations of pellets, plugs and spring can be determined by gammaspectrometry using the radioactivity caused for example by decay of fission products in the pellets with UO_2 and by decay of ^{54}Mn ; an activation product of steel. In the present study, the activity of the capsule was measured for 500 seconds and the displacement bench moved the capsule 0.4 mm higher in front of the collimator after each measurement step. The capsule is not rotated during the displacement, thus the axial distribution of isotopes is determined for a specifically circumferential position. The gamma's of each nuclide excite an amount of electrons in the Ge-detector depending on the applied voltage. A device that emits pulses with an energy of 1.630 MeV with a frequency of 50 Hz is used to correct for dead time. The Ge-detector is a high purity Ge-detector GC1518 with a range between 20 keV to 1700 keV. The precision, measured with a ^{60}Co -source, is 1.9 keV. The collimator slit height and slit width for the EFTTRA-T3 capsules described in chapter 5 were 0.4 mm and 15 mm, respectively [LSO 1997].

Only the relative activity is measured since no radioactive sources are used to calibrate the equipment. The detected number of counts for all capsules is corrected for radioactive decay. This makes it possible to compare the capsules if the absorption of gamma's in each material is taken into account and if the same amount of nuclides could be measured.

2.3.2 Pressure and volume of plenum

Before neutron irradiation, helium in the plenum is at atmospheric pressure. The plenum is that location of the capsule with no solid material. Neutron irradiation of sample material with uranium-oxide generates the fission gases xenon and krypton. Fission gases can be retained in the sample material or released. Release of fission gases result in a higher pressure of the plenum in the capsule.

The volume of the plenum and amount of gas atoms in the plenum must be known in

order to determine this higher pressure in the plenum after neutron irradiation. This paragraph shows that these two parameters are measured in a similar manner. The transport of gas from an unknown volume to a calibrated volume was performed by means of flowing mercury. The amount of gas atoms was determined using a manometer at atmospheric pressure. Figure 2.5 shows a simplified version of the experimental set-up. First, the determination of the plenum volume is described.

The room, in which that part of capsule with plenum was positioned, was gas-tight with the surrounding. This room was filled with helium till atmospheric pressure before perforation of the capsule. This amount of helium was pumped into the room of gas collection (calibrated volume $V_{V,calibrated,V1}$) using a pump-device with which the occupied volume of mercury in tube A determines the flow of gas as shown in Figure 2.5B.

A vacuum pump (Edwards) removes air situated above mercury in the mercury vessel. Gas flows from the perforation room to tube A. Input of air rises the level of mercury in tube A. A capillary barrier is removed when mercury in tube A reaches a certain level. Gas flows from tube A into the burette. The situation in Figure 2.5A is when the input of gas from the mercury tube A to the burette is finished. This process is repeated until all gas from the perforation device is situated in the calibrated volume ($V_{V,calibrated,V1}$).

A manometer positioned above the mercury-pump was composed of one leg as a burette and a tap between both legs. A burette is a tube with graduation, in the present study with an interval of 0.01 ml. The burette was set exactly to the level of 10.00 ml by rising the level of mercury in tube B. The burette was closed from the rest of the volume where helium was collected. The tap between burette and the other leg of the manometer (tube C) was opened. The collected helium in the burette, closed from the rest of helium in the volume of gas collection, was then at atmospheric conditions and the level from the burette was read. All helium in the experimental set-up was pumped to the surrounding till the pressure of the experimental set-up was smaller than 1.3 Pa. This process was repeated two times. The procedure was also performed after perforation of the capsule. The volume of helium in the perforation room is before perforation smaller than after perforation and thereby the level of the burette before perforation ($L_{V,burette,before}$) is smaller than after perforation ($L_{V,burette,after}$) since the perforation room before and after perforation is filled with helium till atmospheric pressure. The volume of the plenum can be determined by:

$$V_{plenum} = \left\{ \frac{L_{V,burette,after} - L_{V,burette,before}}{V_{burette}} \right\} \times V_{V,calibrated,V1} \quad (2.6)$$

where $V_{burette}$ is the calibrated volume of the burette (10.00 ml) and subscripts $_V$ denote that these parameters are used to determine the volume of the plenum.

For determination of the amount of gas in the capsule, the pressure in the experimental set-up was smaller than 1.3 Pa before perforation of the capsule. The puncturing device makes a hole in the capsule and gas in the capsule expands in the perforation room. This gas from the plenum was pumped to a calibrated volume ($V_{P,calibrated,V2}$).

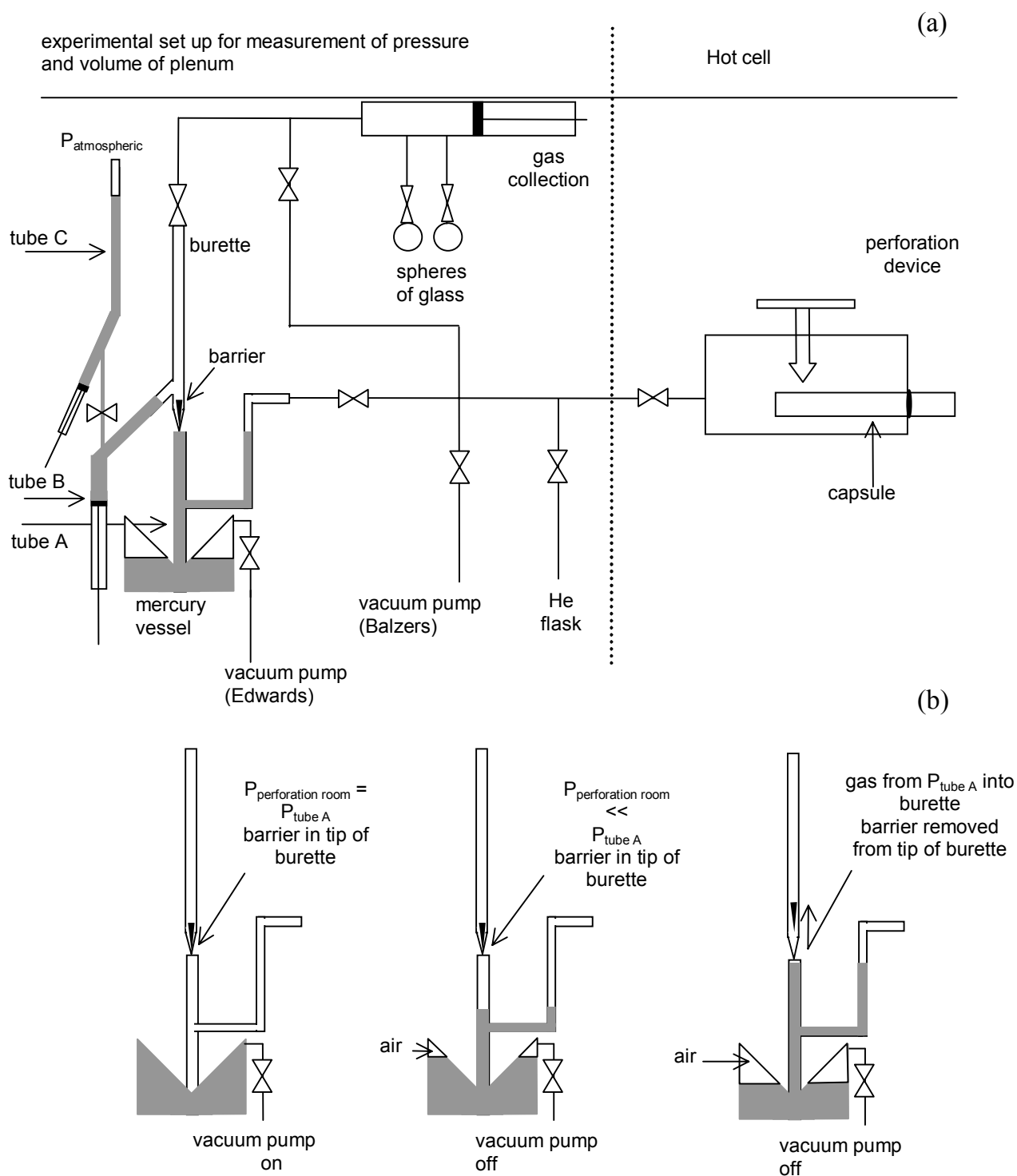


Figure 2.5 (a) Simplified version of experimental set-up for measurement of volume and pressure of plenum (derived from NDO-PUNCT-AV/1 [LSO 1997]). Grey area indicates a volume of Hg occupying the experimental set-up. (b) Flow of gas from perforation room via mercury vessel to the burette.

($V_{P,calibrated,V2}$ is smaller than $V_{V,calibrated,V1}$). Again the level from the burette was read at atmospheric conditions, similarly for the measurement of the plenum volume ($L_{P,burette}$). The pressure in the calibrated volume $V_{P,calibrated,V2}$ before opening the tap between tube B and tube C was:

$$P_{calibrated,V2} = \frac{P_{atm} \times L_{P,burette}}{V_{burette}} \quad (2.7)$$

The pressure of the plenum at temperature conditions of the experimental set-up is:

$$P_{plenum} = \frac{P_{calibrated,V2} \times V_{P,calibrated,V2}}{V_{plenum}} \quad (2.8)$$

The temperature and pressure surrounding the experimental set-up was measured during performance of results, these parameters were usually room-temperature and atmospheric pressure. Some of the gas originating from the plenum was moved to the spheres of glass by opening the valves. The taps on these spheres were closed and detached from the system for measurements of the isotopic composition of gas using mass-spectrometry. This equipment was calibrated with flasks containing difference ratios of helium, krypton and xenon.

The error for the measurement of volume of plenum was 0.06 ml for the results described in this thesis. This error was propagated to the error in the pressure of the capsule. The reproducibility was better than 0.5%. The accuracy of the fission gas analyses with the mass-spectrometry system is better than 5% [Belvroy et al. 1998].

2.3.3 Dimensional measurements

Pellets were measured with a Mitutoyo low force digital micrometer with a precision of ± 0.002 mm. The diameter of the face edges of the micrometer was 6.30 mm. This micrometer consisted of a case with a clack mechanism with a force on the measuring object between 5 to 10 Newton. The measurements were performed at room temperature.

The pellets had a somewhat conical shape (before and after irradiation) which complicates the measurement of the diameter in an identical manner before and after irradiation. Before irradiation, the diameter of the pellet was measured three times with 120 degrees between each measurement. Most pellets could be placed between the face edges of the micrometer and the bottom of these pellets was measured since almost any pellet had a height of less than 6.30 mm. After irradiation, the diameter of the pellet was measured near the top of the pellet and at the bottom of the pellet. The complex remote handling of the pellets in the hot cell after irradiation made it technically impossible to place the complete pellet between the face edges of the micrometer but placing one side of the pellet between the face edges was feasible.

Gammasspectrometry, ceramography and profilometry were used to determine the dimensions of the pellets after irradiation if pellets could not be measured using a micrometer. These techniques are less accurate than the micrometer measurements.

2.3.4 Ceramography

For the preparation of the ceramographic sections, pellets were embedded in the resin Hysol. After solidification of the Hysol, pellets were perpendicularly cut, in transverse and axial sections of the pellets. The sections were grinded down in five subsequent stages using SiC-coated sheets with particles ranging in size from 80 μm down to 20 μm . The grinded sections were polished in three subsequent stages using diamond paste with particles with a size from 6 μm down to 0.25 μm . Photos with magnifications from 15 \times till 500 \times were made from these sections using light microscopy (Leitz MM 5RT).

2.3.5 α -and β,γ autoradiography

For α -autoradiography, the ceramographic sections were placed on an aluminium foil with a thickness of 0.009 mm and the film Kodak-Detector-CN85. The aluminium foil was situated between the ceramographic section and film. This foil had the purpose to render the visibility of scattered emitted α -particles in order to maximise the visibility of α -particles that were more perpendicular emitted with respect to the film. All films were irradiated by α -particles for five minutes.

For β,γ autoradiography, the time of exposure ranges from 5 to 30 minutes on films of Kodak Spectroscopic type 649.O. The variation in time of exposure was performed to maximise the visibility of locations with β,γ -emitting nuclides without burning a hole in the film.

2.3.6 Electron Probe Micro Analysis

The EPMA measurements were performed using CAMECA MS46 [Groot et al. 1988]. For the results described in chapter 5, the acceleration voltage was 25 keV, the diameter of the bundle of electrons was 1 μm , the beam current was varied between 50 to 250 nA. The ceramographic sections (see paragraph 2.3.4) were coated with Au. The coating of Au was necessary to induce electric conduction.

X-rays were emitted during implantation of electrons. Nine crystals were present to identify the wavelength of the emitted X-rays [Groot et al. 1988]. Four detectors were available to measure the intensity, simultaneously, of the X-rays. The detectors were at 18 degrees from the surface of the sample.

About 50 standards were available to obtain quantitative measurements using the measured signal from the sample and the measured signal from the standard [van den Berg et al. 1999]. The ZAF correction, ZA for the correction of absorption of emitted X-rays by the sample and F for the correction of re-emitted X-rays, was used for the transformation of counts of each nuclide to the weight percentage (wt%).

2.3.7 Indentation

Indentation measurements in the ceramographic sections at room temperature in air were performed using a Vickers diamond pyramid with 136 degrees on polished samples. Figure 2.6

shows a simplified figure of the geometry after the indentation.

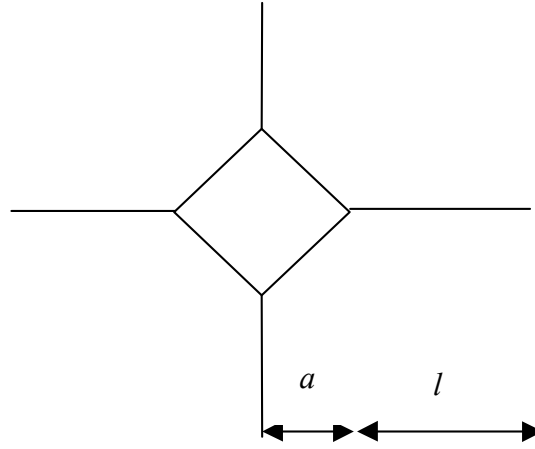


Figure 2.6. Geometry after indentation.

The indentation loads were applied for 10 seconds. The applied load rate was about 1 to 2 gram s^{-1} using a pneumatic device (Leitz Wesar type 16351-560R) with a weight of 100 or 200 grams. The Vickers hardness has been determined using [Morrel 1985]:

$$H_v = 1.8544 \times \frac{M}{\{2 \times a\}^2} \quad (2.9)$$

where M is the indentation load in kilograms and $\{2 \times a\}$ is the size of the imprint diagonal in millimeters. Fracture toughness for $0.25 < l/a < 2.5$ is calculated using [Niihara 1982]:

$$K_{Ic} = \left\{ \frac{0.035 H_v \sqrt{a}}{\Phi} \right\} \times \left\{ \frac{E\Phi}{H_v} \right\}^{0.4} \times \left\{ \frac{l}{a} \right\}^{-0.5} \quad (2.10)$$

where H_v is the Vickers hardness in MPa^2 , E is the Young's Modulus, Φ is the constraint factor with a value of 2.7 [Solomah 1990], l is the crack length from the corner of the indent, l and a both in meters. Cracks have been measured parallel along the diagonal of the indent with the corner of the imprint as the origin. For the experimental condition $l/a > 2.5$, the following equation is used [Niihara 1982]:

$$K_{Ic} = \left\{ \frac{0.129 H_v \sqrt{a}}{\Phi} \right\} \times \left\{ \frac{E\Phi}{H_v} \right\}^{0.4} \times \left\{ \frac{c}{a} \right\}^{-1.5} \quad (2.11)$$

where $c = l + a$. The images of the indentations were directly taken after the indentation using light microscopy (Reichert Telatom) with which photos with a magnification till $1200\times$ were made. The sizes of the crack lengths and diagonals of the indent were measured using image analysis.

² H_v in kg/mm^2 times g is the gravitational acceleration of $9.81 m/s^2$ result in MPa .

3 Modelling of helium in MgAl_2O_4

About 10% of the actinide inventory in long-lived nuclear waste is americium. Fission of americium in an inert matrix would eliminate this actinide and thereby reduce the amount of long-lived nuclear waste. MgAl_2O_4 is a promising inert matrix since it is dimensionally stable during neutron irradiation and its chemical interaction with water and sodium at elevated temperatures is minor. During transmutation of americium, helium is generated in far larger amounts than the fission gases xenon and krypton [see Chauvin et al. 2002]. This helium is either released during irradiation or forms bubbles and thereby causes swelling. Predicting the behaviour of helium in ceramic matrices such as MgAl_2O_4 is therefore an important parameter in order to judge whether it is safe to irradiate americium in for example MgAl_2O_4 .

In this chapter, the modelling of transport of helium in MgAl_2O_4 is considered in a two-way approach. First, the helium interactions in the lattice of MgAl_2O_4 are considered. These atomistic calculations were performed using the Mott-Littleton Methodology as implemented in the code CASCADE. The migration and permeation energy of helium in MgAl_2O_4 and dissociation energy of helium from vacancies and vacancy-clusters as well as swelling due to helium, vacancies and vacancy clusters are calculated using this methodology. Secondly, the transport of helium in MgAl_2O_4 using different diffusion mechanisms is discussed. This rate-diffusion theory is especially written for helium implanted matrices: single crystal semi-infinite media as well as polycrystal semi-infinite media. Such an approach is useful because implantations are used to simulate the behaviour of materials during irradiation without generating nuclear waste.

3.1 Structure of $MgAl_2O_4$

$MgAl_2O_4$ is an ordered solid solution of MgO and Al_2O_3 . The crystal structure of $MgAl_2O_4$ is cubic with spacegroup $227 Fd \bar{3} m$. The three types of atoms occupy the following Wyckoff sites: 8(a) for Mg, 16(d) for Al and 32(e) for O. The coordinates of O within this space group are described by the variable x or u that has a value of 0.387 [Wyckoff 1965 and Hahn 1993]. One unit cell of $MgAl_2O_4$ contains 8 $MgAl_2O_4$ molecules ($Z=8$). Figure 3.1 shows the [100] and [110] projections of the unit cell.

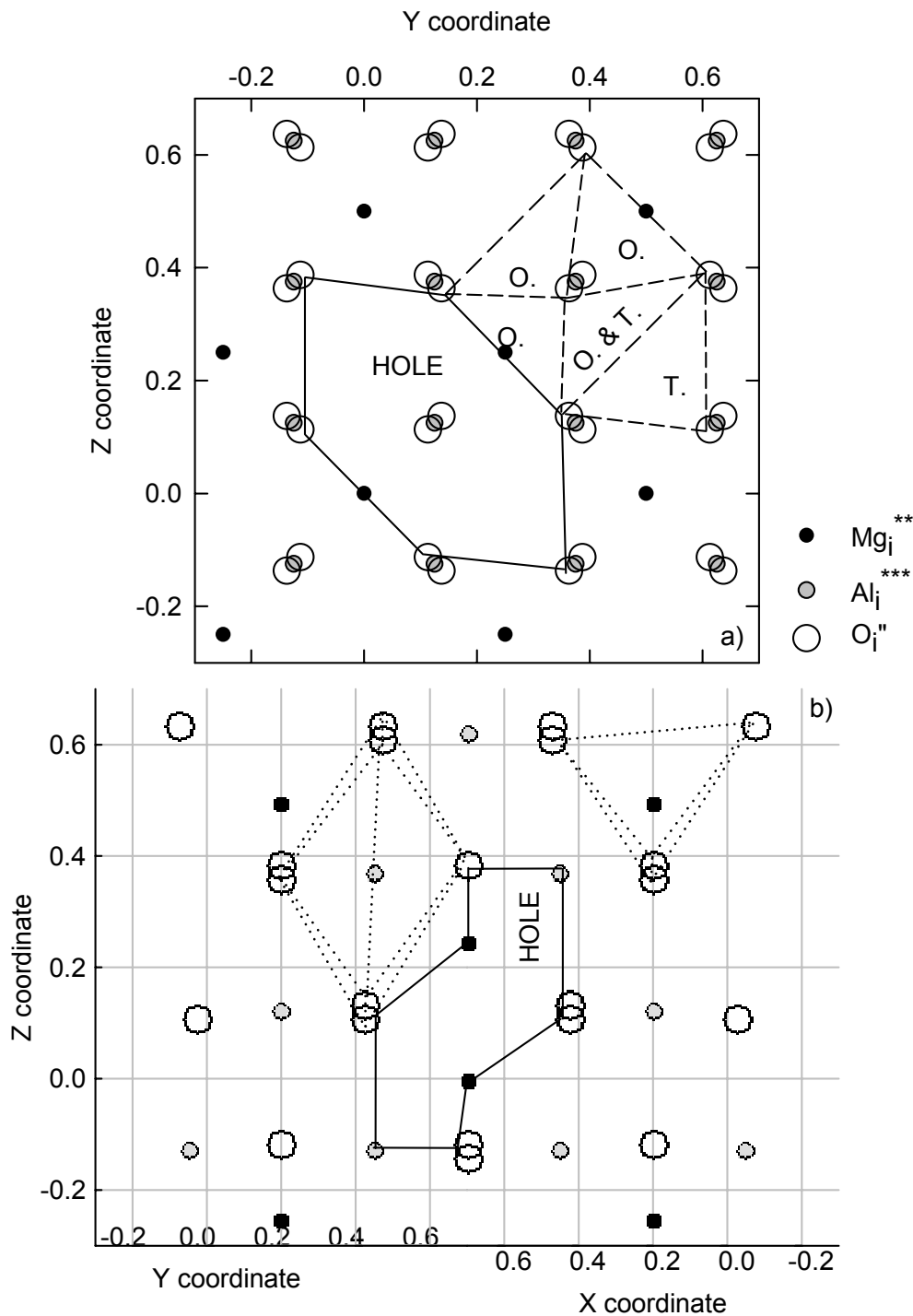


Figure 3.1
Arrangement of ions in unit cell of $MgAl_2O_4$. a) the [100] projection showing a hole (solid lines) and faces of an empty octahedral site (O) and tetrahedral site (T.) (dashed) lines. The centres of the holes are the centres of the empty octahedral sites and b) the [110] projection showing hole (solid lines) and an occupied octahedral site and tetrahedral site (dotted lines).

The oxygen sublattice in the crystal structure of MgAl_2O_4 has an FCC arrangement in which there are octahedral interstitial sites and tetrahedral interstitial sites. In the normal structure, aluminium ions occupy 50% of the octahedral sites and magnesium ions occupy 12.5% of the tetrahedral sites. Other octahedral and tetrahedral sites are empty.

This perfect lattice of MgAl_2O_4 therefore has large unoccupied interstitial sites that will be described as holes. A hole in the structure is an aggregate of six halves and two quarters of empty tetrahedral sites and one empty octahedral site. In Figure 3.1a, one half of an octahedral site of these holes is shown. It does not look like an empty octahedral site in the [100] projection because an aluminium ion and oxygen ion are at about half a unit cell length below the centre of the octahedral site. However, in the [110] projection in Figure 3.1b it can be seen that the hole is empty. Parts of an empty tetrahedral site are drawn in Figure 3.1a for the same hole. The sharing of the empty tetrahedral sites between the empty octahedral sites results in a zigzag network of corridors. Figure 3.1b shows an octahedral site occupied by an aluminium ion and a tetrahedral site occupied by a magnesium ion.

3.2 Mott-Littleton methodology

3.2.1 Theory

The perfect lattice consists of an array of point charges. The point charges of the cations (Mg and Al) are in the model described as cores (X). The anion O consists of a massless shell with a charge (Y) surrounding the core; shell and core are coupled by a harmonic spring^a. The polarizability of an ion using the shell model is:

$$\alpha = \frac{Y^2}{k} \quad (3.1)$$

where k is the spring constant. The effect of electron cloud overlap and dispersion interactions between ions are parameterised into Buckingham potentials (short range potential) [Grimes et al. 1990a]:

$$V(r) = Ae^{-\frac{r_{ij}}{\rho}} - \frac{C}{r_{ij}^6} \quad (3.2)$$

where r_{ij} is the internuclear distance between centres i and j , the parameters A , ρ and C were fitted in order to reproduce the lattice parameters of MgAl_2O_4 , MgO and Al_2O_3 . However, the Young's modulus and dielectric constants can also be calculated and compared to experiment. Two dielectric constants are calculated: the high-frequency dielectric constant^b $\epsilon_{r,\infty}$ (if only shell relaxation effects are considered) and the static dielectric constant $\epsilon_{r,0}$ (if

^a Private communication with R.W. Grimes: Mg and Al cations have such a high spring constant that they may be considered unpolarizable. Therefore, including a massless shell for these ions does not change the calculated results.

^b The permittivity of the material is determined by $\epsilon_r \epsilon_0$ where ϵ_r is the relative permittivity in comparison with free space ϵ_0 with a value of $8.854 \times 10^{-12} \text{ F m}^{-1}$.

both core and shell relaxation are considered) [Grimes et al. 1989]. Two distinct parameter sets were developed:

1) the full charge model: the point charges X or $X + Y$ are equal to the formal charge of the ion; the atomic bonding is essentially ionic, covalent effects are included only through the short range part of the potential;

2) the partial charge model: the point charges X or $X + Y$ have a charge less than the formal charge; the atomic bonding is partly ionic and partly covalent. In this case the charge of oxygen was -1.7 and charges of all other ions follow.

Table 3.1 shows these parameters.

Table 3.1 Potential parameters for the full charge and partial charge model

type			Full charge model	Partial charge model	Reference
<i>short range potentials</i>					
O-O	Buckingham	A (eV)	9547.96	2230386.3	[Grimes 1994]
		ρ (Å)	0.21916	0.1429	
		C (eV Å ⁶)	32.0	32.0	
Al-O	Buckingham	A (eV)	1725.2	1504.05	[Grimes 1994]
		ρ (Å)	0.28971	0.2818	
		C (eV Å ⁶)	0	0	
Mg-O	Buckingham	A (eV)	1284.38	959.3	[Grimes 1994]
		ρ (Å)	0.29969	0.2994	
		C (eV Å ⁶)	0	0	
He-O	Lennard-Jones	A_{12} (eV Å ¹²)	2247.836	2247.836	[Grimes et al. 1990b]
		B_6 (eV Å ⁶)	11.762	11.762	
He-Mg	Buckingham	A (eV)	975.5	975.5	[Busker et al. 2000]
		ρ (Å)	0.2229	0.2229	
		C (eV Å ⁶)	0	0	
He-Al	Buckingham	A (eV)	1046.6	1046.6	
		ρ (Å)	0.21524	0.21524	
		C (eV Å ⁶)	0	0	
He-He	Buckingham	A (eV)	166.8	166.8	[Busker et al. 2000]
		ρ (Å)	0.28096	0.28096	
		C (eV Å ⁶)	0	0	
<i>shell model parameters</i>					
		k (eV Å ⁻²)	54.8	32.2	[Grimes 1994]
		Y_O (e)	-2.8	-2.23	
		X_O (e)	0.8	0.53	
		X_{Mg} (e)	2.0	1.7	
		X_{Al} (e)	3.0	2.55	
		X_{He}	0	0	

In the Mott-Littleton methodology, the crystal lattice is separated into three regions:

1) a spherical inner region I consisting of lattice with a defect in its centre;

- 2) an outer spherical region II consisting of a perfect lattice in which so many ions are taken into account until the calculated defect formation energy is stabilised; region II can be regarded as an infinite region;
- 3) an interfacial region IIa between region II and region I to smoothen the transition from region I to region II.

Region I with its defect is thus embedded into the previously described perfect lattice. Since a charged defect is left when removing an ion from the perfect lattice it is important that the interactions between the defect and the surrounding atoms are calculated explicitly using short range potentials. The positions of the ions in region I are then relaxed to zero force by varying ion positions using energy minimisation procedures. Interactions between Region I and Region IIa are calculated by explicit summation. However, ion displacements are, in order to obtain the lowest lattice energy as possible, determined using the dielectric continuum expression for polarisation (per unit volume). For cubic symmetry this has the simple form [Grimes et al. 1990a]:

$$P = \frac{Q(1 - \epsilon^{-1})}{r^2} \quad (3.3)$$

where Q is the effective charge of the defect, ϵ is the dielectric constant of the material and r is the distance from the defect.

Repulsive and attractive interactions between helium and the massless shell (Y) of oxygen are represented by a Lennard Jones potential (short range potential):

$$V(r) = \frac{A_{12}}{r^{12}} - \frac{B_6}{r^6} \quad (3.4)$$

where the parameters A and B represent, repulsion and attraction, respectively. Other short range interactions of cores with gas and gas-gas interactions were determined from electron gas approximations and fitted to a Buckingham potential [Grimes et al. 1990a, Grimes et al. 1990b, Grimes 1994, Grimes et al. 1989]. Table 3.1 shows the parameters used for the atomistic calculations of He and defects in MgAl_2O_4 .

The results described in the following two subsections are calculated using a region I as large as 0.8 to 1.4 lattice units and Region IIa as large as 2.4 to 3.5 spinel lattice units (one lattice unit is 8.1 Å). Taking smaller regions reduces the computational time but makes the results less accurate. Most results are calculated using a region I of 1.4 lattice units and a Region IIa of 3.5 lattice units. The error in the calculations is about 0.03 eV.

3.2.2 Calculated properties of MgAl_2O_4

Calculated and empirical properties of the perfect lattice of MgAl_2O_4 are described in Table 3.2. The elastic properties in Table 3.2 are: elastic stiffness constants (C_{ij}), Young's modulus (E) and isothermal compressibility (K_T). In the case of experiment, the values were determined at room temperature. The calculated values were derived using potentials that were

fit to room temperature experimental data and therefore relate via the quasi harmonic approximation to room temperature data. The letters i and j in the elastic constant refer to row and column in the matrix for elastic constants. For cubic crystals $C_{11} = C_{22} = C_{33}$, $C_{12} = C_{13} = C_{21} = C_{23} = C_{31} = C_{32}$, $C_{44} = C_{55} = C_{66}$, others are identically zero. The Young's moduli in the present study are calculated using the Hill-Walpole model as described by Suter and Eichinger [Suter et al. 2002]. Expressed in elastic stiffness constants these are, for a cubic symmetry:

$$E = \frac{4C_{11}^2 - 8C_{12}^2 + 4C_{11}C_{12} + 3C_{11}C_{44} + 6C_{12}C_{44}}{5C_{11} + 6C_{12} + C_{44}} \quad (3.5)$$

$$K_T = \left[\frac{1}{3}(C_{11} + 2C_{12}) \right]^{-1} \quad (3.6)$$

Table 3.2 shows that the calculated Young's modulus of the full charge model is similar to the experimental value. The calculated elastic stiffness constants by Mishra and Thomas [Mishra et al. 1977] are most similar to experimental values. Their atomistic calculations were, however, performed without relaxation and anion polarizability. The potential parameters they used included only Coulombic attraction and Born repulsion. Their Born repulsion parameters are consequently totally different from these parameters used for the present study.

Table 3.2 Calculated and empirical properties of $MgAl_2O_4$ at room temperature

	Full charge model ^P	Partial charge model ^P	Experimental	Calculated
lattice parameter (Å)	8.1177	8.1324	8.0831 ¹	8.1439 ²
Lattice energy per $MgAl_2O_4$ (eV)	-202.92	-147.15		-200.51 ²
elastic properties				
C_{11} (GPa)	382	289	280 ³	283 ⁴
C_{12} (GPa)	235	171	155 ³	155 ⁴
C_{44} (GPa)	177	129	156 ³	155 ⁴
E (GPa)	272 [#]	209 [#]	274 ^{3,*}	328 ^{2,\$}
K_T (MPa ⁻¹)	3.520	4.759		
E_{100} (GPa)	202	162		171 ⁵
E_{110} (GPa)	340	258		284 ⁵
E_{111} (GPa)	371	278		404 ⁴ / 364 ⁵
relative permittivities				
$\epsilon_{r,0}$	6.79	5.79		
$\epsilon_{r,\infty}$	2.66	2.62		

^P present study, [#] determined by Hill-Walpole, ^{*} determined by Voight-Reuss-Hill average scheme, ^{\$} average from Voight and Reuss, References: ¹ JCPDS-21-1152 [PCPDFWIN 1997], ² [Chen et al. 1996], ³ [Garner et al. 1994], ⁴ [Mishra et al. 1977], ⁵ [Fang et al. 2000].

The calculated Young's moduli for the various orientations (E_{100} etc.) for cubic structures are determined using [Wachtman 1996]:

$$E^{-1} = s_{11} - [2(s_{11} - s_{12}) - s_{44}] \times \left[\sin^2 \theta \cos^2 \theta + \frac{1}{4} \sin^4 \theta \sin^2 2\varphi \right] \quad (3.7)$$

where for cubic crystals the elastic stiffness constants (C_{ij}) are related to compliance constants (s_{ij}) by $C_{44} = 1/s_{44}$, $C_{11} - C_{12} = (s_{11} - s_{12})^{-1}$, $C_{11} + 2C_{12} = (s_{11} + 2s_{12})^{-1}$, θ and φ are the usual polar angles. These data are important for the evaluation of mechanical properties of single crystals. Empirical data are unknown to the author. The calculated data from Simmons and Wang described by Fang et al. [Fang et al. 2000] are between the calculated properties of the partial and full charge model of the present study. The volume derived from lattice parameters of the full charge and partial charge models are respectively 1.3% and 1.8% larger than the experimental volume. Experimental data of the dielectric constants are unknown to the author.

During irradiation, defects are created. These defects may be vacancies or vacancy clusters. These defects cause swelling that can be calculated. The defect relaxation volume (ν) is described by [Zacate et al. 2000]:

$$\nu = -K_T V_C \left(\frac{\partial f_v}{\partial V_C} \right)_T = -K_T V_C \left(\frac{\partial f_v}{\partial a_c} \right)_T \left(\frac{1}{3a_c^2} \right) = -K_T \left(\frac{\partial f_v}{\partial a_c} \right)_T \left(\frac{a_c}{3} \right) \quad (3.8)$$

where K_T is the isothermal compressibility, V_C is the relaxed unit cell volume, a_c is the relaxed lattice parameter (see Table 3.2), $\left(\frac{\partial f_v}{\partial V_C} \right)_T$ and $\left(\frac{\partial f_v}{\partial a_c} \right)_T$ are the isothermal change in the Helmholtz defect formation energy as a function of respectively the change in unit cell volume and the change in lattice parameter (the Helmholtz energy is approximated by the internal energy of defect formation). Table 3.3 shows the defect formation energies of vacancies and associated swelling. The defect formation energies for vacancies (E^{F,V_x}) is defined as the energy required to remove a lattice ion to infinity and to allow the defective lattice to relax to equilibrium around the now vacant site. The swelling of the aluminium vacancy is not calculated.

Table 3.3 Defect formation energy of vacancies and swelling.

vacancy	defect formation energy, E^{F,V_m} (eV)			swelling			
				ν (\AA^3)		$100 \times \Delta V/V$	
	full charge model	partial charge model	[Chen et al.1996]	full charge model	partial charge model	full charge model	partial charge model
V_{Mg}''	27.03	20.06	27.25	4.72	5.61	0.88	1.04
V_{Al}'''	57.46	42.09	58.94				
$V_O^{\bullet\bullet}$	25.57	19.33	20.04	4.37	5.21	0.82	0.97

The migration energy of a vacancy is determined by migration of a lattice ion as an interstitial from its lattice site to an equivalent empty (vacant) lattice site. Several migration paths were calculated since the most efficient migration path could not directly be deduced from the crystal structure of MgAl_2O_4 . The path that required the minimum energy for an ion to migrate from one lattice site to another initially empty lattice site was the final path that will be observed experimentally for vacancy migration. Figure 3.2 shows the migration energy of the charged vacancy V_{Mg}'' .

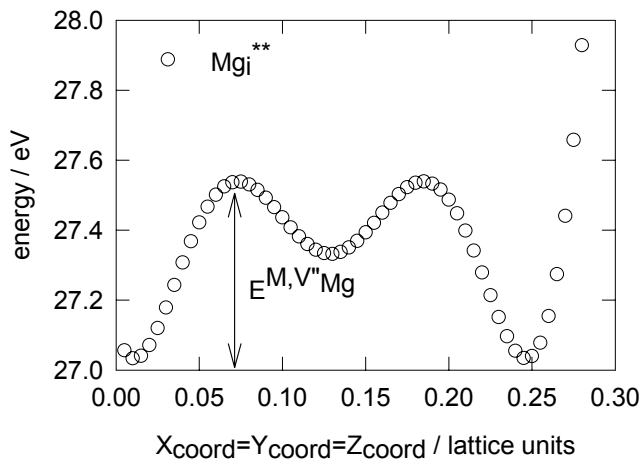


Figure 3.2 Calculation of re-positioning of V_{Mg}'' by migration of Mg_i'' using the full charge model.

Table 3.4 shows the distances between cation sites using unrelaxed coordinates, the number of cation sites surrounding a cation site and the migration energies of vacancies (E^{M,V_x}) using the most energetically favourable migration path. The migration of each cation vacancy is calculated by migration of a lattice ion as an interstitial but also by migration of the other cation by assuming that an anti-site defect is present. Thus for example a magnesium vacancy is calculated to migrate by an adjacent magnesium ion moving from its lattice site to the initially vacant magnesium site with an activation energy of 0.51 eV (full charge model) or via an aluminium ion at a magnesium site moving across with an activation energy of 0.90 eV (full charge model). An aluminium vacancy is calculated to migrate by an adjacent aluminium ion moving from its lattice site to the initially vacant aluminium site with an activation energy of 2.33 eV (full charge model) or via a magnesium ion at an aluminium site moving across with an activation energy of 1.06 eV (full charge model). The difference between these calculations is the direction in migration of the vacancies. The migration of magnesium vacancies takes place in the $\langle 111 \rangle$ direction and the migration of aluminium vacancies takes place in the $\langle 110 \rangle$ direction.

Table 3.4 shows that the unrelaxed distance between a magnesium site and a surrounding aluminium site of 0.415 lattice unit smaller is than this distance between a magnesium site and a surrounding magnesium site of 0.433 lattice unit. The difference between distances is, however, so small that the repulsion of oxygen atoms surrounding the magnesium vacancy may mean that the magnesium sites are closer to the magnesium vacancy than the aluminium sites resulting in migration of magnesium vacancies by migration of magnesium interstitials. The difference in distance between an aluminium site and a surrounding aluminium site of 0.354 lattice unit and an aluminium site and a surrounding magnesium site of 0.415

lattice unit is too large. Therefore, probably migration of aluminium vacancies occurs by migration of aluminium interstitials in the normal spinel structure.

Table 3.4 Geometry of cation sites and calculated migration energies of vacancies.

cation site	surrounding cation sites	d (unit cell edge length)	NC	defect type	migration energy, $E^{M.V_x}$ (eV)		
					full charge model	partial charge model	
Mg_{Mg}	Mg_{Mg}	0.433	4	V_{Mg}''	via Mg_i''	0.51	0.36
Mg_{Mg}	Al_{Al}	0.415	6		via Al_i''''	0.90	0.66
Al_{Al}	Mg_{Mg}	0.415	4	V_{Al}''''	via Mg_i''	1.06	0.85
Al_{Al}	Al_{Al}	0.354	6		via Al_i''''	2.33	1.81
				V_O''	via O_i''	1.49	1.26

d = unrelaxed distance between a cation site and a surrounding cation site in unit cell edge length, NC= Number of surrounding Cation sites.

Empirical migration energies determined by electrical conductivity measurements in single crystals after a pre-heated stage of 1700 K are 1.50, 2.16 and 2.74 eV measured in the temperature range 730-2000 K [Weeks et al. 1980] and 0.43, 1.65 and 2.24 eV measured in single crystals without a pre-heated stage in the temperature range 500-1260 K [Lambert Bates et al. 1981]. The identity of the ionic conduction is unknown. The values of Lambert Bates et al. are similar to the calculated results in the present study representing the migration energy of the magnesium vacancy, oxygen vacancy and aluminium vacancy of 0.43, 1.65 and 2.24 eV, respectively. Possibly the empirical migration energies by Lambert Bates et al. resemble more the migration energies in the normal spinel structure and the empirical migration energies by Weeks et al. more the migration energies in the inverse or random spinel structure since the distribution of cations in tetrahedral and octahedral sites depend on temperature [Navrotsky et al. 1967].

The rate-controlling or slowest vacancy species in $MgAl_2O_4$ was determined to be 2.0 ± 0.7 eV using the shrinkage of interstitial dislocation loops by vacancy absorption [Yasuda et al. 2000]. This experimental result is in coincidence with the data obtained by calculation in Table 3.4. The present study shows that the identity of the slowest vacancy species in $MgAl_2O_4$ is V_{Al}'''' by migration of Al_i'''' . These migration energies are not the activation energies for self-diffusion, these are discussed at the end of this paragraph.

Limited data is calculated for vacancy clusters. Table 3.5 shows available data for vacancy clusters and Figure 3.3 shows the configurations of the vacancy clusters. Comparison of Tables 3.3 and 3.5 shows that swelling induced by either single charged vacancies V_O'' or V_{Mg}'' is larger than the uncharged complex $\{V_{Mg}V_O\}^x$. This is due to repulsion of anions or cations surrounding a vacancy resulting in a larger swelling than the uncharged complex.

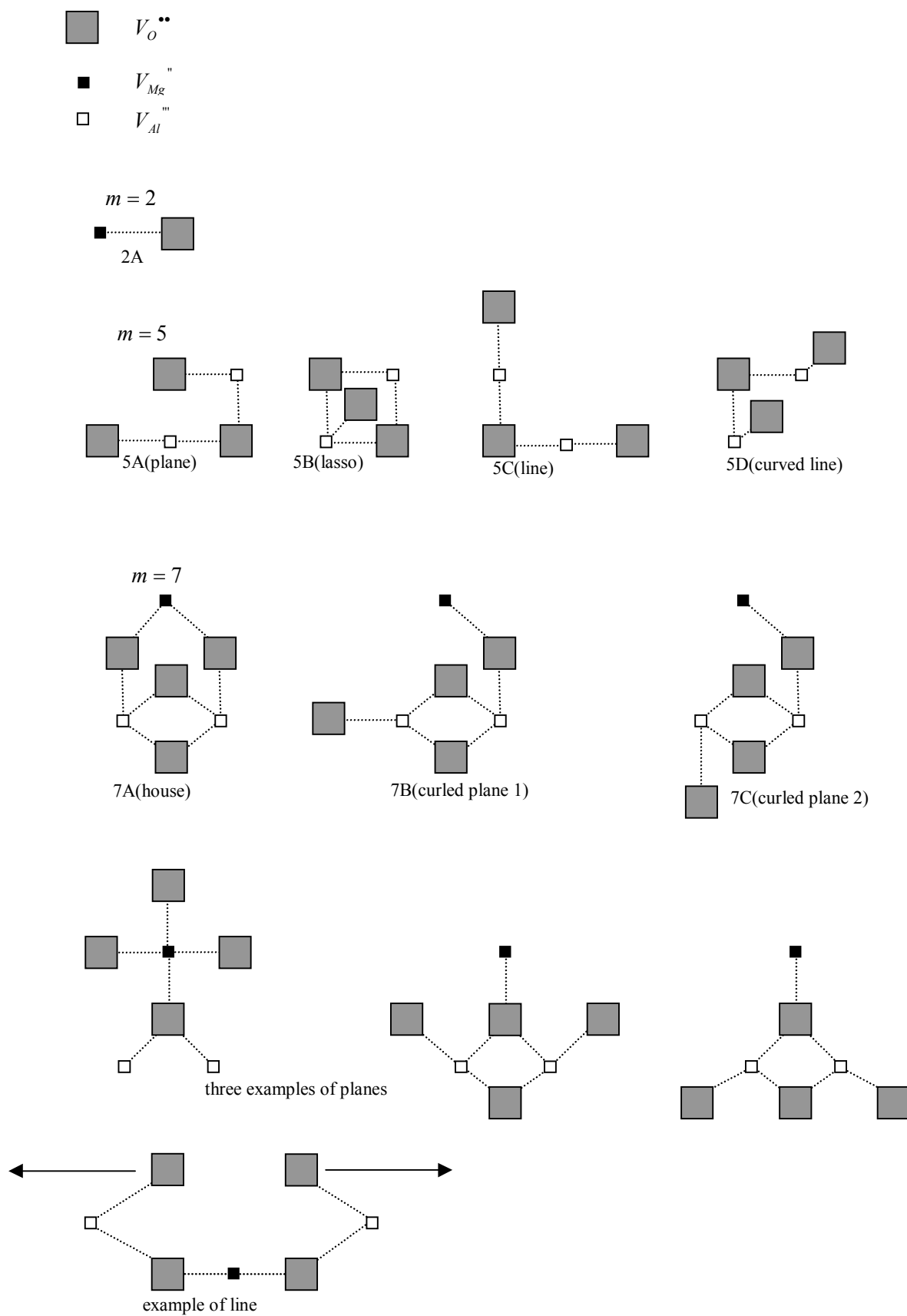


Figure 3.3 Configurations of vacancy clusters

The calculation of larger complexes induced computational problems. Attempts to calculate the configuration in Figure 3.3 5B and 7A failed. A few examples of more configurations that could be calculated are shown in Figure 3.3 but are not calculated by the author. The binding energy of a cluster is [Zacate et al. 2000]:

$$BE_{cluster} = \left[\sum_{components} E^F \right] - E^F_{cluster} \quad (3.9)$$

where $\left[\sum_{components} E^F \right]$ is the sum of the defect formation energies of the vacancies in the present study (see Table 3.3) and $E^F_{cluster}$ is the defect formation energy of the Schottky cluster.

Table 3.5 Defect formation energies of vacancy clusters, binding energy of these clusters and swelling.

partial- and full Schottky clusters	in Figure 3.3	$E^{F,He,V_aV_bV_c}$ (eV)	$BE_{cluster}$ (eV)	$BE_{cluster}$ (eV vacancy ⁻¹)	v (Å ³)	$100 \times \frac{\Delta V}{V}$
full charge model						
$\{V_{Mg}''V_O''\}^x$	2A	48.22	4.38	2.19	3.22	0.60
$\{(V_{Al}''')_2(V_O'')_3\}^x$	5A	173.13	20.50	4.10		
	5B	-				
	5D	177.48				
partial charge model						
$\{V_{Mg}''V_O''\}^x$	2A	35.75	3.64	1.82	4.34	0.81
$\{(V_{Al}''')_2(V_O'')_3\}^x$	5A	126.68	15.50	3.10		
	5B					
	5D	130.20				
$\{V_{Mg}''(V_{Al}''')_2(V_O'')_4\}^x$	7A					
	7B	160.09				
	7C	159.84	21.73	2.72		

The formation energy for a Schottky cluster is:

$$E_{formation} = E_L + E^{F,V_aV_bV_c} \quad (3.10)$$

where $E^{F,V_aV_bV_c}$ is the defect formation energy of the cluster in Table 3.5. The lattice energies of MgO, for determination of the formation energy of the partial Schottky cluster MgO, are -41.16 eV and -29.74 eV per molecule of MgO for the full and partial charge model, respectively [Busker et al. 2000]. The lattice energies for determination of the formation energy of the partial Schottky cluster Al₂O₃, are -161.15 eV and -117.15 eV per molecule of Al₂O₃ for the full charge model [Pirzada 2000] and partial charge model [Cleave 2004], respectively. The lattice energies of MgAl₂O₄ are reported in Table 3.2. Table 3.6 shows the formation energies of (partial) Schottky clusters. The formation energies of the clusters $\{(V_{Al}''')_2(V_O'')_3\}$ and

$\{V_{Mg}''(V_{Al}''')_2(V_O^{\bullet\bullet})_4\}$ should be treated with some caution since it is not clear whether these clusters are the most energetically favourable complexes (i.e. they represent lower bounds).

Table 3.6 Formation energies of partial-and full Schottky clusters.

uncharged vacancy cluster	full charge model (eV)	partial charge model (eV)	full charge model (eV vacancy ⁻¹)	partial charge model (eV vacancy ⁻¹)
$\{V_{Mg}''V_O^{\bullet\bullet}\}$	7.06	6.01	3.53	3.01
$\{(V_{Al}''')_2(V_O^{\bullet\bullet})_3\}$	9.98		2.00	
$\{V_{Mg}''(V_{Al}''')_2(V_O^{\bullet\bullet})_4\}$		12.70		1.59

The activation energies for self-diffusion coefficients for the ions can be calculated with Schottky defects and the migration energies of the vacancies in Table 3.4. Schottky defects are non-interacting vacancies in a stoichiometric ratio. The formation energies of a Schottky defect is:

$$E_{formation} = E_L + \sum E^{F,V_x} \quad (3.11)$$

where E_L is the lattice energy and E^{F,V_x} the defect formation energy of the vacancy in Table 3.4. Table 3.7 shows the formation energies of partial- and full Schottky defects as isolated species.

Table 3.7 Formation energies of partial-and Schottky defects

ratio of non-interacting vacancies	full charge model (eV)	partial charge model (eV)	full charge model (eV vacancy ⁻¹)	partial charge model (eV vacancy ⁻¹)
$\{V_{Mg}''+V_O^{\bullet\bullet}\}$	11.44	9.66	5.72	4.81
$\{2V_{Al}'''+3V_O^{\bullet\bullet}\}$	30.48	25.03	6.10	5.01
$\{V_{Mg}''+2V_{Al}'''+4V_O^{\bullet\bullet}\}$	41.31	34.42	5.16	4.29

Another calculated formation energy of the Schottky heptet $\{V_{Mg}''+2V_{Al}'''+4V_O^{\bullet\bullet}\}$ is 3.54 eV vacancy⁻¹ [Chen et al. 1996] which is smaller than the present value of 5.16 eV vacancy⁻¹ in Table 3.7. The origin of the difference between these two results is probably caused by the much lower defect formation energy of the oxygen vacancy in the study by Chen et al. in comparison with the present study (see Table 3.3).

The calculated Frenkel defect formation energies are in eV atom⁻¹: 4.59 for Mg Frenkel defect, 6.37 for Al Frenkel defect and 5.29 for O Frenkel defect [Chen et al. 1996]. These three Frenkel defect formation energies are all larger than the formation of a Schottky heptet of 3.54 eV vacancy⁻¹ calculated by Chen et al.. Therefore, intrinsic defects in MgAl₂O₄ form predominantly via a Schottky process.

The dissociation energy of the uncharged complex $\{V_{Mg}V_O\}$ is 4.89 eV and 4.00 eV for the full charge and partial charge model respectively. The dissociation energies of other vacancy clusters are equal to the formation energy of the Schottky defects in Table 3.7.

The activation energy for the self-diffusion coefficient is [Grimes 1972]:

$$E^{sd} = E^{formation} + E_{V_x^x}^M \quad (3.12)$$

where $E^{formation}$ is the formation energy of the vacancy and $E_{V_x^x}^M$ is the migration energy of the vacancy. Table 3.8 shows the calculated and experimental activation energies for self-diffusion.

Table 3.8 Activation energies for self-diffusion coefficients in the normal spinel structure.

ions	full charge model	partial charge model	experimental
Mg^{2+}	5.67	4.65	^{26}Mg 3.74 [Grimes 1972]
Al^{3+}	7.49	6.10	
O^{2-}	6.65	5.55	^{18}O 4.55 [Ando et al. 1974]

$$D_0 = 0.89 \text{ cm}^2\text{s}^{-1} \text{ for oxygen [Ando et al. 1974]}$$

The calculated activation energies for self-diffusion are somewhat larger than the experimental values. However, the temperature independent pre-factor by Ando et al. is also quite large for an oxide. Interestingly, using the formation energy of the Schottky heptet by Chen et al. and migration energies of the present study resembles these experimental values more than using the formation of the Schottky heptet calculated in the present study.

3.2.3 Calculated helium interactions in the lattice of $MgAl_2O_4$

Figure 3.4 shows how the migration energy of helium in a perfect lattice of $MgAl_2O_4$ is determined. Importantly, in the regions of maximums and minima, the number of calculated points per unit length is larger than in other regions of the migration path. This is done in order to obtain more precise results.

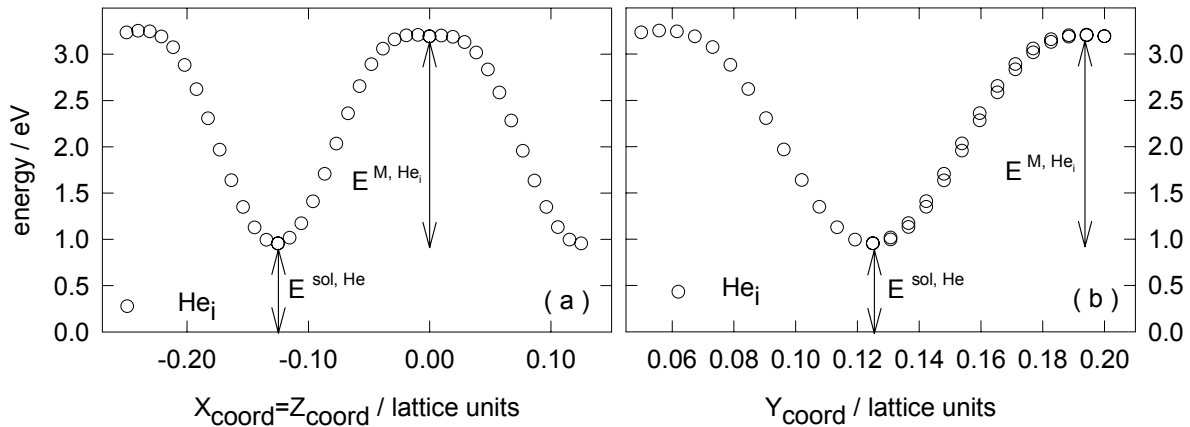


Figure 3.4 (a) X and Z coordinates and (b) Y coordinate along the most efficient migration path of helium in $MgAl_2O_4$ using the full charge model.

When helium is trapped in a pore, the required energy to become dissolved in the crystal lattice is called the solution energy ($E^{sol,He}$). The sum of migration ($E^{M,He}$) and solution energy is called the permeation energy. For helium atoms that are trapped in a pore, the permeation energy is required to allow the diffusion of helium from the pore into the crystal lattice. The defect energy of the helium atoms (E^{F,He_i}) is defined as the energy required to place the helium atoms in the lattice while allowing the resulting lattice to relax to equilibrium. Table 3.9 shows these helium properties in $MgAl_2O_4$. The concentration of helium is defined as the number of helium atoms per unit cell divided by the number of atoms Mg, Al and O per unit cell.

Table 3.9 Properties of helium in a perfect lattice of $MgAl_2O_4$.

property	full charge model		partial charge model	
$E^{M,He}$	2.19		1.89	
$E^{sol,He}$	0.94		0.88	
E^{perm,He_i}	3.13		2.77	
number of helium atoms in unit cell	E^{F,He_i} (eV)	$\langle E^{sol,He} \rangle$ (eV atom ⁻¹)	E^{F,He_i} (eV)	$\langle E^{sol,He} \rangle$ (eV atom ⁻¹)
2	1.93	0.97	1.78	0.89
3	2.90	0.97	2.69	0.90
4	4.05	1.01	3.83	0.96
C_{He} (at % He)	swelling			
	v (Å ³)	$100 \times \Delta V/V$	v (Å ³)	$100 \times \Delta V/V$
1.79	2.87	0.54	2.76	0.51
3.57	5.76	1.08	5.50	1.02
5.36	8.71	1.63	8.30	1.54
7.14	11.83	2.21	11.38	2.12

Helium atoms were placed in centres of the holes present in the crystal structure (see Figure 3.1). Table 3.9 shows that the solution energy of helium in $MgAl_2O_4$ only slightly increases with increasing amount of helium. It indicates that $MgAl_2O_4$ can contain large amounts of helium in the lattice without forming defects. In fact, since there are 8 holes present per unit cell, the concentration can amount to 14 at% He! Table 3.9 shows that the swelling induced by the presence of helium in a defect-free lattice of $MgAl_2O_4$ is small with respect to the concentration of helium. By comparing Tables 3.3 and 3.9, it can be deduced that swelling by a single point defect per unit cell is larger than swelling by a single helium atom per unit cell.

Together Tables 3.4 and 3.9 show that the activation energies for migration of vacancies are smaller than or similar to the migration energy of helium. It indicates that, if the temperature independent pre-factor for helium and vacancies are similar, clustering of vacancies can take place at lower temperatures than migration of helium if the concentration of empty vacancies is high. The activation energies for self-diffusion in Table 3.8 are larger than the permeation

energy of helium indicating that vacancy-assisted migration of helium is much less feasible than permeation of helium in MgAl₂O₄.

The binding energy of helium to a defect ($E_{He_n V_m}^{B,He}$) is described by [Busker et al. 2000]:

$$E_{He_n V_m}^{B,He} = E^{F,He_{n-1}V_m} + E^{sol,He} - E^{F,He_n V_m} \quad (3.13)$$

where $E^{F,He_{n-1}V_m}$ and $E^{F,He_n V_m}$ are the defect energies of defects occupying n-1 and n helium atoms, respectively. A positive energy indicates that energy is required to remove a He atom from the defect/cluster and a negative value indicates that a He atom does not bind to the cluster. The energy to dissociate from the defect ($E_{He_n V_m}^{D,He}$) is determined by [Busker et al. 2000]:

$$E_{He_n V_m}^{D,He} = E_{He_n V_m}^{B,He} + E^{M,He_i} \quad (3.14)$$

This energy is used to determine the diffusion of helium in a lattice with defects when this energy is larger than the migration energy of helium. Table 3.10 shows that the energy to dissociate helium from a point defect increases when the number of helium atoms in defects reduces.

Table 3.10 Defect formation energy of helium occupied vacancies and vacancy cluster and dissociation energy of helium from vacancies and vacancy cluster.

vacancy / vacancy cluster	n He atoms	defect formation energy, $E^{F,He_n V_m}$ (eV)		dissociation energy $E_{He_n V_m}^{D,He}$ (eV)	
		full charge model	partial charge model	full charge model	partial charge model
V_{Mg}''	1	27.31	20.32	2.86	2.50
	2	27.61	20.61	2.83	2.48
	3	27.93	20.92	2.81	2.46
	4	28.28	21.25	2.78	2.44
	5	30.55	23.42	0.86 *	0.60 *
	6	35.76	28.12	-2.07 *	-1.94 *
	7	39.78	31.76	-0.69 *	-0.86 *
V_{Al}'''	1	57.49		3.11	
	2	58.88		1.73 *	
$V_O^{\bullet\bullet}$	1	25.48	19.20	3.22	2.86
	2	26.04	19.71	2.57	2.25
	3	28.03	21.58	1.15 *	0.52 *
He_{MgO}^{\times}	1	48.03	35.56	3.32	2.95
$He_{2,MgO}^{\times}$	2	48.58	36.11	2.58	2.22

* the binding energy of this He atom to the complex of a vacancy and helium atom(s) is negative. Therefore, the dissociation energy of this He atom from the vacancy is smaller than the migration energy of helium.

This is due to the decrease in the pressure of helium in the vacancy. A magnesium vacancy occupied by for example 4 helium atoms has a higher pressure of helium and therefore a higher chemical potential of helium than a magnesium vacancy occupied by 3 helium atoms. A higher chemical potential results in a smaller binding energy of helium to the vacancy [van Veen 1991]. Table 3.10 also shows that the dissociation energy of a single helium atom from an oxygen vacancy and a partial Schottky cluster are larger than the permeation energy. This is probably due to the creation of a potential barrier by expansion and contraction of first and second ion shells surrounding the oxygen vacancy and partial Schottky cluster as described by Busker et al. [Busker et al. 2000].

A fifth, a sixth or even a seventh helium atom is geometrically possible in a magnesium vacancy but not thermodynamically favourable. No geometry could be found in which a third helium atom could fit in an aluminium vacancy or a fourth helium atom in an oxygen vacancy. Table 3.11 shows the swelling of $MgAl_2O_4$ by helium-containing vacancies and cluster.

Table 3.11 Swelling of $MgAl_2O_4$ by helium filled vacancies and vacancy cluster.

vacancy / vacancy cluster	C_{He} (at%)	v (\AA^3)		$100 \times \Delta V/V$	
		full charge model	partial charge model	full charge model	partial charge model
He_{Mg} "	1.79	7.33	9.01	1.37	1.68
He_{2Mg} "	3.57	8.82	10.88	1.65	2.02
He_{3Mg} "	5.36	10.73	13.37	2.01	2.49
He_{4Mg} "	7.14	12.59	15.80	2.35	2.94
He_{5Mg} "	8.93	16.18 *	20.49 *	3.02 *	3.81 *
He_{6Mg} "	10.71	32.32 *		6.04 *	
He_{7Mg} "	12.50	38.91 *		7.27 *	
He_O ••	1.79	4.52	5.95	0.85	1.11
He_{2O} ••	3.57	6.46	7.78	1.21	1.45
He_{MgO}^{\times}	1.79	3.13	4.22	0.59	0.79
$He_{2,MgO}^{\times}$	3.57	6.58	8.84	1.23	1.64

* see Table 3.10

The swelling by a helium occupied aluminium vacancy was not calculated. The swelling due to one or two helium atoms in vacancies and vacancy clusters are larger than the swelling by two helium atoms in two holes (i.e. 1.08-1.02%). The magnesium vacancy can also be viewed as removing, geometrically, the boundary between two holes. The swelling of a helium cluster with 4 helium atoms occupying a magnesium vacancy (i.e. 2.35-2.94%) is larger than solely 4 helium atoms (i.e. 2.21-2.12%). The sum of the swelling by an empty vacancy or

vacancy cluster in Tables 3.3 and 3.5 and the swelling by helium in the perfect lattice in Table 3.9 is nearly always larger than the swelling in Table 3.11. The exception is the magnesium vacancy occupied by a single helium atom. Thus nearly always trapping of helium in defects reduces the swelling by helium in MgAl₂O₄ with defects.

The potential barrier surrounding the oxygen vacancy and Schottky cluster makes comparison between the dissociation energies of helium from different vacancies and partial Schottky cluster and the volume of vacancies and vacancy cluster rather cumbersome.

3.2.4 Conclusions of atomistic calculations and outlook

The calculated migration energies of vacancies range from 0.36 eV to 1.81 eV for the partial charge model and 0.51 eV to 2.33 eV for the full charge model in the normal spinel structure. The presence of anti-site defects increases the migration energy of magnesium vacancies and reduces the migration energy of aluminium vacancies. A concentration of one vacancy per unit cell causes a swelling of about 1 vol%. Electron capture of these vacancies or electron emission from these vacancies can change these migration energies and dilatation [Bourgain et al. 1978]. It would be interesting to calculate this normal ionisation enhanced diffusion and dilatation of F centres and hole centres since these centres are present in oxides like MgAl₂O₄, especially during irradiation conditions.

Limited data is calculated for vacancy clusters and no data is calculated for interstitial clusters. The binding energies of Schottky clusters calculated up till now are all larger than the formation energy of Schottky defects except for $\{V_{Mg} "V_O^{\bullet\bullet}\}$. The dissociation energy of the Schottky cluster $\{V_{Mg} "V_O^{\bullet\bullet}\}$ is 4.89 eV and 4.00 eV for respectively the full and partial charge model. The swelling induced by a single charged point defect (i.e. oxygen or magnesium vacancies) are each larger than a single partial Schottky defect cluster $\{V_{Mg} V_O\}^x$ due to less repulsion of anions or cations. Far more data for vacancy clusters and migration energies of interstitials are required to simulate clustering processes during irradiation conditions.

The formation of intrinsic defects is as a Schottky process. The calculated activation energies for self-diffusion range from 4.65 eV to 6.10 eV for the partial charge model and 5.67 eV to 7.49 eV for the full charge model in the normal spinel structure.

MgAl₂O₄ can contain at least 14 He at% without forming defects. This concentration of helium is way beyond the generated amount of helium by alpha-emitting actinides during irradiation conditions. The swelling by helium in the perfect lattice is about 0.5 vol% per helium atom per unit cell. The solution energy of helium in MgAl₂O₄ negligibly increases with increasing helium content. This may be due to the network of holes present in the perfect lattice. A hole is an aggregate of an octahedral site and six halves and two quarters of tetrahedral sites.

The calculated migration energy of helium is 1.89 eV and 2.19 eV for respectively the partial and full charge model in the normal spinel structure. These migration energies are larger than or similar to the migration energies of vacancies. It indicates that if the concentration of

vacancies is high, clustering of vacancies can take place before helium migrates. It would be interesting to calculate the migration energy of helium in the inverse and random spinel structure. The calculated permeation energy is 2.77 eV and 3.13 eV for respectively the partial and full charge model. These permeation energies are smaller than the activation energies for self-diffusion. Therefore permeation rather than vacancy-assisted diffusion of helium takes place. The presence of vacancies and vacancy clusters render the diffusion of helium. The dissociation energies of helium from the oxygen vacancy and Schottky cluster $\{V_{Mg}''V_O^{\bullet\bullet}\}$ both occupied by one helium atom are larger than the permeation energy. The occupancy of more helium atoms per vacancy or vacancy cluster results in smaller dissociation energies of helium atoms as expected due to increase of the chemical potential. A comparison of calculated and experimental migration, dissociation and permeation energies is discussed in paragraph 4.4. Paragraph 3.3 shows in which equations these energies are used to simulate diffusion of helium in $MgAl_2O_4$.

3.3 Rate diffusion theory

The thermal redistribution of helium in a solid depends on the kind of diffusion mechanism. This paragraph treats the theoretical analysis of transport of helium for helium implanted single crystal and polycrystal semi-infinite media. First, an overview of different diffusion mechanisms is given. Secondly, the mathematical derivation of parameters for the different diffusion mechanisms is discussed. Finally, examples of different mechanisms are given concerning their impact on concentration profiles and helium release rate in order to obtain guidelines for the interpretation of NDP and THDS results, respectively. Many solutions of diffusion equations are obtained from Carslaw and Jeager [Carslaw et al. 1959] for this paragraph. The thermal diffusivity and temperature are replaced by the diffusion coefficient and concentration, respectively, for application of these equations.

3.3.1 Overview impact of implantation on transport of helium in different matrices

Implantation of helium using an electrostatic accelerator with the sample normal at a small angle with the beam yields a concentration of helium localised in depth of the sample. Figure 3.5 shows a simplified picture of helium implanted single crystal and polycrystal semi-infinite media and possible diffusion mechanisms for both matrices.

For single crystal semi-infinite media, see at the left of Figure 3.5, two diffusion mechanisms are considered: *interstitial diffusion* and *defect mediated diffusion*. The helium concentration profile is widened to the surface as well as into depth by interstitial diffusion during heating of the sample. Defect mediated diffusion includes the trapping and re-trapping of helium by defects. The concentration of defects is depth dependent in implanted samples. *Concentration dependent defect mediated diffusion* is used to account for the variation in concentration of defects in depth of the sample. Interstitial diffusion and (concentration dependent) defect mediated diffusion can be modelled using one equation for the transport of helium.

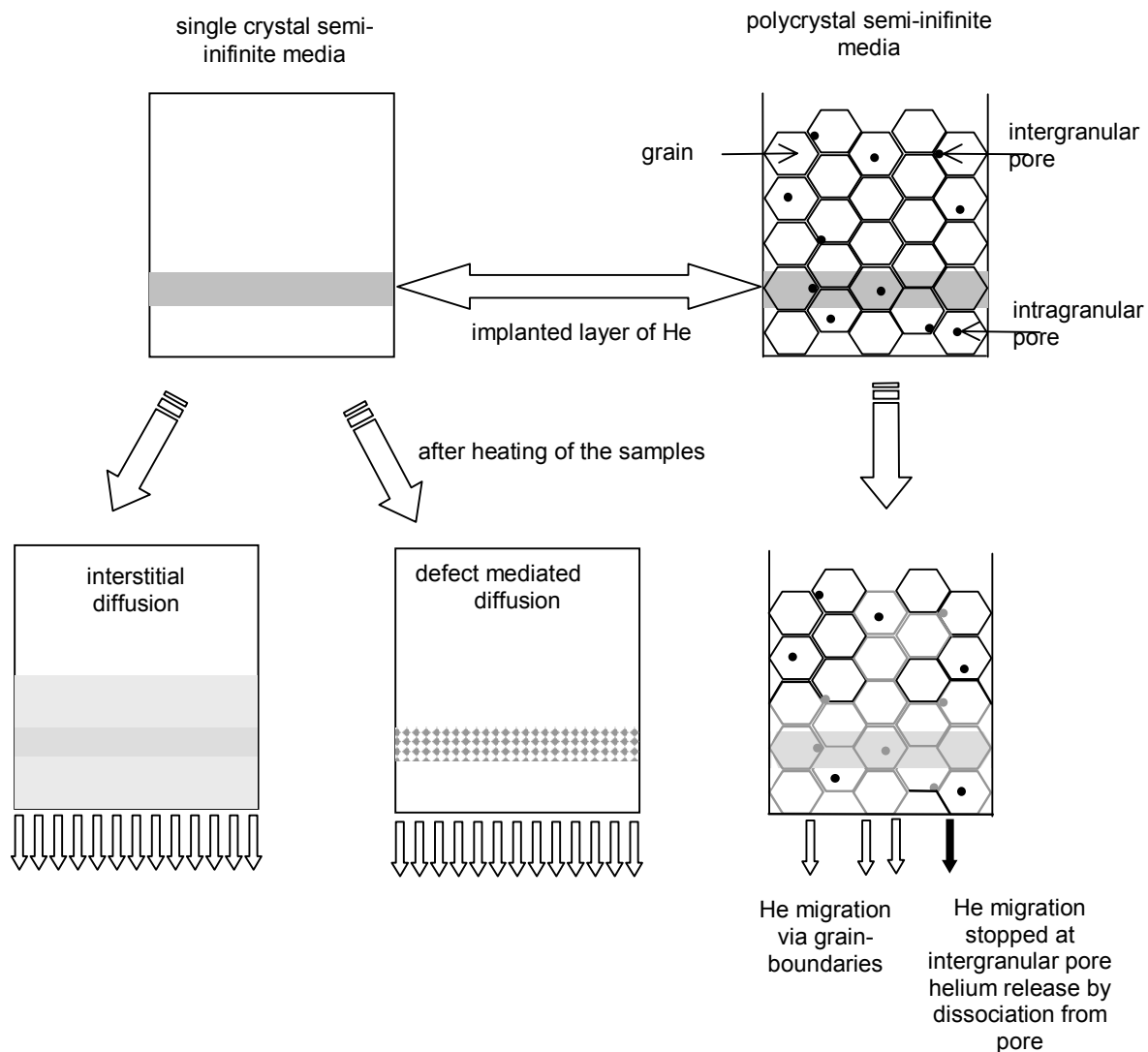


Figure 3.5 Helium release mechanisms in implanted single crystal and polycrystal semi-infinite media.

The diffusion process becomes more complicated when clustering of vacancies is taken into account. Clustering may occur during implantation and during heating of the implanted sample. Helium bonds to vacancies and vacancy clusters and the energy required for helium to dissociate from vacancies and vacancy clusters is the sum of the binding energy and migration energy. For interstitial diffusion only the migration energy is required.

In polycrystal semi-infinite media, same processes as in the single crystal semi-infinite media occur but these processes take only place within the grain. Additional diffusion processes take place at the grainboundaries. Instead of one equation, as for single crystal semi-infinite media, two equations are required to model the thermal redistribution of helium: one for the grains and one for the grainboundaries. These equations are coupled because the concentration of helium at grainboundaries depends on both processes. Once the helium is diffused out of the

grain, it can migrate via the grainboundaries to the outer surface of the sample and be released (white arrows in Figure 3.5) or become trapped in an intergranular pore (black arrow in Figure 3.5).

In general, the migration energy of helium in the grain boundaries is usually less than migration energy of helium in the bulk. The dissociation energy of helium from an intragranular pore (pore within the grain) is equal to the permeation energy. It is unclear whether the dissociation energy of helium from an intergranular pore (pore within grainboundaries) is also equal to this permeation energy. If helium is trapped in the pores to amounts that the pressure of the pore rises over 100 MPa then the de-trapping probability increases due to the increase of the chemical potential of helium in the pore. The relation between entropy and binding energy at higher pressures in a cavity is discussed by van Veen [van Veen 1991]. The above mentioned equations are discussed in the following two paragraphs.

3.3.2 Diffusion in single crystal semi-infinite media

The diffusion equation for interstitial diffusion is:

$$\frac{\partial c_{He,i}}{\partial t} = D_{He,i} \frac{\partial^2 c_{He,i}}{\partial x^2} \quad (3.15)$$

with the boundary conditions $c(0,t) = 0$ for semi-infinite media and $c(x,0) = c_0(x)$ that is the initial concentration of helium; $c_{He,i}$ is the concentration of interstitial helium, $D_{He,i}$ is the diffusion coefficient of interstitial helium which can be expressed as $D_{He,i} = D_0 e^{-\frac{E^M}{kT}}$. D_0 is the temperature independent pre-factor, E^M is the migration energy, k is the Boltzmann constant and T is the temperature. The temperature independent pre-factor can be expressed as $D_0 = Z^{-1} \lambda^2 \nu_0$, where Z is the number of neighbouring interstitial positions, λ is the jumping distance between these interstitial positions and ν_0 is the jump frequency of solved helium. The solution of equation 3.15 is:

$$c(x,t) = \frac{1}{2\sqrt{\pi Dt}} \int_0^\infty c(x',0) \left\{ e^{-\frac{(x-x')^2}{4Dt}} - e^{-\frac{(x+x')^2}{4Dt}} \right\} dx' \quad (3.16)$$

In defect mediated diffusion, the transport of helium is a combined process of trapping and de-trapping from defects. This process is accounted for by assuming an effective diffusion coefficient that is the interstitial diffusion coefficient times the fraction of interstitial helium:

$$D_{eff} = D_{He,i} \times \frac{c_{He,i}}{c_{He,i} + c_{He,t}} \quad (3.17)$$

where $c_{He,t}$ is the concentration of helium trapped in defects. In order to determine this fraction, it is assumed that there is local equilibrium between helium association and dissociation from defects. The time dependent concentration of helium trapped in defects at local equilibrium becomes:

$$\frac{\partial c_{He,t}}{\partial t} = K_A c_{He,i} N_t(x) - K_D c_{He,t} = 0 \quad (3.18)$$

where $K_A = 4\pi r_t D_0 e^{-\frac{E^M}{kT}}$ is the helium association rate to defects and $K_D = \nu e^{-\frac{E^D}{kT}}$ is the helium dissociation rate from defects, r_t is the radius of the trapping centre, E^D is the dissociation energy and $N_t(x)$ is the concentration of defects in layer x . The helium association rate is determined by multiplying the flux of the surface to the trap with the surface area of the trap. Figure 3.6 shows the graphical representation for the derivation of the helium association rate. The mathematical derivation is treated in the Appendix.

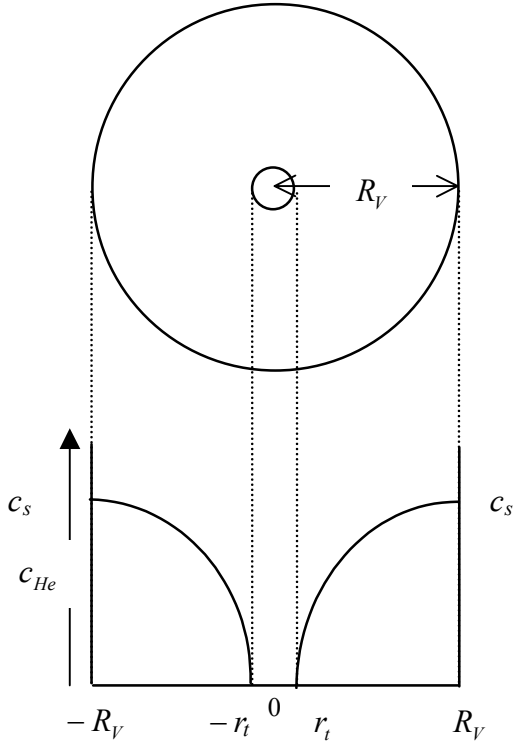


Figure 3.6 Configuration for determination of trapping rate of helium for defects.

Theoretically, every spherical cell contains one defect and therefore the concentration of defects is $N_t = 3[4\pi R_V^3]^{-1}$. Practically, N_t is the concentration of defects caused by displacements. The number of displacements per volume can be determined by TRIM calculations [Ziegler et al. 2002].

This approach yields:

$$D_{eff} = D_{He,i} \times \frac{c_{He,i}/c_{He,t}}{c_{He,i}/c_{He,t} + 1} = \frac{D_0 e^{-\frac{1}{k}\{E_D - \Delta S\}}}{e^{-\frac{1}{k}\{E_B - \Delta S\}} + 4\pi r_t Z^{-1} \lambda^2 N_t} \quad \text{if } \nu = \nu_0 \quad (3.19)$$

For vacancies, the entropy in this approximation is zero [van Veen 1991]. If the concentration of defects is constant in the sample then equation 3.15 can be used because D_{eff} is depth independent. Another equation must be used if the concentration of defects is depth dependent.

The diffusion equation for depth-dependent diffusion is:

$$\frac{\partial c}{\partial t} = \frac{\partial}{\partial x} \left(D_{eff}(x) \frac{\partial c}{\partial x} \right) \quad (3.20)$$

with the boundary conditions: $c(0, t) = 0$ and $c(x, 0) = c_0(x)$. A numerical program is written to solve equation 3.20 in which the condition $2D_{He,i} \Delta t < \Delta x^2$ is fulfilled in order to minimise the error in the calculation.

3.3.3 Diffusion in polycrystal semi-infinite media

All diffusion processes discussed in the previous paragraph take place within the grain of polycrystalline materials. Additional diffusion processes take place at the grainboundaries. In

order to model the transport of helium in implanted polycrystalline materials, the following assumptions are made:

- 1) helium in grains: the sink of this helium are grainboundaries, there is no source of helium to the grains;
- 2) helium in grainboundaries: the source of this helium are grains and intergranular pores and the sink of this helium are intergranular pores and outer surface of sample;
- 3) helium in intergranular pores: the source of this helium are grain boundaries and the sink of this helium are grain boundaries;

All these processes can be included in two sets of diffusion equations: one for helium inside grains and one for helium in grainboundaries. For the modelling of helium in grains, it is assumed that the grains are spherical. The diffusion equation for a sphere is:

$$\frac{\partial c}{\partial t} = D \left\{ \frac{\partial^2 c}{\partial r^2} + \frac{2}{r} \frac{\partial c}{\partial r} \right\} \quad (3.21)$$

with the boundary conditions: $c(r=a, t) = 0$ where a is the radius of the grain and $c(r, 0) = C_0$. D is the diffusion coefficient and r is the co-ordinate. The solution of equation 3.21 is:

$$c(r, t) = -\frac{2aC_0}{\pi r} \sum_{n=1}^{\infty} \frac{(-1)^n}{n} \sin \frac{n\pi r}{a} e^{-\frac{Dn^2\pi^2 t}{a^2}} \quad (3.22)$$

Only the release rate of helium from the grains is required to obtain how much helium from the grain has flown into the grain boundaries. The helium release rate from the grains is obtained by taking the concentration gradient at $r=a$ times the surface area of the grain and the diffusion coefficient at $r=a$:

$$I_{g \rightarrow} = -4\pi a^2 D_{r=a} \left\{ \frac{\partial c}{\partial r} \right\}_{r=a} = \frac{2C_0}{a} \sum_{n=1}^{\infty} e^{-\frac{Dn^2\pi^2 t}{a^2}} \quad (3.23)$$

The increase in concentration in the grainboundaries by release of helium from the grains $\partial c_{g \rightarrow gb}$ is the helium release rate from the grain divided by the volume of the grain:

$$\partial c_{g \rightarrow gb} = -D \left\{ \frac{\partial c}{\partial r} \right\}_{r=a} \frac{4\pi a^2}{\frac{4}{3}\pi a^3} = \frac{6DC_0}{a^2} \sum_{n=1}^{\infty} \left(e^{-\frac{Dn^2\pi^2 t}{a^2}} \right)^{n^2} \quad (3.24)$$

This equation contains, in the exponent, a product with diffusion coefficient and time. It can be shown that for this equation Dt can be replaced by $\int_0^t D(n_t, T) \partial t$. The benefit of this

replacement is that the helium release is independent on the heating procedure. For example, for equations 3.16 and 3.20, the initial concentration profile cannot be used to determine the concentration profile in the fourth isothermal stage in time and thereby determining the helium release rate at the outer surface. With equation 3.24, it is unnecessary to know the concentration profile in the grain at a time-step in order to determine the concentration profile in the grain in the next time-step. In fact, the helium release rate from the grain can be determined without even knowing the actual concentration profile in this time-step. A lot of computation time is

saved by determining the helium release rate from the grain without calculating the concentration profile at each time-step.

The transport of helium at grainboundaries is a combined process of trapping and re-trapping of helium from intergranular pores. This is accounted for by assuming an effective diffusion coefficient for the grainboundaries similarly as shown for modelling of helium in single crystals:

$$D_{\text{eff-gb}} = D_{\text{He,i-gb}} \frac{c_{\text{He,i-gb}}}{c_{\text{He,i-gb}} + c_{\text{He,p-gb}}} \quad (3.25)$$

where $D_{\text{He,i-gb}}$ is the diffusion coefficient of helium at the grainboundaries, $c_{\text{He,i-gb}}$ is the concentration of interstitial helium in the grainboundaries and $c_{\text{He,p-gb}}$ is the concentration of trapped helium in intergranular pores. In order to determine this fraction it is assumed that there is local equilibrium between helium trapping and de-trapping from intergranular pores. The time dependent concentration of helium trapped in intergranular pores becomes:

$$\frac{\partial c_{\text{He,p-gb}}}{\partial t} = K_A' c_{\text{He,i-gb}} N_p - K_D' c_{\text{He,p-gb}} = 0 \quad (3.26)$$

where $K_A' = 2\pi D_0 e^{-\frac{E^{M,gb}}{kT}} \left[\ln \left(\frac{R_A}{r_p} \right) \right]^{-1}$ is the helium association rate to intergranular pores and

$K_D' = v e^{-\frac{\{E^{M,gb} + E^{sol,gb}\}}{kT} + \frac{\Delta S_{p,gb}}{k}}$ is the helium dissociation rate from intergranular pores, $E^{M,gb}$ is the migration energy of helium within the grain boundaries, $E^{sol,gb}$ is the solution energy of helium in an intergranular pore, $\Delta S_{p,gb}$ is difference in entropy between helium in grainboundaries and helium in intergranular pores, N_p is the concentration of intergranular pores per area of grainboundary and r_p is the radius of the intergranular pores. Figure 3.7 shows the configuration for derivation of the association rate of helium to intergranular pores. The mathematical derivation is treated in the Appendix.

Theoretically, every infinite circular cell contains one intergranular pore and therefore the concentration of intergranular pores on grainboundaries is $N_p = [\pi R_A^2]^{-1}$. Practically, N_p is determined using the image analysis of the SEM-pictures:

$$N_p = \sum_{j=1}^{12} N_{j-p} / V_{\text{bulk}} \left[\sum_{j=1}^{12} N_{j-g} / V_{\text{bulk}} 4\pi a_j^2 \right]^{-1}$$
 where $N_{j-p} / V_{\text{bulk}}$ and $N_{j-g} / V_{\text{bulk}}$ are the number of intergranular pores and grains per volume respectively of the Saltykov-group j [ASM 1995] and a_j is the radius of the grain within that group (see for example Figure 4.1).

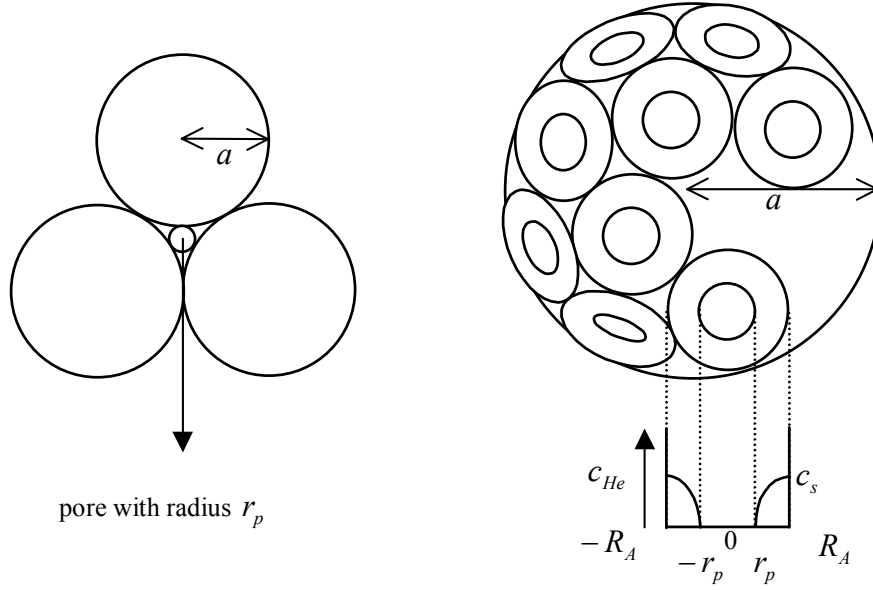


Figure 3.7 Configuration for determination of trapping rate of helium for intergranular pores.

This approach yields:

$$D_{eff,gb} = D_{He,gb} \frac{\frac{c_{He,i-gb}}{c_{He,p-gb}}}{\frac{c_{He,i-gb}}{c_{He,p-gb}} + 1} = D_{He,gb} \frac{K_{D'}}{K_{D'} + K_{A'} N_p} = \frac{D_0 e^{-\frac{\{E^{M,gb} + E^{sol,gb}\} + \Delta S_{p,gb}}{kT}}}{e^{\frac{1}{k} \left\{ \frac{E^{sol,gb}}{T} - \Delta S_{p,gb} \right\}} + \frac{2\pi\lambda^2 N_p}{Z \ln\left(\frac{R_A}{r_p}\right)}} \quad (3.27)$$

The time dependent concentration of interstitial helium at grainboundaries is:

$$\frac{\partial c_{He,i-gb}}{\partial t} = -K_{A'} c_{He,i-gb} + K_{D'} c_{He,p-gb} + \frac{\partial c_{g \rightarrow gb}}{\partial t} \quad (3.28)$$

Equation 3.20 is used to model the transport of helium at the grainboundaries and this is coupled with equation 3.24 as shown in equation 3.28. A numerical program has been written in which the condition $2D_{eff,gb} \Delta t < \Delta x^2$ is fulfilled in order to minimise the error during calculation.

3.3.4 Effect of diffusion mechanisms on the concentration profiles

NDP results show the evolution of concentration profiles after successive isothermal stages. This paragraph is written in order to obtain guidelines for the interpretation of NDP results for single crystal and polycrystal semi-infinite media.

The diffusion equation for *depth independent diffusion* is described in paragraph 3.3.2. This simple diffusion can be either interstitial diffusion or defect mediated diffusion when the concentration of defects is constant in depth. Figure 3.8 shows the evolution of concentration profiles after successive isothermal stages in case of simple diffusion in a single crystal (SC). The initial concentration profile is determined by TRIM using an implantation energy of 30 keV in MgAl₂O₄ at room temperature (RT).

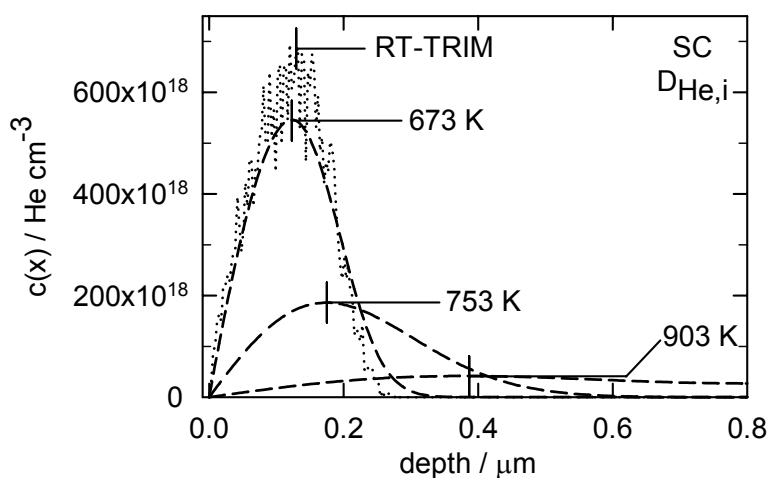


Figure 3.8 Calculated concentration profiles assuming interstitial diffusion for a 30 keV implanted sample. Parameters are: $D_0 = 2.30 \times 10^{-3} \text{ cm}^2 \text{ s}^{-1}$ and $E^M = 1.59 \text{ eV}$. The period of the isothermal stages are 1800, 1800 and 1116 seconds for 673, 753 and 903 K respectively, vertical lines indicate peak of concentration profiles.

Two features are characteristic for diffusion in semi-infinite media with a depth independent diffusion coefficient concerning the concentration profile after successive isothermal stages:

- 1) the peak of the concentration profile shifts into depth;
- 2) the concentration profile broadens.

Although the evolution of concentration profiles after successive isothermal stages for interstitial diffusion and depth independent defect-mediated diffusion are similar, the range in temperature in which release of helium takes place is different. Figure 3.9 shows the released amount of helium versus temperature for the two diffusion mechanisms for a randomly helium implanted single crystal with an energy of 4.52 MeV at room temperature. The concentration of defects created by implantation is by far smaller than the defects created by impurities. In such cases, the concentration of defects may assumed to be uniform. Figure 3.9 shows that the temperature range in which helium release takes place can be smaller for defect mediated diffusion than for interstitial diffusion. The reason that the temperature range in which helium release takes place for defect mediated diffusion smaller is than for interstitial diffusion in Figure 3.9a is explained in Figure 3.9b. It shows the diffusion coefficient versus the reciprocal temperature. Figure 3.9b clearly shows that the slope for defect mediated diffusion larger is than for interstitial diffusion. At lower temperatures (at higher reciprocal temperatures) the diffusion coefficient for defect mediated diffusion is smaller than the diffusion coefficient for interstitial diffusion. More helium release is expected for this interstitial diffusion than for this defect mediated diffusion. This is reflected in Figure 3.9a in which the onset of release of helium is at lower temperatures for interstitial diffusion than for defect mediated diffusion. At higher temperatures (at lower reciprocal temperatures) the diffusion coefficient of defect mediated diffusion is larger than the diffusion coefficient for interstitial diffusion.

^c $Z=6$, $\lambda=3.03116 \text{ \AA}$, $\nu=1.5 \times 10^{13} \text{ s}^{-1}$, ν is determined from the Debye temperature of MgAl_2O_4 in Grimes [Grimes 1972]

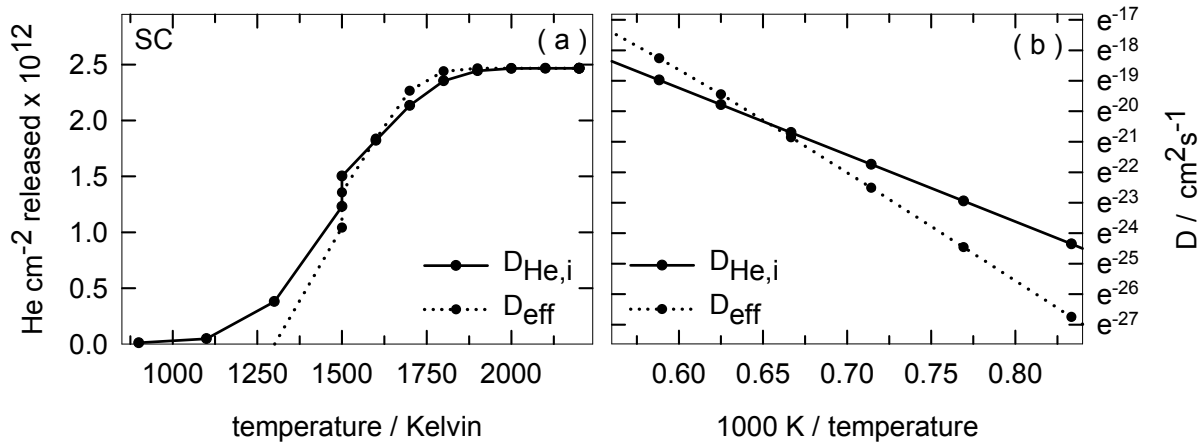


Figure 3.9 (a) Calculated released helium and (b) diffusion coefficients assuming interstitial diffusion and defect mediated diffusion for a randomly 4.52 MeV α -implanted sample. For both mechanisms $D_0 = 2.30 \times 10^{-3} \text{ cm}^2 \text{ s}^{-1}$. For $D_{\text{He},i}$: $E^M = 1.89 \text{ eV}$. For D_{eff} : $E^M = 1.59 \text{ eV}$, $E^B = 1.50 \text{ eV}$, $n_t = 50 \text{ ppm}$, and $r_t = 1 \text{ \AA}$. Period of isothermal stages are 360 seconds.

This is reflected in Figure 3.9a in which the helium release is finished at lower temperatures for defect mediated diffusion than for interstitial diffusion. Another important feature of Figure 3.9b is that only the slope for interstitial diffusion is straight. Figure 3.10 shows a helium implantation profile for a single crystal MgAl_2O_4 using an implantation energy of 900 keV and the measured displacement energies at room temperature of 86, 77 and 130 eV for Mg, Al and O respectively [Crawford et al. 1978]. It clearly shows that the concentration of displacements varies in depth.

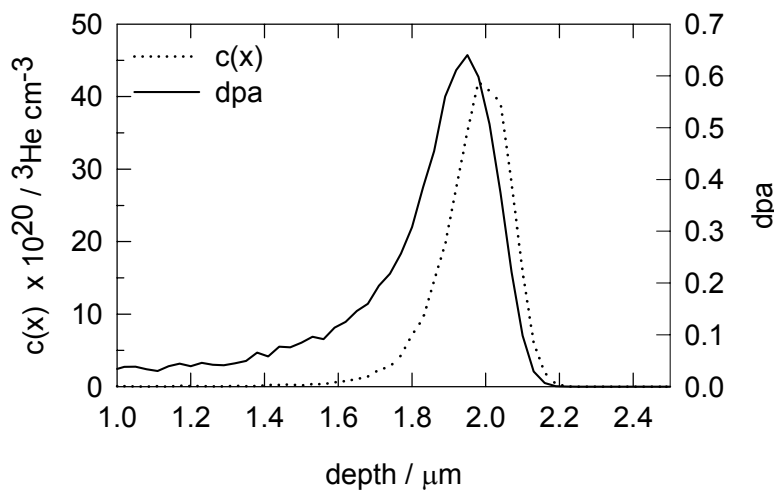


Figure 3.10 Concentration and dpa profile after implantation for a 900 keV helium implanted sample in MgAl_2O_4 at room temperature; sample normal at 20 degrees with the beam.

Only a fraction of the displacements per atom survive and contribute to the amount of defects. As Figure 3.10 clearly shows, the peak of the defect concentration profile is more located towards the surface than the helium concentration profile. Assuming that the trapping of helium in defects depends on the concentration of defects, an equation for *concentration dependent defect mediated* diffusion is required. The derivation of this equation is described in paragraph 3.3.2.

Figure 3.11 shows the evolution of concentration profiles after successive isothermal stages using concentration dependent defect mediated diffusion for a 900 keV implanted

sample. It clearly shows that the lowest diffusion coefficient is at the peak of the defect profile. Due to the used parameters, virtually no re-distribution of helium takes place until 743 K. Two features are characteristic for this diffusion mechanism at the onset of the thermal redistribution of helium:

- 1) a slight shift of the peak of the concentration profile towards the surface;
- 2) broadening of the concentration profile.

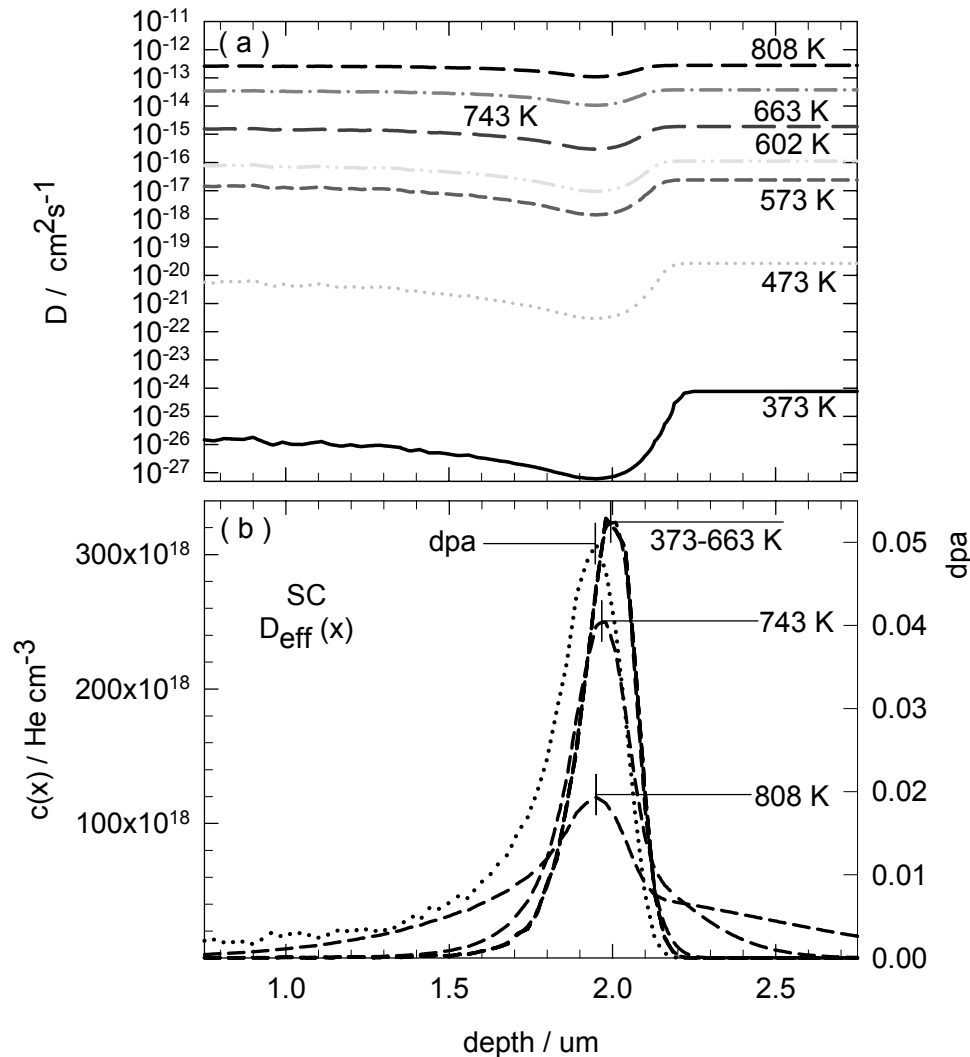


Figure 3.11 (a) Diffusion coefficients versus depth and (b) calculated concentration profiles assuming concentration dependent defect mediated diffusion after isochronal stages of 1 hr for a 900 keV implanted sample. Parameters are: $D_0 = 2.30 \times 10^{-3} \text{ cm}^2 \text{ s}^{-1}$, $E_M = 1.59 \text{ eV}$, $E_B = 0.40 \text{ eV}$, $n_t = 0.05 \times \text{dpa}^d$, $r_t = 1 \text{ \AA}$; vertical lines indicate peak of concentration profiles.

This broadening is due to trapping of helium in the defect profile that is broader than the helium implanted concentration profile. The diffusion mechanism with a constant diffusion coefficient in depth also shows broadening of the helium concentration profile but a large shift of the peak of the helium concentration profile into depth. The difference between the diffusion mechanisms in Figure 3.8 and Figure 3.11 can therefore be recognised by the direction in shift of the peak of the helium concentration profile.

^d $n_t = \frac{N_t}{N_0}$ where N_0 is the number of Mg, Al and O atoms per volume

For implanted polycrystal semi-infinite media, the implanted helium concentration profile and displacement profile are similar to Figure 3.10. They are slightly broader due to a lower density than a single crystal. Figure 3.12a shows increase in helium concentration in the grainboundaries by release of helium from the grains at the end of each temperature step for a 900 keV helium implanted polycrystalline sample.

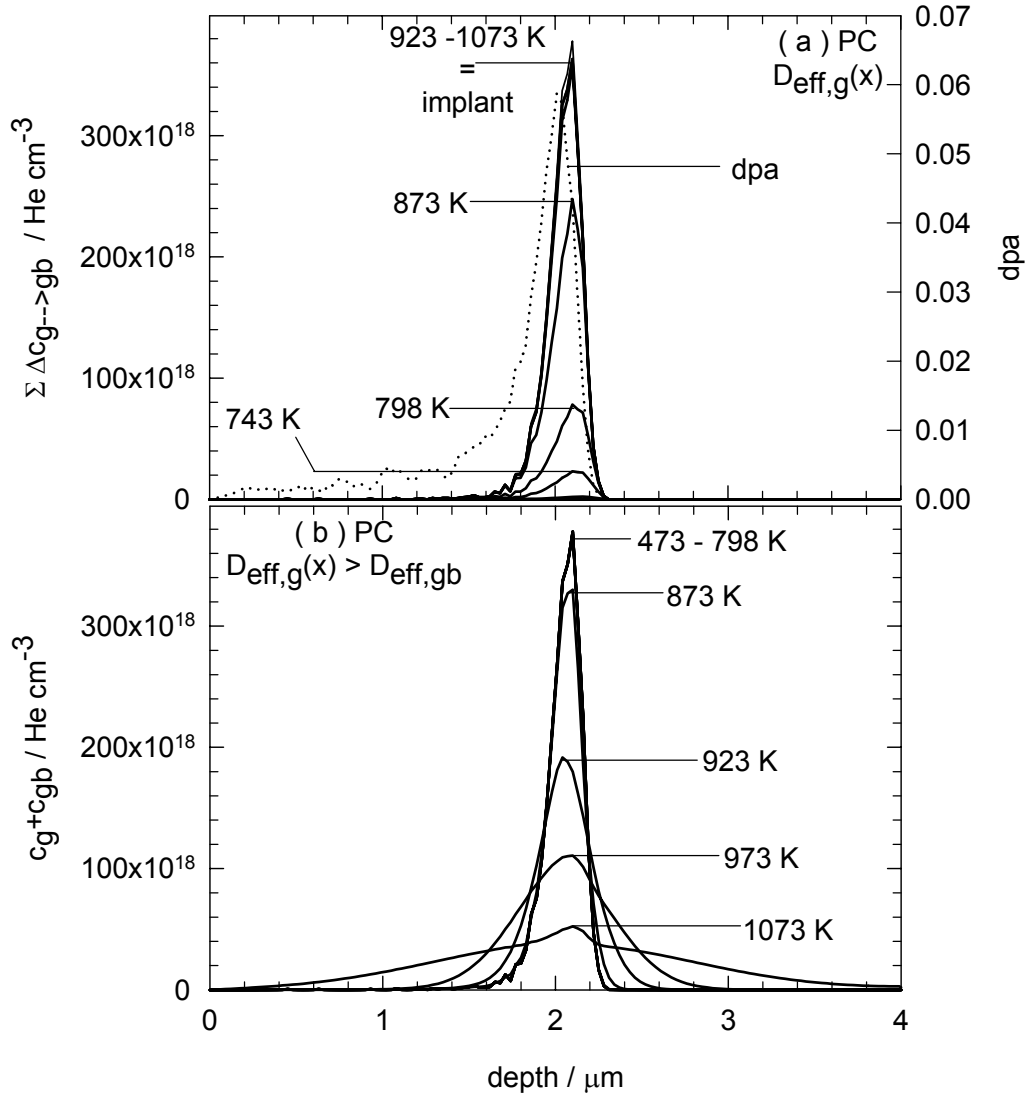


Figure 3.12 (a) Calculated change in concentration in grainboundaries by helium release from grains if no diffusion occurs in grainboundaries and (b) calculated concentration profiles after isochronal stages of 1 hour for a 900 keV implanted sample; for grains: $D_0=2.30 \times 10^{-3} \text{ cm}^2 \text{ s}^{-1}$, $E^M=1.59 \text{ eV}$, $E^B=0.60 \text{ eV}$, $n_t=0.05 \times \text{dpa}$, $r_t=1 \text{ \AA}$, for grainboundaries: $D_0=3.45 \times 10^{-3} \text{ cm}^2 \text{ s}^{-1}$, $a=0.48 \mu\text{m}$, $E^{M,gb}=0.45 \text{ eV}$, $E^{sol,gb}=1.50 \text{ eV}$, $\Delta S_{p,gb}=-1 \times 10^{-3} \text{ eV}$, $N_p=10^{12} \text{ cm}^{-2}$ and $r_p=0.03 \mu\text{m}$.

^c $Z=6$ within grain, $Z=4$ at grainboundaries

It is assumed that the diffusion coefficient in grains varies in depth ($D_{eff,g}(x)$); there are no intragranular pores and the effective diffusion coefficient in grainboundaries ($D_{eff,gb}$) is depth independent. It shows, with the used parameters, that the helium release from grains is completed at 923 K; the sum of concentration of helium remains constant after this isothermal stage in Figure 3.12a. The variation in fluence is due to the implanted helium concentration profile and the varied effective diffusion coefficient in depth since the concentration of defects varies in depth. It also shows that most helium is trapped in grainboundaries. The helium in grainboundaries starts to be redistributed at about 873 K with the used parameters.

Whether or not broadening of the concentration profile takes place depends on the effective diffusion coefficient of the grains and the effective diffusion coefficient in the grainboundaries. In Figure 3.12b an example is shown in which the effective diffusion coefficient of the grains larger is than the effective diffusion coefficient in the grainboundaries. Broadening of the helium concentration profile requires that helium atoms become trapped in the grainboundary volume for polycrystalline samples. This can only occur when the diffusion coefficient in the grains is larger than the diffusion coefficient at the grainboundaries. No broadening of the concentration profile occurs when the diffusion coefficient within the grains is significantly smaller than the diffusion coefficient at the grainboundaries.

3.3.5 Impact of diffusion mechanism on the helium release rate

The NDP results that monitor the concentration profile after successive isothermal stages can be used to identify the diffusion mechanism as discussed in the previous paragraph. Determination of parameters obtained by simulation of the measured helium concentration profile using this simple numerical analysis would still consume a lot of time. The THDS results show the helium release rate during isothermal stages. The helium flux at the onset and end of an isothermal stage is used to determine the activation energy and jumping frequency of dissolved helium [van Veen et al. 1999, Dienes et al. 1957]. This method is tested for different diffusion mechanisms.

The following equation describes the release rate as a first order process:

$$\frac{\partial N}{\partial t} = -Nf \quad (3.29)$$

where N is the amount of helium atoms in the sample and $f = f_{T_i} e^{\frac{-E_a}{kT_i}}$ where f_{T_i} is the jumping frequency of dissolved helium, E_a is the activation energy, and T_i is the temperature at the specific isothermal stage. A similar relation as equation 3.29 holds for the release rate after the temperature step ($T_i + \Delta T$). Upon dividing the release rates before and after the temperature step, the activation energy becomes:

$$E_a = k \ln \left[\frac{\left\{ \frac{\partial N}{\partial t} \right\}_{T_i + \Delta T}}{\left\{ \frac{\partial N}{\partial t} \right\}_{T_i}} \right] \times \left[\frac{1}{T_i} - \frac{1}{T_i + \Delta T} \right]^{-1} \quad (3.30)$$

if $N_{o,T_i+\Delta T} = N_{e,T_i}$ and $f_{T_i+\Delta T} = f_{T_i}$, $N_{o,T_i+\Delta T}$ and $\left\{\frac{\partial N}{\partial t}\right\}_{T_i+\Delta T}$ are the amount of helium and flux, respectively at the onset of the isothermal stage after the temperature step. N_{e,T_i} and $\left\{\frac{\partial N}{\partial t}\right\}_{T_i}$ are the amount of helium and flux respectively, at the end of the isothermal stage before the temperature step (T_i). The jumping frequency results from putting the activation energy in equation 3.29.

Figure 3.13 shows the calculated helium release rate and reduction of helium in the sample during the isothermal stages for a 30 keV implanted single crystal using *interstitial diffusion*.

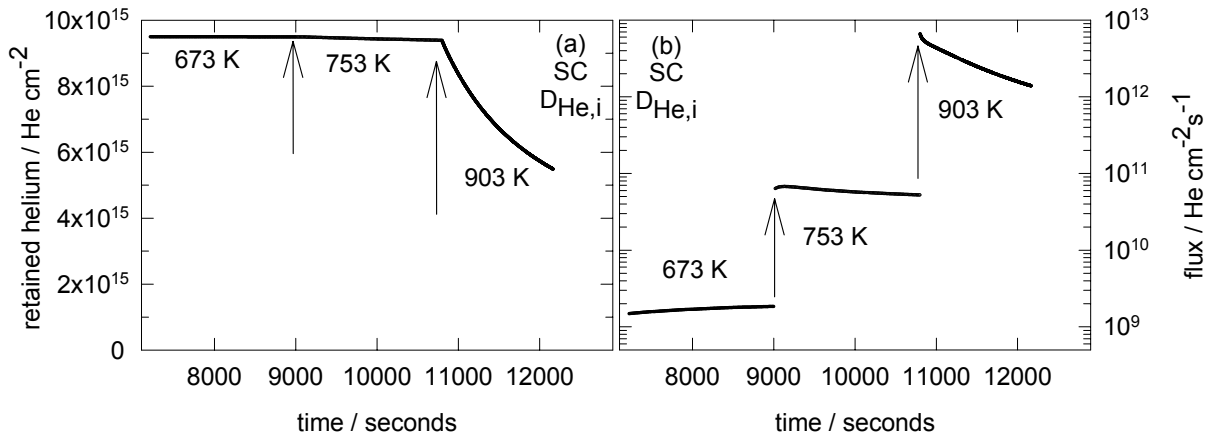


Figure 3.13 (a) Calculated retained helium and (b) helium release rate during isothermal stages using interstitial diffusion for a 30 keV implanted sample; $D_0=2.30 \times 10^{-3} \text{ cm}^2 \text{ s}^{-1}$, $E_M=1.89 \text{ eV}$; arrows indicate onset of successive isothermal stage.

The isothermal stages show a reduction in flux, except for the first isothermal stage of 673 K. This increase in flux may be a computational error for extremely small fluxes. Table 3.12 shows the input parameters and the derived parameters using the change in temperature method. The table shows that for interstitial diffusion, the temperature change method gives activation energies similar to the migration energy.

Figure 3.14 shows the fluxes for depth independent defect-mediated diffusion for a random helium implanted single crystal with energy of 4.52 MeV. It shows that the pre-exponential factor decays exponentially with increasing temperature or reducing retained amount of helium in the sample. Probably, the effective jump frequency depends heavily on the amount of helium left in the sample or temperature. Table 3.12 shows that the activation energy remains on a value equal to the sum of the binding energy and the migration energy.

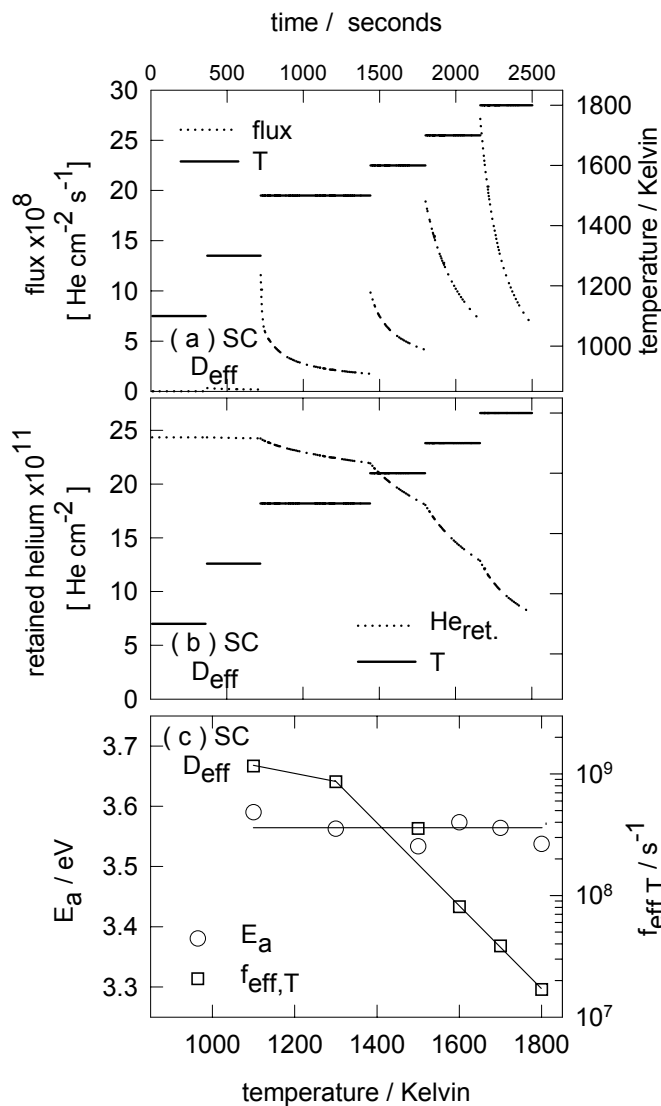


Figure 3.14 (a) Helium release rate and (b) retained helium using depth independent defect mediated diffusion for a randomly 4.52 MeV implanted sample. Parameters are $D_0=2.30 \times 10^{-3} \text{ cm}^2 \text{ s}^{-1}$, $E_M=1.59 \text{ eV}$, $E_B=2.00 \text{ eV}$, $n_i=50 \text{ ppm}$, $r_i=1 \text{ \AA}$. (c) Activation energies and effective jump frequency using the change in temperature method. Lines are drawn to guide the eye.

Concentration dependent defect mediated diffusion is used for 4 situations for 30 keV implanted samples in Table 3.12 (the implantation range μ is 0.2 μm). Figure 3.15 shows fluxes and dose using concentrated dependent defect-mediated diffusion and the activation energies using the change in temperature method. This figure also shows a reduction in the pre-exponential factor with decreasing retained amount of helium in the sample but also a reduction in the derived activation energy. Activation energies determined by the change in temperature method can differ significantly from the sum of the binding energy and migration energy. These results show that the activation

energy differ more from the sum of the binding energy and migration energy than the other two previously described diffusion mechanisms. This difference may initially be smaller than 0.2 eV but this becomes larger when the retained amount of helium reduces (or if the temperature of the isothermal stage increases) according Table 3.12 and Figure 3.15. Table 3.12 also shows an example of concentration dependent defect mediated diffusion for a 900 keV implanted sample. This activation energy is significantly smaller than the sum of the migration and binding energy, despite the method to determine the fluxes.

Table 3.12 Comparison of input parameters and parameters derived from calculated results using the change in temperature method.

Diffusion mechanism	$D_{He,i}$	D_{eff}	$D_{eff}(x)$	$D_{eff}(x)$	$D_{eff}(x)$	$D_{eff}(x)$	$D_{eff}(x)$	$D_{eff}(x)$
Figure Parameters	3.13	3.14				3.15	4.14	4.14
input parameters								
E_M / eV	1.89	1.59	1.59	1.59	1.59	1.59	1.59	1.59
E_B / eV	0	2.00	1.00	0.40	0.80	0.40	0.70	0.70
n_t	0	50 ppm	0.05 dpa	0.1 dpa	0.1 dpa	0.05 dpa	0.1 dpa	0.1 dpa
$r_t / \text{\AA}$	0	1	1	1	1	2	1	1
$\Delta S / eV K^{-1}$	0	0	0	0	0	-1×10^{-5}	0	0
$\mu / \mu m$	0.2	6.4	0.2	0.2	0.2	0.2	2	2
T / K	673-903	900-1800	773-973	673-753	903-953	672-953	973-1073	808-1073
N	3	7	2	2	2	4	2	5
derived parameters								
$f_{eff,T} / s^{-1}$	10^8-10^7	10^9-10^7	$10^{10}-10^9$	$10^{10}-10^9$	10^9-10^8	$10^{10}-10^5$	10^3-10^{2f}	10^2-10^5 ^g
E_a / eV	1.93-1.89	3.59-3.53	2.53	2.08	2.26	2.07-1.44	1.27 ^f	1.70-1.82 ^g
$L_{He} / He cm^{-2}$	10^{16}	10^{12}	$10^{16}-10^{15}$	10^{16}	10^{16}	$10^{16}-10^{14}$	$10^{16}-10^{15}$	10^{16}

Input parameter temperature independent pre-factor (D_0) is for all calculations $2.30 \times 10^{-3} cm^2 s^{-1}$; L_{He} is retained helium in the sample at the onset of the isothermal stage, T= range in temperature of isothermal stages, N = number of successive isothermal stages for the determination of activation energy and effective jump frequency.

^f fluxes determined by subtracting the integrated calculated concentration profile from the previous integrated calculated concentration profile and division of this subtraction by Δt .

^g fluxes determined by $-D_{x \approx 0} \left\{ \frac{\partial c}{\partial x} \right\}_{x=0}$.

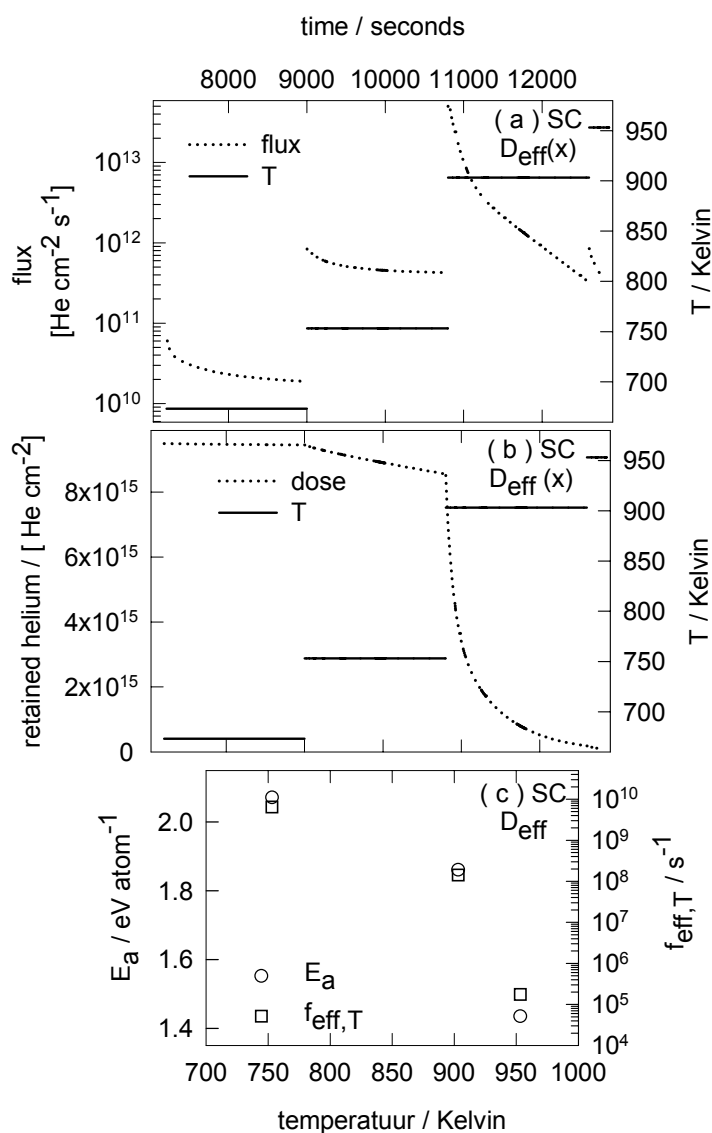


Figure 3.15 (a) Helium flux and (b) retained helium using concentration dependent defect-mediated diffusion for a 30 keV implanted sample.

Parameters are: $D_0=2.30 \times 10^{-3} \text{ cm}^2 \text{ s}^{-1}$, $E_M=1.59 \text{ eV}$, $E_B=0.40 \text{ eV}$, $n_i=0.05 \text{ dpa}$, $r_i=2 \text{ \AA}$, $\Delta S=10^{-5} \text{ eV K}^{-1}$. (c) Activation energies and attempt effective jump frequencies using the change in temperature method.

Figure 3.16 shows the retained dose in grains (g) and grainboundaries (gb), the sum of the two doses (g+gb) and helium release at the outer surface using concentration dependent defect-mediated diffusion for grains and depth independent pore-mediated diffusion in grainboundaries for polycrystalline semi-infinite media during successive isothermal stages. That the retained helium in grains does not approach zero is due to the limited amount of n used for this calculation. For this calculation $n=200$ in equation 3.24. For all calculations, the release of helium is

determined by subtraction of the integrated helium concentration profile from the integrated previous helium concentration profile. For polycrystalline samples, the sum of the concentration in grains and grainboundaries is used. A helium release is calculated although this is actually not so when helium migrates to larger depths than the set-off depth in the calculation. This may have occurred for the helium release at 1073 K.

Figure 3.16c shows the activation energies and jump frequencies using the change in temperature method. The activation energies are initially similar to the sum of the binding and migration energy of helium in the grains and migration and solution energy of helium in grainboundaries which is 4.14 eV. It remains relatively uniform despite the extremely low fluxes. When solely release from the grainboundaries is expected, the activation energy is similar to the sum of the migration and solution energy of helium in the grainboundaries. The effective jump frequency shows a lot of scatter versus temperature.

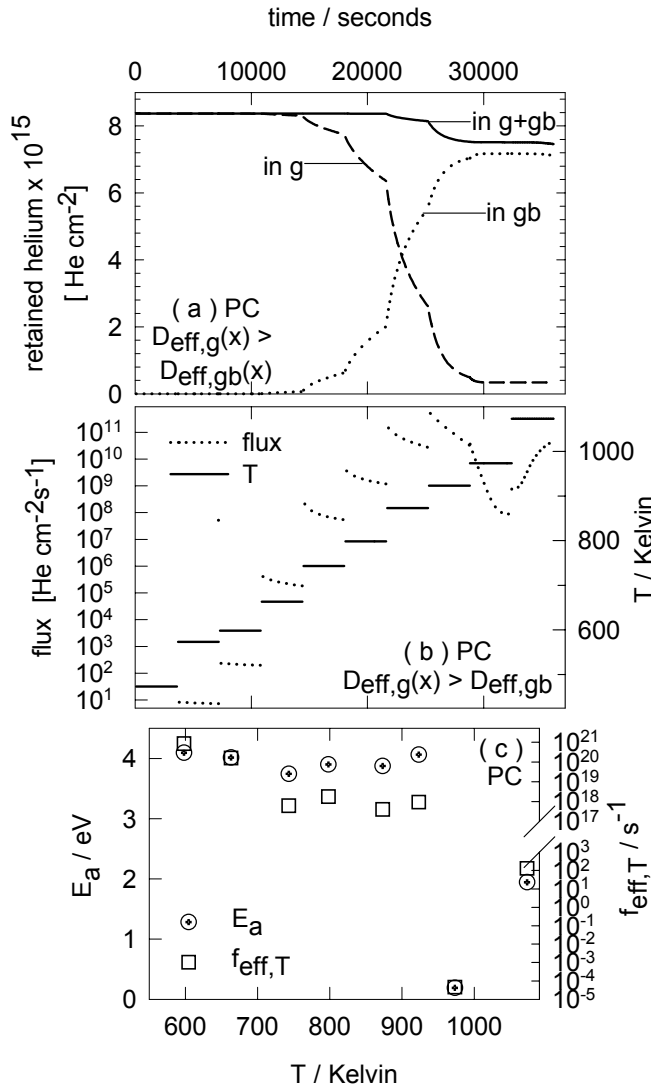


Figure 3.16 (a) Retained dose in grains (g) and grainboundaries (gb) and sum of these two doses (g+gb) and (b) helium release rate using concentration dependent defect-mediated diffusion for grains and depth independent pore-mediated diffusion for a 900 keV implanted sample. Parameters: $D_0=2.30 \times 10^{-3} \text{ cm}^2 \text{ s}^{-1}$, $E^M=1.59 \text{ eV}$, $E^B=0.60 \text{ eV}$, $n_i=0.05 \times \text{dpa}$, $r_i=1 \text{ \AA}$, $E^{M,gb}=0.45 \text{ eV}$, $E^{sol,gb}=1.50 \text{ eV}$, $\Delta S_{p,gb}=-1 \times 10^{-3} \text{ eV K}^{-1}$, $N_p=10^{12} \text{ cm}^{-2}$, $r_p=0.03 \text{ \mu m}$ and $a=0.48 \text{ \mu m}$ (c) Activation energies and attempt jumping frequencies using change in temperature method.

3.3.6 Conclusions of rate diffusion theory

For single crystal semi-infinite media: depth independent diffusion (interstitial diffusion and defect-mediated diffusion) shows broadening of the concentration profile and a shift of the peak of the concentration profile into depth after successive isothermal stages. The activation energies determined by the change in temperature method seem to be

similar to the migration energy of helium or the dissociation energy of helium from vacancies.

For single crystal semi-infinite media: concentration dependent defect mediated diffusion shows, initially, broadening of the concentration profile and a slight shift of the peak towards the surface. This is due to helium trapping in the defect profile that is broader than the initial helium implanted concentration profile and the peak of the defect profile that is more located towards the surface of the sample than the peak of the helium implanted concentration profile. The activation energies determined by the change in temperature method differ from the dissociation energy of helium from vacancies.

For polycrystal semi-infinite media, whether or not broadening of the helium concentration profile occurs after successive isothermal stages depends on the difference between the effective diffusion coefficient within grains and at grainboundaries. Limited calculations are performed for the determination of activation energies using the change in temperature method. The initial results show that the activation energy is similar to the sum of the dissociation energy of helium from defects in grains and the permeation energy of helium from intergranular pores during isothermal stages where helium release from grains and grainboundaries occurs.

4 Diffusion of helium in helium implanted samples of MgAl_2O_4

Modelling of helium in spinel was discussed in the previous chapter. In this Chapter, the empirically derived kinetics of helium implanted samples, single crystal and poly crystal semi-infinite media, are determined. Since this research is performed in order to simulate processes taking place during irradiation of Am in spinel, a paragraph is devoted to the thermal redistribution of helium in a pellet during irradiation conditions.

4.1 Preparation and characterisation of samples

Single crystals of MgAl_2O_4 (Kelpin) were prepared by sawing substrates on the (100) plane and these samples were polished with a suspension of SiO_2 . Contactlessly interferometrical measurements show that roughness of the polished samples was 0.205 ± 0.251 nm using a Kugler KMS microscope. The difference from the (100) plane was $\pm 1^\circ$. These samples were implanted with ^3He at energies of 30 keV with a current of 1-2 μA and 900 keV with a current of 700 nA. Also, one single crystal was implanted with α -particles with an energy of 4.52 ± 0.166 MeV with a rate depending on the radioactivity of the AmO_2 sample. Table 4.1 shows an overview of the implanted samples and the codes that are used for the identification of the samples in this Chapter. Samples showed a brownish colour after implantation. The intensity of this brownish colour increased with implanted dose.

Table 4.1 Overview of samples implanted at RT

Sample	Implantation energy [MeV]	Dose [cm^{-2}]	Dose rate [$\text{cm}^{-2} \text{s}^{-1}$]
S-Am	4.52 ± 0.166	2.5×10^{12}	2.1×10^5
S30L	0.030	6.2×10^{15}	8.3×10^{12}
S30	0.030	1.9×10^{16}	1.2×10^{13}
S30M	0.030	1.6×10^{16}	1.2×10^{13}
S30H	0.030	5.3×10^{16}	1.2×10^{13}
S900L	0.9	8.2×10^{15}	4.4×10^{12}
S900H	0.9	11.2×10^{16}	4.4×10^{12}
P900L	0.9	8.4×10^{15}	5.0×10^{12}
P900H	0.9	9.1×10^{16}	5.0×10^{12}

S = single crystal, P = polycrystalline sample

Two polycrystalline samples were made by pressing powder from GIMEX (S30CR) at 1500 kg using a pneumatic device and a die with a diameter of 20 mm. The resulting pressure on both sides of the pellet was 47 MPa. These green disks were sintered for 1 hour in O_2 at 1873 K. X-ray diffraction films showed that the polycrystalline samples had the crystal structure of stoichiometric spinel. The geometrical density of the two samples was 3.442 and 3.418 gr/cm^3 respectively. The densities as a percentage of the theoretical one for the two samples were 96.2% and 95.5%, respectively using a density of 3.579 gr/cm^3 for a 100% dense spinel. The decrease in volume of the disk from before to after sintering is 42% to 43% assuming similar shrinkage properties of the height and diameter of the disk. In order to minimise the variation in height of the disks these disks were sandblasted resulting in a variation of height of less than 0.01 mm. The size of grains and pores was determined from a (thermally etched) polished surface. Grain boundaries were visible after a thermal etching period of 6 minutes at 1473 K. The two-dimensional distribution of pores and grains, using image analysis of the surfaces, was transformed into a three-dimensional distribution using the Saltykov method [ASM 1995]. Figure 4.1 shows the distribution of pores and grains in the

polycrystalline samples. These two polycrystalline samples have been implanted using a current of 800 nA and an energy of 900 keV.

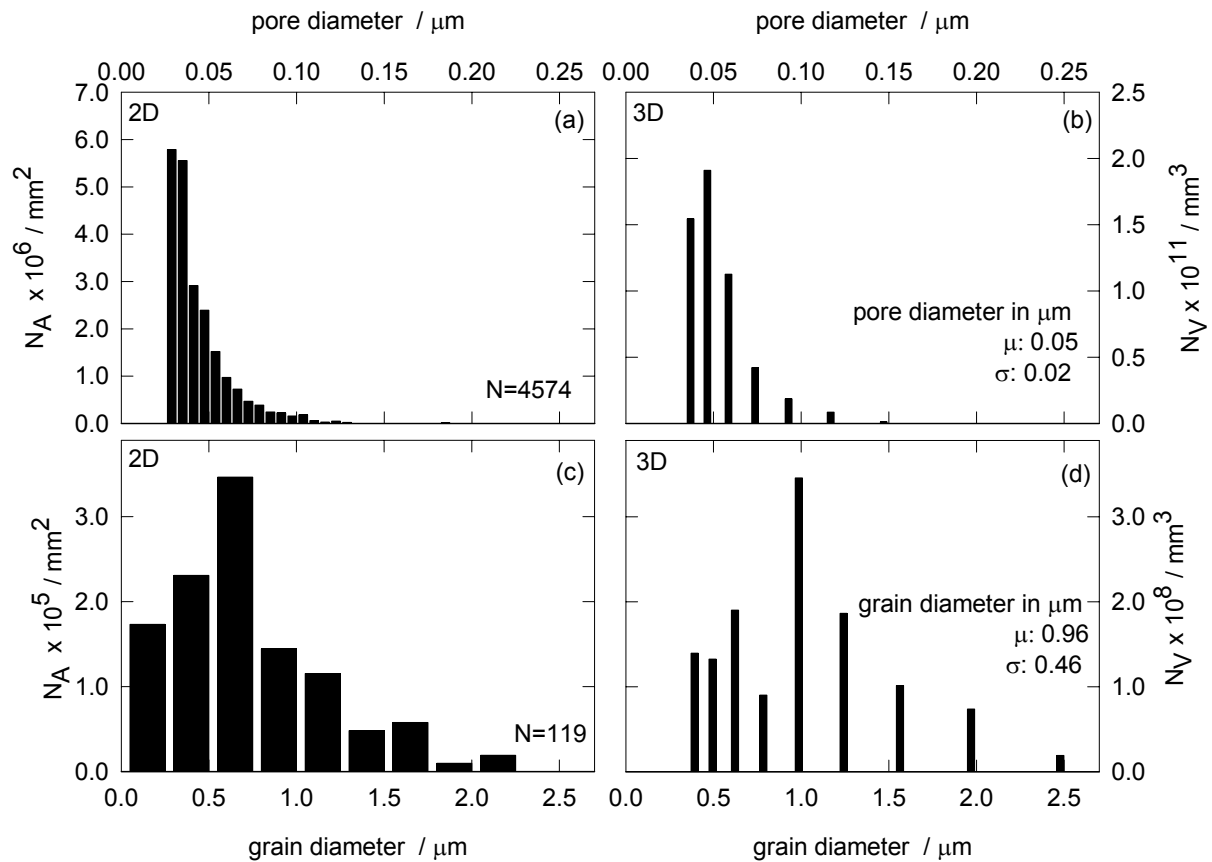


Figure 4.1 Two and three dimensional distribution of (a-b) pores and (c-d) grains of polycrystalline samples of $MgAl_2O_4$ used for helium implantation.

4.2 Identification of diffusion mechanisms from concentration profiles

With Neutron Depth Profiling (NDP), the concentration profiles of the implanted samples can be studied. NDP is a density technique (see paragraph 2.3.1). The concentration profiles described in this section are presented in depth-units by assuming no change in density after implantation and after successive isothermal stages. Table 4.2 shows the Gaussian parameters of the implanted profiles from NDP results and calculated profiles using SRIM [Ziegler et al. 2002].

The NDP results of the single crystals are somewhat broader than the calculated helium implanted profile but agree quite well with the calculated profiles using SRIM. The roughness of polycrystalline samples may have caused the broader profile as measured in comparison with the calculated one.

Table 4.2 Gauss-parameters of implanted profiles at RT¹.

Sample	NDP results			Calculated			<
	μ [μm]	conc. ³ He at μ [at%]	FWHM [μm]	μ [μm]	conc. ³ He at μ [at%]	FWHM [μm]	
S30L	0.109	0.329	0.17	0.106	0.363 ± 0.005	0.14	60
S30	0.062	1.15	0.14				
S30M	0.121	1.01	0.14	0.120	0.988 ± 0.017	0.14	55
S30H	0.113	3.24	0.14	0.120	3.13 ± 0.05	0.14	55
S900L	1.97	0.255 ± 0.005	0.25	1.99	0.309 ± 0.004	0.19 ± 0.03	20
S900H	1.98	3.80 ± 0.02	0.26	1.99	3.98 ± 0.06	0.19	20
P900L	2.04	0.183 ± 0.002	0.41	2.07	0.359 ± 0.005	0.21	20
P900H	2.09	2.05 ± 0.02	0.39	2.07	3.80 ± 0.06	0.21	20

S = single crystal, density 3.579 g cm⁻³, P = polycrystalline sample, density 3.442 g cm⁻³, all values ± 1 σ if stated otherwise 1 σ ≤ 0.01 or 1 σ ≤ 0.001, < = angle of incidence with surface.

The actual implanted profiles differ from a Gaussian profile: the tails towards surface of the sample are larger in depth–units than into depth of the sample. As shall be shown later on, the identification of the diffusion mechanisms may be lost when approximating the concentration profiles by a Gaussian function. In order to obtain a document that could be read well, the values of Gaussian parameters are plotted versus the temperature of the isothermal stage. The dose obtained by integration of the Gaussian function is divided by the actual measured dose in order to have an indication of the difference between the measured concentration profile and the fitted Gaussian concentration profile. Figure 4.2 shows the Gaussian parameters that fit best for the 30 keV implanted profiles. The inserts in Figure 4.2 shows the integrated Gaussian functions divided by the actual dose.

The largest difference between the integrated Gaussian functions and actual dose for these 30 keV implanted samples is at roughly the same temperature of isothermal stage; 753 K and 773 K. Figure 4.3 shows selected concentration profiles of the 30 keV implanted samples after isothermal stages. The lines in these figures are the Gaussian functions. The inserts in Figure 4.3 shows that the tail towards depth is not included in the Gaussian function that fits the concentration profile best.

The largest difference between the integrated Gauss function and actual dose in Figure 4.2 may indicate interstitial diffusion of helium into the bulk of MgAl₂O₄ since the difference is caused by the tail into depth (see Figure 4.3). The increase in this ratio from 0.91 to 0.95 to 0.97 for respectively S30L, S30M and S30H may indicate the increase in fraction of helium atoms trapped in defects. This diffusion mechanism was not observed if only fitted Gaussian functions of the measured profiles were used.

¹ at% is here defined as ³He cm⁻³ ÷ atoms cm⁻³ consisting of Mg, Al and O, times 100 to achieve a percentage

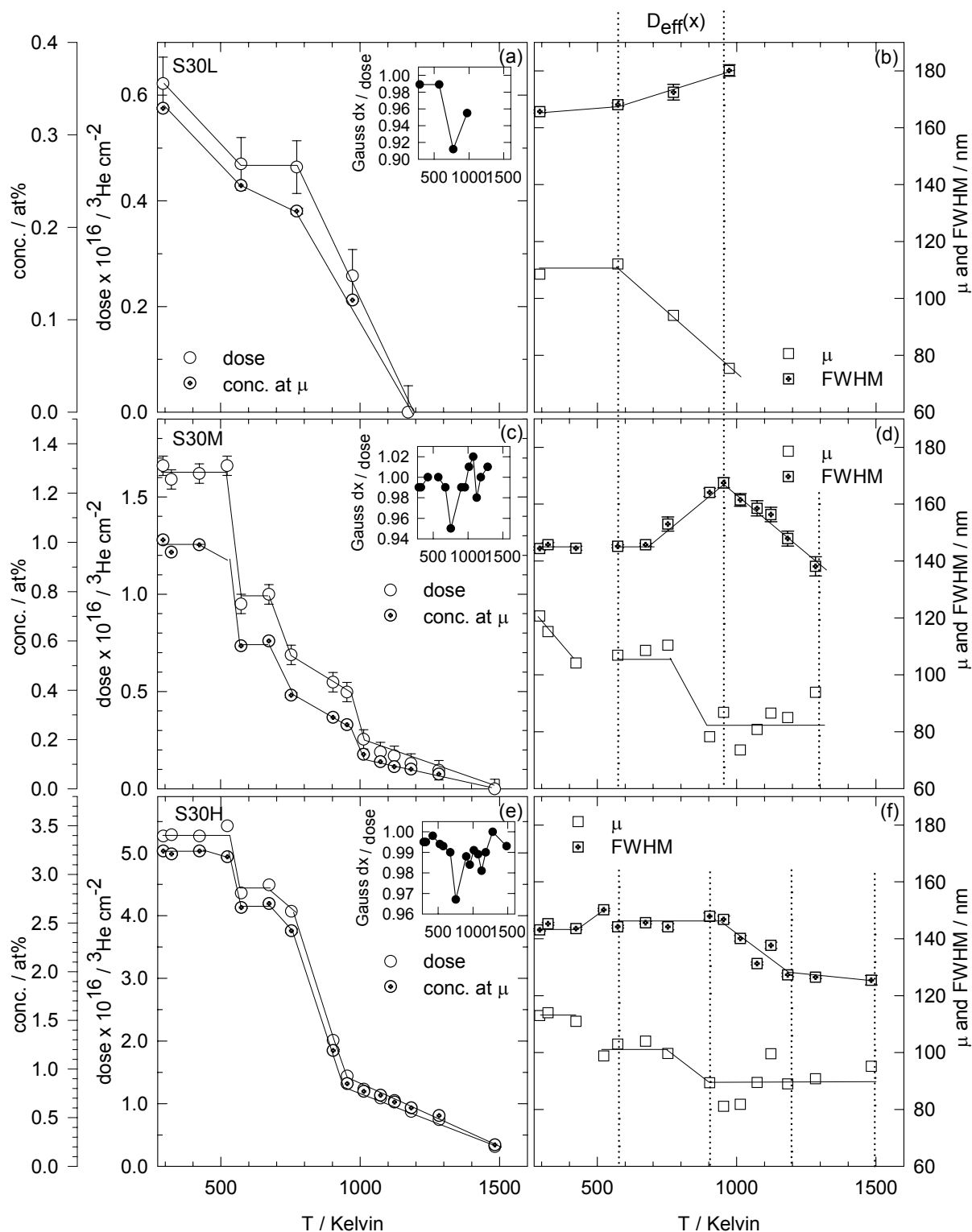


Figure 4.2 Gaussian parameters of 30 keV implanted samples and retained dose versus temperature of isothermal stages of 1800 seconds in air for (a-b) S30L, (c-d) S30M and (e-f) S30H. Solid lines are drawn to guide the eye. Inserts show integrated fitted Gaussian profiles divided by the actual dose. Dotted lines indicate stage of diffusion mechanism, if known.

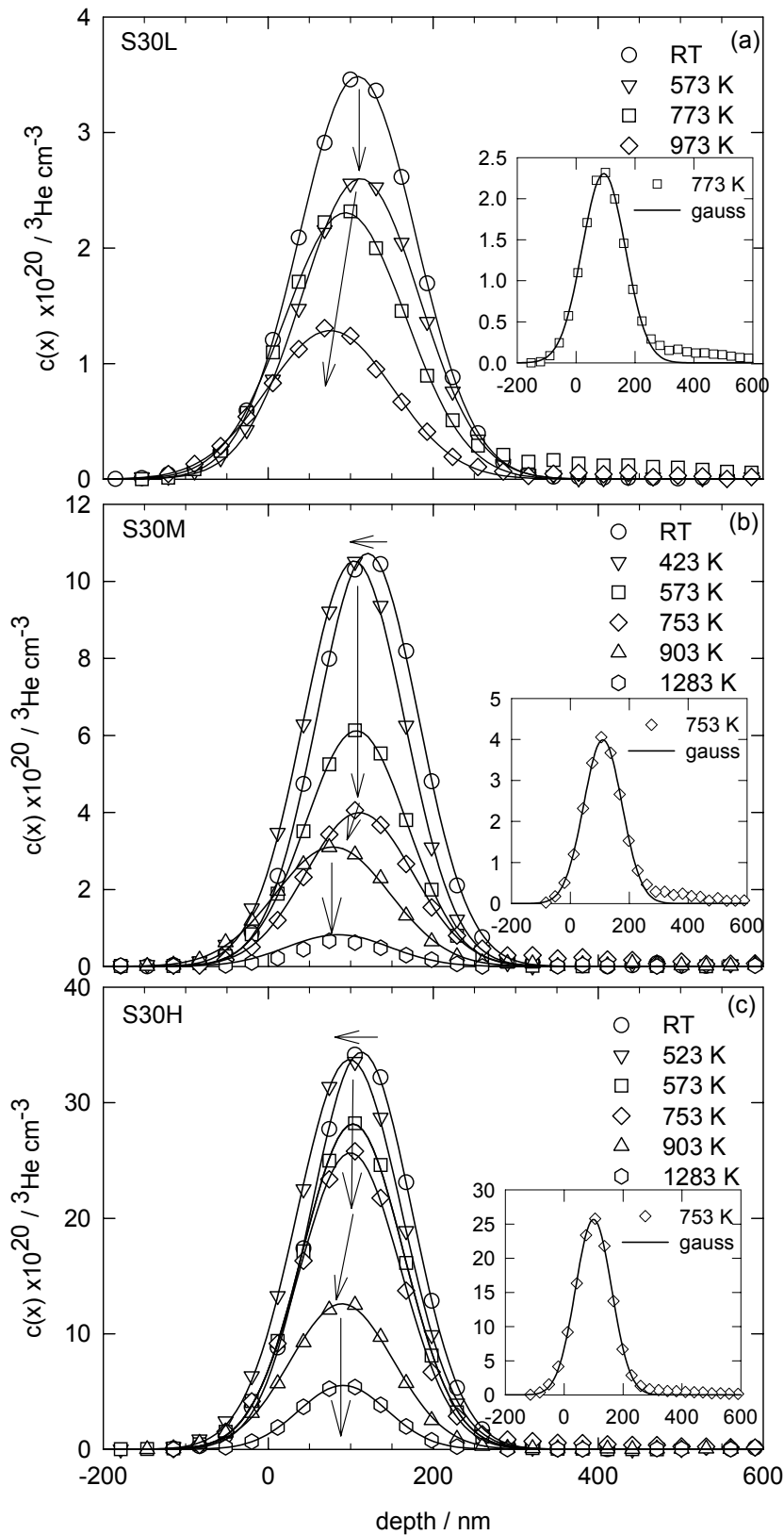


Figure 4.3. Selected concentration profiles (symbols) of the 30 keV implanted profiles after isothermal stages of 1800 seconds in air and the Gaussian profiles that fit these concentration profiles best (solid lines) for (a) S30L, (b) S30M and (c) S30H; arrows are drawn to indicate the trend. Inserts show concentration profiles with the smallest ratio between integrated fitted Gaussian function and actual dose.

The characteristics for concentration dependent defect mediated diffusion as modelled in chapter 3 are broadening of the concentration profile and a slight shift of the peak towards the surface of the sample for implanted samples after successive isothermal stages. Figure 4.2 shows that this is the diffusion mechanism for S30L at all isothermal release stages and for S30M at the isothermal stages till a temperature of 1000 K.

Clustering is not taken into account for concentration dependent defect mediated diffusion

described in Chapter 3. The assumption that no clustering occurred during thermal treatment of S30L is encouraged by Positron Beam analysis (PBA) for S30L. PBA is only performed on

S30L after isothermal stages. It showed that the amount of open volume (bubbles or clustered defects) after implantation and after the isothermal stages is identical to the initial open volume present in the non-implanted single crystal [Neeft et al. 1999]. It can therefore be assumed that no swelling took place and thereby no clustering occurred for S30L.

The release after the isothermal stage of 573 K is due to the low implantation depth since the 900 keV implanted samples do not have such a release stage. The brownish colour created after implantation, disappeared at 573 K. At this temperature, recovery of defects may have occurred resulting in release of helium when these helium atoms are located at the surface. The high dose implanted samples P900H and S900H show this stage by a slight redistribution in the concentration profile without release at the same temperature.

The first release stage caused by diffusion mechanisms of helium occurred for the medium/high dose implanted samples S30M and S30H during the isothermal stage at 753 K and for the low-dose implanted sample S30L during the isothermal stage at 973 K. The reason for this feature can only be caused if the pressure of helium in defects is higher for S30M and S30H than for S30L. The higher pressure of helium in defects in S30M and S30H in comparison with S30L results in a smaller dissociation energy for S30M and S30H than for S30L resulting in a lower temperature of release in comparison with S30L.

For concentration dependent defect mediated diffusion as modelled in chapter 3, the binding energy (and entropy) was constant in depth, only the concentration of defects varied in depth. The entropy and binding energy can however also vary in depth. For example in regions with a high concentration of implanted defects, clustering of defects may have occurred while clustering may be absent in regions with a low concentration of implanted defects. Then, the probability of a helium atom, released in a region with a high concentration of implanted defects, to become trapped in regions with a lower concentration of implanted defects during the isothermal stage reduces further. This may be to such an extent that only helium in the region with a high concentration of implanted defects is visible after the isothermal stage. This may result in a constant width of the concentration profile or even a reduction in the width of the concentration profile with increasing temperature of isothermal stage.

Figure 4.4 and Figure 4.5 show the NDP results of the 900 keV implanted samples: S900L, P900L and P900H. The 900 keV low dose implanted samples: S900L and P900H have a too small helium concentration to perform NDP measurements well at a depth of 2 μm ; the scattering in these samples is quite large. This is due to an increasing background with increasing depth.

S900L shows broadening of the helium concentration profile and a slight shift of the peak towards the surface of this sample in Figure 4.4. This process is characteristic for concentration dependent defect mediated diffusion, similarly as discussed for S30L. The profile measured after the isothermal stage of 973 K in Figure 4.5a shows a large tail towards the surface. This tail is characteristic of helium trapped in defects, similarly as shown in Figure 3.11. Why S30L shows a tail into depth indicating interstitial diffusion and S900L not, is discussed in paragraph 4.4.1.

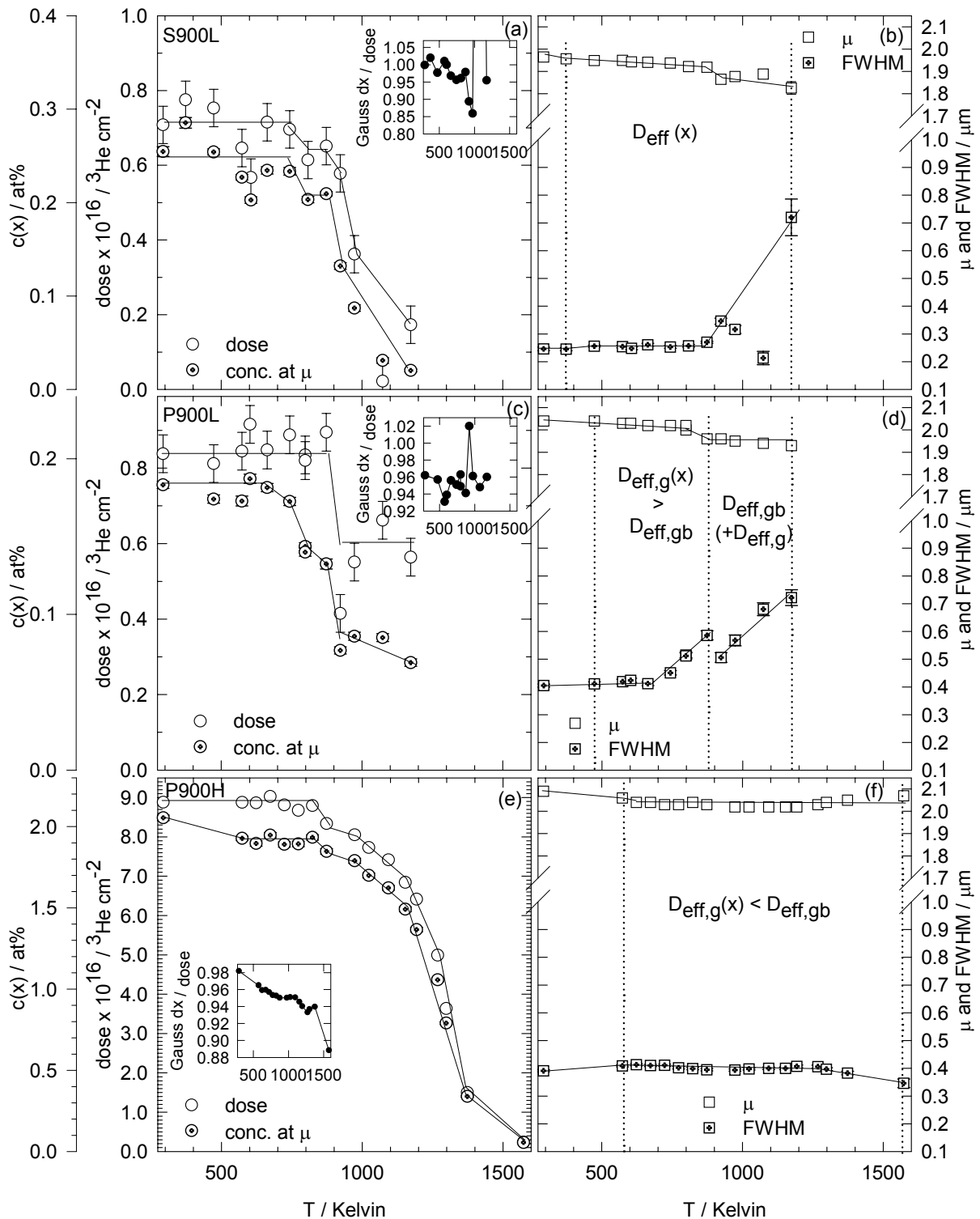


Figure 4.4 Gaussian parameters of 900 keV implanted samples and retained dose versus temperature of isothermal stages of 3600 seconds in air for (a-b) S900L, (c-d) P900L and (e-f) P900H. Solid lines are drawn to guide the eye. Dotted lines indicate stage of kind of diffusion mechanism, if known. Inserts show the integrated fitted Gaussian profiles divided by the actual dose.

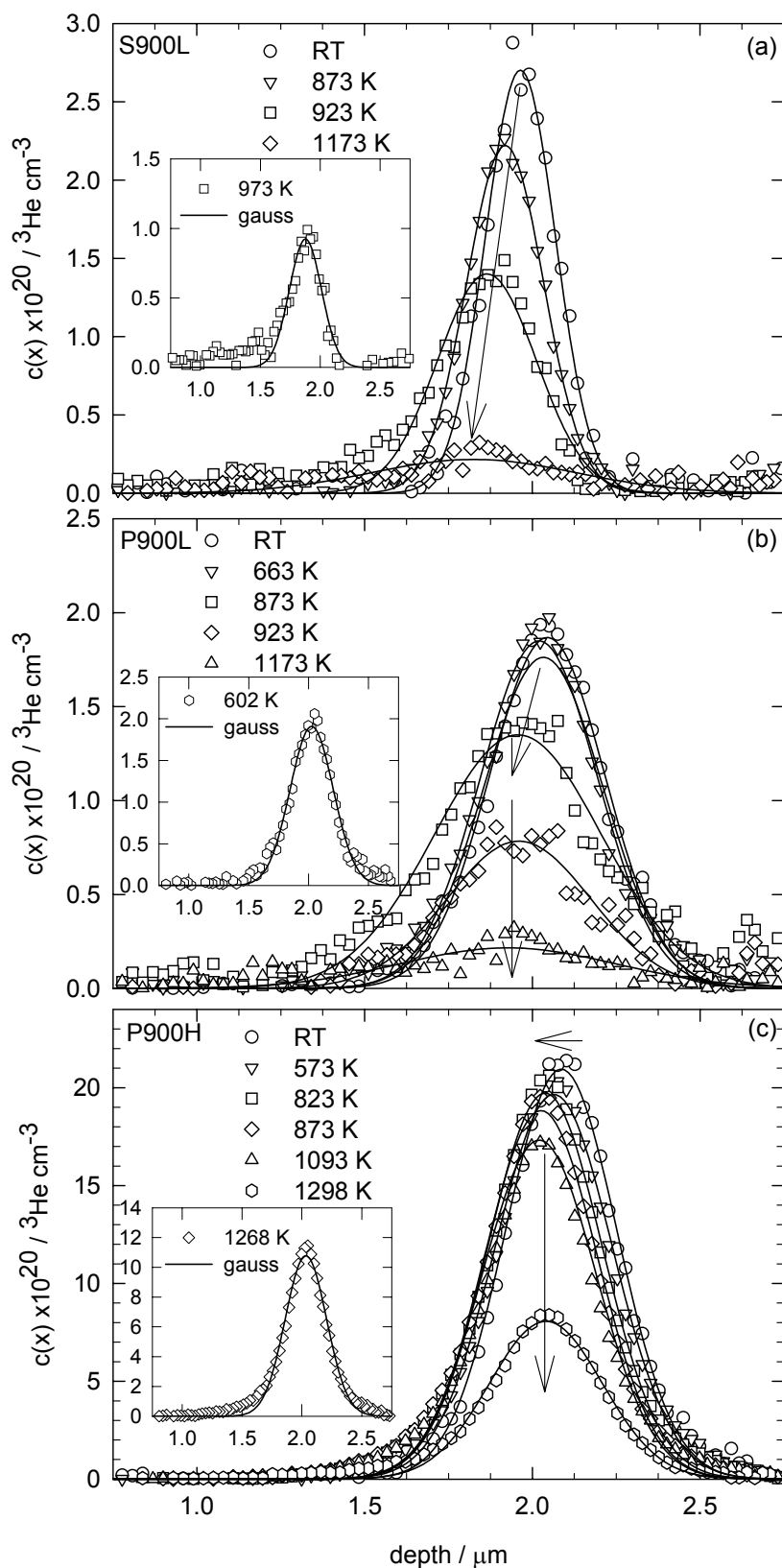


Figure 4.5 Selected concentration profiles (symbols) of the 900 keV implanted profiles after isothermal stages of 3600 seconds in air and the Gaussian functions that fit the measured profile best (solid lines) for (a) S900L, (b) P900L and (c) P900H; arrows are drawn to indicate the trend. Inserts show concentration profiles with the smallest ratio between integrated fitted Gaussian function and actual dose.

Figure 3.12 showed a calculation of diffusion of helium in polycrystal semi-infinite media. A slight shift of the helium concentration peak towards the surface of the sample occurred at stages in which helium release from grains took place and redistribution of helium in grainboundaries was present. In this stage, a fraction of helium was not trapped in intergranular pores and released to the outer surface. The parameters for grains and pores used for this modelling are derived from the experimental data in Figure 4.1. The process described and modelled in Figure 3.12 is similar to the concentration profiles of P900L although the binding and migration energy and entropy in Figure 3.12 may differ from the actual energies and entropy. In the second stage, two mechanisms may have occurred:

1) all helium is released from grains and trapping and de-trapping of helium in intergranular pores occurred;

2) no helium is left in vacancies and vacancy clusters; all helium is present in inter- and intragranular pores; helium redistribution occurred by de-trapping and trapping of helium from pores.

The helium concentration profile is broadened and a slight shift of the peak into depth of the sample occurred in Figure 3.12 when assuming the absence of intragranular pores. Figure 4.5 shows a broadening of the concentration profile and the peak of the concentration profile remains constant in this second stage.

Almost no broadening occurred after the isothermal stages and the position of the peak remains constant for P900H. It is expected that helium released from the grains will be trapped and de-trapped at a higher rate at grainboundaries than within the grain resulting in the absence of helium outside the helium implanted profile after successive isothermal stages.

Figure 4.6 shows the NDP and laserprofilometry results of the high dose implanted single crystal S900H. This sample showed after a tiny release of helium at 773 K, flaking at 823 K. The arrows, indicating examples of regions with similar geometry, show that the flaked areas still contain helium.

Flaking or interbubble fracture occurs if the concentration of (pressurised) bubbles with a specific radius exceeds at certain pressure. The implanted dose of polycrystalline sample P900H showed no flaking although the dose is similar to S900H. The (100) plane of MgAl_2O_4 is most susceptible for crack growth in comparison with the (110) and (111) plane [Fang et al. 2000]. This is probably the reason why flaking is observed by NDP for S900H but not for P900H since polycrystalline samples of MgAl_2O_4 have fracture properties similar to the (111) plane in case of transgranular fracture [Stewart et al. 1981].

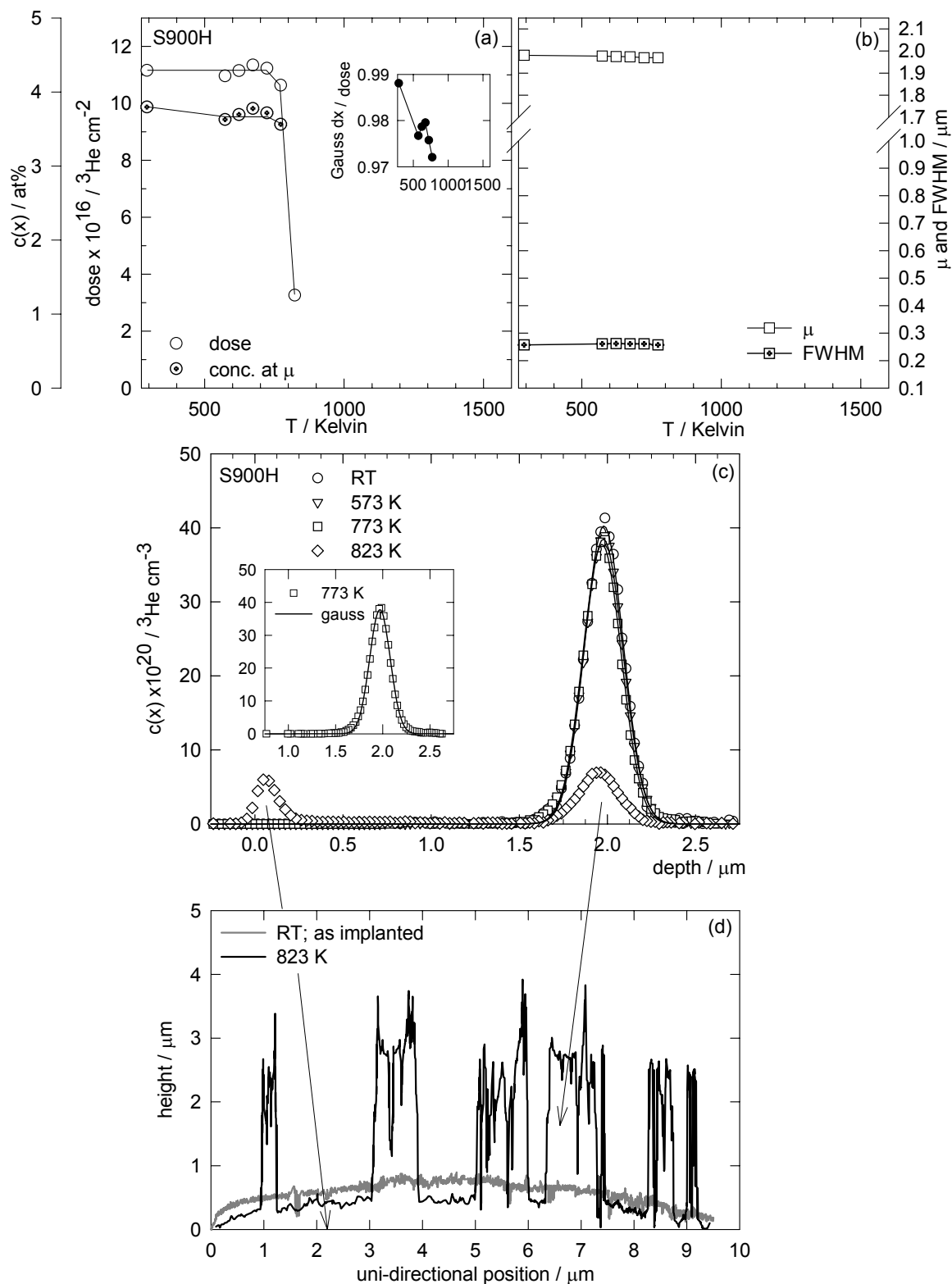


Figure 4.6 S900H showing after isothermal stages of 3600 seconds in air (a) retained dose, concentration of peak of Gaussian profile and ratio of integrated Gaussian profile and actual dose, (b) location of peak of Gaussian profile and FWHM (c) selected concentration profiles after isothermal stages (symbols) Gaussian functions that fit the measured profile best (solid lines) and (d) laserprofilometry. Arrows are drawn to guide the eye.

4.3 THDS

With Thermal Helium Desorption Spectroscopy (THDS), the kinetics of the helium release can be studied. All samples were implanted with ^3He , except for the single crystal that is implanted with α -particles originating from the decay of ^{241}Am . The disadvantage of using ^3He is the difficulty to discern by mass ^3He from the background containing hydrogen ($^2\text{H}-^1\text{H}$).

4.3.1 ^3He and background

Figure 4.7 shows an example of a THDS result for a low dose implanted sample; the low dose implanted single crystal S900L.

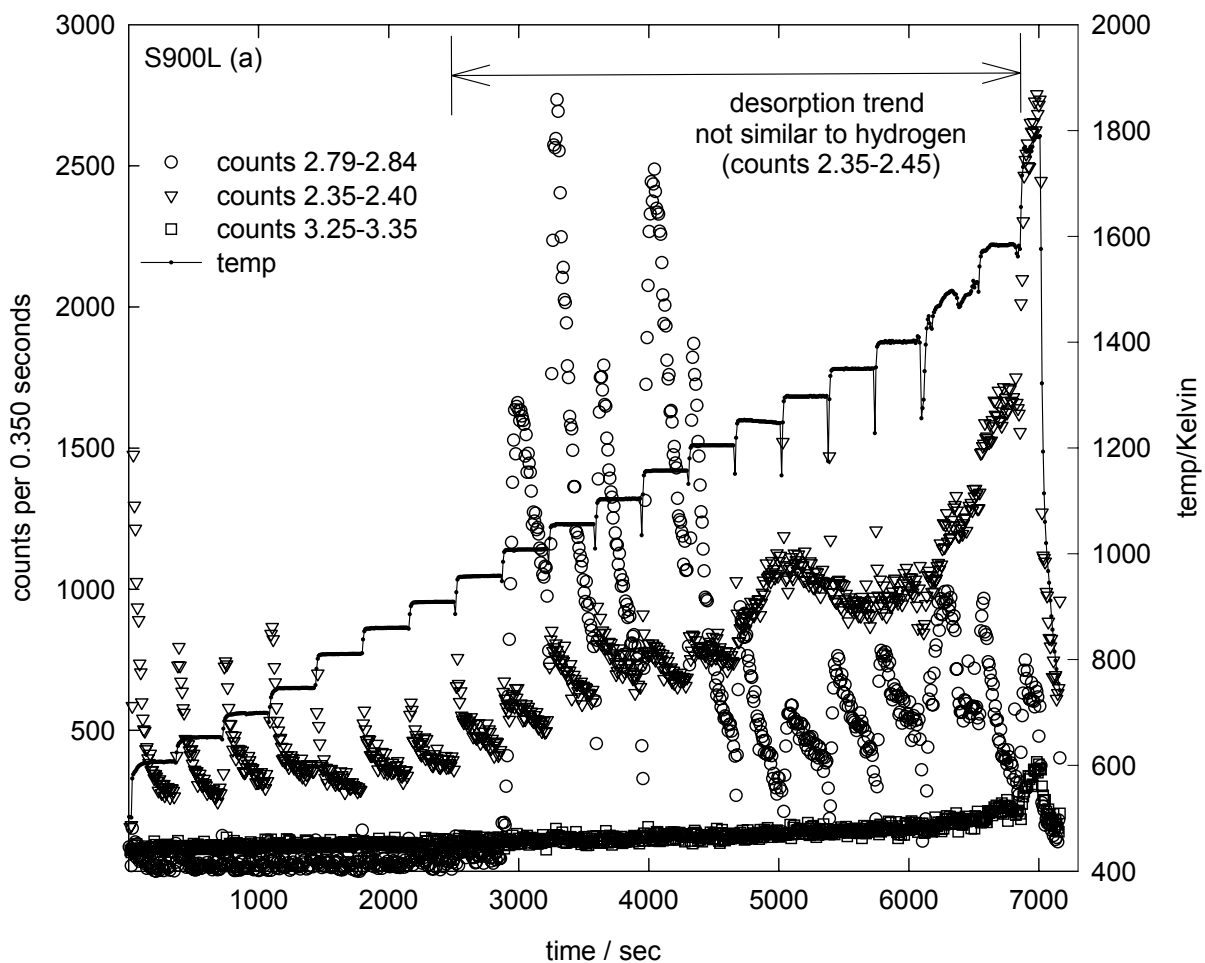


Figure 4.7. Uncorrected release and temperature versus time of low dose implanted single crystal S900L (a).

The mass of ^3He is 3.016029 amu and the mass of $^1\text{H}-^2\text{H}$ is 3.021927 amu [Ohanian 1989]. The quadrupole mass-spectrometer cannot discern this atom and this molecule because of their small difference in mass. Although the natural composition of ^2H is small: 0.015 at% of ^1H , at temperatures higher than 1200 K release of $^2\text{H}-^1\text{H}$ can be more than ^3He , especially for the low dose implanted samples, despite the hours of heating of the furnace by an external source to remove absorbed hydrogen.

An attempt was performed to deduce whether or not a constant ratio between ^1H - ^1H and ^1H - ^2H exists with increasing temperature. This failed. However, the trend in release with temperature and time is similar for ^2H - ^1H and ^1H - ^1H . For the present study, the release in time for particles between the mass 2.79-2.84 amu is defined as ^3He if the trend of the release in time is not similar for counts of particles between mass 2.25-2.45. (The results of the measurement of the used quadrupole mass-spectrometer can always be defined as a Gaussian profile with a sigma of about 0.2 amu. The experimental value of ^1H - ^1H is about 1.87 amu. ^1H - ^1H is thereby characterised by 1.9σ to 2.9σ). Figure 4.7 shows that helium can be discerned from hydrogen by the trend of its release. Figure 4.7 also clearly shows that during each isothermal stage, the helium release rate similarly decays as calculated in Figures 3.14 and 3.15.

4.3.2 Difference between temperature of sample holder and sample

Electron bombardment on the sample holder tungsten results in emission of radiation in the near-infrared region. To reach the adjusted temperature takes on average about 14 seconds for the sampleholder W and 57-58 seconds for the samples MgAl_2O_4 using the helium flux within 5% of the peak value. MgAl_2O_4 is measured to be transparent at wavelengths smaller than $4\ \mu\text{m}$ (temperature conditions unknown but probably at room temperature) [Kingery et al. 1975]. The emitted wavelength range of tungsten is $0.35\text{-}2.5\ \mu\text{m}$ and the energy output in the visible region is approximately about the fourth power of the operating voltage [Skoog et al. 1980]. In terms of temperature, the emissivity in the visible region of tungsten is about 10-20% of the total emissivity at temperatures higher than 1000 K [Handbook of Chemistry and Physics 2003]. Impurities and defects in MgAl_2O_4 have some absorption in the visible region and this could have an effect on the difference in time achieving the adjusted temperature between the sampleholder tungsten and MgAl_2O_4 . Figure 4.8 shows the delay in time for the samples MgAl_2O_4 and W until the adjusted temperature is achieved. The difference in delay in time between single crystal (S900L) and polycrystalline sample (P900L) indicate that porosity possibly had an effect on the absorption of γ 's to heat the sample in the low temperature regime. The single crystal is therefore presumably mainly heated by contact between the sample and the sampleholder. Samples were heated using isothermal stages to ensure that the temperature of the sample is the same as the sample holder.

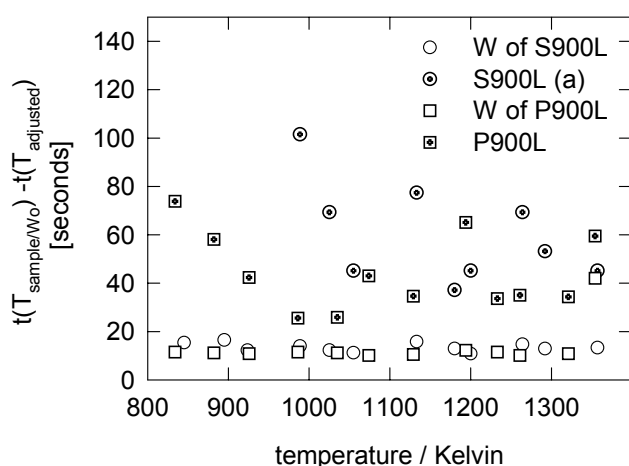


Figure 4.8. Delay in time for sample MgAl_2O_4 and sampleholder W achieving adjusted temperature.

This delay in time at which the temperature reaches the adjusted temperature for each isothermal stage will result in too small activation energies when the method described in paragraph 3.3.6 is used, if this method could be used.

Microprobe measurements show W on the desorped samples. The vapor pressure of tungsten is 1×10^{-4} Pa at 1400 K when assuming a linear relation between the logarithm of pressure and temperature from the data in Handbook [Handbook of Chemistry and Physics 2003]. This pressure is similar to the pressure in the crucible during measurements (see paragraph 2.2.2) At higher temperatures, the vapor pressure of tungsten increases and thereby more tungsten is evaporated on the samples since the pressure of the crucible is smaller than the vapor pressure of tungsten. W had been evaporated on the surface of the samples during the THDS experiments.

A piece of low dose 900 keV implanted single crystal could not be removed from the crucible after an isothermal stage of 2045 K due to melting. It is unclear whether this melting was caused by elements that had been evaporated on the surface within the crucible during previous experiments with the THDS equipment since the samples implanted with α -particles after isothermal stages till 2200 K do not show melting of these single crystals.

4.3.3 Results

Figure 4.9 shows the retained fraction of helium using THDS for 900 keV implanted samples. It shows for similar isothermal stages in which the major release of ^3He (0.2 to 0.8 retained fraction, see dotted lines in Figure 4.9) took place is at:

- 800-1150 K for the high dose implanted single crystal S900H;
- 1050-1300 K for the low dose implanted single crystal S900L (a) and (b);
- 1050-1450 K for the high dose implanted polycrystalline sample P900H (a) and (b);
- 1000-1500 K for the low dose implanted polycrystalline sample P900L; this sample required the highest temperatures to complete the helium release.

Differences in retained fraction of THDS measurements and retained dose of NDP samples (Figure 4.5 and Figure 4.6) are due to differences in time of isothermal stages.

If the helium release rate suddenly increased during the isothermal stage, other than at the onset of the isothermal stage, then flaking had occurred. This occurred for the high dose implanted single crystal S900H at many stages and for the high dose implanted polycrystalline sample P900H at some stages. Flaking after the isothermal stages used for the NDP measurements could be observed for the high dose implanted single crystal S900H but not for the high dose implanted polycrystalline sample P900H. The formation of pressurised bubbles occurred at a faster rate during the THDS experiments than NDP experiments because the isothermal stages were shorter in time for THDS than for NDP. The chance of a non-thermodynamic equilibrium, which is flaking, is therefore higher for THDS than for NDP. Since equation 3.30, used for determination of the activation energy, is depth-independent, it can be used for flaked samples in this perspective.

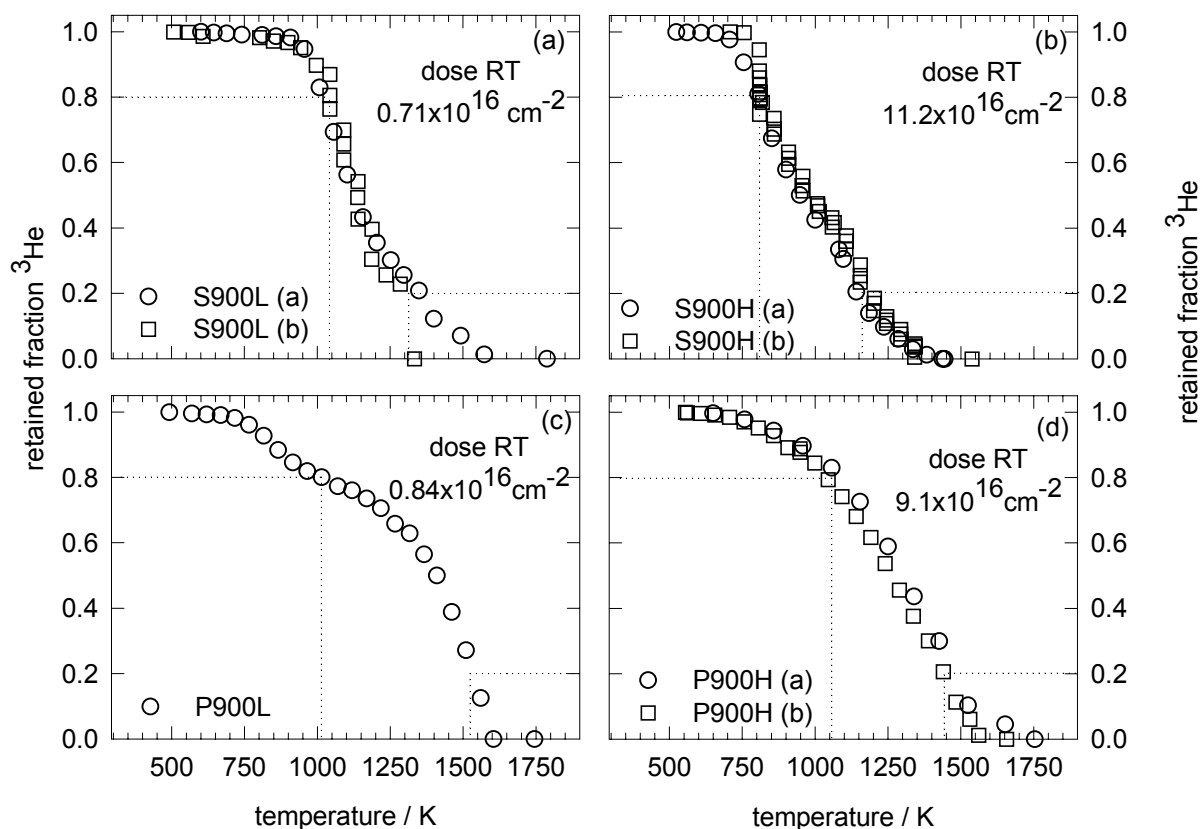


Figure 4.9 Retained fraction of 900 keV implanted samples versus temperature for (a) S900L, (b) S900H, (c) P900L and (d) P900H. Retained fraction profiles composed of circles have less isothermal stages than the retained fraction profiles composed of squares.

Figure 4.10 shows the activation energies and effective jump frequencies using the helium release rate at onset and end of isothermal stages as described in paragraph 3.3.5. It shows that the scatter in activation energy for the high dose implanted samples is significantly larger than for the low dose implanted samples. This is in agreement with the calculated results in paragraph 3.3.5 that showed for the samples with a high concentration of implanted defects scatter in activation energies and for the low dose implanted samples more uniform activation energies. The use of the helium release rate at onset and end of the isothermal stage is therefore inapplicable for high dose implanted samples as concluded in paragraph 3.3.5. This feature is explained in Figure 4.11.

The measured effective jump frequency is by far smaller than the calculated effective jump frequency in paragraph 3.3.5. Nevertheless, the trend of a reducing effective jump frequency with reducing retained amount of helium during a diffusion process or with increasing temperature of isothermal stage (see Figures 3.14 and 3.15) can also be viewed in the result of the low dose implanted single crystal S900L in Figure 4.10.

The rather uniform effective jump frequency for the low dose implanted polycrystalline sample P900L is similar to the calculated one in figure 3.16.

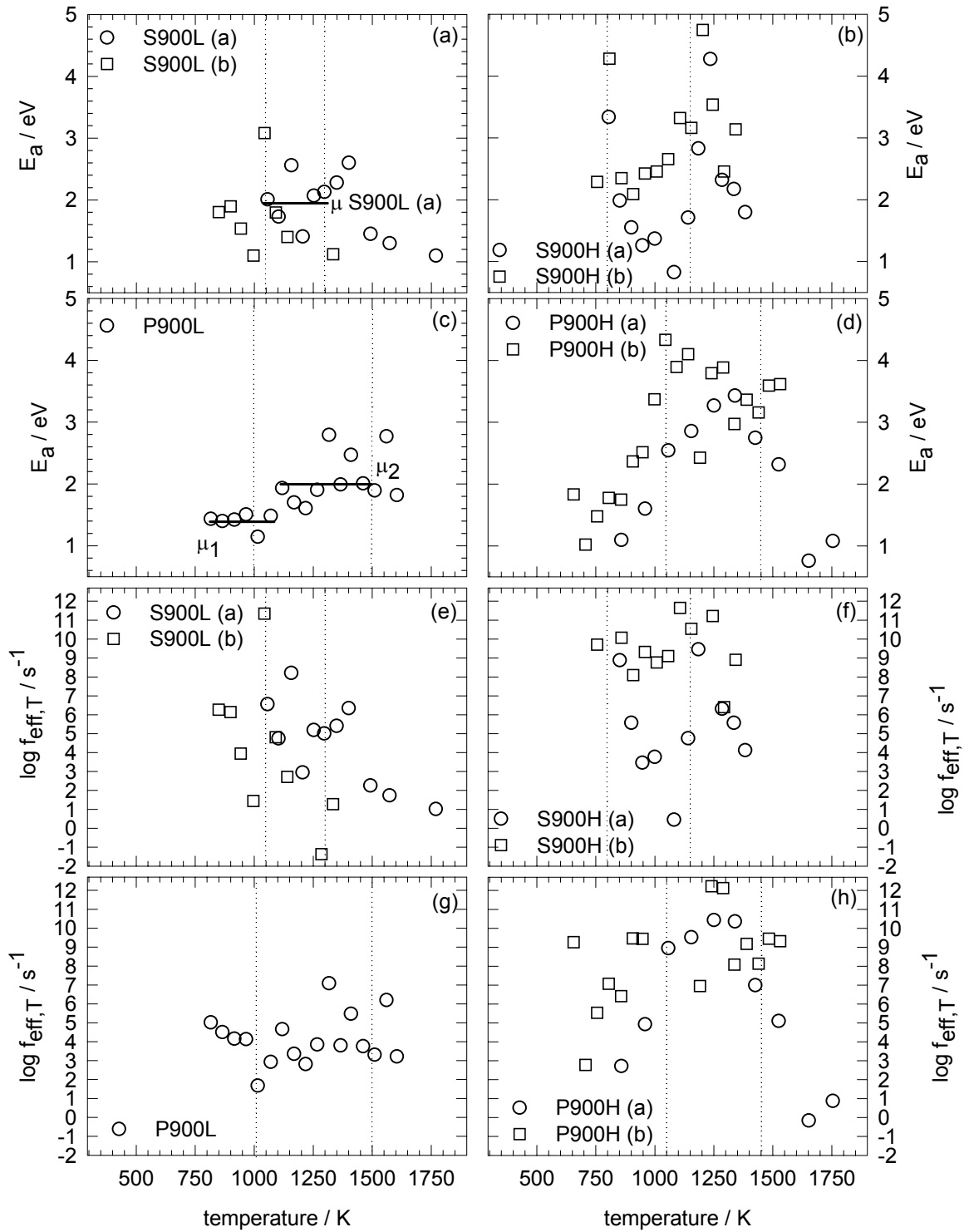


Figure 4.10 Activation energies for 900 keV implanted samples: (a) S900L, (b) S900H, (c) P900L, (d) P900H and effective jump frequencies for (e) S900L, (f) S900H, (g) P900L and (h) P900H. These parameters have been determined by the helium release rate at onset and end of isothermal stages. Dotted lines represent temperature of retained fraction 0.8 and 0.2 from Figure 4.9.

But the released amount of helium in the calculation of figure 3.16 is rather small so more calculations have to be performed to confirm whether the determination of the jump effective jump frequency for low dose implanted polycrystalline samples is uniform when an Arrhenius relationship is used.

The increase (or decrease) of the activation energy with increasing temperature seems to be accompanied with the increase (or decrease) of the effective jump frequency in Figure 4.10. One could derive that by fitting a plot of $\ln f_{eff,T} e^{-E_a/[kT]}$ versus the reciprocal temperature more uniform activation energies result from the slope. This is true but yields small activation energies. For example, the five last measurement points of S900L(a) in Figure 4.10a seem to have a linear relationship upon plotting $\ln f_{eff,T} e^{-E_a/[kT]}$ versus the reciprocal temperature. The slope of the linear relationship of these five data points yields an activation energy of 1.25 eV. This is smaller than the average of these five last measurement points.

Figure 4.11 shows an example of the effective diffusion coefficients for a low dose implanted sample and a high dose implanted sample in which defects have clustered. It shows that the logarithm of the effective diffusion coefficient versus the reciprocal temperature is in the large temperature range linear for a low dose implanted samples but not for a high dose implanted sample.

The Arrhenius equation ($\ln f = \ln f_{eff,T} - \frac{E_a}{kT}$ in this study) is a linear relationship. The concave shape for the high dose implanted sample in Figure 4.11a results in too large activation energies at lower temperatures and too low activation energies at higher temperatures when assuming a linear relationship between the dissociation energy and the reciprocal temperature. This could be the reason that the activation energy in Figure 4.10b reduces with increasing temperature in roughly two to three stages for S900H and in Figure 4.10d after about 1250 K for P900H. Possibly, the Arrhenius equation could also not be applied for the low dose implanted samples S900L and P900L but at respectively higher temperatures than 1400 K (see Figure 4.10a) and at higher temperatures than 1600 K (see Figure 4.10c).

Figure 4.11b shows that the binding energy and entropy term $\left(e^{-\frac{1}{k} \left\{ \frac{E_B}{T} - \Delta S \right\}} \right)$ becomes larger than the defect term $(4\pi r_i Z^{-1} \lambda^2 N_i)$ for the high dose implanted sample at higher temperatures. In such a case only the migration energy of the effective diffusion coefficient is reciprocal with temperature. In a reverse situation, the dissociation energy of the effective diffusion coefficient is reciprocal with temperature. In case of pressurised defects/bubbles, the binding energy and entropy term can become larger than the defect term at lower temperatures than in case of vacancies occupied by one helium atom as for low dose implanted samples.

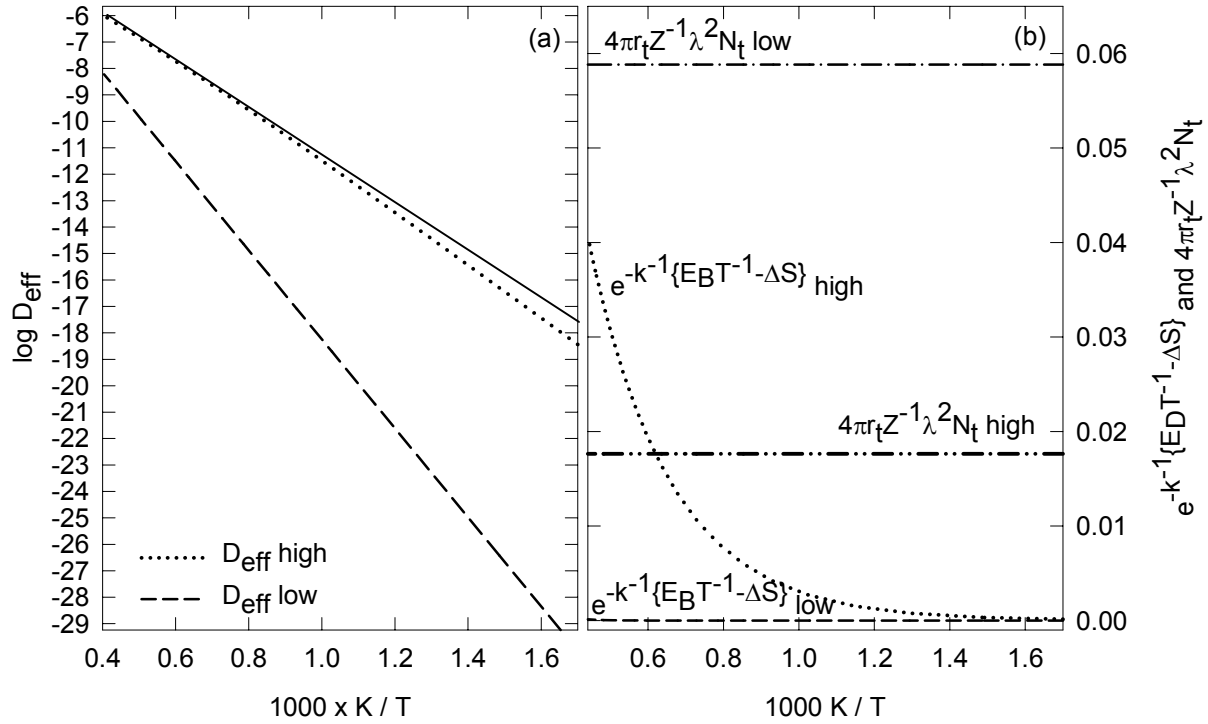


Figure 4.11 (a) Effective diffusion coefficients for a low (D_{eff} low) and a high (D_{eff} high) dose implanted sample versus the reciprocal temperature; solid linear line is drawn to guide the eye. (b) binding energy and entropy term for a low ($e^{-k^{-1}\{E_B T^{-1} - \Delta S\}}$ low) and a high ($e^{-k^{-1}\{E_B T^{-1} - \Delta S\}}$ high) dose implanted sample and defect term for a low ($4\pi r_i Z^{-1} \lambda^2 N_i$ low) and a high ($4\pi r_i Z^{-1} \lambda^2 N_i$ high) dose implanted sample. Parameters for both samples: $D_0 = 2.30 \text{ cm}^2 \text{ s}^{-1}$, $\lambda = 3.03 \text{ \AA}$, $Z = 6$ and $E_M = 1.59 \text{ eV}$. Only for low dose implanted sample: $N_i = 3.1 \times 10^{21} \text{ cm}^{-3}$, $r_i = 1 \text{ \AA}$, $E_B = 1.75 \text{ eV}$ and $\Delta S = 0 \text{ eV K}^{-1}$. Only for high dose implanted sample: $N_i = 3.1 \times 10^{20} \text{ cm}^{-3}$, $r_i = 3 \text{ \AA}$, $E_B = 0.40 \text{ eV}$ and $\Delta S = -1 \times 10^{-4} \text{ eV K}^{-1}$.

The defect-term ($4\pi r_i Z^{-1} \lambda^2 N_i$) and the temperature independent pre-factor (D_0) determine the temperature independence in equation 3.19 when the defect-term is larger than the binding energy and entropy term $\left(e^{-\frac{1}{k} \left\{ \frac{E_B}{T} - \Delta S \right\}} \right)$. The defect term for high dose implanted samples is smaller than for low dose implanted samples (see for example Figure 4.11b) due to clustering of defects in high dose implanted samples and absence of clustering of defects in low dose implanted samples. On average, there are therefore larger ratios between D_0 and the defect term for high dose implanted samples than for low dose implanted samples. This can also be observed in Figure 4.10 where the effective jump frequencies for the high dose implanted samples are larger than the effective jump frequencies for the low dose implanted samples.

Mathematically, when the binding energy and entropy term becomes larger than the defect term, not only the migration energy is reciprocal with temperature instead of the

dissociation energy but also the independence with temperature is limited to D_0 . This is smaller than the ratio between D_0 and defect term. Practically, high (low) activation energies will also result in high (low) effective jump frequencies because of the high (low) slope to determine the activation energy. This may be the reason that the effective jump frequency reduces in Figure 4.10.

Figure 4.12 shows the retained fraction of a 30 keV implanted single crystal.

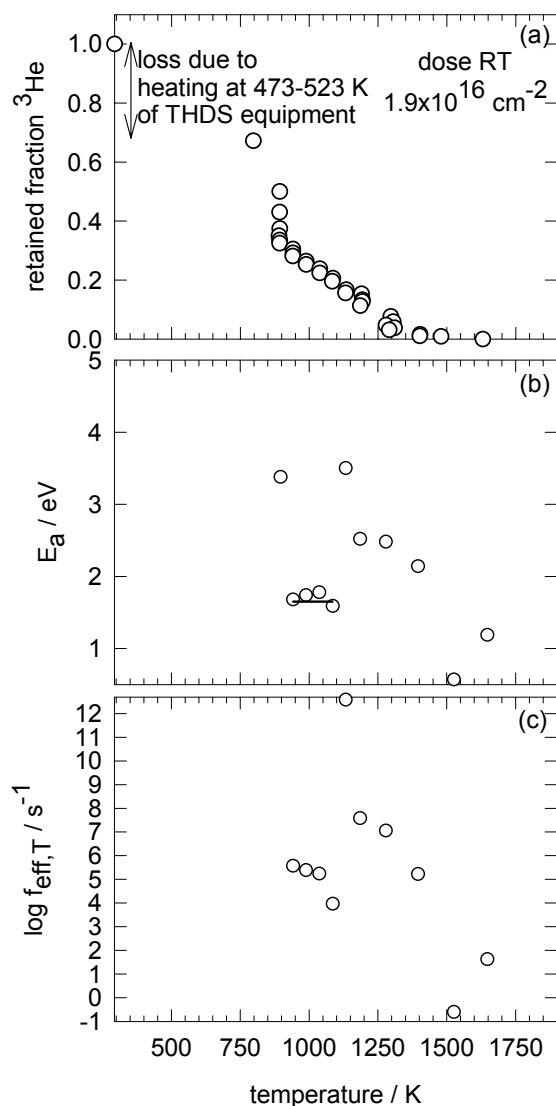


Figure 4.12 (a) Retained fraction of 30 keV implanted sample S30, using the helium release rate at end and onset of isothermal stages (b) activation energies and (c) effective jump frequency.

Since the THDS equipment is pre-heated to reduce the background of hydrogen during desorption (see paragraph 2.2.2), a significant amount of helium is lost due to recovery of defects similarly as described for the 30 keV implanted samples used for NDP analyses (see paragraph 4.2).

The firstly derived activation energy of 3.38 eV in Figure 4.12 is probably due to not achieving the temperature of the sampleholder in the previous isothermal stage. This also occurred for S900L in which the firstly derived activation energy was 6.75 eV (not shown in Figure 4.10). Two release stages can be viewed in Figure 4.12. The first release stage has an activation energy of 1.7 eV. When the effective jump frequency increases again, the second release stage has started from which the activation energy cannot be determined due to

scattering similarly as described for Figure 4.10.

The helium release of the 30 keV implanted single crystal S30 takes place at lower temperatures than the 900 keV low dose implanted single crystal S900L although the activation energy and effective jump frequency are similar. This may be due to the difference in implantation depth; helium is implanted more near the surface in S30 than S900L. Therefore with similar activation energy and effective jump frequency, it takes more time (or a higher temperature) to release helium in sample S900L than S30. On the other hand, Table 3.12 showed that for a 900 keV implanted sample with concentration dependent defect mediated

diffusion, the activation energy is significantly smaller than the sum of the binding and migration energy in comparison with the calculated results for the 30 keV implanted samples.

The sample implanted with α -particles had during isothermal stages a too small helium flux to derive the rate constants by the method described in paragraph 3.3.6. Only iterative functions can be used to determine the activation energies.

4.4 Comparison of calculated energies and empirically determined energies

In Chapter 3, the energies for diffusion in helium are calculated using the full and the partial charge model. In this paragraph, these calculated results are compared with the simulations of experimental results.

4.4.1 Single crystals

The calculated migration energy of helium for the partial charge model is 1.89 eV in the normal spinel structure (see paragraph 3.2.3). Figure 3.13 shows no helium release at 673 K and 753 K when a temperature independent factor (D_0) of $2.30 \times 10^{-3} \text{ cm}^2 \text{ s}^{-1}$ and a migration energy of helium of 1.89 eV are used although helium release occurred during these isothermal stages for the 30 keV implanted samples S30M and S30H. Also, the extent of the helium concentration profile showing tailing into depth as measured for all the 30 keV implanted samples after the isothermal stage of 753-773 K would occur after the isothermal stage of 903 K when using this migration energy. It is therefore assumed that the calculated migration energy of 1.89 eV is too large for the implanted spinel in the present study. Figure 3.8 showed the simulation of the 30 keV implanted samples using D_0 of $2.30 \times 10^{-3} \text{ cm}^2 \text{ s}^{-1}$ and a migration energy of 1.59 eV. This simulation resembles the measured results concerning the extent of tailing into depth that the measured helium concentration profile showed for these 30 keV implanted samples.

A migration energy of $1.59 \text{ eV atom}^{-1}$ would result in a helium release at too low temperatures for the sample implanted by α -particles by decay of ^{241}Am . The concentration of defects created by this implantation is expected to be far smaller than the defects that are

present before implantation due to the growth process of the single crystal and impurities. Figure 4.13 shows the measured and calculated helium release. It shows that sample B could be well modelled with the used parameters.

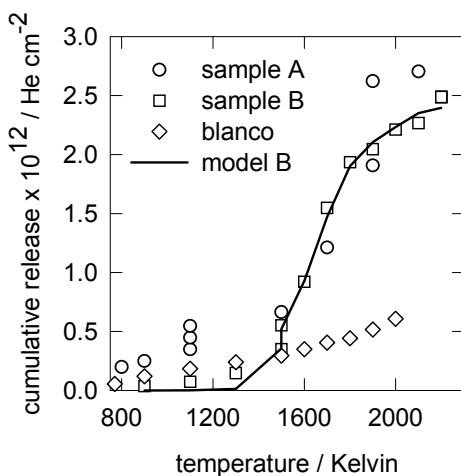


Figure 4.13 Measured and calculated (solid line) release of helium for a random α -implanted sample with a dose of $2.47 \times 10^{12} \text{ He cm}^{-2}$. Parameters for depth independent defect mediated diffusion: $D_0 = 2.30 \times 10^{-3} \text{ cm}^2 \text{ s}^{-1}$, $E^M = 1.59 \text{ eV}$, $E^B = 1.75 \text{ eV}$, $n_i = 100 \text{ ppm}$, $r_i = 1 \text{ \AA}$, $\lambda = 3.03 \text{ \AA}$ and $Z = 6$.

The actual amount of defects in this sample may be smaller or larger and this variation results in respectively a larger or a smaller dissociation energy to obtain the same results as model B in Figure 4.13.

The location of the measured peak of the helium concentration profile in Table 4.2 for the 30 keV implanted samples is only similar to the location of peak of the calculated helium concentration profile if a high angle perpendicular to the beam is used to simulate the implantation using SRIM. This high angle would also result in a cut-off of the defect profile. The resulting defect profile has a smaller width than the calculated helium concentration profile. No broadening would be expected when simulating concentration dependent defect mediated diffusion using the calculated helium and defect concentration profile at such a high angle of implantation. But Figure 4.2 clearly shows broadening and a slight shift of the peak towards the surface of the sample for the helium concentration profiles in S30L and initially in S30M. It is therefore assumed that the measured location of the peak of the helium implanted concentration profile is too small in depth or that the calculations are not accurate using SRIM. The results for the 30 keV implanted samples are not simulated since the calculated defect profile of SRIM is used to calculate the diffusion of helium.

Figure 4.14 shows a simulation of the thermal evolution of helium concentration profiles for S900L. The calculated helium concentrations in the peak of the fitted Gaussian profiles are higher than the measured helium concentrations in the peak since the calculated profile is smaller in width than the measured profile at room temperature (see Table 4.2) due to lateral resolution (see paragraph 2.2.1). The simulation can therefore better be compared with the ratios between the helium concentration in the peak of the profiles after isothermal stages and the helium concentration in the peak of the profile at room temperature. The actual results of the measurements and simulation are used for the location of the peak and width of the fitted Gaussian profile. Figure 4.14 shows that the trend in properties of the calculated helium concentration profiles agrees well with the trend in properties of the measured helium concentration profiles in Figure 4.4 and Figure 4.5. The difference between measured and calculated dose could be due to the low concentrations of helium in the tail towards the surface. Probably, the concentration of helium in the tail towards the surface is below the detection limit of the NDP equipment.

As remarked in paragraph 4.2, the NDP results of the 30 keV implanted samples showed a tail into the depth of the sample but the thermal evolution of helium concentration profiles in the 900 keV implanted sample S900L does not show this tail into depth of the sample. This could be due to a higher background at depths larger than 2 μm but may also be due to different densities of helium in the vacancies. Figure 3.11 showed the simulation of a 900 keV implanted sample with a binding energy of 0.40 eV and a concentration of defects of 0.05 dpa. These parameters are in Figure 4.14 0.7 eV and 0.1 dpa. Figure 3.11 showed besides a tail towards the

surface of the sample, caused by helium trapping in defects, also a tail into depth of the sample caused by interstitial diffusion.

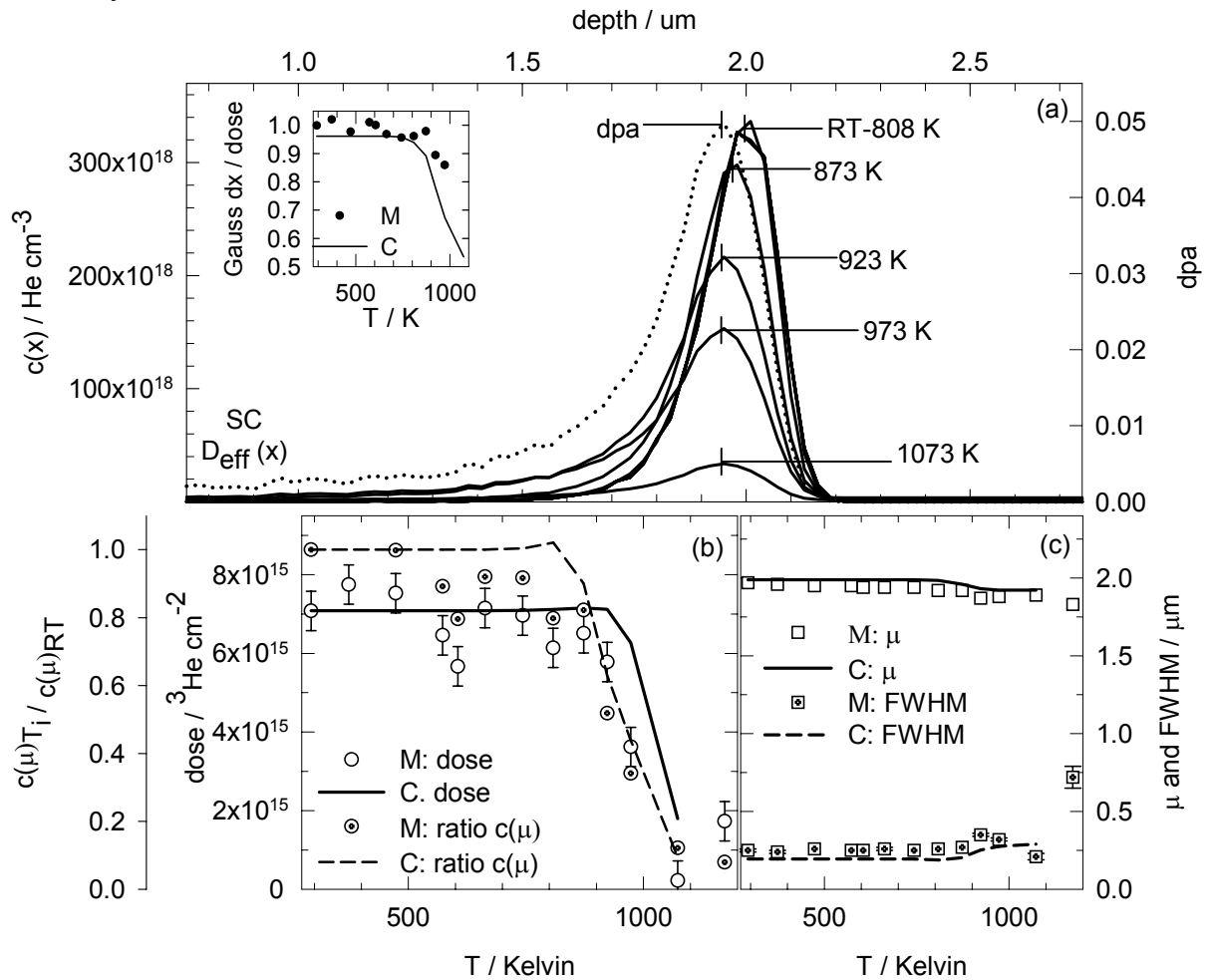


Figure 4.14 (a) Calculated concentration profiles after isothermal stages of 1 hour (except for 1073 K, this isothermal stage was 2978 seconds) using concentration dependent defect mediated diffusion. Insert shows the integrated dose of the Gaussian profile divided by the actual dose for the measured (M) and calculated (C) results. (b) Calculated (C) and measured (M) (S900L) retained dose and ratio between helium concentration in peak of Gaussian profile of isothermal stages and helium concentration in peak of Gaussian profile at room temperature for measurements (M) and calculated results (C). (c) Location of peak and width of Gaussian profile for measurements (M) and calculated (C) results. Measurements are indicated by symbols and results of the simulation are indicated by lines. Parameters for simulation are: $D_0=2.30 \times 10^{-3} \text{ cm}^2 \text{ s}^{-1}$, $E^M=1.59 \text{ eV}$, $E^B=0.70 \text{ eV}$, $n_i=0.1 \text{ dpa}$, $r_i=1 \text{ \AA}$, $Z=6$ and $\lambda=3.03 \text{ \AA}$.

The magnitude of the diffusion coefficient for interstitial diffusion is similar to the effective diffusion coefficient in Figure 3.11 at temperatures higher than 743 K. Helium starts to be redistributed at about 743 K with the parameters of 0.4 eV and 0.05 dpa. Thus interstitial diffusion and this defect mediated diffusion take place at the same temperature. At temperatures higher than 1573 K, the effective diffusion coefficient in Figure 4.14 becomes similar to the diffusion coefficient for interstitial diffusion. This temperature is way beyond the temperature

of redistribution of helium during laboratory conditions. Thus once a helium atom is trapped in a vacancy, it will not be de-trapped during the temperature stage of interstitial diffusion with the parameters used in Figure 4.14 but it can be de-trapped with the parameters used in Figure 3.11. The concentration of helium in S30L is about 30% higher than in S900L. Possibly, the density of helium in the vacancies of S30L is larger than S900L by which they had lower binding energies of helium to vacancies.

The calculated activation energy is 1.27 eV using the change in temperature method of the simulation in Figure 4.14 (see Table 3.12). This is similar to 1.25 eV derived from a plot of $\ln f_{eff,T} e^{-E_a/[kT]}$ versus the reciprocal temperature of S900L (a) described in paragraph 4.3.3. The mean measured activation energy of 1.99 ± 0.40 eV for S900L (a) in Figure 4.10 is only slightly larger than the calculated activation energy of 1.82-1.70 eV using the change in temperature method for the flux at the surface of the sample. Thus, the derived activation energy is not equal to the dissociation energy although the calculated activation energy may be similar to the measured activation energies using the change in temperature method or the activation energy derived from a plot of $\ln f_{eff,T} e^{-E_a/[kT]}$ versus the reciprocal temperature.

The reason for the higher binding energy of helium to vacancies for S-Am in comparison with S900L may be due to the higher trapping chance of helium by oxygen vacancies for S-Am than for S900L since the trapping length is larger but the concentration of initially present vacancies may also be underestimated in the simulation for the alpha-implanted sample. The concentration of vacancies has to be about half the concentration of ions in the crystal lattice in order to obtain a similar diffusion coefficient with a binding energy of 0.7 eV that would suit the simulation in Figure 4.13. This concentration of vacancies is far too high. It confirms the hypothesis that in the sample S900L, helium was trapped in magnesium, aluminium and oxygen vacancies yielding on average a binding energy of helium to the vacancies of 0.7 eV. For the α -implanted sample, the binding energy of helium to vacancies is larger since the diffusion of helium was dominated by oxygen vacancies.

This empirical binding energy of 0.7 eV is similar to the calculated binding energy of helium to the magnesium vacancy of the full charge model of 0.67 eV. It may be the average of the binding energy of helium to the magnesium vacancy and aluminium vacancy of the partial charge model. Less oxygen vacancies than magnesium and aluminium vacancies are generated during implantation since the energy of displacement for cations is about half the energy of displacement of the anion oxygen. The diffusion of helium may be dominated by aluminium and magnesium vacancies due to the higher generated amount of cation displacements with respect to oxygen displacements.

Flaking during irradiation conditions is unknown to the author. Flaking is therefore assumed to be characteristic for the thermal treatment of samples with high doses implanted at low temperatures. No time is therefore invested to investigate this further.

4.4.2 Polycrystalline samples

The effect by implantation in the low dose implanted polycrystalline sample P900L within the grain should be similar to S900L in terms of dissociation energy of helium from defects and surviving defect fraction. Therefore, the parameters used for the simulation of the low dose implanted single crystal S900L in Figure 4.14 are used for the simulation within the grain of the low dose implanted polycrystalline sample P900L. The migration energy of helium is probably smaller at grainboundaries than within the lattice of MgAl_2O_4 . For simplicity, it is assumed that there are only intergranular pores. Grain size and pore size distribution are derived from SEM analysis (see Figure 4.1). Figure 4.15 shows a simulation of the thermal evolution of helium concentration profiles of the low dose implanted polycrystalline sample P900L.

The ratio between the integrated Gaussian profile and actual dose is not put in Figure 4.15 since their difference is negligible. This ratio varies between 0.93-1.02 for the measurements and increases from 0.96 at room temperature to 0.99 after the isothermal stage of 1173 K for the simulated helium concentration profiles. The measured dose of P900L is difficult to simulate since there are a few inconsistencies in the measurements for example the increase in dose after the isothermal stage of 923 K. The helium concentration in the peak of the Gaussian profile and width of the peak both increase after the isothermal stage of 923 K to 973 K which is not possible in this combination. It is therefore assumed that the data of the isothermal stages of 923 K and 973 K are incorrect.

The drop in retained dose as measured is also observed for the simulation but not in such an extent as measured. This drop is due to helium released from grains and not being trapped in the intergranular pores of the grainboundaries. For the simulation, a uniform grain size is used. Possibly, a simulation using the variation in grainsize in Figure 4.1 will result in the measured drop of retained dose and the measured onset of broadening of the concentration profile at 800 K. The helium released from larger grains will result in less trapping of helium at grainboundaries and the helium released from smaller grains will result in an earlier broadening of the concentration profile than now simulated. Taking into account the variation in grainsize takes a lot of computation time and is therefore not performed. The parameters used for the grainboundaries agree quite well with the measured results concerning:

- 1) the trend in broadening of the helium concentration profile;
- 2) the helium concentration in peak of the profile after the last two isothermal stages 1073 K and 1173 K.

The low concentration of helium in the regions close to the surface of the sample and into depth may have caused that the width of the Gaussian profile of 1173 K of the calculated helium concentration profile larger is than the measured one. The NDP equipment may not be able to measure the concentration in these regions resulting in a smaller width and smaller retained dose than simulated.

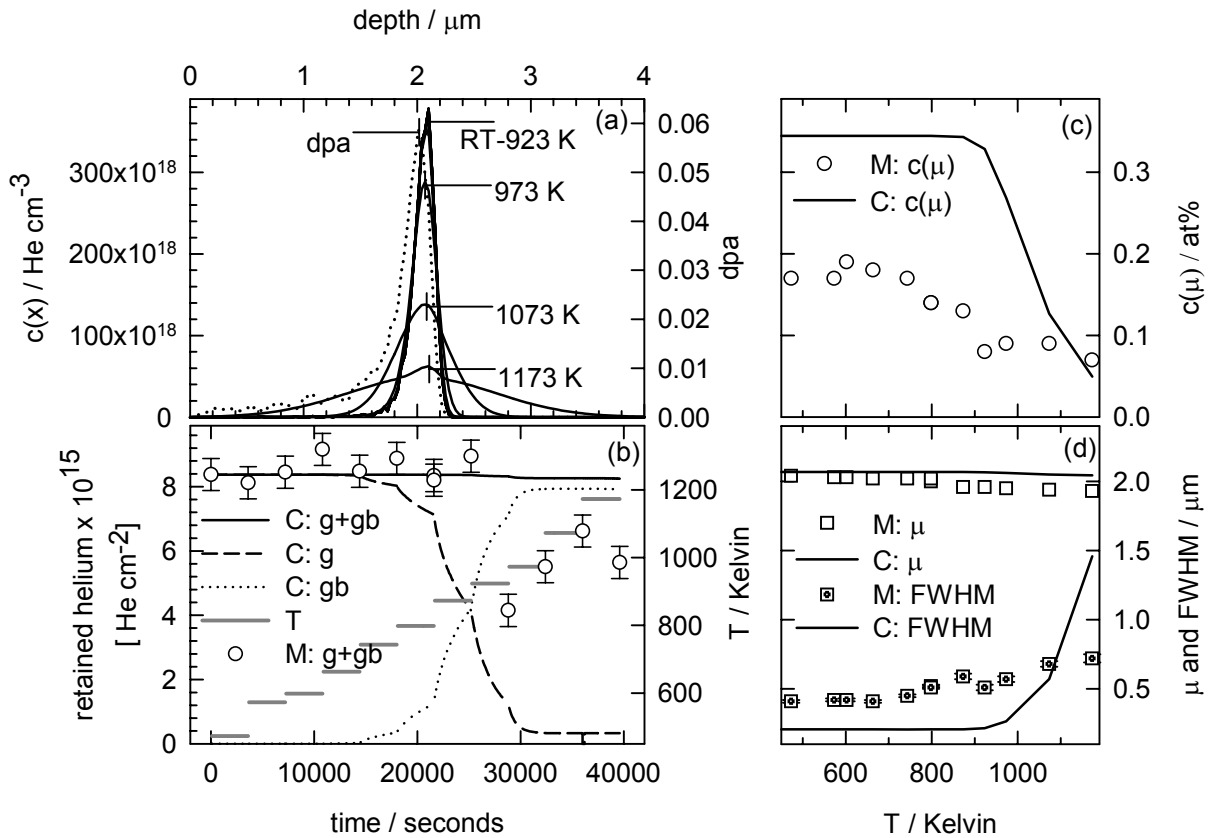


Figure 4.15 (a) Calculated concentration profiles after isothermal stages of 1 hour using concentration dependent defect mediated diffusion for grains and depth independent pore mediated diffusion for grainboundaries. Parameters are for grains: $D_0=2.30 \times 10^{-3} \text{ cm}^2 \text{ s}^{-1}$, $E^M=1.59 \text{ eV}$, $E^B=0.70 \text{ eV}$, $n_t=0.1 \text{ dpa}$, $r_t=1 \text{ \AA}$, $Z=6$ and $\lambda=3.03 \text{ \AA}$, for grain boundaries: $D_0=3.45 \times 10^{-3} \text{ cm}^2 \text{ s}^{-1}$, $E^{M,gb}=0.45 \text{ eV}$, $E^{sol,gb}=1.75 \text{ eV}$, $\Delta S_{p,gb}=-1 \times 10^{-3} \text{ eV atom}^{-1} \text{ K}^{-1}$, $N_p=10^{12} \text{ cm}^{-2}$, $r_p=0.03 \text{ μm}$, $a=0.48 \text{ μm}$, $Z=4$ and $\lambda=3.03 \text{ \AA}$. (b) calculated (C) retained dose in grains (g), grain boundaries (gb) and the sum of these two doses (g+gb) and temperature versus time of thermal treatment and measured (M) retained dose. (c) helium concentration in peak of Gaussian profile for measured (M) and calculated (C) concentration profiles. (d) location of peak and width of Gaussian profile of measured (M) and calculated (C) concentration profiles.

The pressure of the pores would be about 16 MPa at 298 K for P900L and 171 MPa at 298 K for P900H when using the data of pores in Figure 4.1 if all helium, present in the peak of the helium concentration profiles, was released into the pores. It is therefore expected that the pressure of helium in intergranular pores for P900H will become so large during release of helium from the grains that these pores are pressurized. Therefore for P900H, a smaller binding energy and a smaller entropy of helium in intergranular pores are expected than for P900L. Figure 4.16 shows the simulation of the thermal evolution of the helium concentration profiles for P900H. It is expected that clustering had occurred in the sample of P900H. Therefore, the amount of defects is taken significantly smaller than 0.1 dpa. The sum of the binding and migration energy for helium to dissociate from the assumed nano-sized bubbles within the grain

is 2.89 eV. This value is between the permeation energy of 2.77 eV for the partial charge model and 3.13 eV for the full charge model.

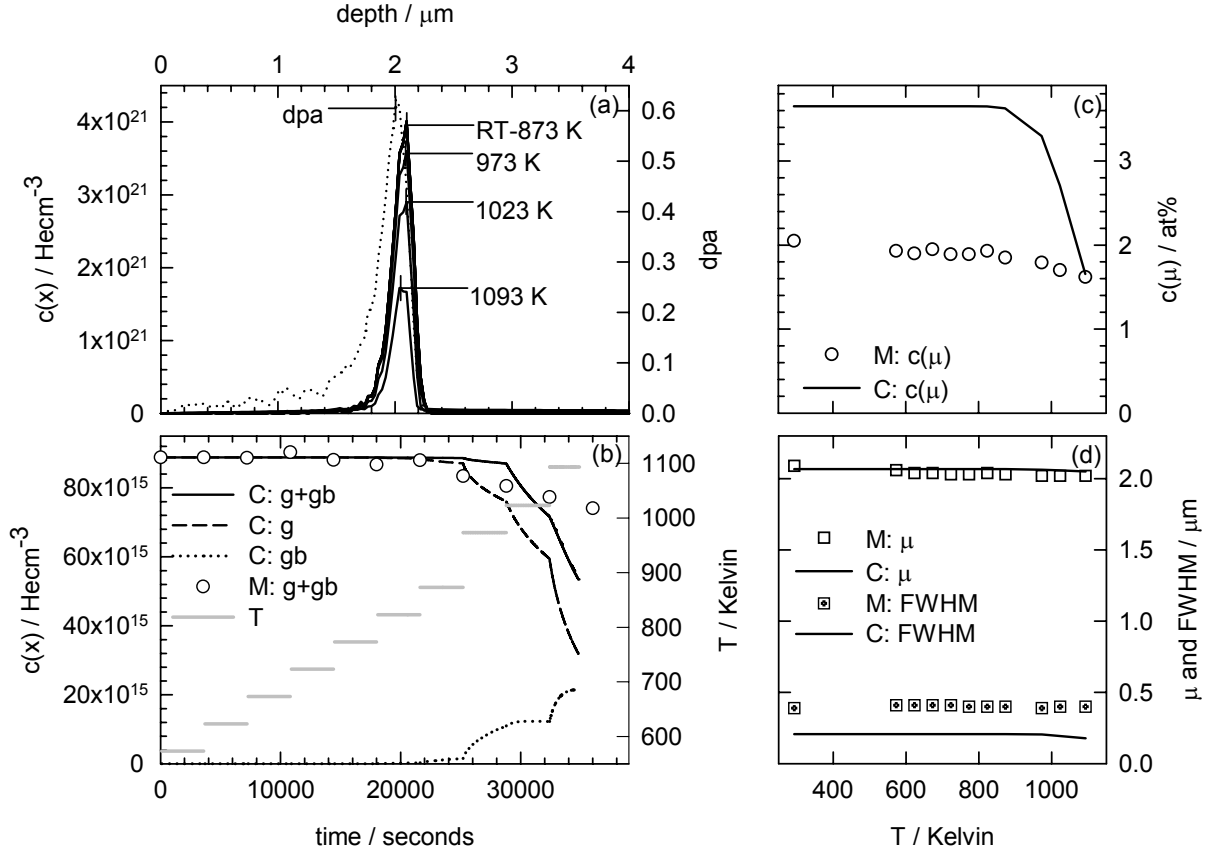


Figure 4.16 (a) Calculated concentration profiles after isothermal stages of 1 hour (except for 1093 K, this isothermal stage was 2412 seconds) using concentration dependent defect mediated diffusion for grains and depth independent pore mediated diffusion for grainboundaries, (b) calculated and measured (P900H) retained dose and concentration of peak of concentration profile, (c) helium concentration in peak of Gaussian profile for measured results (M) and calculated results (C) and (d) location of peak and width of Gaussian profile for measured results (M) and calculated results (C). Parameters for grains: $D_0=2.30 \times 10^{-3} \text{ cm}^2 \text{ s}^{-1}$, $E^M=1.59 \text{ eV}$, $E^B=1.30 \text{ eV}$, $n_t=0.0001 \text{ dpa}$, $\Delta S_{p,gb}=-1 \times 10^{-4} \text{ eV K}^{-1}$, $r_t=10 \text{ \AA}$, $Z=6$ and $\lambda=3.03 \text{ \AA}$; for grain boundaries: $D_0=3.45 \times 10^{-3} \text{ cm}^2 \text{ s}^{-1}$, $E^{M,gb}=0.45 \text{ eV}$, $E^{sol,gb}=1.60 \text{ eV}$, $\Delta S_{p,gb}=-7 \times 10^{-4} \text{ eV K}^{-1}$, $N_p=10^{12} \text{ cm}^{-2}$, $r_p=0.03 \text{ μm}$, $a=0.48 \text{ μm}$, $Z=4$ and $\lambda=3.03 \text{ \AA}$.

Figure 4.16 shows no broadening of the calculated concentration profile. This is due to a smaller diffusion coefficient within grains than at grainboundaries. It even shows a shrinkage of the FWHM at higher temperatures in Figure 4.16d despite the presence of helium at grainboundaries (see Figure 4.16b). Three parameters could be changed to obtain a uniform FWHM during increasing temperature of isothermal stages as measured:

- 1) the binding energy of helium to the defects should be smaller at the peak of the helium implanted concentration profile;

- 2) the amount of remaining defects should be smaller at the peak of the concentration profile;
- 3) the effective diffusion coefficient at grainboundaries should be smaller.

Broadening of the concentration profile would occur if the parameters for grainboundary diffusion of P900L in Figure 4.15 would be used for the simulation of P900H. This confirms the hypothesis that the intergranular pores became pressurised during thermal treatment of the sample P900H. Figure 4.5c did also not show broadening of the concentration profile. The reduction in the helium concentration in the peak of the profile in Figure 4.16 is not similar to the measured results. S900H and P900H could be simulated using diffusion processes with the same activation energies for all isothermal stages. Possibly the binding energy of helium to defects and difference in entropy of helium between defects and crystal lattice within the grain increased by clustering of defects with increasing temperature of isothermal stage for P900H.

4.5 Relation between results of implanted samples and irradiation

The study on the diffusion of helium in implanted samples was performed to simulate the diffusion of helium during irradiation conditions. The parameters derived for the low dose implanted polycrystalline sample (P900L) and high dose implanted polycrystalline sample (P900H) are used to simulate the diffusion of helium during the irradiation conditions of EFTTRA-T4. The concentration of helium of P900L is about half of the helium concentration at the End Of Irradiation (EOI) of EFTTRA-T4 and the concentration of helium of P900H is about 5 times the helium concentration at the End Of Irradiation (EOI) of EFTTRA-T4. Using the parameters of P900H for the simulation would result in a too large release of helium and using the parameters of P900L would result in a too small release of helium. This is due to the larger chemical potential of helium in pores, vacancies and vacancy clusters for P900H with respect to P900L. First aspects of the EFTTRA-T4 fabrication and irradiation are given and secondly the simulation. These aspects are mainly parameters that can be used for the simulation and for comparison with the literature data of helium implantations in spinel in paragraph 4.6.

4.5.1 Summary of fabricated fuel and irradiation of EFTTRA-T4

For the EFTTRA-T4 experiment, pellets were prepared by impregnation of an americium solution in porous MgAl_2O_4 pellets. Americium-oxide and MgAl_2O_4 form the compound AmAlO_3 (during sintering). The average diameter of the fabricated EFTTRA-T4 pellets was 5.39 ± 0.02 mm, the average height was 7.06 ± 0.02 mm and the average density as a percentage of the theoretical one was 97.0 ± 0.5 %. The average Am content in the pellets was 11.1 ± 0.7 wt%. The concentration of americium was not uniform. In the centre of the pellet and periphery, the americium concentration was about 9 wt%. An Am-rich shell with about 14 wt% was present with a thickness of about 200 μm at about 0.7 of the radius and at 0.7-0.8 of half the initial height. These fabricated pellets were packed in 15/15 Ti stainless steel capsules with an inner diameter of 5.65 mm and an outer diameter of 6.55 mm. These capsules were placed in an Al-drum containing thermocouples and other measurement devices.

Figure 4.17 shows the predicted helium generation and fission power during irradiation [Konings et al. 2000].

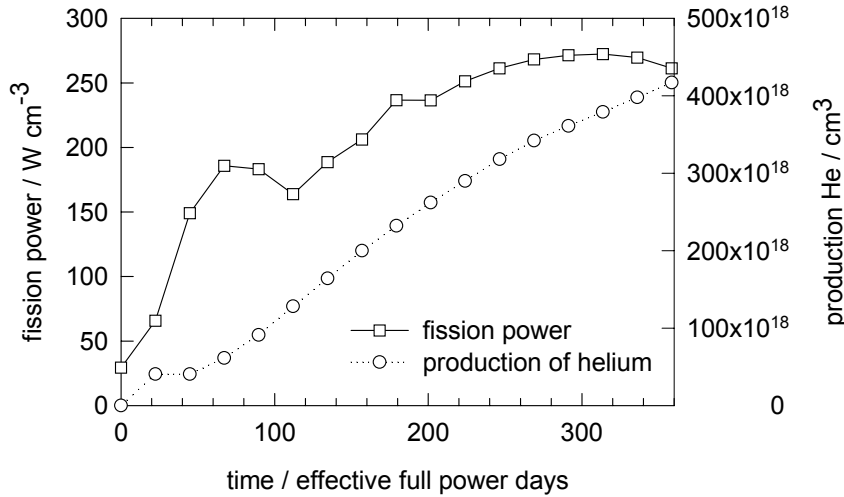


Figure 4.17 Predicted helium generation and fission power [data from Konings et al. 2000].

The predicted radial temperature difference across the pellet was 20 K at Begin Of Irradiation (BOI) and 75 K at End Of Irradiation (EOI). The temperature of the Al-drum was measured to be 673 K during irradiation using thermocouples. The predicted radial difference between the centre of the pellet and these thermocouples was 130 K at BOI and 371 K at EOI. The calculated maximum temperature of the centre of the pellet in a worst case scenario was 1153 K. The helium release of helium generated during irradiation was 20%. The average porosity after irradiation was 18%; the porosity in the centre of the pellet and periphery was 16% and the porosity was 40% in the Am-rich shell. The swelling of the pellets was 18% [Konings et al. 2000].

4.5.2 Diffusion of helium during neutron irradiation conditions

The temperatures at the centre (T_C) and outer edge (T_S) can be approximated to a relation with the fission power by [Holbert]:

$$T_C - T_S = \frac{Pa_c^2}{4\bar{\lambda}} \quad (4.1)$$

where P is the fission power, a_c is the radius of the cylinder and $\bar{\lambda}$ is the average thermal conductivity. The predicted radial temperature difference of 20 K at BOI and 75 K at EOI suggest that the thermal conductivity at EOI is at least twice the value at BOI when using the fission power at BOI of 29.4 W/cm³ and EOI of 261.3 W/cm³ in Figure 4.17. This radial temperature difference seems to be incorrect since the thermal conductivity always reduces during irradiation.

Another inconsistency in the report by Konings et al. is the concentration of americium. The average concentration of americium is at the most 9.9 wt% instead of 11.1 wt% when using the data in paragraph 4.5.1 concerning the geometrical properties, size of the Am rich shell and the theoretical densities of AmO₂ and MgAl₂O₄ of 11.68 g/cm³ and 3.579 g/cm³ respectively. Since the average of 11.1 Am wt% is used to determine power density and helium production,

the size of the Am rich shell is changed to 620 μm in order to obtain 11.1 Am wt% for the simulation.

The diffusion equations for grains and grainboundaries could be coupled for the simulation of the diffusion of helium during irradiation of EFTTRA-T4 as performed for polycrystalline semi-infinite media as discussed in paragraph 4.4.2 and paragraph 3.3.3. However, during irradiation helium is generated in the grain and the simulations in paragraph 4.4.2 and paragraph 3.3.3 are performed with equation 3.24 that can only be used if no helium is generated within the grain. For simplicity, it is therefore first assumed that the generated amount of helium during irradiation is directly released from the grain to the grainboundaries. In this perspective, the calculated helium release is thereby overestimated.

A geometric difference between the polycrystalline semi-infinite media of the implanted samples in the present study and a pellet has to be solved in order to simulate the diffusion of helium during irradiation conditions. The diffusion equation for depth dependent diffusion in a cylinder is [Crank 2001]:

$$\frac{\partial C}{\partial t} = \frac{1}{a_c} \left\{ \frac{\partial}{\partial r_c} \left(a_c D_{eff}(r) \frac{\partial C}{\partial r_c} \right) + \frac{\partial}{\partial \theta} \left(\frac{D}{a_c} \frac{\partial C}{\partial \theta} \right) + \frac{\partial}{\partial z} \left(a_c D_{eff}(r) \frac{\partial C}{\partial z} \right) \right\} \quad (4.2)$$

in terms of the cylindrical coordinates r_c, θ, z . The third term in equation 4.2 is neglected to save computation time for the simulation of diffusion of helium in the pellet. The condition $2D_{eff,gb}(r_c = 0)\Delta t < \Delta r_{c,min}^2$ is fulfilled in order to minimise the error in the calculation. The diffusion is assumed to be only temperature dependent. The temperature distribution of the pellet is approximated to a simple parabolic function [Olander 1976]:

$$T(r) = \left[1 - \left(\frac{r_c}{a_c} \right)^2 \right] \times (T_C - T_S) + T_S \quad (4.3)$$

The predicted temperature difference between centre of pellet and thermocouple suggests a temperature of 783 K at the outer edge (T_S) of the pellet at BOI. Figure 4.18 shows the used temperature profile for the simulation of the thermal re-distribution of helium, the effective diffusion coefficients, the concentration profile if no thermal re-distribution of helium occurred, the calculated helium concentration profiles at EOI and calculated fractional contents when using the parameters for diffusion in grainboundaries of P900L and P900H in Figures 4.15 and 4.16. The pore and grain size distribution of the EFTTRA-T4 pellets is unknown. It is therefore assumed that they are similar to the fabricated polycrystalline samples P900L and P900H of the present study.

The fraction of retained helium is for both simulations 100%; thus no release of helium is expected. (A minor computation error results in a fraction of retained helium of 2% larger than theoretically possible for P900H).

There are two features that may result in a larger release of helium than calculated in Figure 4.18:

- 1) the temperature distribution may not be parabolic as used in this simulation since the actinide concentration is not uniform in the pellet;
- 2) ionisation can lower the activation energy for diffusion [Bourgain et al. 1978]; experimental values on migration of gases known to the author show a reduction in diffusion coefficient of one order magnitude [Matzke et al. 2000].

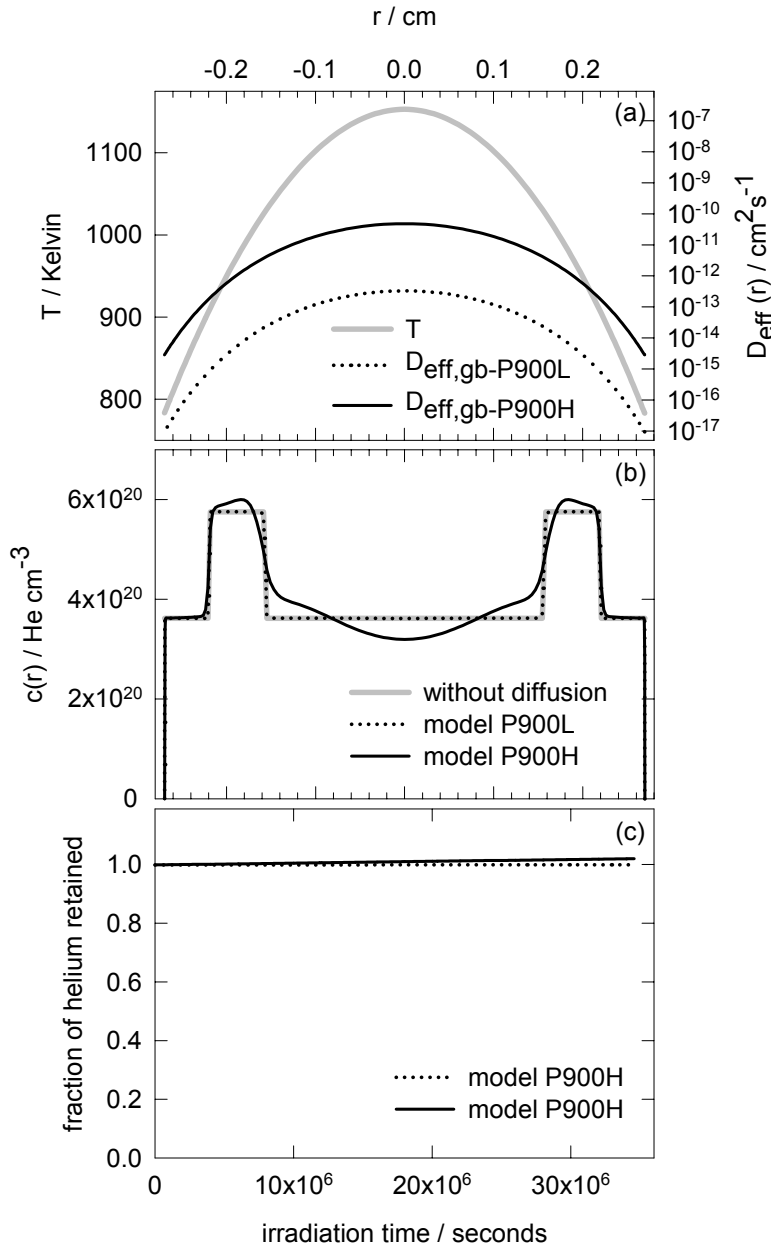


Figure 4.18 (a) Temperature profiles (grey line) and effective diffusion coefficients (black lines) used for simulation and (b) helium concentration profile if no diffusion of helium occurred (grey line), calculated helium concentration profiles at EOI using parameters for diffusion in grainboundaries of P900L and P900H (black lines) and (c) fractional content during irradiation using parameters for diffusion in grainboundaries of P900L and P900H.

However, if release of helium would occur in the simulation, this release would be an overestimation since:

- 1) all helium generated in the grains is considered to be directly released to the grainboundaries;
- 2) the temperature of the pellet is taken as high as in a worst case scenario;

Therefore, the release of helium is not expected to differ much from the present calculated

results when the difference in power in the temperature profile and ionisation enhanced diffusion are taken into account. This simulation of the thermal redistribution of helium shows that EFTTRA-T4 does not have the properties of thermal diffusion of helium in spinel.

4.6 Relation between helium implantations and irradiation

Many helium implantations in MgAl_2O_4 have been reported in the literature. During these implantations, defects are only created by implantation of helium. The helium implantation rates in the peak of the helium concentration profiles during these implantations are 10^5 - 10^7 times larger than the helium implantation rate during the EFTTRA-T4 experiment. (Helium is generated during irradiation by decay of an actinide for example ^{241}Am .) The amount of dpa created by a fission product, for example ^{95}Zr with an energy of 98 MeV is about 150 times larger than helium, for example ^4He with an energy of 5.5 MeV. On average, at BOI 9.2×10^{11} fissions/ cm^3 per second take place and at EOI 8.2×10^{12} fissions/ cm^3 per second take place using the fission power in Figure 4.17 and assuming 165 MeV kinetic energy released per fission. The displacement rate during helium implantations is 1 - 10^3 times larger than the displacement rate caused by fission products during this irradiation. Thus the helium implantation rate is significantly larger for helium implantations in comparison with the irradiation of EFTTRA-T4 but the displacement rate during helium implantations is comparable to or slightly larger than this irradiation.

Figure 4.19 shows the dose and implantation energy of all helium implantations known to the author; excluded experiments previously described in this chapter. The dotted line in Figure 4.19 indicates the helium concentration profile with a peak of 0.8 He at%. This boundary is assumed to be able to simulate the concentration profiles in the EFTTRA-T4 irradiation at EOI in a worst case scenario. This dotted line should, for increasing implantation energy, increase with dose but the dotted line does not always increase with the implantation energy due to differences in angle for implantation.

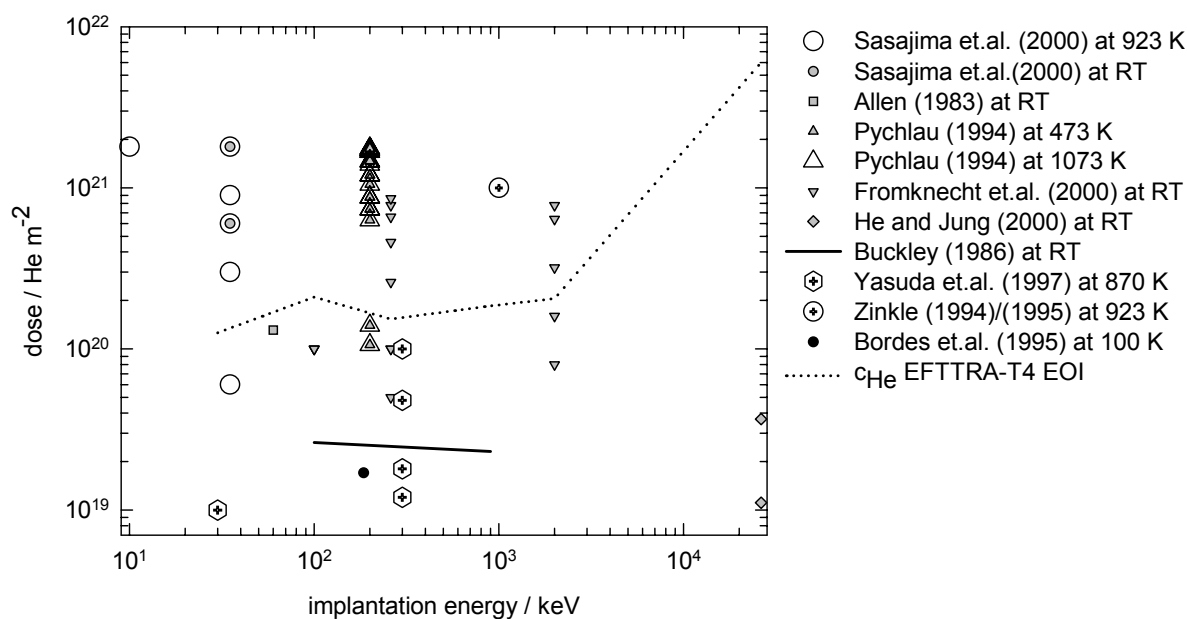


Figure 4.19 Helium implantations from literature, peak in helium concentration of profile of 0.8 He at% (dotted line).

Figure 4.19 shows that many helium implantations had a concentration of helium far larger than the concentration of helium at EOI of EFTTRA-T4. Several aspects from these studies are discussed.

Nano-sized bubbles were observed using TEM in the study by Sasajima et al.. but the swelling by this helium implantation cannot be given since the density of the bubbles is not indicated in their article. Size and density of the bubbles were measured using TEM in the study by Pychlau; at 473 K the maximum swelling was 2 vol% at a helium dose about 10 times larger than EFTTRA-T4 at EOI. At 1073 K, no bubbles were observed. The distribution of helium during implantation is simulated for these studies using parameters for diffusion of helium determined in this thesis in order to understand the difference between helium implantations at 1073 K, 923 K and 473 K. Figure 4.20 shows the simulation of the distribution of helium after implantation by the study of Pychlau at 473 K and at 1073 K and by the study of Sasajima et.al. at 923 K till the highest helium doses.

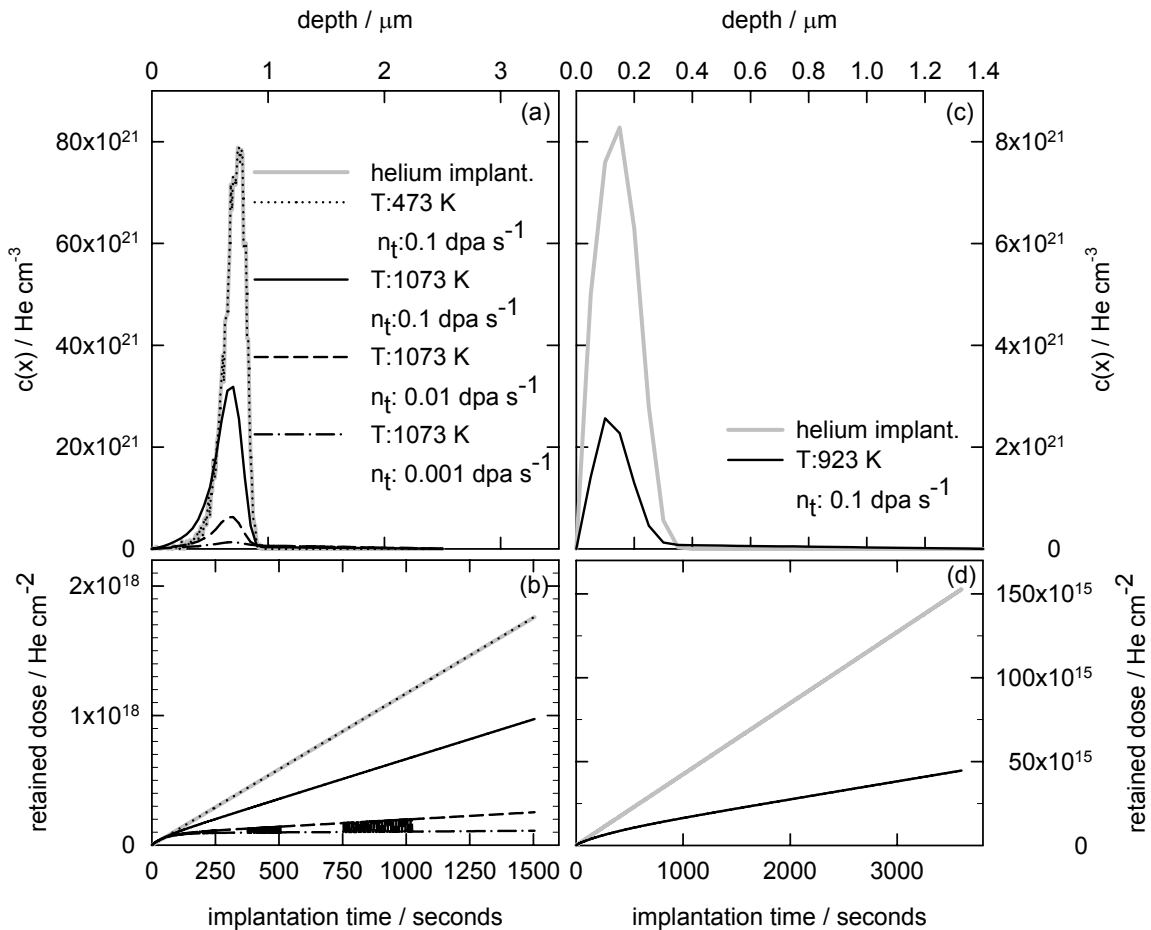


Figure 4.20 (a) and (c) Concentration profiles of helium after implantation if no diffusion of helium occurs (grey line: helium implant) and calculated concentration profiles with diffusion (black lines); (b) and (d) retained amount of helium during implantation. (a-b) Pychlau with parameters $l=2.5 \mu\text{m}$, $T=473 \text{ K}$ and 1073 K , implantation rate $11.7 \times 10^{13} \text{ He cm}^{-2} \text{ s}^{-1}$ (c-d) Sasajima et al. with parameters $l=1.4 \mu\text{m}$, $T=923 \text{ K}$, implantation rate $5 \times 10^{13} \text{ He cm}^{-2} \text{ s}^{-1}$. Parameters for simulation of diffusion $D_0=2.30 \times 10^{-3} \text{ cm}^2 \text{ s}^{-1}$, $E^M=1.59 \text{ eV}$, $E^B=0.40 \text{ eV}$, $r_t=1 \text{ \AA}$, $Z=6$, $\lambda=3.03 \text{ \AA}$.

The average diameter of the grains of MgAl_2O_4 in the study by Pychlau is about $5\ \mu\text{m}$ and in the study by Sasajima et al. the grain size of MgAl_2O_4 was $1.0\text{-}1.8\ \mu\text{m}$. The helium implantation rate was $11.7 \times 10^{13}\ \text{He}/\text{cm}^2\text{s}^{-1}$ for the highest doses in the study by Pychlau and $5 \times 10^{13}\ \text{He}/\text{cm}^2\text{s}^{-1}$ in the study by Sasajima et al.. The grains are visualised as thick slabs and the binding energy of helium to defects is uniform. No clustering is taken into account and consequently, the concentration of defects increases with implantation time.

The observation by Pychlau that no dots or bubbles could be viewed in samples implanted at $1073\ \text{K}$ may be due to the extensive release of helium from the grain and high annealing defect rates. The concentration of helium assuming a surviving defect fraction of $0.001\ \text{dpa}\ \text{s}^{-1}$ in Figure 4.20 is still too high for the absence of clustering.

For the simulation of the study by Sasajima et al. at $923\ \text{K}$, the helium concentration in the peak of the profile is about 7 times this helium concentration of S30M at $903\ \text{K}$ when the width of the helium concentration profile starts to reduce indicating clustering. The helium occupied vacancies could probably not be annealed resulting in helium occupied vacancy clusters and finally in helium filled nano-sized bubbles during implantation.

Implantations at room temperature show that helium occupies the vacant octahedral sites. The preference for this site by helium resulted in the absence of clustering of defects till a helium concentration of $1.09\ \text{He}\ \text{at}\%$ at room temperature [Allen 1993]. The preference of helium for this site is not studied for larger concentrations and higher temperatures. This study showed that the solubility of helium in spinel is high. This result is in agreement with the atomistic calculations in Chapter 3. Atomistic calculations in Chapter 3 showed that the preference site for helium in the perfect lattice of normal spinel is the centre of the empty octahedral sites.

The experimental measured swelling at room temperature is $0.03\ \text{vol}\%$ and $0.06\ \text{vol}\%$ [He et al. 2000] for respectively 400 to 100 times lower helium concentrations than the study by Allen. These swellings are deduced from strain measurements of single crystals. During thermal treatment, a reduction of strain occurred till about 10% of its value at room temperature till $823\ \text{K}$. At $1073\ \text{K}$, the strain starts to increase.

No swelling could be measured on the beam spots after implantation at room temperature using profilometry in the study by Fromknecht et al.. Flaking was observed in their study during heating of single crystals that were implanted at room temperature for doses at least 3 to 4 times larger than at EOI of EFTTRA-T4. Formation of micron-sized bubbles was observed after thermal treatment at $773\ \text{K}$ for concentrations similarly at EOI of EFTTRA-T4. It's questionable whether the high concentration of helium occupied defects at higher temperatures in their study would be present during irradiation since continuous annealing takes place during irradiation and in their implantation study, defects could only be annealed in a fraction of time. Also the observation of micron-sized bubbles, when the implantation range is $0.8\ \mu\text{m}$, is questionable. Probably, ellipsoidal shapes were formed instead of bubbles. Ellipsoidal cavities are formed in implanted materials because the concentration of helium and defects is not uniform.

Implantation at cryogenic irradiation conditions in the study by Bordes et al. show defect clusters and dislocation loops [Bordes et al. 1995]. Annealing of defects cannot take place at these conditions and this study can therefore not be related to the irradiation conditions.

Fission products create defects by displacements of ions in the crystal lattice, but fission products also emit beta's. Limited research is known to the author about the behaviour of spinel during ionising radiation. Virgin MgAl_2O_4 samples and helium implanted samples of MgAl_2O_4 show no difference during ionising irradiation [Buckley 1986]. The effect of ionising radiation in MgAl_2O_4 in the temperature range 1120-1320 K is phase separation into MgO and Al_2O_3 , formation of epitaxial Al/Mg metal islands on specimen surfaces, small spherical pores and cavities and other material degradation characteristics [Buckley 1986]. The emission of betas by each fission product created during irradiation is required in order to relate these ionising radiation experiments to the irradiation conditions. This is beyond the scope of this thesis.

There are also contradictory results on the effect by ionising radiation in (helium implanted) MgAl_2O_4 . An ENSP^{II} larger than 10 would result in the absence of dislocation loops in MgAl_2O_4 at 923 K in the study by Zinkle but these loops are observed during these experimental conditions at 870 K in the study by Yasuda et al. [Yasuda et al. 1997].

4.7 Americium in spinel

The implantations performed at higher temperatures than room temperature (Sasajima et al. and Pychlau) do not show the formation of bubbles in MgAl_2O_4 at such an extent as EFTTRA-T4, despite the far higher helium concentrations in these implantations than EFTTRA-T4. From these implantations it could be deduced that MgAl_2O_4 is an excellent inert matrix for the transmutation of americium considering the small swelling in MgAl_2O_4 till high helium implanted concentrations.

The simulation of diffusion of helium in spinel for hypothetical worse EFTTRA-T4 conditions in this thesis and the helium implantations from literature disagree with the EFTTRA-T4 result in terms of helium release and swelling. It is therefore suspected that the generation of a solid solution between MgAl_2O_4 and AmO_2 resulted in a material that is highly susceptible for bubbles during helium implantation. This hypothesis is enhanced by comparison with another irradiation study with MgAl_2O_4 . The implantation zones of EFTTRA-T3 contain (inert) gas concentration comparable to EFTTRA-T4. Paragraph 5.9.2 shows that these implantation zones do not show bubbles.

Another feature is the behaviour of EFTTRA-T4 samples after neutron irradiation at vacuum conditions. Damen [Damen 2003] showed that samples of EFTTRA-T4 evaporated during an isothermal stage of 1700 K. Mg and Al are not monitored during THDS experiments of the helium implanted MgAl_2O_4 samples in the present study. But Gritsyna et al. [Gritsyna et al. 2000] annealed single crystals of MgAl_2O_4 in vacuum at 1800 K in order to remove defects

^{II} ENSP: ratio of ionising/electronic and displacive/nuclear stopping power

created during the growth process. It is not indicated in their article how they performed this annealing in vacuum. They probably did not do this in tungsten crucibles since W evaporates at 1800 K in vacuum (see paragraph 4.3.2) and their research was focussed on the optical properties of MgAl_2O_4 . Evaporation of MgAl_2O_4 should be considered to take place in a two-way approach; first the oxygen atoms dissociate from MgAl_2O_4 and then Mg and Al evaporate. During sintering at reducing conditions, the partial pressure of oxygen is similar to vacuum. Paragraph 5.3 shows no evaporation of Mg and Al after sintering of pellets with MgAl_2O_4 and UO_2 in a reducing atmosphere at 1873 K otherwise the structure of stoichiometric spinel could not be measured with X-ray diffraction. Thus, the evaporation of Mg and Al of EFTTRA-T4 at 1700 K is not a property of MgAl_2O_4 .

The limiting factor for the use of MgAl_2O_4 as an inert matrix may be the severe material degradation by ionising radiation at temperatures higher than 1100 K although this experiment performed by Buckley has to be extrapolated to reactor conditions. In the implantation zones of MgAl_2O_4 in EFTTRA-T3 for the macro-dispersed fuel, these material degradation characteristics like bubbles could be not observed and the temperature of the fuel was about 700-1000 K. An irradiated pellet of MgAl_2O_4 with micron sized UO_2 inclusions (EFTTRA-T4ter) shows no bubbles but depletion in Mg near uranium rich regions. The temperature in the centre of the pellet was 1253 K at BOI and 675 K at EOI; the temperature of the cladding was kept at 575 K during irradiation of EFTTRA-T4ter [Klaassen et al 2003]. It is unclear where the sink of Mg was in the EFTTRA-T4ter experiment.

Until the impact of ionising radiation on MgAl_2O_4 is unclear, MgAl_2O_4 should still be considered as a promising inert matrix for transmutation of americium. But the formation of another phase by the formation of a solid solution between MgAl_2O_4 and AmO_2 may be the limiting factor. Coating of AmO_2 particles with an oxide that does not interact with MgAl_2O_4 can prevent the chemical interaction between both compounds that resulted in a phase that shows large swelling during irradiation. Ytria-stabilised Zirconia (YSZ) does not chemically interact with MgAl_2O_4 during sintering till about 1873 K for 5 hours [Sasajima et al. 2000 and Schram et al. 2001]. Another reason for the use of an YSZ coating is the fission product swelling of MgAl_2O_4 and the swelling of YSZ by helium.

The swelling by fission products in zirconia is about 2-5 times the swelling by fission products in UO_2 [Bleiburg et al. 1962]. The swelling by fission products in MgAl_2O_4 is at least 10 times the swelling by fission products in UO_2 (see paragraph 5.10.2.1).

The size of the bubbles in MgAl_2O_4 is significantly smaller than Ytria Stabilised Zirconia during the same helium implantations at 923 K [Sasajima et al. 2000]. PBA measurements show for the same helium implantation dose of $6 \times 10^{15} \text{ cm}^{-2}$ implanted with the same energy at room temperature and during similar thermal treatment, clustering of defects in YSZ [Damen 2003] but no clustering in MgAl_2O_4 [Neeft et al. 1999]. Thus, for the implantation of fission products YSZ is a better inert matrix than MgAl_2O_4 , but for the implantation of helium, MgAl_2O_4 is a better inert matrix than YSZ. It is therefore best to use both materials YSZ and MgAl_2O_4 . YSZ to obtain the smallest swelling by fission products known for ceramic

inert matrices without actinides, MgAl_2O_4 to obtain the smallest swelling by helium known for ceramic inert matrices without actinides. A coating of YSZ with a thickness of about $9\ \mu\text{m}$ on the AmO_2 spheres and embedding these particles in MgAl_2O_4 is possibly the best fuel for the transmutation of americium. The fission products are then implanted in YSZ and the helium, diffusing away from the coated AmO_2 spheres, can be contained in MgAl_2O_4 .

4.8 Conclusion

All concentration profiles of helium implanted single crystals of MgAl_2O_4 show after isothermal stages concentration dependent defect mediated diffusion. The empirical derived parameters were obtained by simulation of thermally evolved helium concentration profiles in single crystals using a temperature independent pre-factor of $2.30 \times 10^{-3}\ \text{cm}^2\text{s}^{-1}$ and a vacancy concentration of 0.1 dpa. These parameters are when no clustering occurred: 1.59 eV for the migration energy of helium and 2.29 eV for the dissociation energy of helium from vacancies that probably occupied one helium atom. This migration energy of helium is smaller than the calculated migration energy of helium in normal spinel. The average binding energy of helium to these vacancies is similar to the calculated binding energies of helium to vacancies. Helium implanted single crystals with vacancies that occupied more than one helium atom show interstitial diffusion of helium into depth of the sample during thermal treatment. The activation energies derived from THDS measurements by assuming an Arrhenius relationship are smaller than the dissociation energies of helium from defects derived by numerical analysis.

The concentration profiles of polycrystalline samples could be well modelled using concentration dependent defect mediated diffusion for grains and depth independent pore mediated diffusion at grainboundaries. The empirical derived parameters were obtained by simulation of thermally evolved helium concentration profiles in a low dose helium implanted polycrystalline sample using a temperature independent pre-factor of $3.45 \times 10^{-3}\ \text{cm}^2\text{s}^{-1}$. These parameters are for diffusion of helium at grainboundaries: 0.45 eV for the migration energy of helium at grainboundaries, 1.75 eV for the solution energy of helium in intergranular pores and an entropy of $-1 \times 10^{-3}\ \text{eV atom}^{-1}\text{K}^{-1}$ for intergranular pores. Pressurised intergranular pores have smaller solution energies and differences in entropies. Simulation of thermally evolved helium concentration profiles for a high dose helium implanted polycrystalline sample could be well performed using the assumption of the presence of pressurized nano-sized bubbles within the grain with a dissociation energy of helium from these bubbles of 2.89 eV. This energy is similar to the calculated permeation energies.

The thermal behaviour of helium implanted MgAl_2O_4 is excellent. Concerning this property, MgAl_2O_4 is a promising uranium-free matrix to cope with the amount of helium generated during transmutation of americium.

5 Inert matrix fuels

In the EFTTRA^A-programme, the transmutation of actinides in inert matrices is studied. In the EFTTRA-T3 project, fissile phases containing uranium were embedded in the inert matrices: MgO, MgAl₂O₄, Y₃Al₅O₁₂, Y₂O₃ and CeO₂. These macro-dispersed fuels consisted of large fissile inclusions embedded in matrices. The fissile phases were either UO₂ inclusions or (U,Y)O_x inclusions. The (U,Y)O_x inclusions are diluted in fissile actinides in order to reduce the locally fission product concentration at similarly overall burn-up; adverse effects like swelling of the inclusions and fission-gas release are expected to be less in comparison with the UO₂ inclusions. Also, one micro-dispersed fuel with (sub)micron sized UO₂ inclusions embedded in the matrix MgAl₂O₄ was tested to study the impact of fissile size on irradiation behaviour. The content of UO₂ in these inert matrix fuels was similar (2.5 vol% to 3.0 vol%) to study the differences of these inert matrices at similar concentrations of fission products and irradiation temperature. The IMF with (U,Y)O_x inclusions contained 19.5 vol% (U,Y)O_x which corresponds to 3.0 vol% UO₂. Inert matrices without fissile inclusions were neutron irradiated to single out the effect of fission products.

The crystal structure, microstructure, mechanical properties, isotopic and chemical composition of fissile phases and matrices were analysed prior to neutron irradiation.

These pellets were neutron irradiated in pins in the High Flux Reactor in Petten and the composition of actinides and fission products after neutron irradiation is calculated. The post irradiation examination of the pins included: diameter measurements, composition of gas in the plenum and axial distribution of γ -emitting nuclides. The post irradiation examination of the pellets included: dimensions and weight of the pellets, microstructure, distribution of α - and β , γ emitting and non-radioactive products and mechanical properties.

These results are used to determine and/or predict: fission product distribution in the pellet, swelling of the fissile inclusions, fracture behaviour of the inert matrix fuels, fission-gas and cesium release from the targets.

Uranium was used as a fissile phase instead of plutonium or americium, since uranium is easier to handle during preparation of the targets. This experiment is therefore a pilot-study for the transmutation of actinides in uranium-free matrices.

^A Experimental Feasibility of Targets for Transmutation, a European Project in which CEA, NRG, FzK, JRC-ITU and JRC-IE cooperate.

5.1 Characterisation of UO_2 used for macro-dispersed fuel

UO_2 powder was obtained from the stock of NRG. Figure 5.1 shows a SEM-photograph of the powder. It shows that the variation in diameter of the particles in the UO_2 powder is very large. As will be discussed later, fractional emission of fission products from the fissile inclusions by fission depends on the size of the fissile phase (and fission fragment recoil range of fissile phase). Therefore, attempts have been made to determine the size of the UO_2 inclusions. These UO_2 particles were used for the fabrication of fuels for the following pins: 1, 5, 11, 15 and 18.

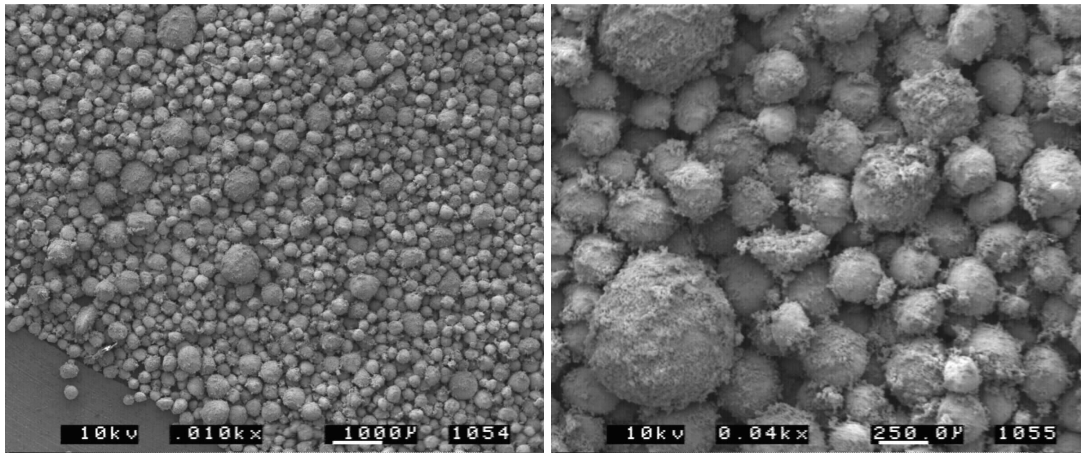


Figure 5.1. SEM-photographs of UO_2 powder.

Quantification of the size distribution of the UO_2 spheres was performed by creating four fractions in which the size of UO_2 spheres is similar in order to avoid the large UO_2 spheres being predominant in the image by hiding the smaller UO_2 spheres. Table 5.1 shows the characteristics of these four sieving fractions. The UO_2 particles were spherical in the sieving fractions 1, 2 and 3. Particles in sieving fraction 4 look like the dust covering the microspheres that can clearly be observed on the large microspheres in Figure 5.1. They pass the grid with an aperture of 25 μm .

A sample of each sieving fraction was heated in a molybdenum cup at the same sintering conditions as the fuels for EFTTRA-T3: 5 hours at 1873 K in Ar / H_2 (95% / 5%). X-ray diffraction analysis of the sintered UO_2 spheres showed that the lattice parameter was $5.48 \text{ \AA} \pm 0.02 \text{ \AA}$ and that the crystal structure was fluorite, both are UO_2 characteristics.

Samples of each of the four sieving fractions were measured using Isotope Neutron Activation Analysis (INAA) and the uranium standard NBS 960 was used as a reference [Woittiez 1999]. Table 5.1 shows that general enrichment of the UO_2 powder is 20%. It also shows that the variation between the sieving fractions 1, 2 and 4 in enrichment of ^{235}U is small indicating that these UO_2 particles are probably from the UO_2 powder created from one batch. The enrichment of ^{235}U of group 3 is about 1.5 at% less than the other sieving fractions. It can be suggested that this UO_2 powder was made by mixing two batches of UO_2 powder with a

variation in enrichment.

The dimensional change by sintering of the particles is determined using the average volume of the particles in each batch before and after sintering. Table 5.1 shows the previously discussed properties of the UO₂ microspheres.

Table 5.1 Characteristics of the UO₂-microspheres.

Sieving fraction	1	2	3	4
aperture (Ø) of iron grid sieves in µm	Ø > 150	150 > Ø > 53	53 > Ø > 25	Ø < 25
W_i (± 0.0013)	0.4882	0.3688	0.0896	0.0535
N_i	<i>B</i>	168	404	113
	<i>A</i>	159	265	142
$\overline{D}_{N,V}$ / µm ^a	<i>B</i>	288	168	63.30
	<i>A</i>	193	112	42.17
$\Delta V/V \times 100$	-69.8	-70.1	-70.4	-2.9
²³⁵ U / at%	19.998 ± 0.001	19.998 ± 0.010	18.391 ± 0.003	19.848 ± 0.007

N_i = number of microspheres/particles used for analysis, *B* = Before sintering, *A* = After sintering.

Figure 5.2 shows the normalised distribution of the sintered microspheres, with an interval of 1 µm. The average diameter in volume of all these particles ($\overline{D}_{V,V}$) before sintering amounts 349 µm and becomes after sintering 193 µm. The median in volume ($D_{V,50}$) is before sintering 198 µm and 146 µm after sintering. The median in number of particles ($D_{N,50}$) is before sintering 6 µm and 5 µm after sintering. The median in volume and number of sintered particles are indicated in Figure 5.2.

5.2 Fabrication of pellets

Pellets with and without uranium (²³⁵U = 20 U at%) oxides were prepared for the EFTTRA-T3 programme. The fabrication of these pellets is described by Boshoven et al. [Boshoven et al. 1997]. In this section, a summary of the fabrication is presented^b.

The inert matrix fuels (IMF) with uranium oxide contained the matrices MgO, MgAl₂O₄, Y₃Al₅O₁₂, Y₂O₃ and CeO₂. These IMF were prepared by mixing of dry powders, containing

$$^a \overline{D}_{N,V} = 2 \times \sqrt[3]{\frac{\sum V_j}{N_i} \div \frac{4\pi}{3}}, \text{ where } V_j \text{ is the volume of an individual microsphere}$$

^b In this paragraph also additional data obtained by private communication with H.Hein and J.C. Boshoven concerning the fabrication is included as well as data from labjournals that is excluded in Boshoven et al..

UO₂ and matrix, for about five minutes using pestle and mortar. MgO was heated at about 800°C in air to ensure dehydration before mixing this powder with fissile phase. Pellets with MgAl₂O₄ and UO₂ were also prepared by coprecipitation.

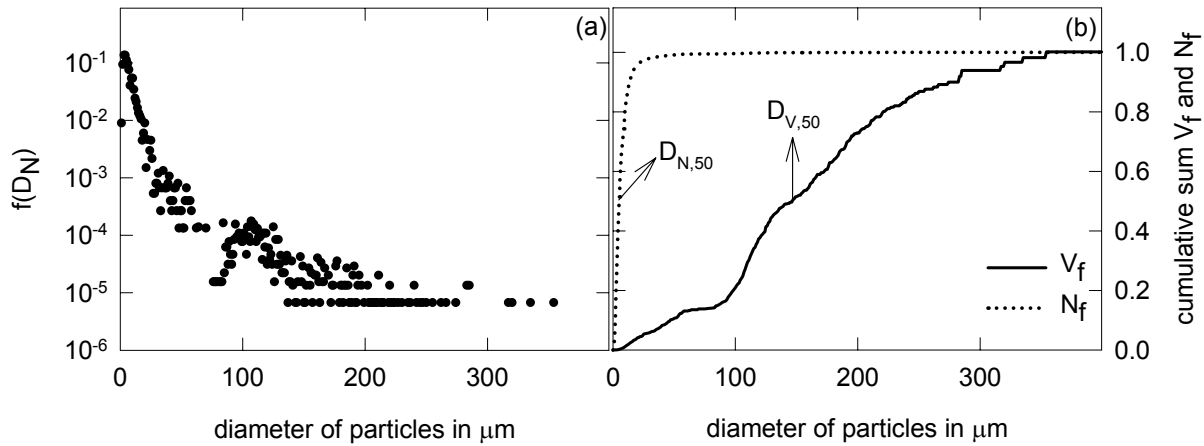


Figure 5.2 (a) Normalised distribution of sintered UO₂ particles: $f(D)_N$ and (b) dotted line cumulative sum of fraction in number of particles (N_f), solid line cumulative sum of fraction in volume of particles (V_f).

Coprecipitation of this composite was performed by dissolving MgO, UO₂ and Al(NO₃)₃·9H₂O in nitric acid. Ammonia was added to cause precipitation. This precipitate was washed respectively with water, acetone, diethylphthalate and acetone. This precipitate was heated at 1073 K in air for about a day. Besides UO₂ as a fissile phase, a diluted fissile phase containing (U,Y)O_x was prepared using coprecipitation by dissolving Y₂O₃ and UO₂. This coprecipitate was washed and heated at 1073 K similarly as discussed for the coprecipitate of MgAl₂O₄ and UO₂. The chemical composition after coprecipitation and heating was measured to be U:Y=1:5.94±0.02 and this coprecipitate consisted, most probably, of yttrium-carbonates besides uranium-and yttrium oxides after heating at 1073 K [Neef 2003]. Powders of the diluted fissile phase of (U,Y)O_x with powders of either MgO or MgAl₂O₄ were mixed using pestle and mortar. Pellets without a fissile phase: MgO and MgAl₂O₄ were also prepared by coprecipitation. The purity of the powders, from which the pellets are prepared, ranged from 98.0% till larger than 99.99%.

Pellets were prepared by uni-axial pressing of the mixtures of powders with pressures between 255-640 MPa. A film of coconut fat was applied inside the stamp to facilitate the removal of the pressed pellets from the stamp. The pellets without uranium oxide: MgO, MgAl₂O₄, Y₃Al₅O₁₂, Y₂O₃, CeO₂ and BaZrO₃ were sintered in air. Pellets with uranium oxide were sintered in an atmosphere composed of 95% Argon and 5% Hydrogen. Both series of pellets were sintered for 5 hours at 1873 K to 1973 K. Table 5.2 shows the characteristics of the pellets before neutron irradiation: number of pellets measured (N_p), the average diameter of the pellets (\bar{D}) and the sum of the height of the pellets ($\sum h$). Both dimensions were obtained

upon using a micrometer.

Table 5.2. Characteristics of pellets prior to neutron irradiation.

ceramic composite	pin	N_p	\overline{D} mm	Σh mm	UO ₂ vol% ^c	density g cm ⁻³	relative density % of T.D
CeO ₂ + UO ₂	1	6	5.358 ± 0.047	69.40	2.62	6.329 ± 0.139	86.6±1.9
MgO ^{cp} + UO ₂	5	15	5.266 ± 0.035	70.43	2.63	3.371 ± 0.093	89.2±2.5
MgO+ UY _z O _x ^{cp}	7	12	5.107 ± 0.155	75.80	3.05	3.269 ± 0.185	80.8±4.6
(MgAl ₂ O ₄ + UO ₂) ^{cp}	9	12	5.077 ± 0.073	67.95	2.55	3.387 ± 0.122	89.9±3.2
MgAl ₂ O ₄ + UO ₂	11	12	5.206 ± 0.033	69.40	2.62	3.592 ± 0.030	95.3±0.8
MgAl ₂ O ₄ + UY _z O _x ^{cp}	13	13	5.206 ± 0.012	70.30	3.04	3.733 ± 0.032	92.4±0.8
Y ₃ Al ₅ O ₁₂ + UO ₂	15	12	5.388 ± 0.019	70.77	2.62	4.265 ± 0.031	90.4±0.7
Y ₂ O ₃ + UO ₂	18	15	5.335 ± 0.014	72.79	2.62	4.908 ± 0.050	94.6±1.0
matrices							
CeO ₂	2	7	5.239 ± 0.022	71.82		6.697 ± 0.076	92.8±1.1
Y ₂ O ₃	4	17	5.379 ± 0.017	81.18		4.834 ± 0.036	96.1±0.7
MgO ^{cp}	6	15	5.234 ± 0.043	79.76		3.128 ± 0.045	89.8±1.3
MgO	8	18	5.490 ± 0.030	82.19		2.925 ± 0.100	81.6±2.8
MgAl ₂ O ₄ ^{cp}	10	16	5.246 ± 0.047	81.44		3.424 ± 0.023	95.7±0.6
MgAl ₂ O ₄	12	15	5.204 ± 0.017	80.69		3.146 ± 0.038	95.4±1.1
BaZrO ₃	14	16	5.250 ± 0.108	79.06		4.609 ± 0.037	74.0±0.6
Y ₃ Al ₅ O ₁₂	16	17	5.312 ± 0.009	80.88		4.239 ± 0.034	93.1±0.8

^{cp} compounds made by coprecipitation, $z = 5.94$, $x \approx 11$, all values $\pm 1\sigma$, other symbols are indicated in text.

The average geometrical density of the pellets was determined by weight and dimensional volume of each pellet. These pellets are encapsulated in pins with numbers indicated in Table 5.2. The theoretical densities of the inert matrices are in g/cm³: 7.215, 3.585, 3.579, 4.553, 5.032, 6.229 and 10.93 for CeO₂, MgO, MgAl₂O₄, Y₃Al₅O₁₂, Y₂O₃, BaZrO₃ and UO₂ respectively. These are used to determine the density of the theoretical one.

Before irradiation, a number was written by pencil on the sintered pellets to distinguish the pellets in each series after neutron irradiation. This was done to determine the individual mass and volume change of the pellets. Spare pellets of each series were packed in tubes of glass. Handling of these tubes caused fragmentation of the CeO₂+UO₂ spare pellets while the other spare pellets remained intact.

5.3 Characterisation of IMF pellets prior to irradiation

Prior to neutron irradiation, the Inert Matrix Fuel (IMF) pellets were characterised by X-ray diffraction, Isotope Dilution Thermal Ionisation Mass Spectrometry (IDTIMS) and

^c UO₂ vol% is determined by UO₂ wt%

ceramography in order to determine the crystal structure, distribution of UO_2 between pellets, size and shape of UO_2 inclusions in pellets and porosity of fissile phase embedded in the matrix. These parameters are, besides the density, required to interpret the post-irradiation results.

5.3.1 X-ray diffraction

X-ray diffraction analysis was performed on powder obtained from one sintered pellet with enriched uranium in each series of these pellets [van Vlaanderen 2000]. This X-ray diffraction examination was made to identify compounds in the pellets and the patterns were compared with an X-ray diffraction database [PCPDFWIN 1997]. Table 5.3 shows the identification of phases including the measured lattice parameter of these phases. The measured lattice parameter is always 0.02 Å larger in comparison with the X-ray diffraction database, probably due to the offset of the X-ray equipment.

Table 5.3 shows that no solid solution could be measured in the following ceramic composites with UO_2 : MgO , MgAl_2O_4 and $\text{Y}_3\text{Al}_5\text{O}_{12}$. It also shows that the lattice parameter of UO_2 measured in the pellets is similar with the one measured for the solely sintered UO_2 microspheres in paragraph 5.1. Phase diagrams [Phase Equilibria Diagrams 1994] show that both, MgO and Al_2O_3 do not form a solid solution with UO_2 under reducing conditions, which explains the absence of chemical interaction between UO_2 and both, MgO and MgAl_2O_4 , in the present experiment.

Table 5.3. Phases in sintered pellets including measured lattice parameter ^a.

Pin	IMF	fissile phase		matrix	
		crystal structure	a / Å	crystal structure	a / Å
1	$\text{CeO}_{2-x} + \text{UO}_2$	lattice parameters of range of fluorite phases are undetectable		CeO_2	5.42
18	$\text{Y}_2\text{O}_3 + \text{UO}_2$	UO_2	5.48	Y_2O_3	10.60
		fluorite	5.32		
5	$\text{MgO} + \text{UO}_2$	UO_2	5.48	MgO	4.21
7	$\text{MgO} + \text{UY}_{5.94}\text{O}_x$	fluorite (1)	5.37	MgO	4.21
		fluorite (2)	5.33		
		Y_2O_3	10.60		
9	$\text{MgAl}_2\text{O}_4 + \text{UO}_2$	UO_2	5.48	MgAl_2O_4	8.10
11	$\text{MgAl}_2\text{O}_4 + \text{UO}_2$	UO_2	5.48	MgAl_2O_4	8.10
13	$\text{MgAl}_2\text{O}_4 + \text{UY}_{5.94}\text{O}_x$	fluorite (1)	5.39	MgAl_2O_4	8.10
		fluorite (2)	5.35		
		unidentified phase	-		
15	$\text{Y}_3\text{Al}_5\text{O}_{12} + \text{UO}_2$	UO_2	5.48	$\text{Y}_3\text{Al}_5\text{O}_{12}$	12.02

^auncertainty in lattice parameter is about 0.02 Å.

No literature data has been found on possible chemical interaction between $\text{Y}_3\text{Al}_5\text{O}_{12}$ and UO_2 but since Y_2O_3 can form a solid solution with UO_2 it cannot be excluded that this chemical interaction may occur. However, for the present experiment, no interaction between

$Y_3Al_5O_{12}$ and UO_2 was observed.

Phase diagrams show that Y_2O_3 , MgO , Al_2O_3 and $MgAl_2O_4$ remain stoichiometric in oxygen concentration under reducing conditions. For CeO_2 some oxygen sub-stoichiometry might be induced by sintering in a reducing atmosphere, this compound is therefore presented as CeO_{2-x} . The crystal structure of CeO_{2-x} was measured to be fluorite with a lattice parameter of 5.42 Å. These two properties can only be found for $0 < x < 0.17$, indicating that the present pellets were in this stoichiometry range. The X-ray diffraction analysis of the pellets was only to identify compounds; the measurement accuracy was too low to obtain detailed information on the possible oxygen sub-stoichiometry for the present samples.

More than two phases were measured in pellets with UO_2 and the inert matrices Y_2O_3 and CeO_{2-x} ; the inert matrix phase and (two) different fluorite phases. Phase diagrams show that both, CeO_{2-x} and Y_2O_3 can form solid solutions with UO_2 under reducing conditions. The crystal structures of CeO_2 and UO_2 are both fluorite and their difference in lattice parameter is about 0.06 Å. The lattice parameters of UO_2 or $(Ce,U)O_2$ were undetectable due to the small volume of UO_2 . The difference in scattering factors of Ce and U is very small in comparison with U and Mg, Y or Al. Therefore, the low volume content of UO_2 in the other targets was no problem for identification of the compounds, but it is for $CeO_{2-x}+UO_2$.

An inert matrix phase: MgO or $MgAl_2O_4$ and, among others, a range of fluorite phases were observed for pellets with $UY_{5.94}O_x$ inclusions. The cubic Y_2O_3 phase and fluorite phases can be attributed to the $(U,Y)O_x$ particles.

5.3.2 Ceramography prior to irradiation

Before neutron irradiation, one individual pellet of each series was embedded in Hysol and transverse sections were made of these fuels except for $MgAl_2O_4+UO_2$ (macro-dispersed); an axial section was made of this fuel. Before neutron irradiation, the ceramographic section with UO_2+CeO_{2-x} (pin 1) could not be polished and therefore no ceramographic section of UO_2 inclusions embedded in this matrix is presented. The images of all ceramographic sections are presented in the paragraph 5.9.2 together with images after neutron irradiation.

Cracks in pellets

Before neutron irradiation, no cracks in the pellets were observed, except for the ceramic composite $MgO+UY_{5.94}O_x$ (pin 7, see Figure 5.17a, b and c). This ceramic composite shows cracks in the matrix from fissile to fissile inclusion. Sometimes, these cracks run into the inclusions.

5.3.2.1 Macro-dispersed fuels

UO_2 inclusions: porosity and size

In the matrices: $Y_3Al_5O_{12}$ and $MgAl_2O_4$, a gap surrounding the UO_2 inclusions was

observed. Such a gap is created if the reduction in volume by sintering for these UO_2 inclusions larger is than the surrounding matrix and no chemical interaction occurred during sintering between matrix and UO_2 .

Before neutron irradiation, one optical microscopy photo was made of a UO_2 inclusion embedded in a matrix in each series of pellets. The porosity of UO_2 inclusions embedded in MgAl_2O_4 and Y_2O_3 could not be measured using ceramography before neutron irradiation. In these UO_2 -inclusions, outbreak of UO_2 occurred while polishing these ceramic composites. Outbreak is characterised by sharp edges while pores have a more smooth shape. Determination of porosity is limited to two UO_2 inclusions before neutron irradiation due to a single image taken in each series of pellets of UO_2 inclusions and outbreak. These were one inclusion embedded in MgO with a porosity of 9.4% and one in $\text{Y}_3\text{Al}_5\text{O}_{12}$ with a porosity of 0.9%.

The UO_2 inclusions embedded in matrices in the transverse sections are circular in shape, they are elliptical in shape in an axial section. The initial UO_2 microspheres were extremely porous before sintering since paragraph 5.1 showed that the general volume change after sintering is about -70% . During pressing of the mixtures with inert matrices into pellets, the highly porous UO_2 microspheres are pressed into an ellipsoidal shape. The general diameters of the UO_2 inclusions, measured in the sections, range from 100-150 μm .

The axial and radial distribution of the inclusions is not uniform in the pellet [Neeft 2003]. Chemical analysis of sintered pellets showed that the distribution of the fissile phase is not uniform for all pellets and [Woittiez 2000].

UY_{5,94}O_x inclusions: porosity and size

Figure 5.17b shows large porosity in, but more near the $\text{U,Y}_{5,94}\text{O}_x^d$ inclusions embedded in MgO and Figure 5.16b shows large porosity near, but more in the $\text{U,Y}_6\text{O}_x$ inclusions embedded in MgAl_2O_4 . The porosity in the UY_6O_x inclusions embedded in MgAl_2O_4 and MgO were $20\% \pm 4\%$ and $12\% \pm 4\%$, respectively using image analysis of the ceramographic sections. The UY_6O_x inclusions embedded in MgO have a uniform colour. The UY_6O_x inclusions embedded in MgAl_2O_4 show a dark and a light phase. The general diameters of the $\text{U,Y}_{5,94}\text{O}_x$ inclusions, measured in the section, range from 100-200 μm .

5.3.2.2 Micro-dispersed fuel

The SEM image (figure 5.15c) of the micro-dispersed fuel: $\text{MgAl}_2\text{O}_4+\text{UO}_2$ shows that submicron-sized UO_2 particles are embedded in MgAl_2O_4 . The porosity from the transverse section is measured to be 7.6%. This smaller value in porosity in comparison to the 11.1% porosity determined by geometrical density, is possibly due to the conical shape of the pellets and the measurement technique.

5.4 Microstructure of matrices without fissile phase

^d in the rest of this chapter $\text{UY}_{5,94}\text{O}_x$ is abbreviated into UY_6O_x

SEM images shows that spherical pores in CeO_2 are present in the grains [Neeft 2003]. The intergranular pores are angular shaped. MgO shows qualitatively a similarly porosity distribution. The porosity in the grains is significantly larger than between the grains for the pellets MgO and CeO_2 and the dominant diameter of the pores is about $2\ \mu\text{m}$.

Solely angular-shaped intergranular pores could be observed in the matrices Y_2O_3 , $\text{Y}_3\text{Al}_5\text{O}_{12}$ and MgAl_2O_4 using SEM. The dominant diameter of the intergranular pores in these 3 matrices is $0.5\ \mu\text{m}$. Micron-sized intragranularly perfectly spherical pores are observed in the grains of CeO_2 and MgO, intergranular pores are angular-shaped. The ranges in size of grains were determined by grain boundaries otherwise the distance between intergranular pores is used. Table 5.13 shows the grainsize.

5.5 Irradiation pins

The pellets were loaded in 15/15 Ti steel pins. These pins have a length of 168 mm, an inner diameter of 5.65 mm, and an outer diameter of 6.55 mm. Before loading, the bottom of the capsules is welded in air using a laser. The pins are loaded with steel plugs, pellets with and without UO_2 and a spring. The pins are filled with helium using a specific welding-technique [Boshoven et al. 1997] in which some air can be incorporated during welding [Neeft 2003]. Figure 5.3 shows a drawing of a pin with fuel.

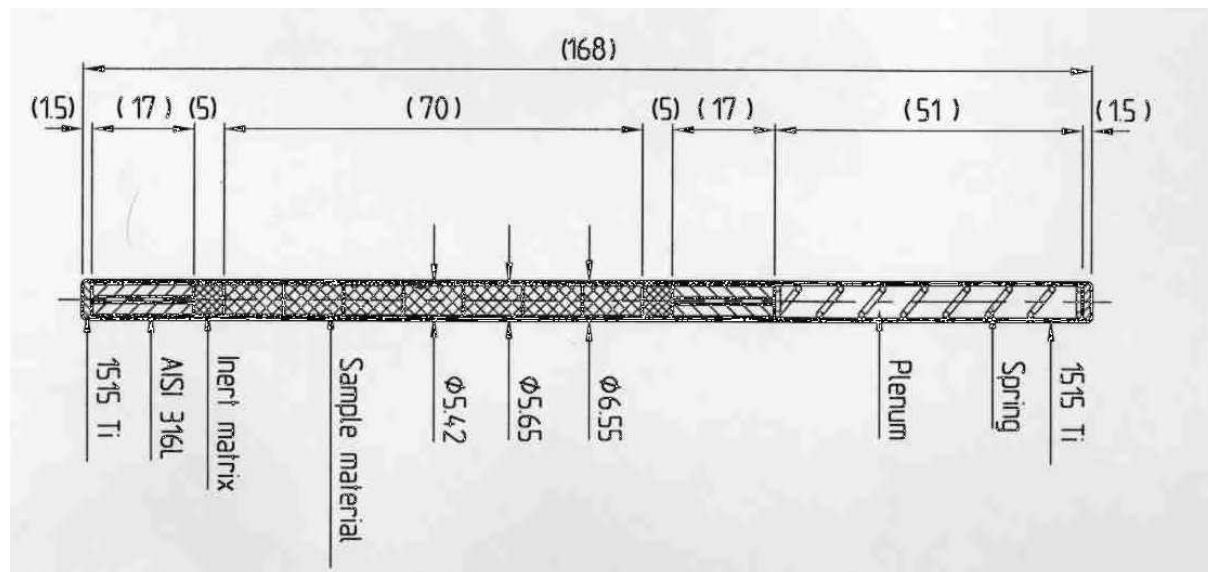


Figure 5.3 Drawing of T3 capsule [Conrad 1997].

5.6 Neutron irradiation

The capsules were irradiated for 198.87 Effective Full Power days in the sample holder in the Refa/140 rig that was positioned in the reactor position C3 of the High Flux Reactor in Petten.

At each pin, two neutron monitor sets were oppositely placed at the same axial level to determine the neutron fluence after neutron irradiation. The quantitative activity of Ni-, Fe-, Ti- and Nb from pieces of wires, that the neutron monitor sets contained, was measured using a calibrated HP GeLi-detector in order to obtain the neutronic spectrum, with which the capsules were irradiated [Paardekooper 1999, Dassel et al. 1999]. The neutronic spectrum is determined from the absolute amount of radioactive atoms. Along the capsules, stainless steel wires were placed to obtain the axial neutron fluence distribution. The neutronic spectrum is calculated as well as measured.

Solely the concentration of the uranium atoms is taken into account for the calculation of burn-up, neutronic absorption of the matrix has been neglected since this is expected to be negligible. The burn-up of the samples after 198.87 Effective Full Power Days was calculated to be 17.1-19.8% Fissions per Initial Metal Atom; Initial Metal Atom refers in these IMF only to Uranium [Sciolla 2000]. The power at Begin Of Irradiation (BOI) and End Of Irradiation (EOI) was calculated [Sciolla 2002]. The uncertainty in both calculations is 10 to 15%.

Table 5.4 shows the average values of the neutronic monitor sets at each individual capsule with enriched uranium. The standard deviation of each group of neutrons at an identically axial level was measured to be 1-2% of the measured fluences (see Table 5.4). This small variation indicates that the absorption of neutrons in the pins is very small, which is expected considering the small diameters of the pellets and the low vol% of actinides. The temperature of the targets with fissile phase during neutron irradiation was estimated to be 700 K to 1000 K [Neeft et al. 2001]. The calculated average temperature of pellets without fissile phase is about 640 K to 690 K [Schram et al. 1999]. During irradiation, the average temperature of the aluminium support material was measured to be 600 ± 25 K using thermocouples [Conrad 1997].

Table 5.4. Neutron fluence, power and burn-up

Pin	1	5	7	9	11	13	15	18
thermal neutron fluence $\times 10^{24} \text{ m}^{-2}$	28.2 ± 0.1	28.9 ± 0.6	28.6 ± 0.5	34.0 ± 0.0	34.4 ± 0.4	34.1 ± 1.1	34.1 ± 0.5	28.6 ± 0.1
intermediate neutron fluence $\times 10^{24} \text{ m}^{-2}$	4.0 ± 0.0	3.9 ± 0.3	4.1 ± 0.0	4.3 ± 0.1	4.5 ± 0.0	4.6 ± 0.0	4.4 ± 0.1	3.8 ± 0.4
fast neutron fluence $\times 10^{24} \text{ m}^{-2}$	31.2 ± 0.6	33.0 ± 0.6	31.7 ± 0.2	36.2 ± 1.1	38.0 ± 0.4	38.3 ± 0.4	36.7 ± 0.8	32.7 ± 0.4
$E_{\text{neutron}} > 0.1 \text{ MeV} \times 10^{24} \text{ m}^{-2}$	58.9 ± 1.1	62.3 ± 1.1	59.8 ± 0.5	68.2 ± 2.0	71.8 ± 0.8	72.4 ± 1.2	69.3 ± 1.5	61.7 ± 0.8
$E_{\text{neutron}} > 1.0 \text{ MeV} \times 10^{24} \text{ m}^{-2}$	28.2 ± 0.6	29.6 ± 0.4	29.8 ± 0.6	28.6 ± 0.3	32.7 ± 0.9	34.4 ± 0.4	34.6 ± 0.6	33.2 ± 0.7
Power at BOI in W/cm	47	45	45	51	56	63	59	50
Power at EOI in W/cm	17	16	16	18	20	23	21	18
FIMA in %	17.1	17.5	17.3	19.1	19.7	19.8	19.3	17.2

5.7 Post irradiation examination of pins and wires

5.7.1 Gammasspectrometry of wires

With gammasspectrometry of the stainless steel wires, the axial neutron fluence can be determined. The neutron dosimeter sets with which the neutronic spectrum is measured, also contained a piece of stainless steel wire. The activity of each piece measured with the calibrated HP GeLi detector is correlated with the activity measured from each stainless steel wire with the Ge detector. The axially fast and thermal neutron fluence (ϕ) is determined from the activity of ^{54}Mn and ^{60}Co , respectively. The reactions for determination of the thermal neutron fluence is $^{59}\text{Co}(n,\gamma)^{60}\text{Co}$ and for the fast neutron fluence $^{54}\text{Fe}(n,p)^{54}\text{Mn}$ [Paardekooper 1999]. The axial position of the neutron dosimeter sets from which this neutronic spectrum is determined, is shown in Figure 5.4. These sets are positioned at 60 mm from the bottom of the capsule; 60 mm is in the middle of the fission stack length. It also shows the axially thermal and fast neutron fluence. The pins in the lower level: pin 9, 11, 13 and 15 have a neutron fluence of about 20% more than the pins in the upper level: pin 1, 18, 5 and 7.

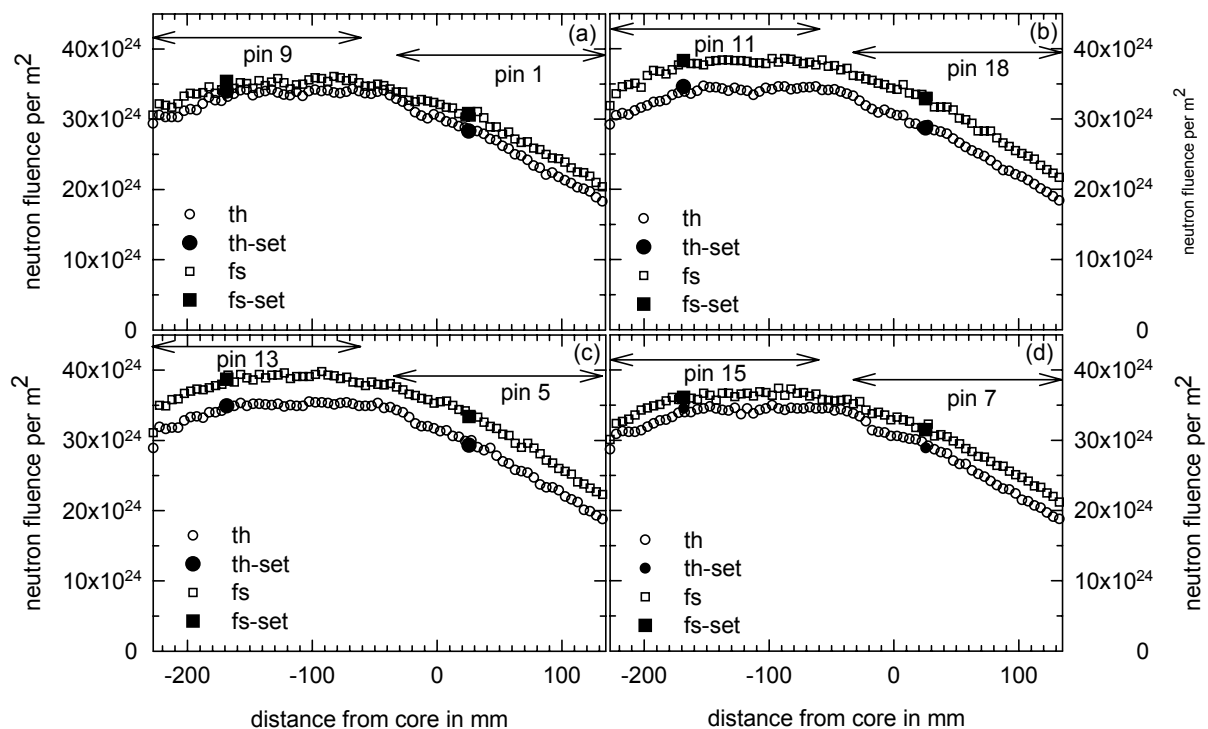


Figure 5.4 Open symbols: axial neutron fluence: fast (fs) determined by $^{54}\text{Fe}(n,p)^{54}\text{Mn}$ and thermal (th) determined by $^{59}\text{Co}(n,\gamma)^{60}\text{Co}$ of (a) pin 9 and 1, (b) pin 11 and 18, (c) pin 13 and 5 and (d) pin 15 and 7. Closed symbols: position of neutron dosimeter sets. Arrows indicate location and length of pins.

5.7.2 Gammaspectrometry of pins

The axial distribution of γ -emitting fission products is observed with gammaspectrometry of the capsules. The following isotopes could be measured 6 months after neutron irradiation: ^{144}Ce , ^{103}Ru , ^{134}Cs , ^{95}Zr , ^{95}Nb , ^{58}Co , ^{54}Mn , ^{141}Ce and ^{51}Cr [Buurveld 1999].

Axial distribution of γ -emitting nuclides

Figure 5.5 shows the axially fast neutron fluence and the axial profiles of fission products that are known to be immobile in UO_2 and an activation product from the steel plugs ^{54}Mn . For pin 1 in Figure 5.5a, the loading of the capsule in Figure 5.3 can clearly be observed: the steel plugs from the activity of ^{54}Mn , the inert matrix pellet from the activity of solely ^{139}Ce , and the fission stack length from the activity of ^{144}Ce . For the other pins, no neutron activation of the uranium free matrices could be observed.

Pin 5 in Figure 5.5b shows that the profiles of ^{95}Zr and ^{144}Ce are nearly identical. Profiles of immobile fission products ^{95}Zr , ^{95}Nb , ^{144}Ce , ^{141}Ce , ^{103}Ru and ^{106}Ru are nearly identical for all capsules and therefore not all presented. This is in agreement with the expectation that these fission products are immobile. For the other capsules, the profile of the fission stack length is therefore solely presented as ^{95}Zr . Gaps between pellets can clearly be observed in the ^{95}Zr profile of pin 5, 7 and 18. The other capsules have less gaps between the pellets.

The pins 18, 5, 11 and 15 show a rough pattern. These macro-dispersed fuels are fabricated with the UO_2 microspheres (see paragraph 5.1). The low concentration of fissile phase (~2.5 vol%) and highly local concentration of uranium in the pellet results in occasional presence of a UO_2 particle at that particularly axial position. This caused the rough pattern observed for the macro-dispersed fuels with UO_2 as a fissile phase using gammaspectrometry [Neeft 2003].

Pin 13 in Figure 5.5f shows a rather smooth pattern. This macro-dispersed fuel contained a high volume of fissile phase (19.5 vol% instead of 2.5 vol%). The gammaspectrometry of pin 9 with pellets prepared by co-precipitation containing (sub)micron-sized UO_2 inclusions, clearly shows the onset and end of each pellet and in the pellet the pattern is smooth in Figure 5.5d. That the onset and end of the pellet in pin 9 can clearly be observed, is caused by the conical shape of these pellets as can clearly be viewed in an axial section of these pellets (see Figure 5.15).

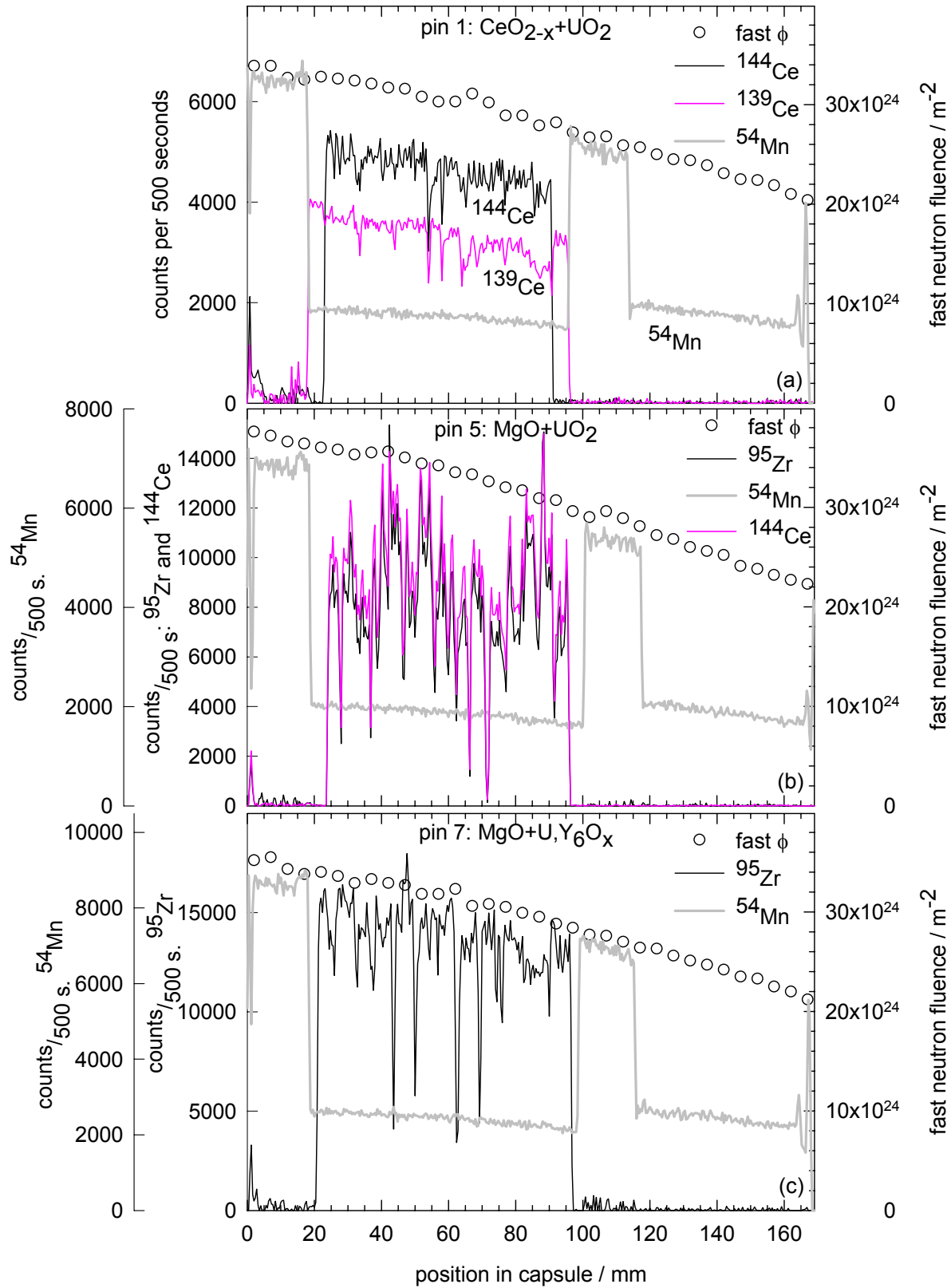


Figure 5.5 Count rate for activation product of steel (^{54}Mn), immobile fission products (^{95}Zr and ^{144}Ce) and fast neutron fluence versus position of pin for (a) pin 1, including activation product of matrix (^{139}Ce), (b) pin 5 and (c) pin 7.

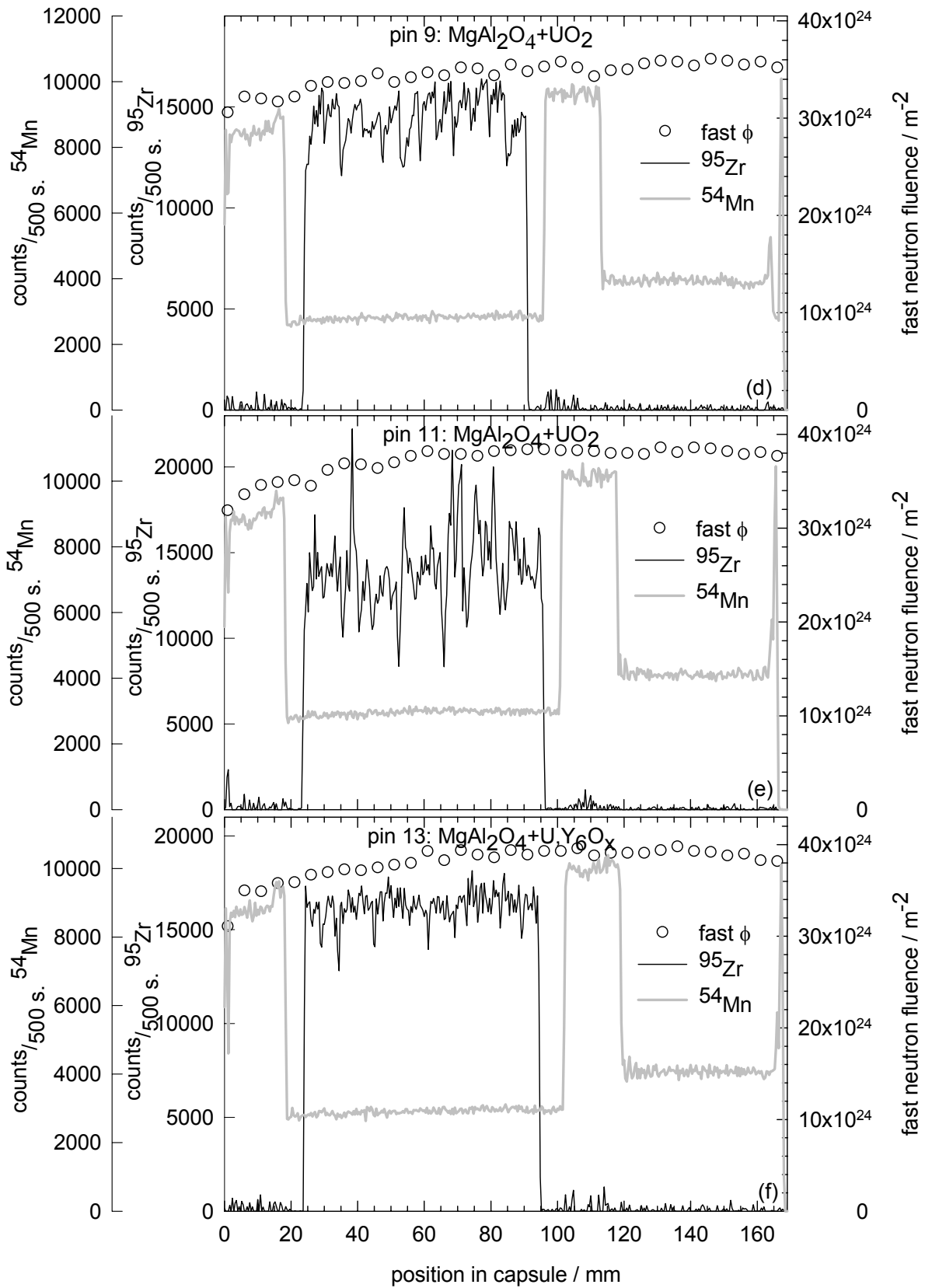


Figure 5.5 Count rate for activation product of steel (^{54}Mn), immobile fission products (^{95}Zr and ^{144}Ce) and fast neutron fluence versus position of pin for (d) pin 9 (e) pin 11 and (f) pin 13.

Cesium

The volatile fission compound CsI, which is released from defective fuel, can react with steam resulting in the very volatile compound HI [de Boer 1997]. Although this compound can be contained in the primary cooling system and is therefore not in contact with the surrounding environment, the release of cesium from pellets should be prevented in order to limit the radiation dose for reactor employees in case of failure of the cladding. An indication of the cesium release can be given with gammaspectrometry.

Figure 5.6 shows a few examples of the count rate of the cesium isotopes and the thermal neutron fluence. It shows that the general slope of ^{134}Cs larger is than ^{137}Cs . This is due to the different origin of ^{137}Cs and ^{134}Cs . ^{137}Cs is mainly generated by decay of fission products and ^{134}Cs by transmutation of ^{133}Cs that originates from decay of ^{133}Xe . The generation of ^{134}Cs requires therefore one neutron more than ^{137}Cs . This is clearly reflected in the profiles of pin 1, 18 and 7 with a clearly varying axial neutron fluence in comparison with the profiles of pin 9, 11, 13 and 15 with an almost uniformly axial neutron fluence.

Figure 5.6 also clearly shows that cesium is present outside the fission stack length in pin 1 and 7. This is also observed for pin 11 and 15. The fuel stack is measured after 6 months EOI and the regions outside the fuel stack about 1 year after EOI. The axial distribution of 2 to 3 isotopes could not be measured about 1 year after EOI. The regions outside the fission stack length were measured about a year after EOI. These regions have a larger background than the data made after six months of the neutron irradiation due to the 2 to 3 extra isotopes that contribute to the background [Neeft 2003]. The observation of cesium outside the fission stack length may be due to a larger background, fragmentation of the pellets or release of cesium from the fission stack length. Discerning these three factors is possible [Neeft 2003]. Table 5.5 shows the cesium release assuming a uniform distribution of cesium within the pellet in which background, fragmentation and shielding are taken into account.

Table 5.5 ^{137}Cs and ^{134}Cs release.

Pin	IMF	^{134}Cs / %	^{137}Cs / %
1	$\text{CeO}_{2-x} + \text{UO}_2$	5.9-6.5	1.2-4.1
18	$\text{Y}_2\text{O}_3 + \text{UO}_2$	< 0.1	< 0.4
5	$\text{MgO} + \text{UO}_2$	< 0.1	< 0.6
7	$\text{MgO} + \text{UY}_6\text{O}_x$	< 0.1	< 0.7
9	$\text{MgAl}_2\text{O}_4 + \text{UO}_2$	< 0.1	< 0.1
11	$\text{MgAl}_2\text{O}_4 + \text{UO}_2$	0.4-0.6	< 1.4
13	$\text{MgAl}_2\text{O}_4 + \text{UY}_6\text{O}_x$	0.0-0.9	0.0-0.2
15	$\text{Y}_3\text{Al}_5\text{O}_{12} + \text{UO}_2$	0.8-1.0	< 1.5

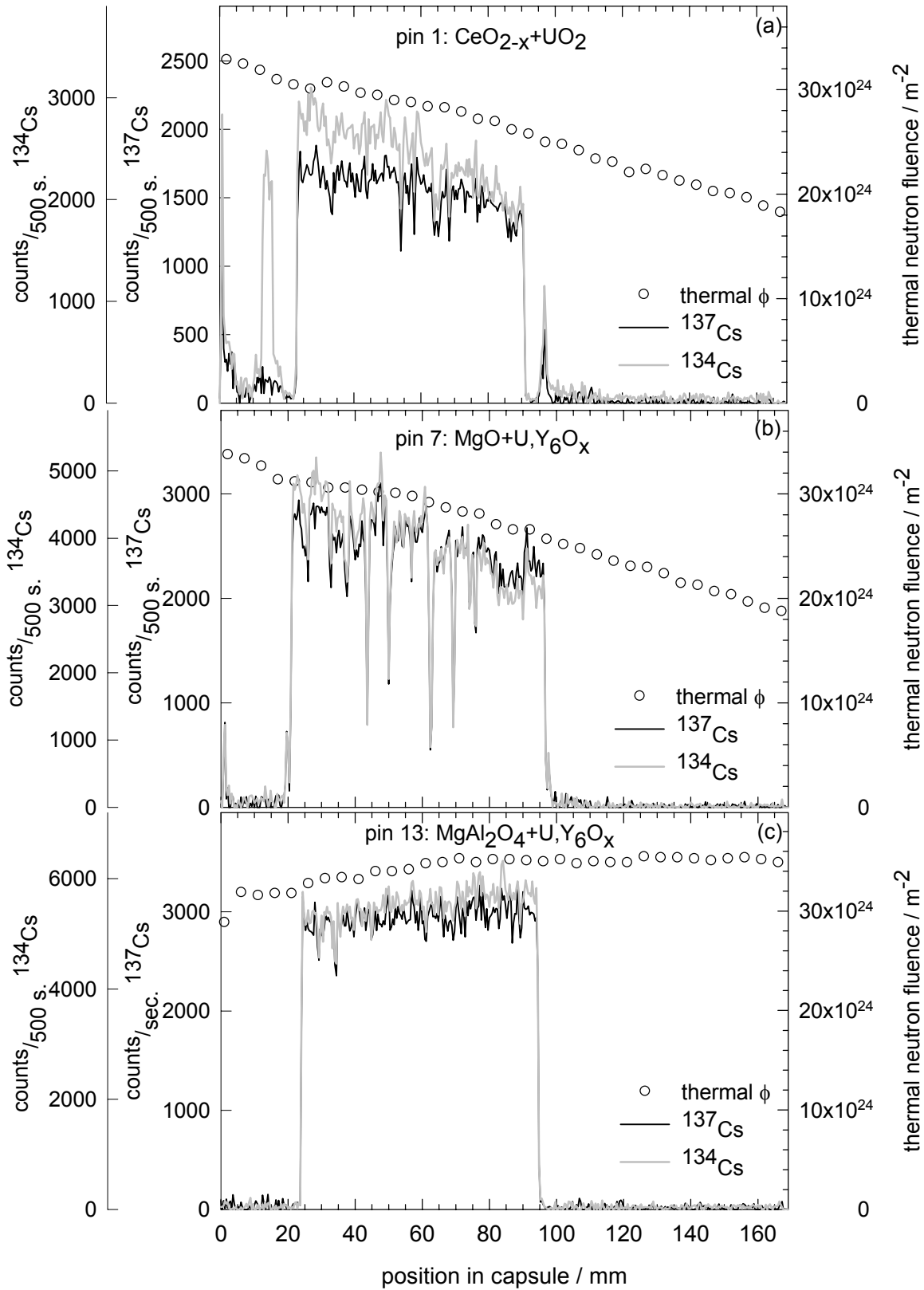


Figure 5.6 Count rate for ^{134}Cs and ^{137}Cs and thermal neutron fluence versus position of pin for (a) pin 1 (b) pin 7 and (c) pin 13.

5.7.3 Profilometry

None of the capsules showed deformation of the cladding after neutron irradiation, except pin 15 ($Y_3Al_5O_{12}+UO_2$). Figure 5.7 shows that the cladding deformed at the location of the fuel stack. The average diameters of the cladding are determined by an average of 3 measurements of the outer diameter at similarly axial positions. Especially, for the region of 97 to 120 mm for the cladding of the pin with $Y_3Al_5O_{12}+UO_2$ pellets, a slight bowing of capsule 15 resulted in an irregular average diameter in this region. Pin 16 with $Y_3Al_5O_{12}$ pellets without fissile phase showed no deformation of the cladding.

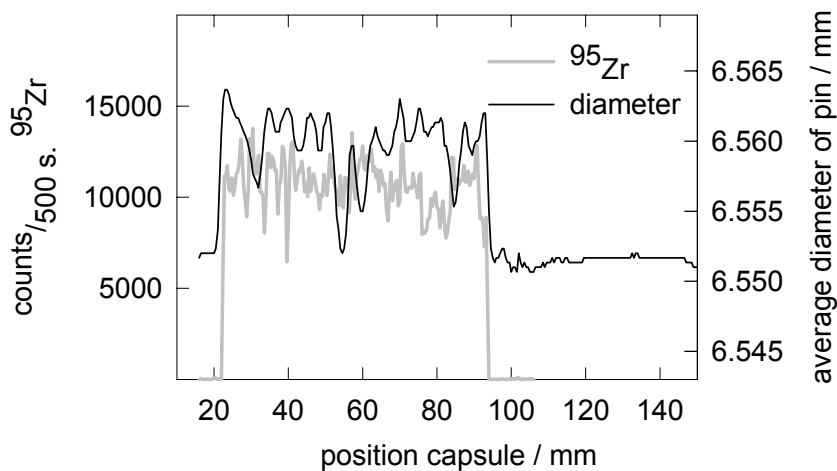


Figure 5.7 Profilometry and γ -spec signal of ^{95}Zr of pin 15 ($Y_3Al_5O_{12}+UO_2$).

5.7.4 Fission-gas release

Release of xenon and krypton from the fuel reduces the thermal conductivity of the helium filled gap and the pressure inside the pin may become larger than the pressure of water surrounding the pin. Both effects result in a higher temperature of the fuel, resulting in more release of xenon and krypton etc.. Inert matrix fuels should therefore have a small release of xenon and krypton during irradiation in order to keep a sufficiently low temperature. Table 5.6 shows the pressure and volume of the plenum at 298 K [Dassel 1999] and the composition of the gas from the plenum [Beemsterboer 2001] as measured after irradiation. It shows, as expected, fission-gases and helium but also air and CO_2 . The composition of gas from the plenums was measured twice for pins 7 and 9. The standard deviation for these volumes of gas, range from 0.01 to 0.66 vol% for these two pins, but especially for small volumes of gas, the relative standard deviation is large.

Figure 5.8 shows the pressure of the plenum versus several components of gas. The line drawn in the figures indicates the linear relation that would exist if the gases plotted in the figures are released during irradiation and the pressures in the pins prior to neutron irradiation were uniform.

Table 5.6 Pressure and volume of plenum and composition of gas.

Pin	P / bar at 298 K	V ^σ ml	He vol%	N ₂ vol%	O ₂ vol%	Ar vol%	CO ₂ vol%	Kr vol%	Xe vol%
1	1.56 ± 0.06	1.58	83.49	9.45	1.97	0.11	0.21	0.43	4.34
18	1.27 ± 0.06	1.33	87.87	5.21	1.25	0.33	0.17	0.46	4.70
5	1.39 ± 0.06	1.48	94.41	1.76	0.46	0.19	0.18	0.31	2.70
7	1.62 ± 0.06	1.82	79.90	5.22	0.35	0.04	12.78	0.21	1.51
		± 1 σ in vol%	0.37	0.40	0.01	0.00	0.66	0.01	0.10
9	1.30 ± 0.05	1.65	98.27	1.18	0.25	0.04	0.16	0.02	0.10
		± 1 σ in vol%	0.21	0.18	0.02	0.01	0.04	0.01	0.01
11	1.87 ± 0.08	1.43	68.53	0.00	0.10	0.05	0.48	2.80	28.04
13	1.39 ± 0.06	1.50	95.40	0.65	0.17	0.38	0.14	0.28	2.98
15	2.10 ± 0.10	1.28	65.44	0.00	0.16	0.39	0.52	3.20	30.30

^σ in volume 1 σ = 0.06 ml

In Figure 5.8 the fission gases versus the pressure of the plenum show approximately a linear relation. But, capsule 1, 18 and 7 remain outside this linear relation. Including CO₂ in the analysis lifts capsule 7 into the linear relation indicating that CO₂ is released during irradiation. The figure of fission gases + CO₂ + air lifts capsule 1 into the linear relation indicating that air is released during neutron irradiation. Incomplete evacuation of air present in the samples before welding of pins may have occurred that resulted in the observation of air especially for pin 1 that may have released during the neutron irradiation period. Possibly, open porosity was present in the pellets CeO_{2-x}+UO₂ (the density of the theoretical one is 0.87) by which air was incorporated during storage. Capsule 18 remains to fall out of a linear relation with the other capsules.

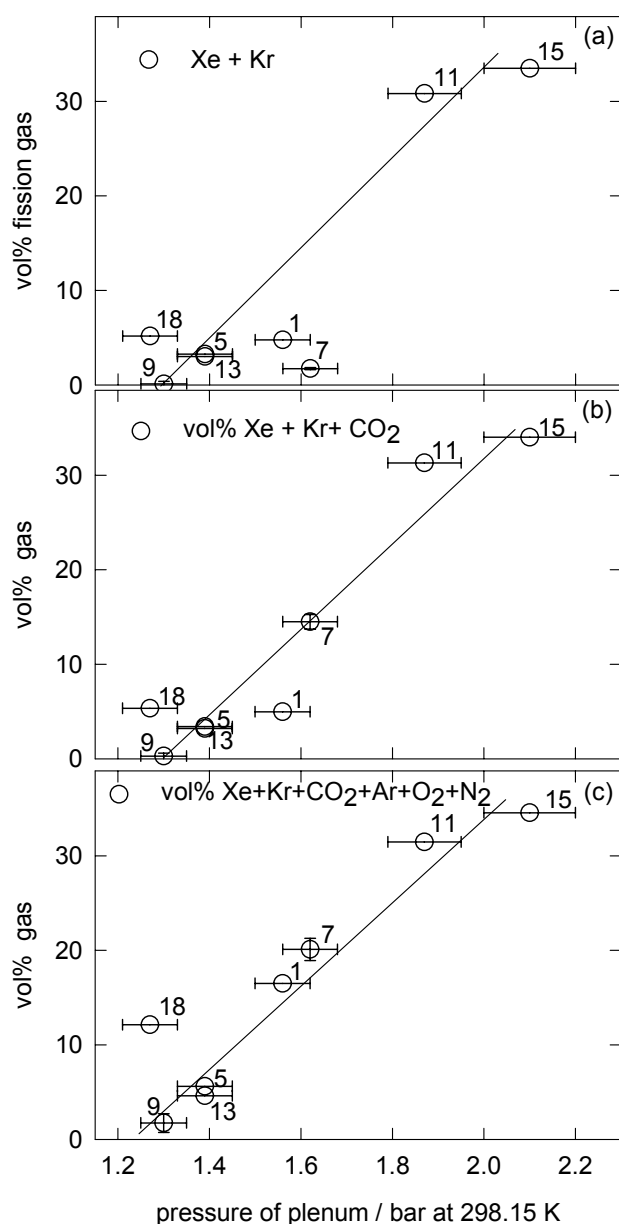


Figure 5.8. Pressure of plenum versus vol% (a) Xe+Kr, (b) Xe+Kr+CO₂ and (c) Xe+Kr+CO₂+Ar+O₂+N₂. Lines indicate linear relation if $P_{initial} = \text{uniform}$.

The amount of gas atoms from the gas in the plenum is determined using the ideal gas law. Release is determined by the amount of gas atoms measured in the plenum divided by the calculated amount of produced gas atoms after irradiation [Sciolla 2000]. Table 5.7 shows these results in fission-gas release and the amount of U atoms that is used for these computations. Table 5.7 shows that the fractional release of krypton, for all targets, is always slightly larger than xenon. The standard deviation of the fractional release is determined by the errors/standard deviations from the measurements of gas in plenum and the error in calculation of the produced gas atoms is set to 10%.

Table 5.7 Fission gas release of inert matrix fuels.

description targets for determination of produced fission gas atoms per pin			Produced atoms $\times 10^{18}$ per pin*		Fractional release / %		
Pin	IMF	U atoms $\times 10^{20}$	Kr	Xe	Xe/U $\times 100$	Kr	Xe
1	CeO _{2-x} + UO ₂	8.62	3.17	34.9	4.04	8.2 \pm 0.9	7.5 \pm 0.8
18	Y ₂ O ₃ + UO ₂	9.84	3.65	40.2	4.08	5.2 \pm 0.6	4.8 \pm 0.6
5	MgO + UO ₂	8.76	3.30	36.4	4.15	4.7 \pm 0.5	3.7 \pm 0.4
7	MgO + UY ₆ O _x	9.23	3.44	37.8	4.10	4.3 \pm 0.5	2.8 \pm 0.4
9	MgAl ₂ O ₄ + UO ₂	7.57	3.11	34.5	4.55	0.3 \pm 0.1	0.1 \pm 0.1
11	MgAl ₂ O ₄ + UO ₂	8.98	3.81	42.3	4.71	47.6 \pm 5.6	43.0 \pm 5.0
13	MgAl ₂ O ₄ + UY ₆ O _x	10.20	4.36	48.4	4.75	3.2 \pm 0.4	3.1 \pm 0.4
15	Y ₃ Al ₅ O ₁₂ + UO ₂	9.32	3.88	43.0	4.62	53.7 \pm 6.5	45.9 \pm 5.5

* uncertainty in calculation 10% to 15%

5.8 Post irradiation examination of pellets without uranium

The dimensions and weight of the pellets were measured after neutron irradiation. Table 5.8 shows the number of pellets that were used to determine the average height and diameter of the pellets after neutron irradiation. The change in dimension and weight of the pellets is determined from the average change of the individual pellets.

Table 5.8. Pellets of matrices: dimensions after irradiation and change in dimensions and weight.

Matrix	pin	N _p	\overline{D} mm	\overline{h} mm	$\frac{\Delta D}{D} \times 100$	$\frac{\Delta h}{h} \times 100$	$\frac{\Delta m}{m} \times 100$
CeO ₂	2	3	5.236 ± 0.012	10.265	0.343 ± 0.149	-0.094 ± 0.156	-0.741 ± 0.897
Y ₂ O ₃ ^e	4	17	5.377 ± 0.018	4.758	-0.035 ± 0.096	-0.350 ± 0.191	-0.203 ± 0.137
MgO ^{cp}	6	9	5.220 ± 0.032	5.139	0.006 ± 0.238	-1.680 ± 0.662	-1.263 ± 0.557
MgO	8 ^f	10	5.503 ± 0.021	4.603	0.107 ± 0.071	0.233 ± 0.287	-0.026 ± 0.022
MgAl ₂ O ₄ ^{cp}	10	16	5.242 ± 0.050	5.069	-0.092 ± 0.102	-0.422 ± 0.230	-0.079 ± 0.034
MgAl ₂ O ₄	12	15	5.148 ± 0.017	5.297	-1.064 ± 0.079	-1.532 ± 0.148	-0.315 ± 0.148
BaZrO ₃	14	0					
Y ₃ Al ₅ O ₁₂	16	12	5.298 ± 0.004	4.739	-0.324 ± 0.042	-0.417 ± 0.342	-0.473 ± 0.647

^{cp} coprecipitation, ± 1 σ

For most pins, the number of pellets that are used for the determination of the change in dimension is smaller than the number of pellet that is fabricated. This is due to the fact that some pellets were broken after neutron irradiation or could no longer be identified after neutron irradiation.

The diameter of pellets was measured at two sides of the pellet, each side three times in order to take into account the slightly conical shape [Neeft 2003]. “Two sides” means that each side (top or bottom of the pellet) was located in the sampling faces of the micrometer. For conic pellets, the largest diameter can be measured (the bottom of the pellet) but not the smallest diameter (the top of the pellet) since the sampling face can be stopped before it reaches the top of the pellet.

Pellets of BaZrO₃ could not be measured since only small fragments were left after irradiation. Table 5.10 shows the dimensional volume change of the uranium free matrices in order to compare them with the inert matrix fuels. Table 5.8 shows that the dimensional changes measured after neutron irradiation, taken into account mass loss, are negligible, except for MgAl₂O₄ (pin 12). All pellets have dark edges after neutron irradiation containing fission products. These pellets were therefore probably prepared in a stamp polluted with uranium. The dark colour is probably a large concentration of defects created by implantation. These edges of MgAl₂O₄ (pin 12) are quite large 100 μm to 480 μm. The notches in these edges observed after

^e only one side was measured for these pellets

^f for these 10 pellets both sides were measured, for the other 8 pellets (not included in Table) this was not performed.

measurement were created during measurement using the micrometer [Neeft 2003]. It seems that deformation of these dark edges during micrometer measurements caused the negatively geometrically volume change for MgAl₂O₄ (pin 12) instead of mass loss.

Roughly in the bulk of the pellets, no change in geometry or density of the pores could be observed by comparison of SEM-photos before and after neutron irradiation.

5.9 Post irradiation examination of IMF-pellets

5.9.1 Dimensional measurements

After irradiation, pellets are measured if possible using a micrometer, otherwise using profilometry^p, ceramography^c and gammaspectrometry^g. All micrometer measurements in diameter were performed three times at two sides of the pellet. For pin 11 fragmentation of pellets took place *during* the measurement of the diameter of three pellets using a micrometer. Measurements of the other pellets in pin 11 were not done in order to keep intact pellets for the preparation of ceramographic sections. The pellets in capsule 15 with Y₃Al₅O₁₂+UO₂ could not be removed from the capsule due to swelling of the pellets. The dimensional change in diameter of these pellets is determined from the outer diameter of the cladding and initial gap between pellet and inner diameter of the cladding; the reduction in thickness of the cladding is neglected.

The weight is not measured for these pellets and therefore it cannot be determined whether or not the negative changes in dimensions are due to fragmentation of the pellets or to shrinkage of the pellets. Determination of the change in height of the pellets using γ -scan data is less accurate than micrometer measurements. However, no fragmentation of pellets can take place during gammaspectrometry. Table 5.10 shows the fission stack length using γ -scan data performed 6 months after neutron irradiation from which the change in height is determined using the initial height as presented in Table 5.2. The geometrical volume change is determined using micrometer measurements unless stated otherwise.

Table 5.9 Pellets of matrices with fissile phase: dimensions after irradiation and change in dimensions.

Pin	Fuel	\bar{D} mm	\bar{h} mm	$\frac{\Delta D}{D} \times 100$	$\frac{\Delta h}{h} \times 100$
1	CeO _{2-x} +UO ₂	5.288 ± 0.020 ³	9.502 ³	-1.196 ± 0.647	-15.991 ± 8.009
5	MgO+UO ₂	5.284 ± 0.030 ¹⁴	4.753 ¹²	0.444 ± 0.388	0.054 ± 0.587
7	MgO+UY ₆ O _x	5.112 ± 0.169 ¹⁰	6.123 ⁹	0.045 ± 0.522	-0.395 ± 0.378
9	MgAl ₂ O ₄ +UO ₂	5.072 ± 0.079 ⁶	5.892 ⁶	0.068 ± 0.480	-0.963 ± 0.337
11	MgAl ₂ O ₄ +UO ₂	5.217 ^c	6.106 ⁷	0.69 ± 2.5 ^c	5.085 ± 0.598
13	MgAl ₂ O ₄ + UY ₆ O _x	5.264 ± 0.010 ¹²	5.439 ¹²	1.167 ± 0.238	0.547 ± 0.293
15	Y ₃ Al ₅ O ₁₂ +UO ₂	-	-	4.996 ± 0.378 ^p	
18	Y ₂ O ₃ +UO ₂	5.334 ± 0.010 ⁸	4.792 ⁸	-0.062 ± 0.103	-1.267 ± 0.378

numbers in superscript refer to the number of pellets measured using a micrometer,

^c ceramography, ^p profilometry, all values ± 1 σ

Table 5.10 Geometrical volume change and fission stack length using γ -scan.

Matrix	$\frac{\Delta V^{\text{dim}}}{V} \times 100$	Fuel	$\sum h$ mm	$\frac{\Delta \sum h}{h} \times 100$	$\frac{\Delta V^{\text{dim}}}{V} \times 100^*$
CeO ₂	0.59 ± 0.14	CeO _{2-x} +UO ₂	67.67	-2.5 ± 0.8	-4.9 ± 1.5 ^g
MgO ^{cp}	-1.67 ± 0.98	MgO ^{cp} +UO ₂	71.90	2.1 ± 0.8	0.94 ± 0.97
MgO	0.45 ± 0.22	MgO+UY ₆ O _x ^{cp}	76.38	0.8 ± 0.8	-0.30 ± 1.11
MgAl ₂ O ₄ ^{cp}	-0.61 ± 0.27	{MgAl ₂ O ₄ +UO ₂ } ^{cp}	66.92	-1.5 ± 0.8	-0.83 ± 1.02
MgAl ₂ O ₄	-3.62 ± 0.20	MgAl ₂ O ₄ +UO ₂	72.19	4.0 ± 0.8	6.5 ± 5.0 ^c
		MgAl ₂ O ₄ + UY ₆ O _x ^{cp}	72.09	2.5 ± 0.8	2.88 ± 0.56
Y ₃ Al ₅ O ₁₂	-1.06 ± 0.29	Y ₃ Al ₅ O ₁₂ +UO ₂	71.12	0.5 ± 0.8	10.5 ± 1.1 ^{g,p}
Y ₂ O ₃	-0.42 ± 0.26	Y ₂ O ₃ +UO ₂	73.31	0.7 ± 0.8	-1.39 ± 0.43

* $\frac{\Delta V}{V} = 2 \frac{\Delta D}{D} + \frac{\Delta h}{h}$, all values ± 1σ, ^g gammaspectrometry, ^c ceramography, ^p profilometry.

Table 5.10 shows that pellets from pin 1 and 9 both have a negative change in height, but the -16% in Table 5.9 for CeO_{2-x} + UO₂ is rather probably due to fragmentation. The measured increase in height for capsule 5, 13 and 18 is due to the presence of gaps between the encapsulated pellets, these can clearly be viewed in Figure 5.5. The larger change in height as measured in capsule 11 by micrometer measurements in comparison with gammaspectroscopy measurements could be due to the larger change in height of pellets that could be measured using a micrometer or could be due to the suppressing force of the spring that is present during gammaspectrometry measurements but this suppressing force was absent during micrometer measurements. The result obtained from gammaspectrometry includes all pellets. Table 5.10 shows that pellets with fissile phase for pin 1, 11 and 15 have a significantly differently volume change compared to pellets without fissile phase.

5.9.2 Ceramography and α and β,γ -autoradiographs of IMF

Before neutron irradiation, one individual pellet of each series was embedded in Hysol (see paragraph 5.3.2). After neutron irradiation, two individual pellets of each series were embedded in Hysol and both, an axial and a transverse ceramographic section were made of these samples. Figure 5.9 to Figure 5.17 shows a selection of the ceramographic photographs and the α and β,γ -autoradiographs of all samples. Figure 5.15f shows that pellets prepared from a co-precipitate MgAl₂O₄ + UO₂ (pin 9) are conical shaped, all other pellets are more cylindrical shaped as can be observed from the axial sections. For this (sub)micro-dispersed fuel (pin 9), also a SEM image before irradiation is shown.

Cracks in fissile inclusions and matrix

Pellets with MgO show no axial cracks. Pellets with MgAl₂O₄ and Y₂O₃ show a single axial crack through the entire pellet. The transverse sections of IMF with CeO_{2-x} and Y₃Al₅O₁₂ show several axial cracks. These axial cracks run through the inclusions and are presumably caused by the thermal stresses in the pellet due to the radial temperature gradient, similarly as

described for axial cracks in UO_2 observed after neutron irradiation [Gittus 1972].

5.9.2.1 Matrix in macro dispersed fuels

Cracks in matrices

Cracks from UO_2 inclusion to UO_2 inclusion that do not run through the UO_2 inclusion are observed in the IMF $\text{MgO}+\text{UO}_2$, $\text{MgAl}_2\text{O}_4+\text{UO}_2$, rarely in $\text{Y}_2\text{O}_3+\text{UO}_2$ and solely in the core to half the radius for the pellet $\text{Y}_3\text{Al}_5\text{O}_{12}+\text{UO}_2$. These cracks are less visible in the matrix $\text{Y}_3\text{Al}_5\text{O}_{12}$ from about half the radius of the pellet $\text{Y}_3\text{Al}_5\text{O}_{12}+\text{UO}_2$ to the edge. The number of cracks, perpendicular to the height of the pellet, is 15 to 17 cracks for the ceramic composite $\text{MgAl}_2\text{O}_4 + \text{UO}_2$ (pin 11) and 10 cracks for $\text{MgO} + \text{UO}_2$. The width of these cracks can be quite large as for example Figure 5.12d clearly shows. The general crack width is 4.2-4.3 μm for $\text{MgO}+\text{UO}_2$ and 16.1-17.9 μm for $\text{MgAl}_2\text{O}_4+\text{UO}_2$ [Neeft 2003]. These cracks from UO_2 inclusion to UO_2 inclusion could not be observed in the matrix CeO_{2-x} .

Cracks from UY_6O_x inclusion to UY_6O_x inclusion were present before and after irradiation in $\text{MgO}+\text{UY}_6\text{O}_x$. Cracks from UY_6O_x inclusion to UY_6O_x inclusion that do not run through the inclusions are observed in $\text{UY}_6\text{O}_x+\text{MgAl}_2\text{O}_4$ solely after irradiation.

Figure 5.10e and Figure 5.12f of UO_2 inclusions embedded in the ceramic matrices MgAl_2O_4 and $\text{Y}_3\text{Al}_5\text{O}_{12}$ clearly show that cracks are positioned some distance away from the interface between the ceramic matrix and UO_2 . Table 5.11 shows this Distance from the Interface between the inclusion and Matrix: DIM.

Matrix surrounding fissile inclusions

Figure 5.10e shows that in the core to half the radius of the pellet, micron-sized bubbles with a radius of about 1 to 10 μm are present in areas of the matrix $\text{Y}_3\text{Al}_5\text{O}_{12}$ that surround the UO_2 inclusion. In the rest of this pellet near and in the UO_2 inclusions, extremely large bubbles can be observed that can be as large as 75 μm .

No micron-sized bubbles could be observed in the other matrices: MgAl_2O_4 , Y_2O_3 and CeO_{2-x} . Figure 5.11f shows outbreak of the matrix MgO concentrated at areas that surround the UO_2 inclusion. This outbreak is more visible in the axial section of the pellet than in the transverse section of the pellet. Both IMF: $\text{MgO}+\text{UO}_2$ and $\text{MgO}+\text{UY}_6\text{O}_x$ show more outbreak in the matrix MgO after irradiation than before irradiation.

5.9.2.2 Fissile phase in macro-dispersed fuel

Porosity of UO_2 inclusions

The porosity of the UO_2 inclusions is measured using optically microscopy photos, except for the UO_2 inclusions embedded in MgO and Y_2O_3 . The distribution in pore size and density, could only be viewed in these UO_2 inclusions embedded in MgO and Y_2O_3 with electron absorption images with a larger magnification factor than was able with optical microscopy. All UO_2 inclusions show a high density of pores after neutron irradiation. Six

images of UO₂ inclusions were made of each series of pellets. In the axial sections, many UO₂ inclusions show pore alignment. Large almost ellipsoidal pores in the UO₂ inclusions are aligned *parallel* to the height of the pellets for UO₂ inclusions embedded in Y₂O₃ and in Y₃Al₅O₁₂. These large ellipsoidal pores in UO₂ inclusions are aligned *perpendicular* to the height of the pellet for UO₂ inclusions embedded in MgAl₂O₄. These large ellipsoidal pores have a significant impact on the porosity. From the image analysis performed on optically microscopy photos, no difference could be observed between porosity in the UO₂ inclusions measured at the edge of the pellet and at the core of the pellet for all IMF studied. Table 5.11 shows the porosity of these UO₂ inclusions. The distribution in size of pores can be viewed in Neft [Neft 2003].

Table 5.11 Porosity of the UO₂ inclusions and DIM.

UO ₂ embedded in matrix	FIMA %	C/E	N	S	Meas. area mm ²	porosity UO ₂ % range	porosity UO ₂ % average	DIM μm
CeO _{2-x}	17.1	C	2	T	0.061	35 to 42	32 ± 8	no cracks at UO ₂ inclusion
			3	T	0.010	21.5 to 34.6		
Y ₂ O ₃	17.2	E	5	T	0.018	14.0 to 39.9	27.3 ± 10.0	rare cracks at UO ₂ inclusion n.m.
MgO	17.5	E	4	T	0.003	11.9 to 13.3	12.4 ± 0.6	4.3
			A	5.9 to 7.2				
MgAl ₂ O ₄	19.7	C	2	T	0.055	32 to 37	39 ± 6	0 to 5.3
			2	A	0.074	40 to 46		2.1 to 8.9
Y ₃ Al ₅ O ₁₂	19.3	C	3	T	0.021	37 to 41	42 ± 4	21.9
			3	A	0.024	40 to 50		

Image analysis from ceramographic images (C) or electron absorption images (E), transverse section (T), axial section (A), ± 1σ.

The porosity of UO₂ inclusions in CeO_{2-x} and Y₂O₃ is similar (about 30%) and in UO₂ inclusions embedded in MgAl₂O₄ and Y₃Al₅O₁₂ have a porosity of about 40%. This high porosity is in good agreement with the high porosity observed in the high burn-up rim region of UO₂ pellets. After a burn-up of 170 MWd/kgU in the RIM region 50% porosity was observed in UO₂. [Wiesenack 2000]. The temperature conditions of the irradiated UO₂ in the present study are similar to those in the RIM-region.

The porosity of UO₂ inclusion in MgO is small in comparison with the other UO₂ inclusions at similar burn-up. The measured area of this inclusion is also quite small and therefore perhaps the observation of a large pore is missed.

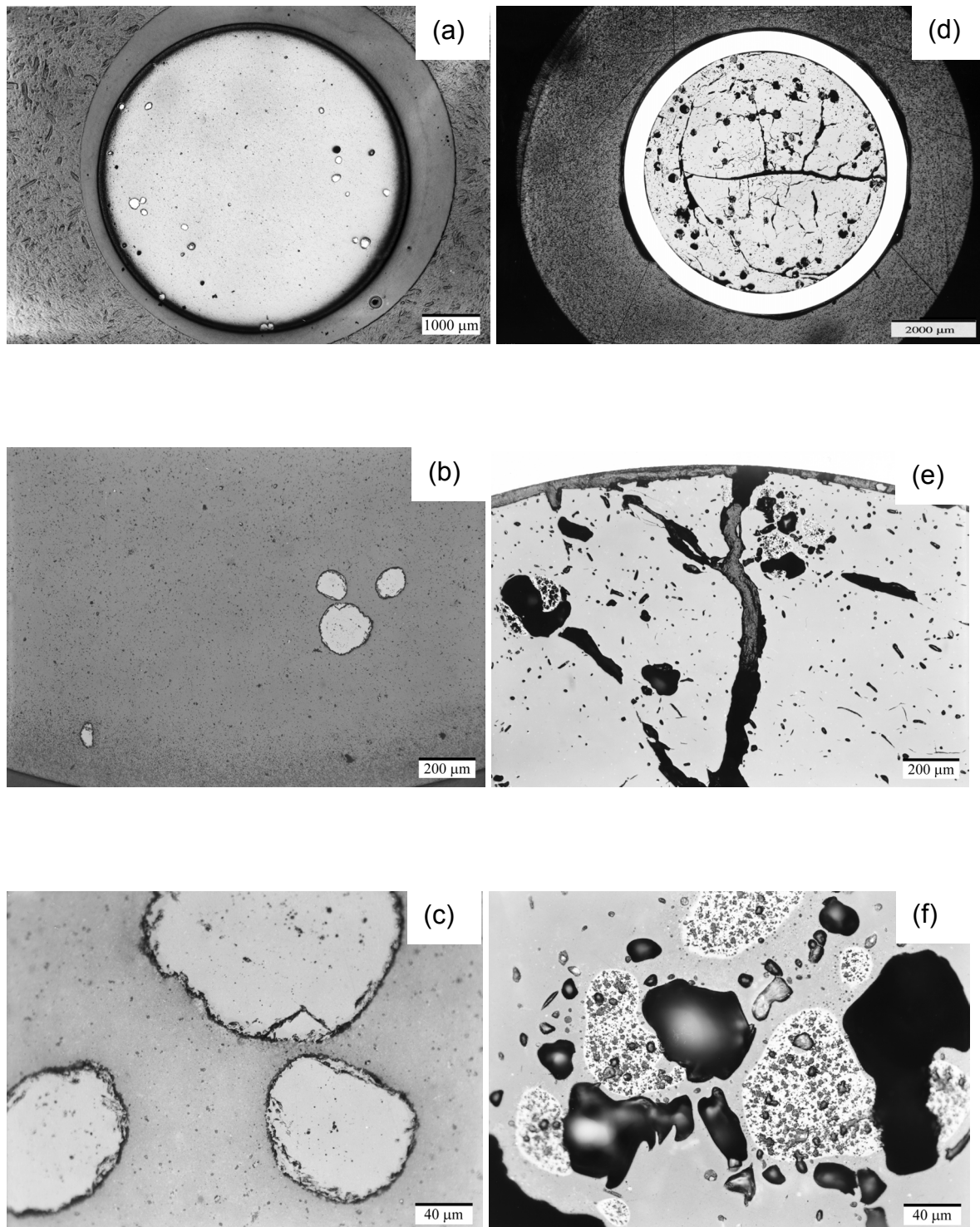


Figure.5.9 Transverse sections of (a-c) an unirradiated pellet containing $Y_3Al_5O_{12}+UO_2$ and (d-f) irradiated pellets of pin 15.

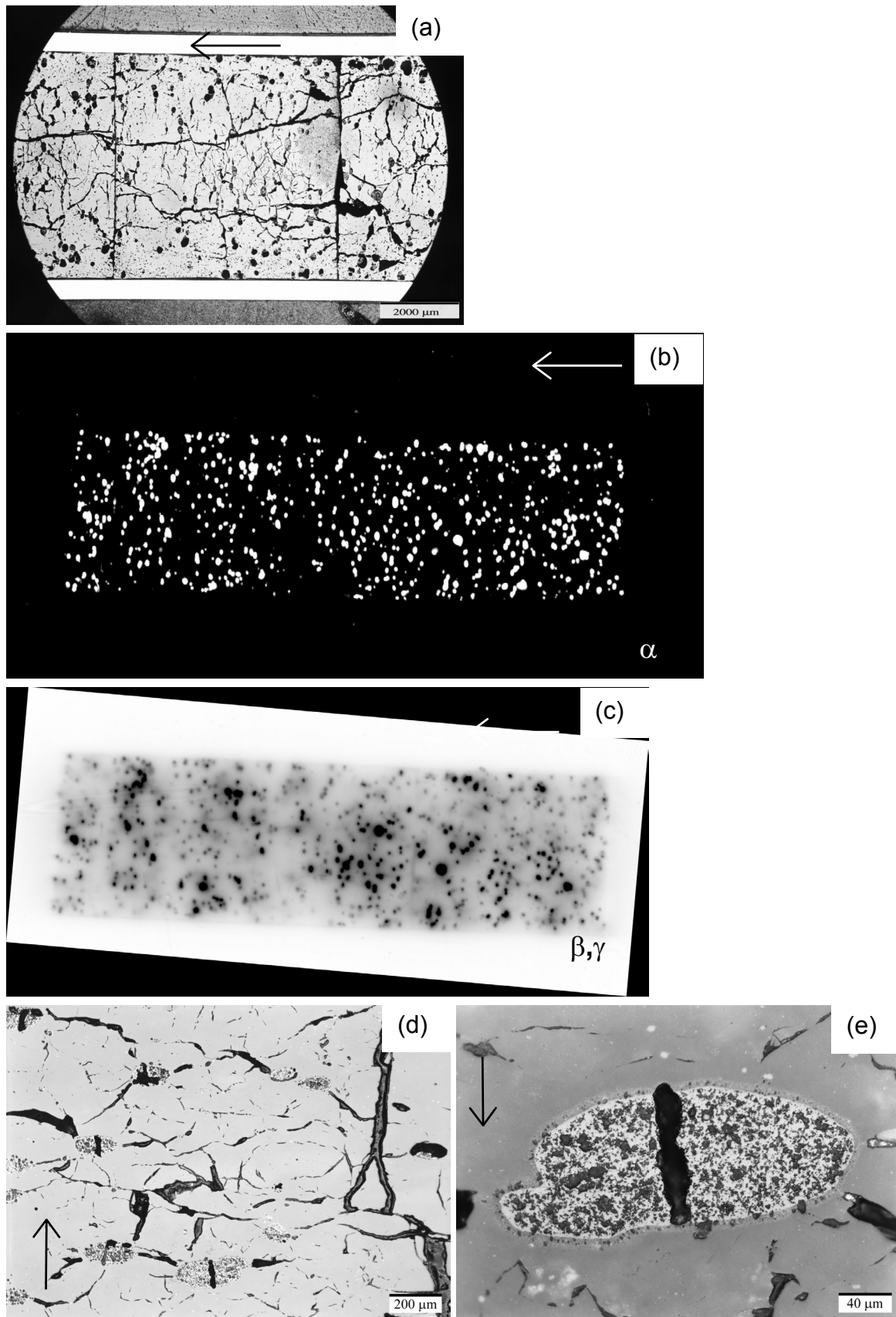


Figure 5.10 Axial section of irradiated pellet containing $Y_3Al_5O_{12} + UO_2$ of pin 15 (arrow: axial direction).

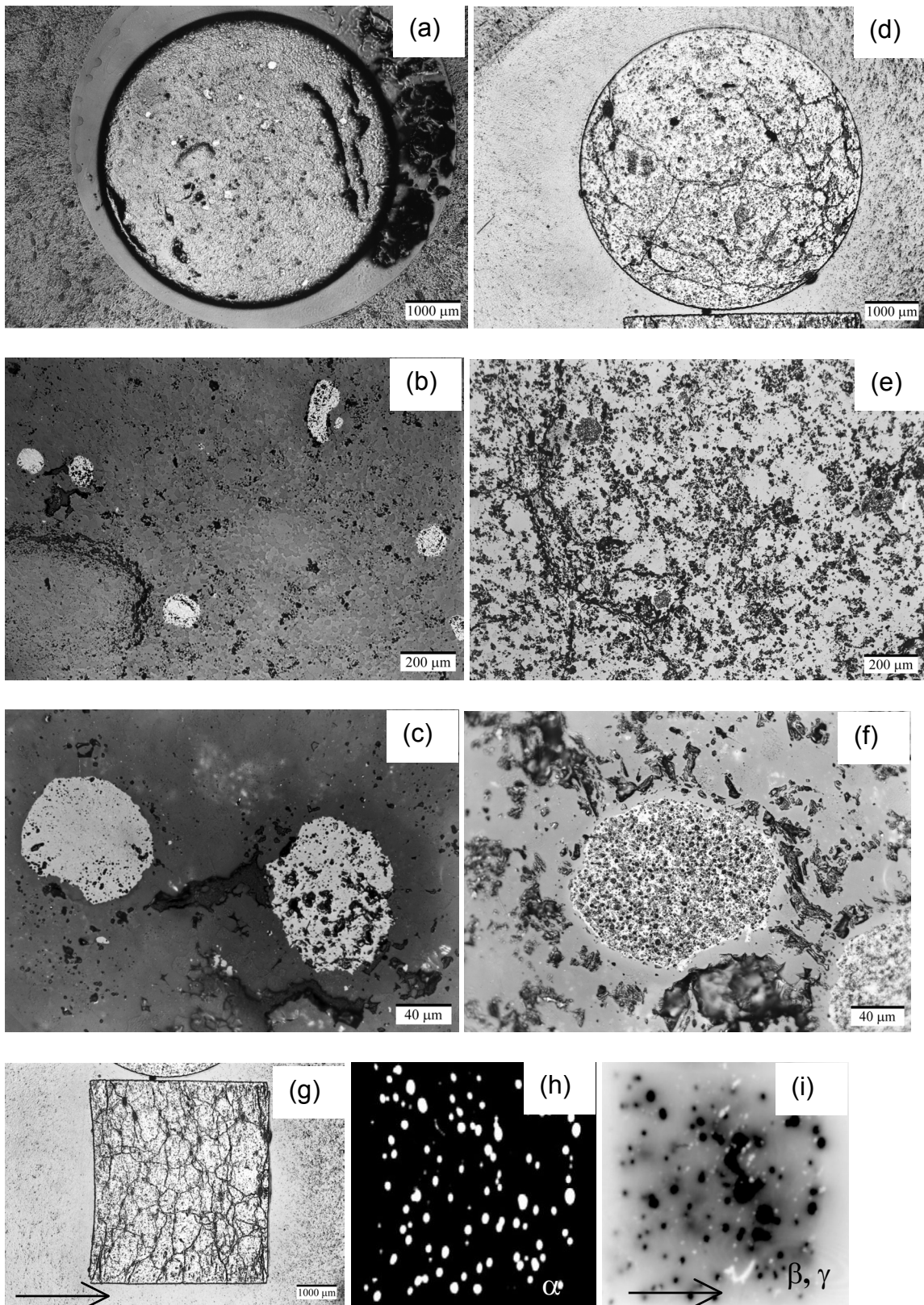


Figure 5.11 Transverse sections of (a-c) unirradiated pellet containing $MgO + UO_2$ and (d-f) irradiated pellet of pin 5. (g-i) Axial section of irradiated pellet of pin 5 (arrow: axial direction).

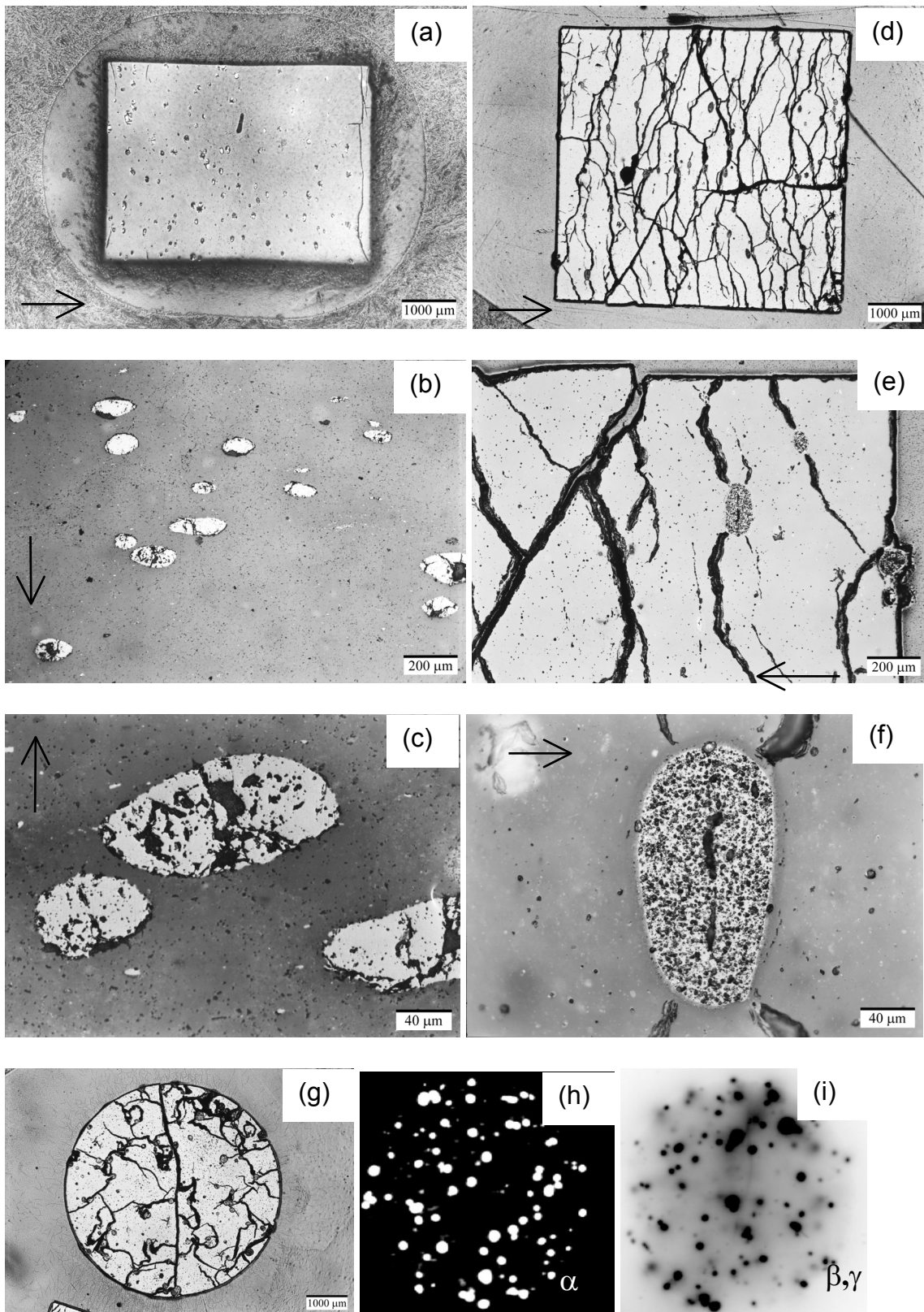


Figure 5.12 Axial sections of (a-c) an unirradiated pellet containing $MgAl_2O_4 + UO_2$ and (d-f) irradiated pellet of pin 11, (g-i) transverse section of an irradiated pellet of pin 11 (arrow: axial direction).

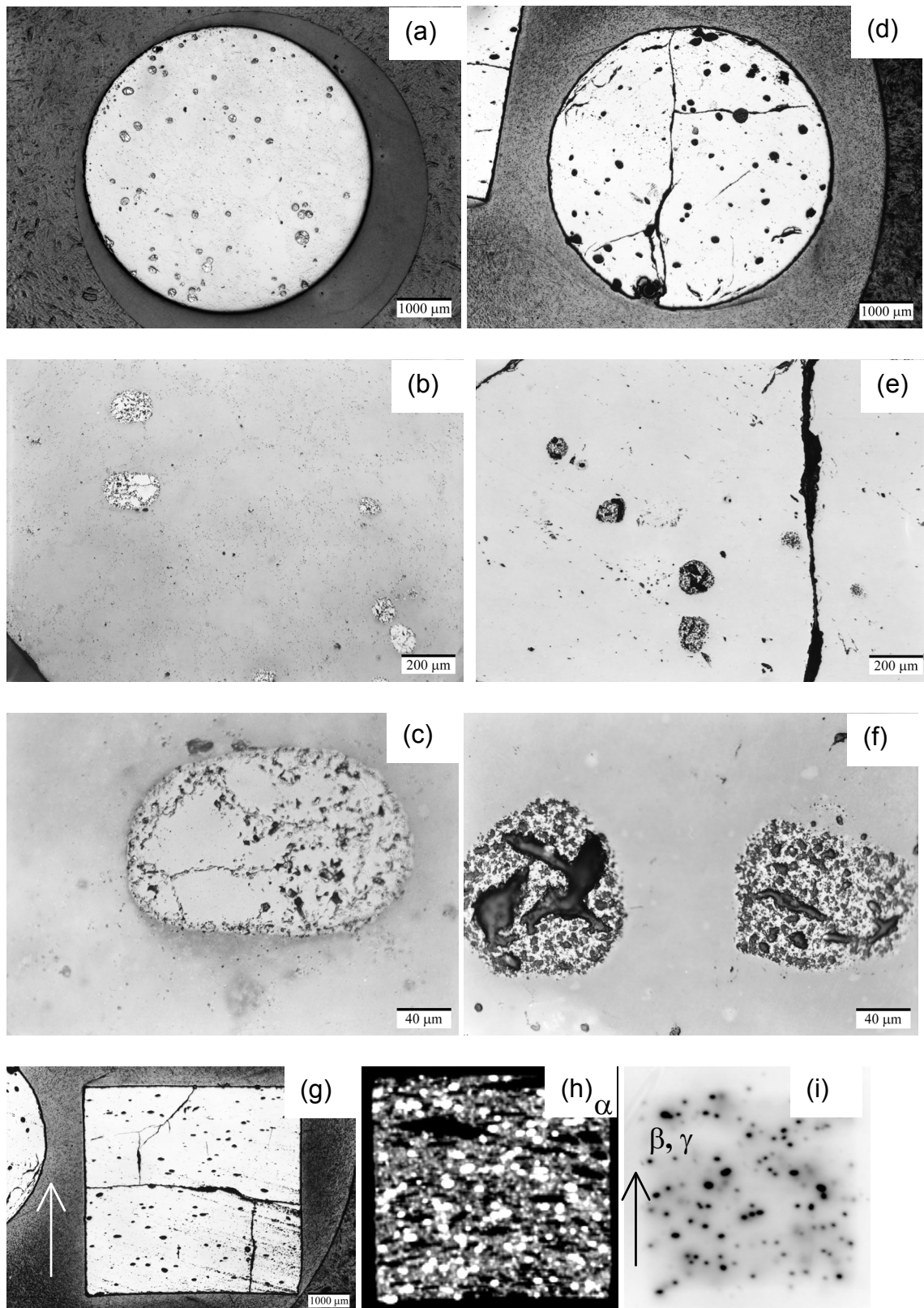


Figure 5.13 Transverse sections of (a-c) unirradiated pellet containing $Y_2O_3 + UO_2$ and (d-f) irradiated pellet from pin 18. (g-i) Axial section of irradiated pellet from pin 18 (arrow axial direction).

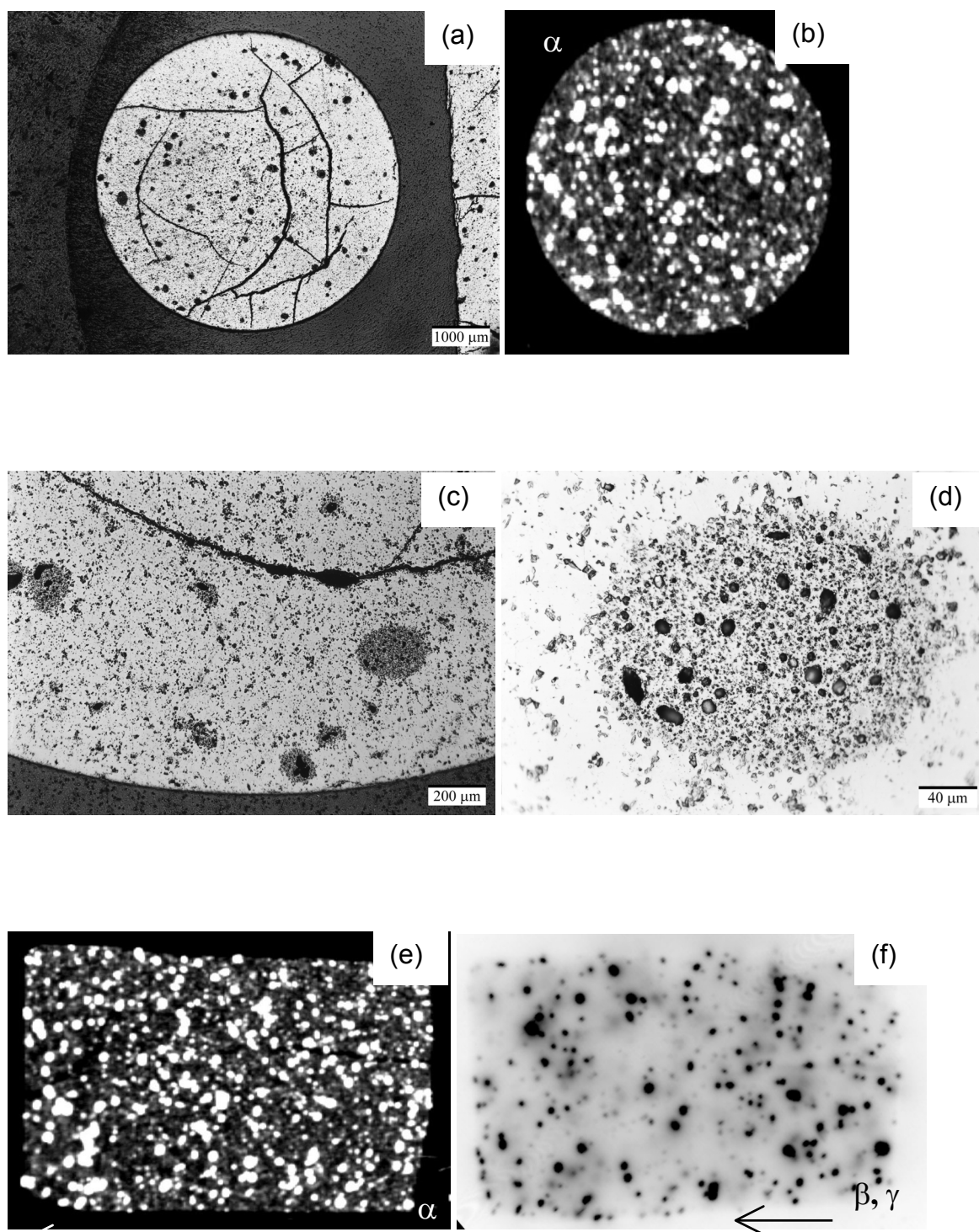


Figure 5.14 (a-d) Transverse section of irradiated pellet containing $CeO_{2-x} + UO_2$ from pin 1 and (e-f) axial section of irradiated pellet from pin 1 (arrow: axial direction).

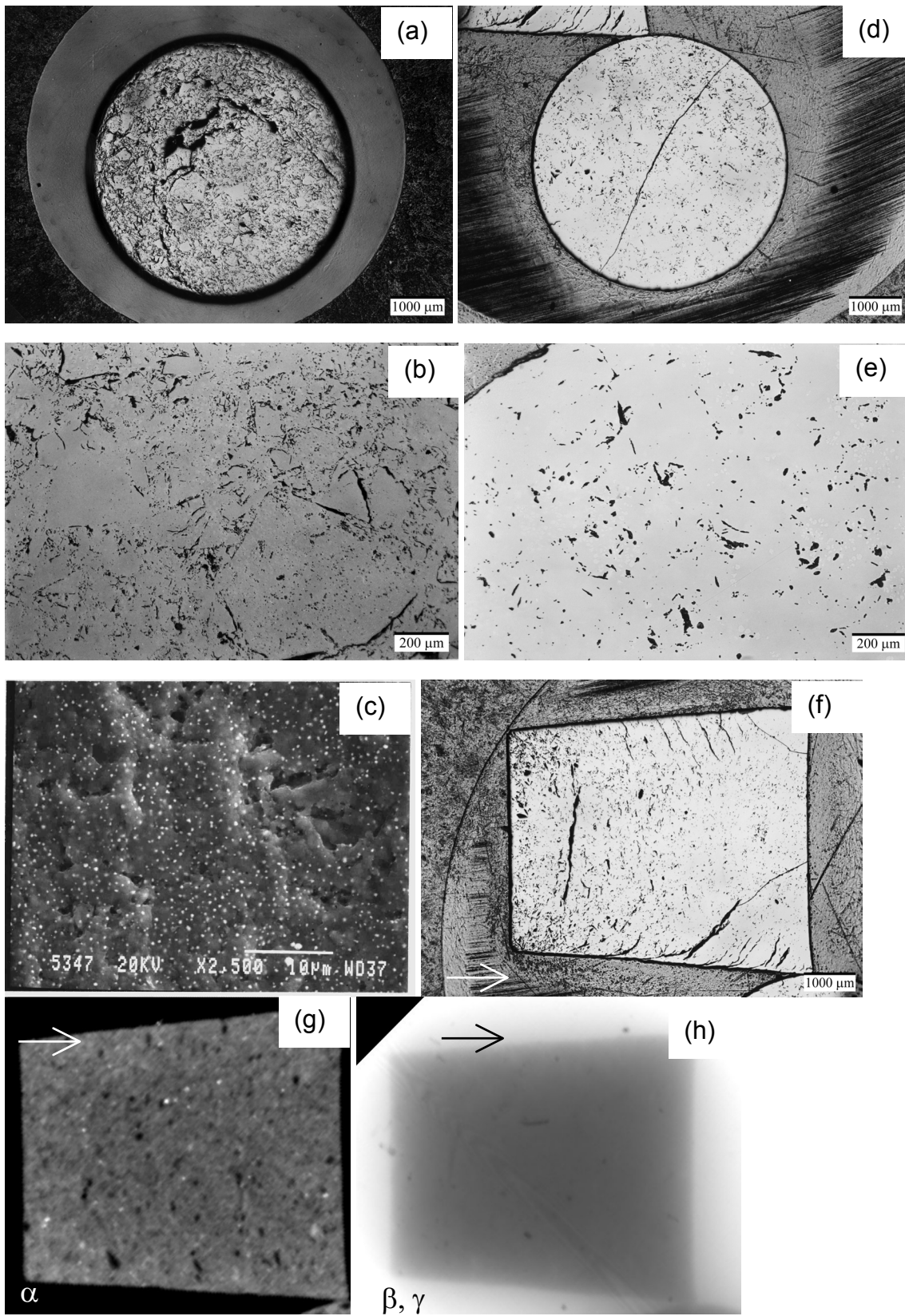


Figure 5.15 Transverse sections of (a-b) an unirradiated pellet containing $MgAl_2O_4 + UO_2$ and (d-e) irradiated pellet from pin 9. (c) SEM image of an unirradiated pellet containing $MgAl_2O_4 + UO_2$ and (g-h) axial section of irradiated pellet of pin 9 (arrow axial direction).

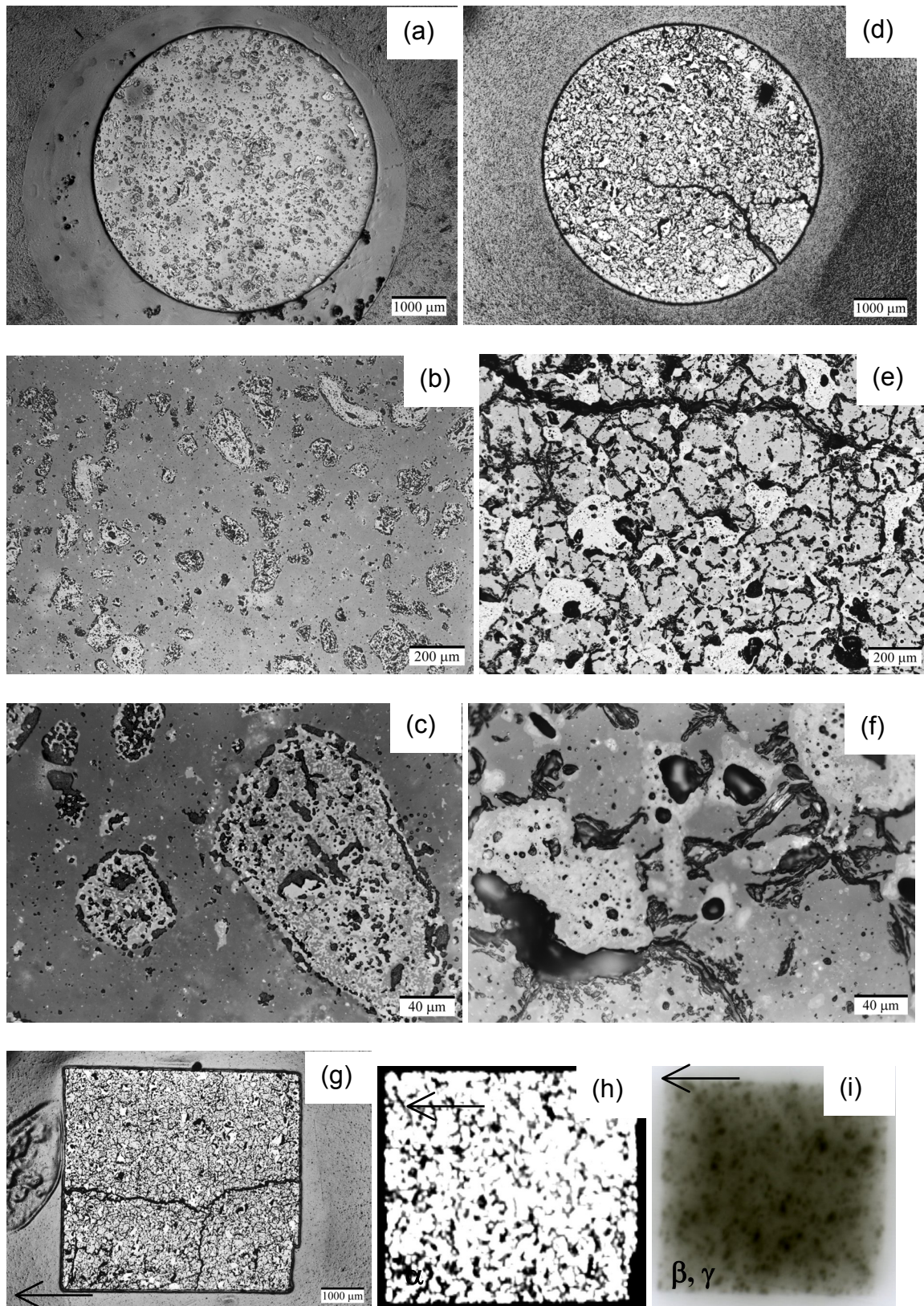


Figure 5.16 Transverse sections of (a-c) an unirradiated pellet containing $MgAl_2O_4 + UY_6O_x$ and (d-f) irradiated pellet of pin 13. (g-i) Axial section of irradiated pellet of pin 13 (arrow: axial direction).

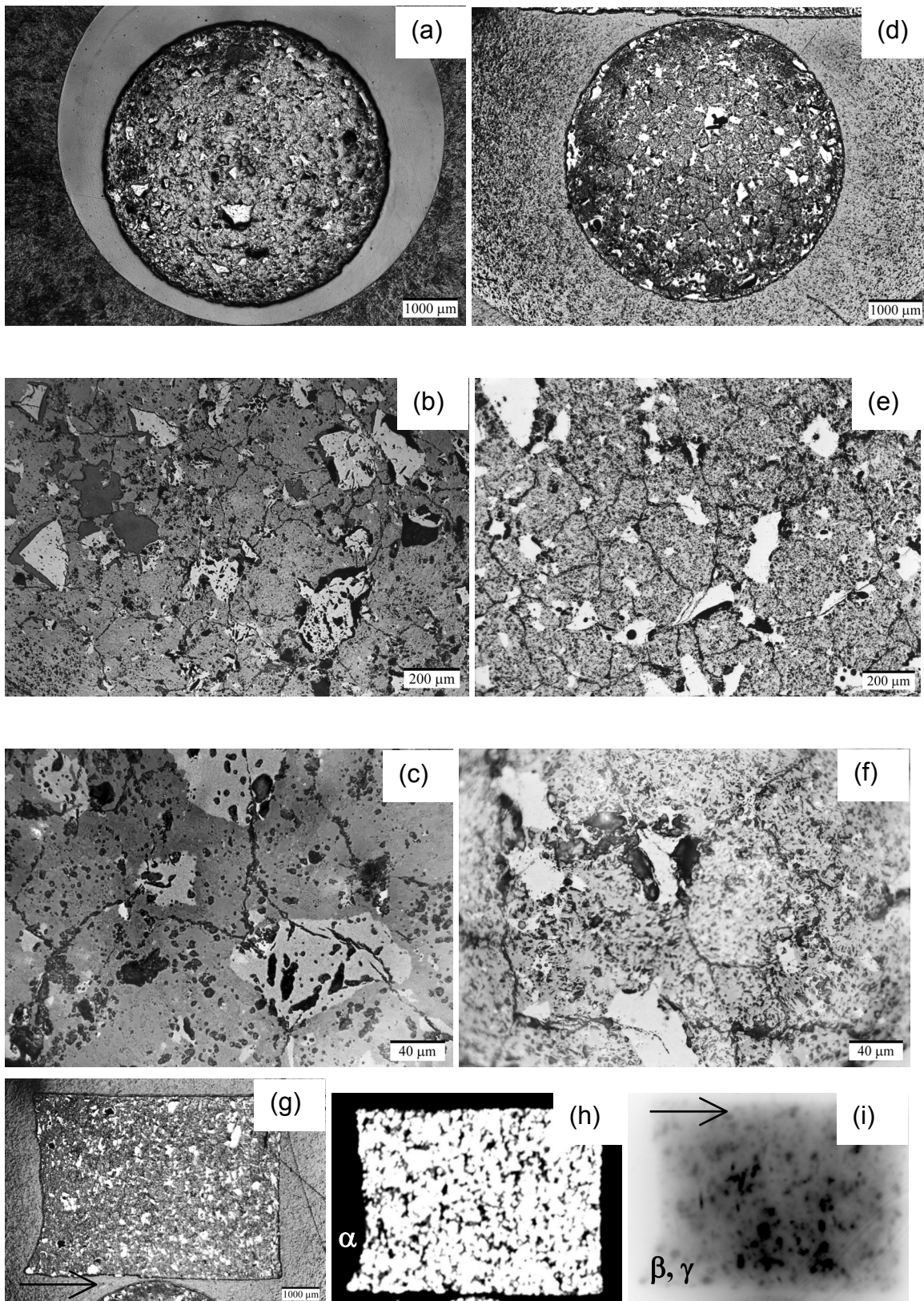


Figure 5.17 Transverse sections of (a-c) unirradiated pellet containing $\text{MgO} + \text{U}, \text{Y}_6\text{O}_x$ and (d-f) irradiated pellet of pin 7. (g-h) Axial section of irradiated pellet of pin 7, (arrow: axial direction).

UY₆O_x inclusions

The porosity in these UY₆O_x inclusions embedded in MgO reduced from 12% before irradiation to 7% after irradiation. The porosity in UY₆O_x inclusions embedded in MgAl₂O₄ reduced from 20% before irradiation to 12% after irradiation. The dimensional change of UY₆O_x inclusions embedded in MgAl₂O₄ is larger than for these inclusions embedded in MgO [Neeft 2003].

Possibly an yttrium-aluminium compound was formed during sintering of the pellets that exhibits in-pile swelling when implanted with fission products, like Y₃Al₅O₁₂ as observed in the fuel Y₃Al₅O₁₂+UO₂. Paragraph 5.9.3.1 shows that pores are mainly present in the phase that contains both yttrium and aluminium. Also the slight difference in burn-up may possibly have resulted in the larger dimensional swelling of these inclusions embedded in MgAl₂O₄ in comparison with the ones embedded in MgO. That the swelling of the UY₆O_x inclusions embedded in MgO cannot be observed in the dimensional change of the pellet in Table 5.10 may be due to the presence of large pores near these inclusions before irradiation (see paragraph 5.3.2.1). This porosity allowed swelling of these fissile inclusions of about 10 vol% without causing a dimensional change of the pellet.

α- and β,γ autoradiography

The α-autoradiographs of UO₂ inclusions embedded in the matrices: MgO, MgAl₂O₄ and Y₃Al₅O₁₂, show α-emission from UO₂ inclusions that are nearly all visible in the ceramographic sections. The α-autoradiographs of UO₂ inclusions embedded in the matrices: Y₂O₃ and CeO_{2-x} show α-emission from UO₂ inclusions but also in the vicinity of the UO₂ inclusions, that is the grey area. The α-autoradiographs of MgAl₂O₄+UY₆O_x and MgO+UY₆O_x show α-emission from the whole area of the pellet.

The grey area as observed for the α-autoradiographs of UO₂+CeO_{2-x} and UO₂+Y₂O₃ may be due to the chemical interaction between the matrix and UO₂, as observed in the X-ray diffraction after sintering of these fuels. However, this hypothesis can only be confirmed by performing an α-autoradiograph before irradiation from these ceramic composites.

The time of irradiation for the fabrication of the β,γ-autoradiographs is not uniform for all sections made of the fuels as it is for the α-autoradiographs. This is done to prevent burning of a hole in the film by a large concentration of β,γ emitting fission products.

The β,γ-autoradiograph of UO₂ inclusions embedded in the matrices: MgO, MgAl₂O₄, Y₂O₃, CeO_{2-x} and Y₃Al₅O₁₂, show mainly β,γ-emission near/from UO₂ inclusions. The difference between α-autoradiographs with also α-emission outside the UO₂ inclusions and β,γ-autoradiograph with nearly no β,γ emission visible outside the UO₂ inclusion for IMF CeO_{2-x}+UO₂ and Y₂O₃+UO₂ is due to irradiation time of the autoradiographs. β,γ emitting fission products are present outside the UO₂ inclusions but their concentration with respect to the UO₂ inclusions is too small to be visible. The migration of fission products in the matrix seems to be limited. In fact, line electron microprobe measurements from the UO₂ inclusions to the surrounding matrix show that the fission products are located within the fission fragment range (see paragraph 5.9.3.1). The β,γ-autoradiographs of UY₆O_x inclusions embedded in the

matrices: MgO and MgAl₂O₄ show vaguely some locations with a larger intensity of β/γ emitting fission products.

5.9.2.3 Micro-dispersed fuel

For the micro-dispersed fuel MgAl₂O₄+UO₂ from pin 9, image analysis was performed on the ceramographic sections. The porosity using both sections becomes 4.25%±0.69% after irradiation. This is smaller than the 7.6% measured before neutron irradiation (see paragraph 5.3.2.2).

The overlap in area's of α-emission from the (sub)micron sized UO₂ inclusions in MgAl₂O₄ resulted in an almost uniform area of α intensity. The β,γ-autoradiograph of the micro-dispersed fuel MgAl₂O₄+UO₂ shows a uniform distribution of β/γ emitting fission products.

5.9.3 EPMA

Electron Probe Micro Analysis (EPMA) was performed on the irradiated IMF.

5.9.3.1 Macro-dispersed fuel

Line microprobe measurements were performed from the large fissile inclusions into the matrix. Figure 5.18 shows the images as measured after irradiation. Figure 5.18 shows that the fuels MgO+UO₂ (b), MgAl₂O₄+UO₂ (c) and Y₃Al₅O₁₂+UO₂ (d) have a range of about 5 μm in which both the metal atoms of the inert matrix and uranium are measured. During EPMA measurements scattering of electrons in the implanted material takes place. The scattering causes a lateral resolution of about 5 μm for these fuels which is inherent to this technique. The range in which both metal atoms from the matrix and uranium are measured is in the order of 15 μm to 20 μm in Figure 5.18a and e for respectively CeO_{2-x}+UO₂ and Y₂O₃+UO₂. This range is too large to be due to this scattering. This is due to the formation of solid solutions as observed with X-ray diffraction prior to neutron irradiation (see paragraph 5.3.1). The large scattering in wt% of the UO₂ phase in comparison with the inert matrix phase is caused by the irregular distribution of pores. The drop for Mg in the implantation zone of MgO in Figure 5.18b is due to outbreak of the matrix.

Figure 5.18f-i shows the fission product distribution with the same uranium profile as in Figure 5.18a-e. Nd and Zr are fission products that are immobile in UO₂. These elements are also measured in the matrix. This profile is due to implantation of fission products from the UO₂ inclusion into the matrix during irradiation of these IMF. Figure 5.18 shows that the fission fragment recoil range of the immobile fission products in the matrix do not differ from fission products Cs and Xe. These fission products are measured to be mobile in UO₂ at sufficiently high irradiation temperatures. Thermally induced migration of Cs and Xe in the matrices (outside the implantation zones) did not occur. The relatively low concentration of Xe in UO₂ in comparison in the implantation profile at the interface between matrix and UO₂ is due the presence of Xe merely in the pores of UO₂, possibly fission-gas release from the UO₂ phase and absence of pores in the matrix phase. Pores are cut open during preparation of the ceramographic sections and Xe is lost.

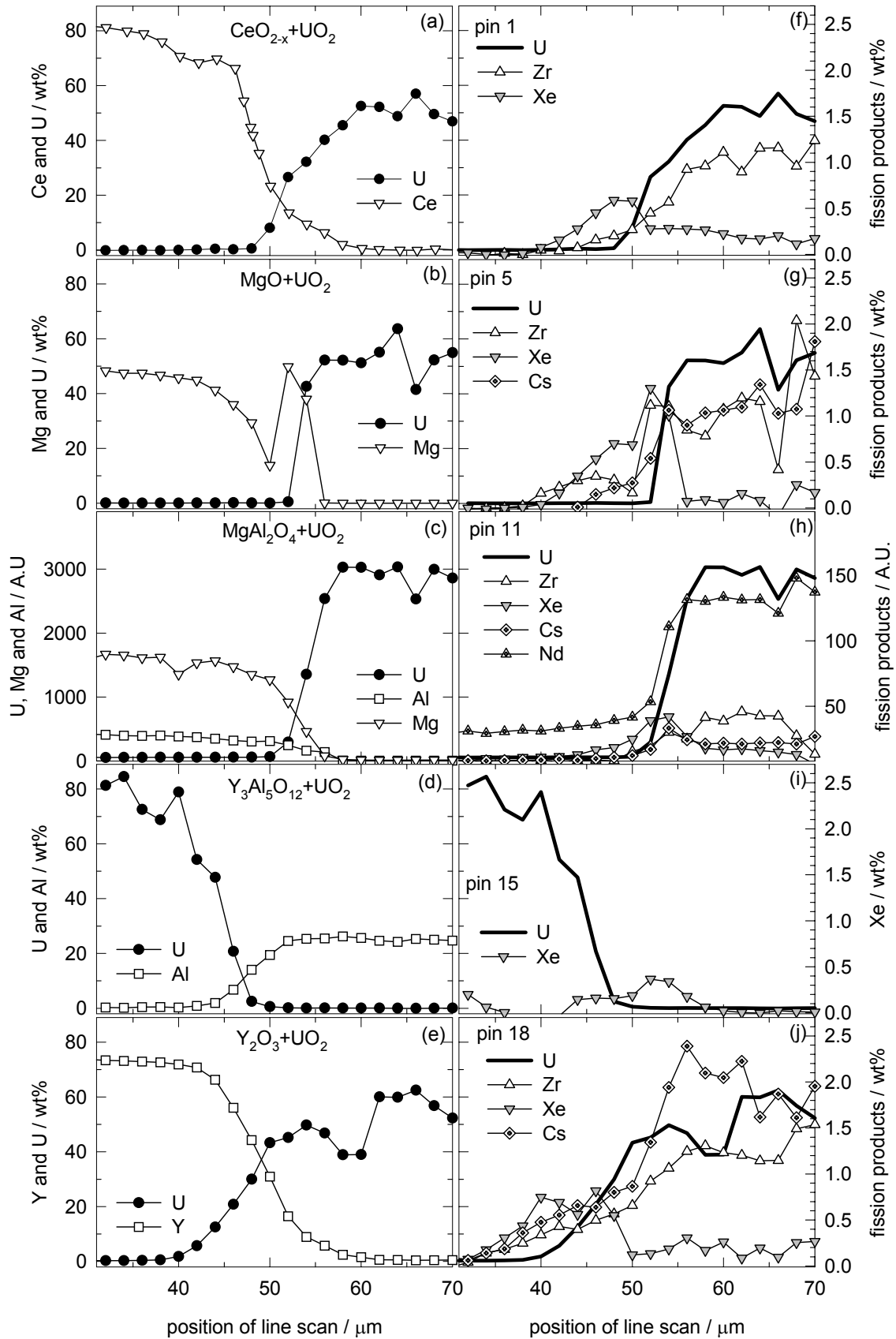


Figure 5.18 EPMA of macro-dispersed fuels after irradiation (a-e) of elements that were also present before neutron irradiation and (f-j) of U and fission products.

Figure 5.19 shows a calculated implantation profile that occurs during irradiation of IMF using SRIM [Ziegler et al. 2002]. SRIM is a computer program in which the implantation range in materials can be calculated. The diameter of the UO_2 inclusions is assumed to be $193\ \mu\text{m}$ (see paragraph 5.1). The density as a percentage of the theoretical one is assumed to be 90% for UO_2 and MgO . The scattering especially in the matrix in Figure 5.19 is due to insufficient statistics. Fitted lines are therefore drawn to guide the eye.

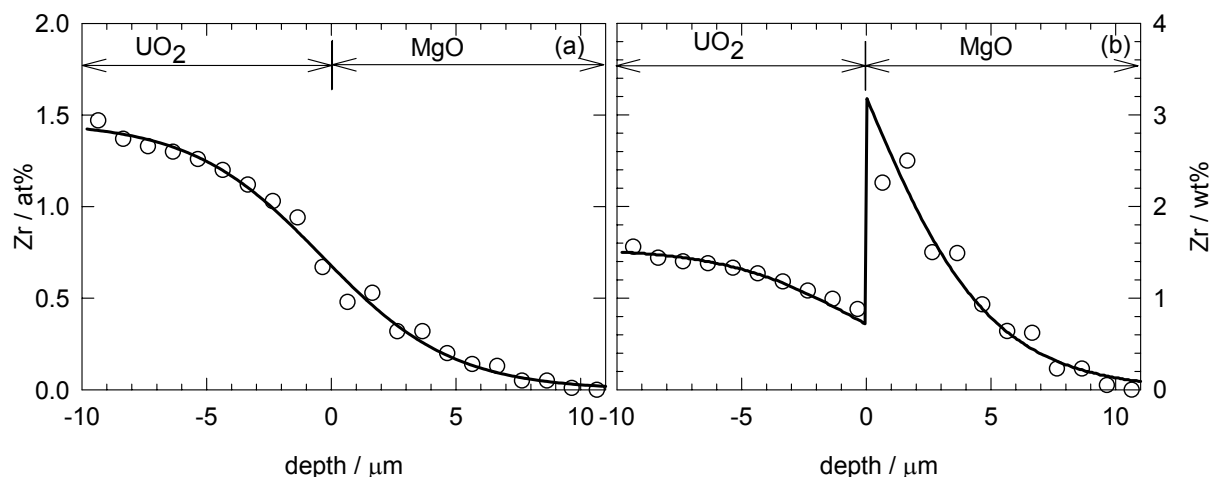


Figure 5.19 Implantation profile of UO_2 in MgO with Zr in (a) at% and (b) in wt%, fitted lines are drawn to guide the eye.

The wt% of Zr in UO_2 in the calculated implantation profile is similar to the measured profiles in Figure 5.18. The wt% of MgO is expected to be larger since fission products like Zr are relatively heavy in comparison with Mg and O . That this distinction in wt% of Zr in both phases is not observed in the measured profiles may possibly be due to the lateral resolution.

The EPMA results of UO_2 are similar to the EPMA-results in MOX with plutonium inclusions embedded in UO_2 with an immobile fission product distribution as expected by implantation and a maximum concentration of Xe in PuO_2 of 0.3 wt% [Walker et al. 1996]. It is measured that the maximum concentration of Xe in solid UO_2 is 0.25 wt% [Koo et al. 2001].

Figure 5.20 shows images of an irradiated UO_2 inclusion embedded in MgO . The light phases in the X-ray maps are the locations of x-rays emitted from atoms indicated in the images. The backscattered electron image clearly shows porosity in the UO_2 inclusion and a crack in MgO . All X-ray maps show background that becomes relatively larger when the concentration of the element to be measured is smaller; the locations containing uranium and magnesium can more clearly be discerned than zirconium, cesium and xenon. Nevertheless the areas, in which zirconium and cesium have a larger intensity, are larger than the area of uranium. This is due to implantation zones as discussed previously. The intensity of xenon is larger in the matrix surrounding the UO_2 inclusion than the UO_2 inclusion itself. The zone in MgO with less intensity of Xenon is background. This rim of xenon, which is the implantation

zone in MgO, is due to negligible porosity for MgO in the implantation zone in comparison with the UO₂ inclusion and/or fission-gas release from the UO₂ inclusion. The detector used for EPMA is 18° from the surface. The X-rays originating from the crack do not reach the detector due to this geometry in equipment resulting in the visibility of the crack in the X-ray map of Mg.

Figure 5.21 shows a backscatter image and X-ray maps of the fuel fabricated of UY₆O_x and MgAl₂O₄ after irradiation. The backscatter image clearly shows in Figure 5.21 a light grey phase, a medium grey phase and a black phase. It also shows that most bubbles are present in the medium grey phase. The X-ray maps shows that this medium grey phase contains yttrium and aluminium. The light grey phase contains magnesium and aluminium and the black phase yttrium and uranium. The formation of solid solution between the fissile phase UY₆O_x with MgAl₂O₄ results in concentrations of uranium that are larger than if no formation of a solid solution occurred. (The reverse took place for the formation of solid solution between fissile phase UO₂ with the matrices CeO_{2-x} and Y₂O₃ where uranium diffusing into the matrices resulted in a larger volume of phase with uranium.) The inclusion in Figure 5.21 is quite small and not representative for the general size of the inclusions. The relatively large yttrium-aluminium phase in comparison with the uranium-yttrium phase may be due to the relatively large area with which the matrix could interact during sintering in comparison with larger inclusions. From these pictures it cannot be deduced whether or not the formation of this yttrium-aluminium phase continued during irradiation or was only formed during sintering. The formation of the yttrium-aluminium phase is a negative aspect of this fuel since this phase shows fission-gas bubbles after irradiation, indicating swelling. In matrices, no fission-gas bubbles could be observed except for Y₃Al₅O₁₂. The area of zirconium is larger than uranium and due to emission of fission products from the uranium phase. Xenon seems to be less present in the uranium-yttrium phase than in the yttrium aluminium phase.

Figure 5.22 shows a backscatter image and X-ray maps of the fuel fabricated of UY₆O_x and MgO after irradiation. The backscatter image in Figure 5.22 shows two phases; a black phase and a light grey phase. The black phase is composed of uranium and yttrium and nearly no pores can be observed in this phase. The light grey phase is MgO. From these images, it can clearly be deduced that no chemical interaction occurred between the matrix and fissile phase. This MgO phase clearly shows outbreak. Fission products known to be immobile in UO₂ like Nd have a slightly larger area than uranium and yttrium due to emission. Xenon is located at similar positions of Nd, no thermal migration occurred.

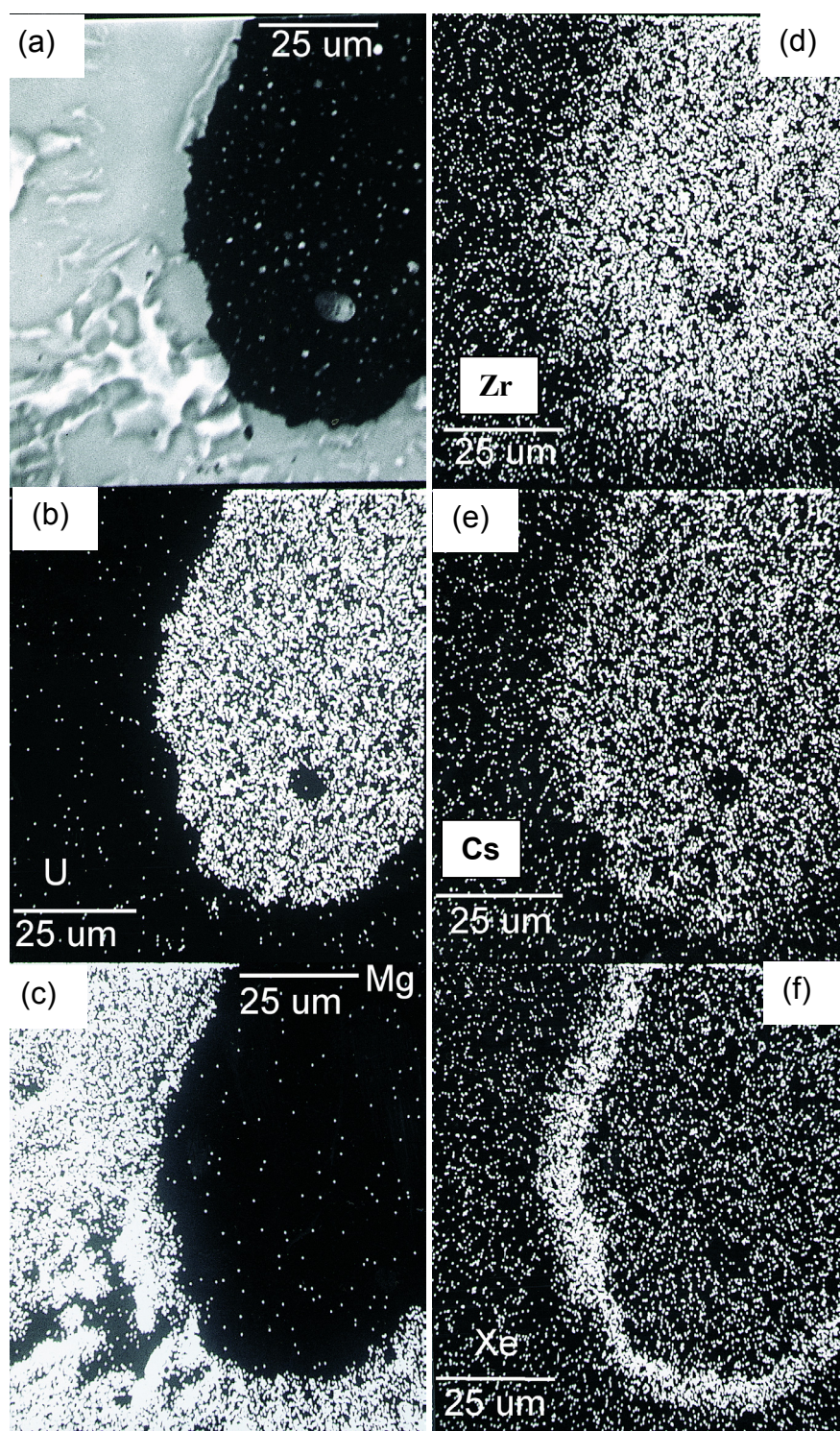


Figure 5.20 (a) Backscattered electron image of UO_2 in MgO after irradiation and X-ray maps of (b) U, (c) Mg, (d) Zr, (e) Cs and (f) Xe.

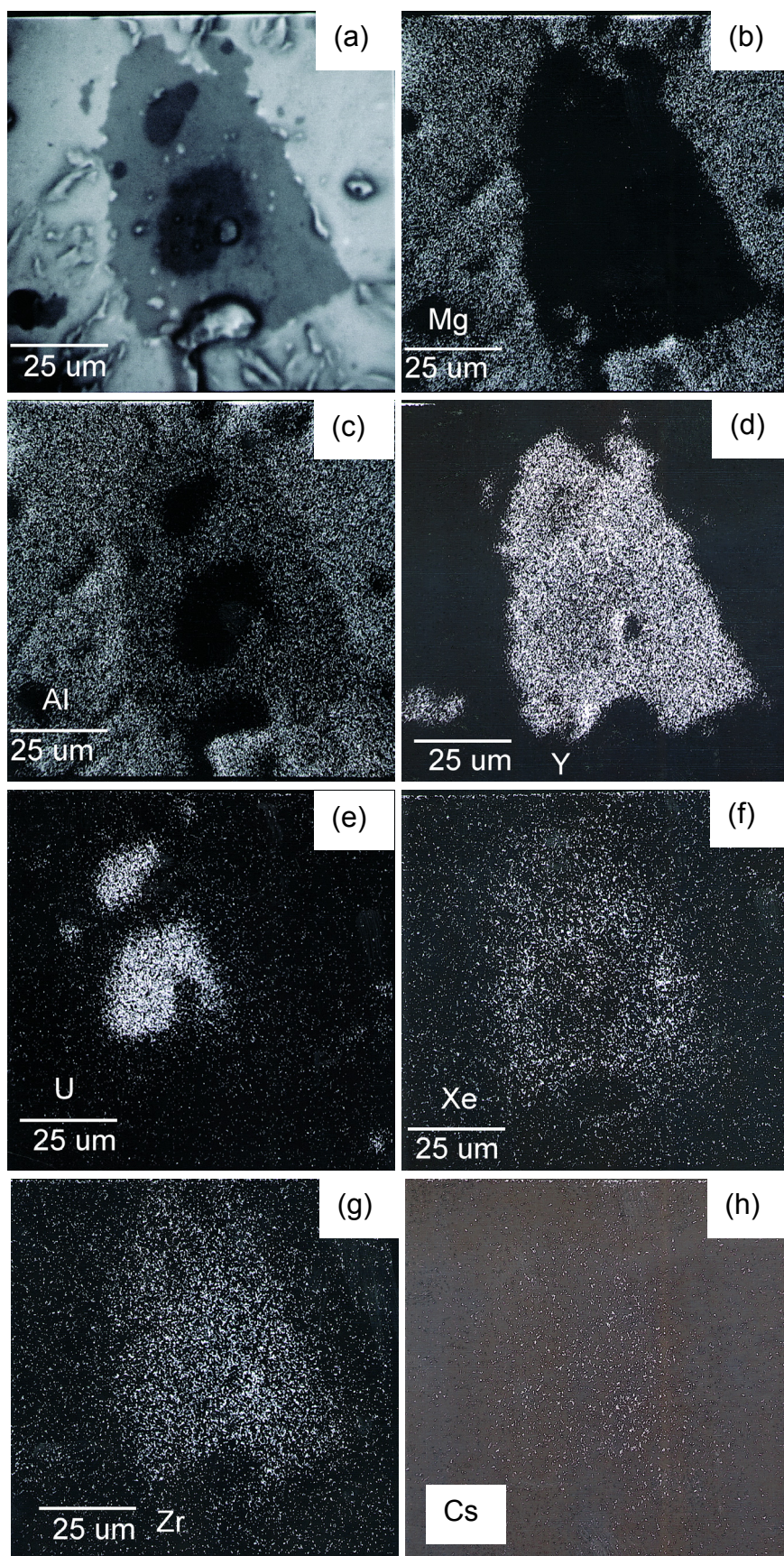


Figure 5.21 (a) Backscattered electron image of UY_6O_x in $MgAl_2O_4$ after irradiation and X-ray maps of (b) Mg, (c) Al, (d) Y, (e) U, (f) Xe, (g) Zr and (h) Cs.

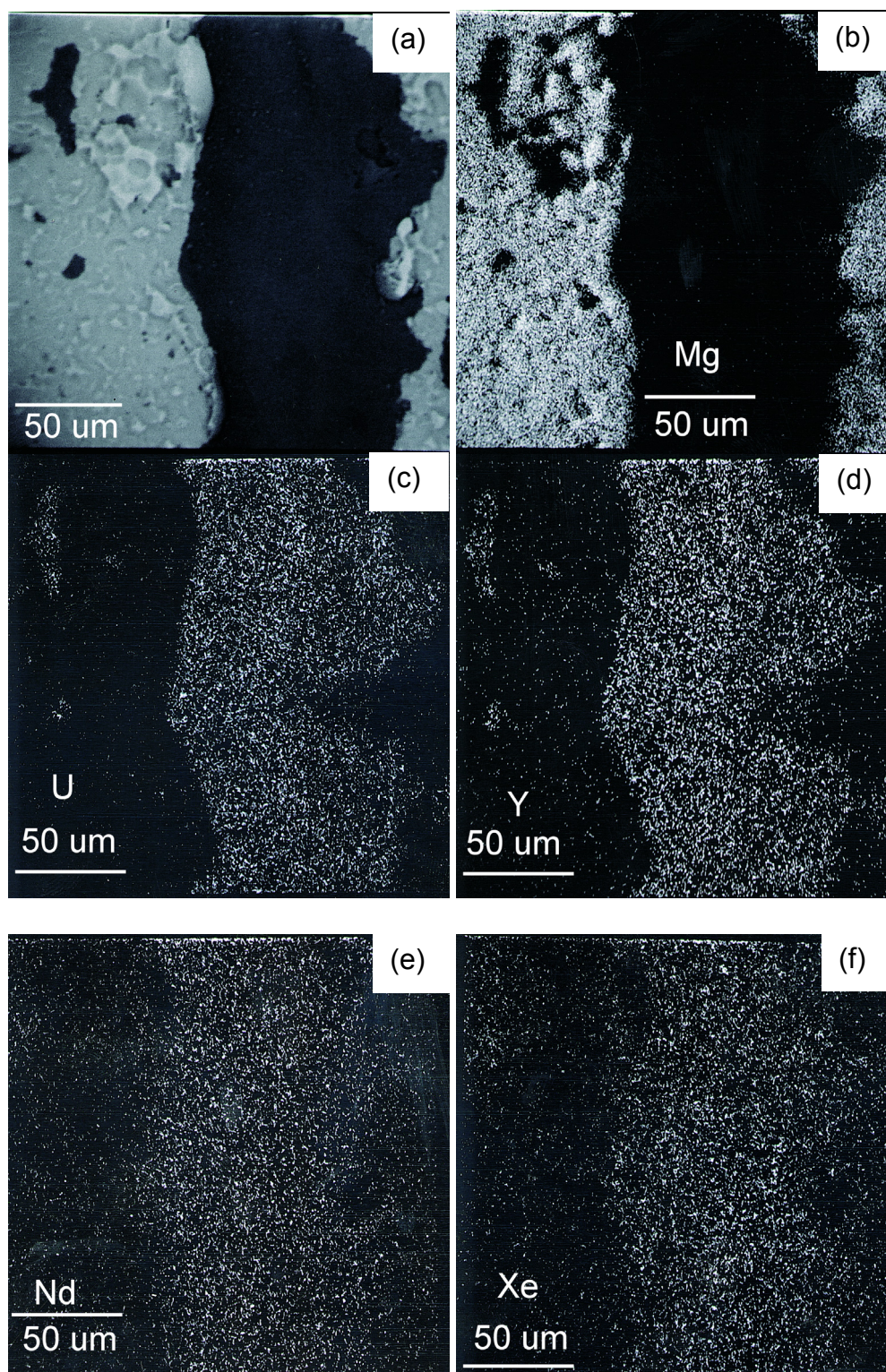


Figure 5.22 (a) Backscattered electron image of UY_6O_x in MgO after irradiation and X-ray maps of (b) Mg, (c) U, (d) Y, (e) Nd, (f) Xe.

5.9.3.2 Micro-dispersed fuel

Figure 5.23 shows the distribution of fission products and uranium in fuel with (sub)micro-dispersed UO_2 inclusions in MgAl_2O_4 .

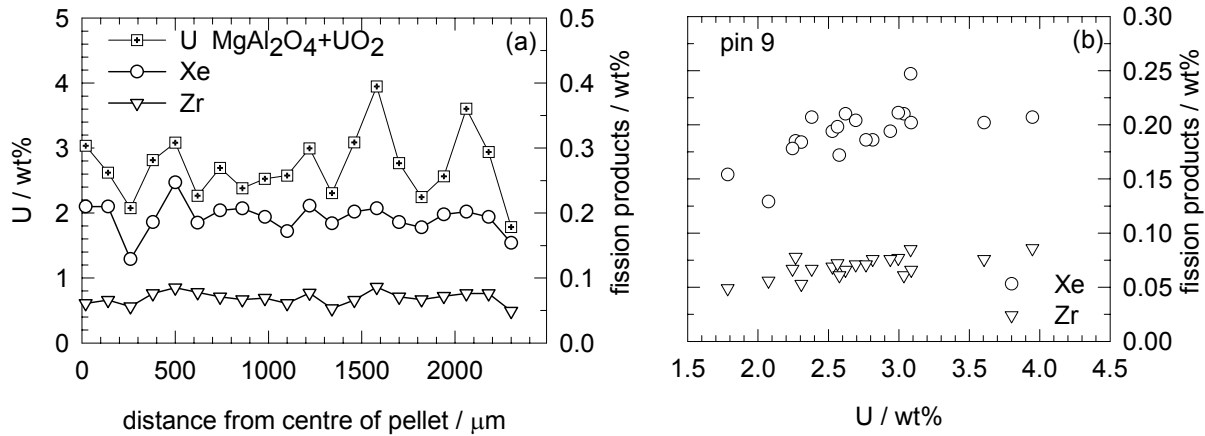


Figure 5.23 (a) U, Xe and Zr versus depth and (b) Xe and Zr versus U of a pellet micro-dispersed UO_2 in MgAl_2O_4 after irradiation.

Figure 5.23a shows nearly no difference between the concentration of fission products in the core and edge of the pellet. For xenon, the concentration in the core could be smaller than at the edge of the pellet by thermally induced migration. This is however not observed. Figure 5.23b shows that the concentration of fission products is rather linearly related to the concentration of uranium. Such a relation is typical for a fuel in which no thermally induced migration occurs. The uranium concentration could be higher in the core than at the edge of the pellet. Neutronic shielding could have occurred by which at the edges of the pellet a higher burn-up is expected than at the core of the pellet, similarly for the RIM region of ordinary reactor fuel. This is also not observed; the pellet shows a uniform burn-up of uranium.

5.9.4. Calculated fission product distribution in macro-dispersed UO_2 fuel

Paragraph 5.9.2 and 5.9.3.1 showed that thermal migration of fission products into the matrices is negligible or absent (outside the implantation zones). The volume of matrix containing fission products is therefore solely dependent on implantation from the fissile phase. The distribution in size of the sintered UO_2 particles in Figure 5.2 can be used to determine the fission product distribution. The fraction of matrix that received fission products by emission from the UO_2 inclusions can be calculated, assuming no overlap of the zones in the matrix that received fission products. The fraction of matrix implanted with fission products ($V_{fp,m}$) is:

$$V_{fp,m} = \left\{ \sum_{j=1}^{N_j} \int_{R_j}^{R_j+\lambda_m} 4\pi R^2 dR [V_j]^{-1} V_{j,v} V_f \right\} \div (1 - V_f) \quad (5.1)$$

where R_j and V_j are the radius and volume of an individual UO_2 microsphere, $V_{j,v}$ is the volume fraction of the UO_2 microsphere, N_j is the total number of microspheres measured in sieving

fractions (see Table 5.2), λ_m is the fission fragment recoil range of the matrix and V_f is the volume fraction of UO_2 in the pellet. Figure 5.24 shows the incremental sum of matrix volume that is implanted with fission products versus increasing size of diameter of the UO_2 particle using a volume fraction of UO_2 (V_f) of 0.025 and a fission fragment recoil range (λ_m) of $10\ \mu\text{m}$. The volume fraction of the matrix that received fission products by emission becomes $0.045 \times 0.975^{-1} = 0.046$. The major part of fission products in the matrix is from the UO_2 particles measured in sieving fraction 4 with the smallest particles. The fraction of emitted fission products to the matrix for each particle ($E_{fp,particle}$) is described by [White et al. 1956]:

$$E_{fp,particle} = 3\lambda_f [4^{-1}] - [4^{-2}] \left\{ \frac{\lambda_f}{R_j} \right\}^3 \quad \text{for} \quad 2R_j > \lambda_f \quad (5.2)$$

where λ_f is the fission fragment recoil range of UO_2 . If $2R_j < \lambda_f$, it is assumed that all fission products are emitted to the matrix. Assuming a uniform enrichment of the UO_2 microspheres, the total amount of produced fission products that are emitted to the matrix becomes:

$$E_{fp} = \sum V_{j,V} \times E_{fp,particle} \quad (5.3)$$

Figure 5.24 shows that the total fraction of fission products that are emitted from fissile phase is 13% of the produced fission products. So most of the fission products (87%) are implanted in the UO_2 inclusions.

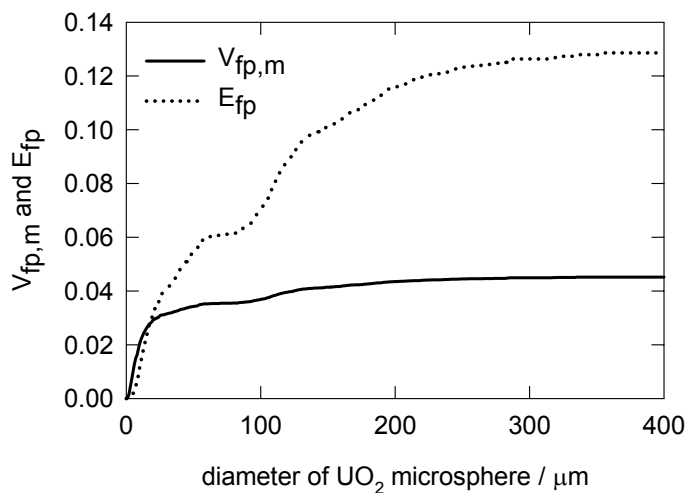


Figure 5.24 Solid line: incremental volume fraction of matrix implanted with fission product; dotted line: incremental fraction of fission products emitted to the matrix versus diameter of the UO_2 particles.

5.9.5 Mechanical properties

5.9.5.1 Indentation measurements in ceramic matrices

Indentation measurements were performed before and after irradiation of IMF in the matrix. The small volume of matrix implanted with fission products (4.6%) indicates that the indentation measurements are mainly performed in the matrix without fission products if no chemical interaction between matrix and fissile phase occurred during sintering. Table 5.12 shows the literature data of the mechanical properties (Young's modulus, Poisson's ratio and shear modulus) and their empirical relation with porosity. These mechanical properties of $\text{Y}_3\text{Al}_5\text{O}_{12}$ are calculated from the experimentally elastic constants [read in Kuklja et al. 1999]

using the Hill-Walpole model [read in Suter et al. 2002]. The Poisson's ratio for CeO₂ of 0.515 [Samsonov 1982] is assumed to be incorrect, a value of 0.3 is used to derive the Young's modulus from the shear modulus.

Table 5.12 shows that the Young's moduli for MgAl₂O₄ slightly decreased after neutron fluences far larger than the present study. The Young's modulus for MgO significantly reduced after a neutron fluence very small in comparison with the present neutron irradiated MgO. However, the temperature of irradiation is below 353 K; a temperature significantly lower than the present study: 700 K to 950 K. This includes that the annihilation of defects in the present study larger is and therefore the reduction of the Young's modulus may be smaller. Other data concerning the impact of neutron irradiation for the Young's moduli for these polycrystalline matrices are unknown to the author.

Table 5.12 Literature data of mechanical properties

Material	E [GPa]	A_E	G [GPa]	A_G	ν	P [%]	literature
Y ₂ O ₃ ^Y	180.1 ± 4.8	3.05	69.3 ± 2.96 2.0		0.299 ± 0 0.004		[Yehekel et al. 1999]
MgO ^W	317.7	4.74	139.5	4.9	0.138	0	[Wachtman 1996]
MgAl ₂ O ₄ ^M	274	-	108	-	0.27	0.8	[Garner et al. 1994]
Y ₃ Al ₅ O ₁₂ ^M	279	-	111	-	0.25	0	Calculated, see text
CeO ₂		-	62.47	-	0.515	-	[Samsonov 1982]
CeO ₂	162		62.47		0.3	-	
UO ₂ ^R	220	2.34	82	2.03	0.341	0	[Roque et al. 2000]
Material	E [GPa]	$\Delta E/E$ [%]	neutron irradiation conditions			Literature	
			T [K]	ϕ [m ⁻²]	E_{neutron} [MeV]		
MgAl ₂ O ₄	274	0	658	24.9×10 ²⁶	> 0.1	[Garner et al. 1994]	
	273	- 0.36	677	5.3×10 ²⁶	> 0.1	[Garner et al. 1994]	
	276	+ 0.73	1023	5.6×10 ²⁶	> 0.1	[Garner et al. 1994]	
	273	- 0.36	1023	13.7×10 ²⁶	> 0.1	[Garner et al. 1994]	
	271	- 1.09	1023	21.7×10 ²⁶	> 0.1	[Garner et al. 1994]	
MgO	-	- 4.85 ^S	< 353	0.8×10 ²⁰	> 1	[Stevanovic et al. 1967]	

^{Y/R} $E = E_0 \times \{1 - A_E P\}$, ^W $E = E_0 \times \{1 - e^{-A_E P}\}$, ^M $E = E_0 \times \{1 - 1.9P + 0.9P^2\}$, P is porosity fraction, ^S complete recovery after annealing at 1273 K for 24 hours.

CeO_{2-x} showed excessive crack branching after indentation, before as well as after neutron irradiation. The indents in other ceramic matrices showed more or less straight cracks.

No indentations are performed before irradiation in MgO. Table 5.13 shows the indentation measurements before neutron irradiation of the ceramic matrices. The Young's modulus is, amongst others, required to determine the fracture toughness. The porosity of the matrices in Table 5.1 is used to determine the Young's moduli for the fracture toughness in Table 5.13. The empirically determined relations for porosity and Young's moduli are used if available for the specific compound, otherwise the relation described in Morrell [Morrell 1985] is used (^M in Table 5.12).

Table 5.13 Indentation in matrices before irradiation

Matrix	Pin	E GPa	M kg	N	H_V kg mm ⁻²	l μm	grain size [∅] μm	K_{Ic} MPa m ^{1/2}
CeO _{2-x} ^u	1	162	0.1	6	532 ± 155	9.97 ± 2.55	10-30	1.2 ± 0.2
MgO	5	197	no indentations performed				10-20	
Y ₂ O ₃ ^u	18	159	0.2	8	842 ± 26	10.76 ± 2.92	2-5	1.7 ± 0.2
MgAl ₂ O ₄	11	251	0.2	9	1615 ± 113	8.13 ± 2.47	2-5	2.5 ± 0.4
MgAl ₂ O ₄	13		0.2	8	1741 ± 136	7.00 ± 2.98	2-5	2.8 ± 0.5
Y ₃ Al ₅ O ₁₂	15	243	0.2	9	1446 ± 67	7.97 ± 2.09	2-5	2.5 ± 0.4

[∅] determined from matrices without UO₂^u matrix possibly contained uranium, N = number of measurements, all values ± 1 σ

Table 5.14 shows the results of the indentations performed after neutron irradiation. The Young's moduli and porosity are assumed to be identical to these parameters used for the indentations performed before neutron irradiation. The magnification of the optically microscopy images was smaller for the images of indents in neutron irradiated matrix than for the images of indents in non-neutron irradiated matrix. Cracks at the indents at the edge of the pellet with Y₃Al₅O₁₂ could not be measured with the magnification taken for the images in neutron irradiated matrix.

The average hardness increases for CeO_{2-x} and Y₂O₃ upon neutron irradiation, it decreases for Y₃Al₅O₁₂. For MgAl₂O₄ it remains more or less constant. The hardness is very sensitive to porosity. The Knoop Hardness of UO₂, (Pu,U)O₂ and PuO₂ was measured to exponentially decrease with increasing porosity [Wick 1967]. Data for the presently studied ceramics that show the impact of porosity on the hardness are unknown to the author.

Table 5.10 showed that change in dimensional volume for CeO_{2-x}+UO₂ was -4.9% and for Y₂O₃+UO₂ was -1.4%. These matrices without fissile phase show a negligible dimensional volume change; the volume change was 0.6% for CeO₂ and -0.4% for Y₂O₃^D. The grey area in the α-autoradiograph of both ceramic composites indicated that uranium was also present in low concentrations in the matrices. The volume of fission induced sintering for these ceramic

^D For Y₂O₃ diameter measurements were performed at one side of the pellet. Thus, the negative change in dimension may also be due to the difference in cylindrical shape of the pellet (see paragraph 5.8.)

composites is larger than in the other composites with UO_2 . Taken into account the volume swelling of UO_2 in Table 5.16, the matrices may have densified with 6% to 6.5% for CeO_{2-x} and 2.5% to 2.7% for Y_2O_3 . Using these densification data and assuming a similar relation between porosity and hardness as UO_2 , $(\text{Pu,U})\text{O}_2$ and PuO_2 [Wick 1967], the Vickers hardness for these matrices would increase in hardness with a value of +43% for CeO_{2-x} and +14% for Y_2O_3 . The increase in Vickers hardness for CeO_{2-x} of $+66\% \pm 22\%$ and for Y_2O_3 of $+16\% \pm 2\%$ seems to be possibly due to densification of the matrices. Fission induced sintering is probably negligible for the matrices MgAl_2O_4 , MgO and $\text{Y}_3\text{Al}_5\text{O}_{12}$ since X-ray diffraction as well as the α -autoradiograph showed no formation of a solid solution with UO_2 . Therefore fission induced sintering is limited to about 4.6 vol% of matrix implanted with fission products.

Table 5.14 Indentations in matrices after irradiation and change in hardness and crack length

Matrix	Pin	M	N	H_V	l	K_{Ic}	$\frac{\Delta H_V}{H_V}$	$\frac{\Delta l}{l}$
		kg		kg mm ⁻²	μm	MPa m ^{1/2}	%	%
CeO_{2-x} ^u	1	0.1	10	883 ± 171	7.74 ± 3.39	1.5 ± 0.4	66 ± 22	-22 ± 3
MgO	5	0.1	3	1068 ± 102	6.26 ± 1.77	1.8 ± 0.3		
		0.2	7	998 ± 37	9.96 ± 3.83	2.0 ± 0.5		
Y_2O_3 ^u	18	0.1	13	1066 ± 94	4.00 ± 1.67	2.1 ± 0.4		
		0.2	14	975 ± 67	7.51 ± 2.79	2.1 ± 0.4	16 ± 2	-30 ± 5
MgAl ₂ O ₄	11	0.2	5	1663 ± 175	12.18 ± 2.24	2.0 ± 0.2	3 ± 5	50 ± 5
MgAl ₂ O ₄ ^u	13	0.1	9	1785 ± 441	2.88 ± 1.15	3.1 ± 0.7		
		0.2	5	1702 ± 211	8.95 ± 4.40	2.6 ± 0.5	-2 ± 6	28 ± 6
$\text{Y}_3\text{Al}_5\text{O}_{12}$	15	0.1	8	1036 ± 70				
		0.2	6 ^{edge}	992 ± 60			-31 ± 2	
		0.2	12 ^{core}	940 ± 166	16.15 ± 13.08	1.9 ± 0.5 [*]	-35 ± 3	103 ± 14

^u matrix with fission products, N = Number of measurements; all values $\pm 1 \sigma$, change in $\pm \sigma/\sqrt{N}$, * calculated with K_{Ic} -formulae for $\{l/a + 1\} > 2.5$ [Niihara 1982]

The present study shows that the fracture toughness increases with increasing neutron fluence for the matrices CeO_{2-x} and Y_2O_3 and decreases for the matrices MgAl_2O_4 and $\text{Y}_3\text{Al}_5\text{O}_{12}$ (solely in the core of the pellet) using the same Young's modulus before and after neutron irradiation. It is unclear whether or not the increase in resistance for the crack formation for the fuels with CeO_{2-x} and Y_2O_3 is due to densification of the matrix. For $\text{Y}_3\text{Al}_5\text{O}_{12} + \text{UO}_2$, the hardness of the matrix $\text{Y}_3\text{Al}_5\text{O}_{12}$ measured in the core of the pellet (small porosity) is similar to the hardness measured at the edge of the pellet (large porosity). The indents were performed as far as possible from the micron-sized bubbles thus the large generated but localised porosity should not have an impact on the indents. The reduction in hardness and decrease in resistance to fracture seems to be a property change of neutron irradiated polycrystalline $\text{Y}_3\text{Al}_5\text{O}_{12}$. The decrease in resistance to fracture for MgAl_2O_4 is also solely ascribed to neutron irradiation.

5.9.5.2. Literature data of ceramic matrices

Literature data of unirradiated polycrystalline materials concerning the Vicker's hardness at comparable loads are presented in Table 5.15.

Table 5.15 Literature data of unirradiated ceramic matrices

Material	M [kg]	H_V [kg mm ⁻²]	ρ [g cm ⁻³]	P [%]	N	Literature data
CeO ₂	0.2	387 ± 82	6.70	6.1	10	[Maschio et al. 1990]
MgO	0.05 to 0.1	760	3.40	5.6		[Samsonov 1982]
MgAl ₂ O ₄	0.1	1500				[Morrell 1985]
Y ₂ O ₃		739				[Samsonov 1982]
		612				[de With et al. 1985]
Y ₃ Al ₅ O ₁₂	0.1	2263 ± 173		≤ 0.2	5	[de With et al. 1985]
Y ₃ Al ₅ O ₁₂	0.2	1835 ± 51		≤ 0.2	5	[de With et al. 1985]
Material	grain size μm	K_{IC} MPam ^{1/2}	ρ g cm ⁻³	P %		Literature data
MgO	10	1.8				[Munro et al. 1998]
MgO	28	1.6				[Munro et al. 1998]
MgAl ₂ O ₄	1.5	3.0	3.491	2.5		[Munro et al. 1998]
MgAl ₂ O ₄	5	1.94 ± 0.10		≈ 0		[Stewart et al. 1980]
Y ₃ Al ₅ O ₁₂	3 to 6	1.7 ± 0.1		≤ 0.2		[de With et al. 1985]

P = porosity and N is number of measurements

The hardness in the present study before irradiation is comparable to literature data if porosity and load are taken into account. After a fast neutron fluence of $2.3 \times 10^{24} \text{ m}^{-2}$ at a neutron irradiation temperature of 823 K, the increase in Vickers hardness was 1.8% for MgAl₂O₄ [Yano et al. 1994]. After fast neutron fluences of $2.2 \times 10^{26} \text{ m}^{-2}$, $2.4 \times 10^{26} \text{ m}^{-2}$ and $2.5 \times 10^{27} \text{ m}^{-2}$ at a neutron irradiation temperature of 658 K, the increase in Vickers hardness of MgAl₂O₄ was 5%, 10% and 12%, respectively [Yano 1999]. MgAl₂O₄ of the present study showed an increase of $3\% \pm 5\%$ and was neutron irradiated at about 700-1000 K with a fast neutron fluence of $7.0 \times 10^{25} \text{ m}^{-2}$. The result of the hardness of neutron irradiated MgAl₂O₄ of the present study is in agreement with the other two studies, although the scatter in data of the present study is quite large. Other data of the Vicker's hardness of neutron irradiated polycrystalline present studied matrices could not be found.

Table 5.15 shows literature values of the fracture toughness measured by (point) bending techniques with comparable grain sizes as the polycrystalline materials of the present study. Although the scatter in the fracture toughness is quite large in the present study;

MgAl₂O₄ and Y₃Al₅O₁₂ are within the ranges measured in the literature data before neutron irradiation. Literature data of the fracture toughness of neutron irradiated polycrystalline present studied matrices are unknown to the author.

5.10 Discussion

5.10.1 Swelling of UO₂

The swelling of UO₂ is determined by three methods:

- 1) image analysis of the size of the UO₂ inclusions before and after irradiation;
- 2) image analysis of the porosity before and after irradiation;
- 3) image analysis of the crack widths in matrices and size of the UO₂ inclusions.

Figure 5.26 shows the methods for the determination of swelling for the UO₂ inclusions.

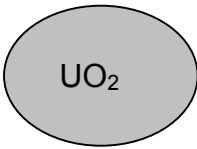
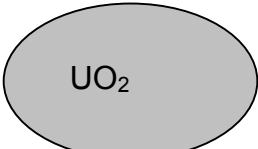
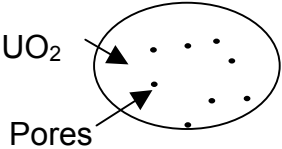
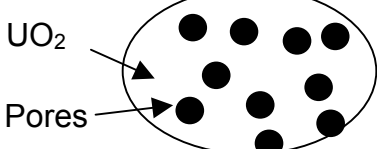
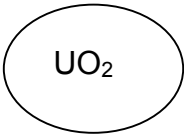
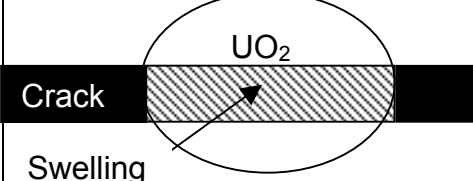
Method	Before irradiation	After irradiation
Image analysis		
Porosity + fission product swelling		
Crack measurement		

Figure 5.25 Determination of swelling of the UO₂ inclusions using three methods.

Volume swelling of UO₂ inclusions determined by dimensional measurements

The dimensional swelling of UO₂ can be determined by comparing the area of the UO₂ inclusions before and after neutron irradiation. Two sections, a transverse and an axial section, were made after neutron irradiation for each series of pellets. Before neutron irradiation, an axial or transverse section was made for each series of pellets. The absence of a section before irradiation makes determination solely by comparison of the area before and after irradiation impossible. The distribution of the sintered UO₂ microspheres in Figure 5.2 is used to complement for the missing data [Neeft 2003].

Volume swelling of UO₂ inclusions determined by solid fission products and porosity

The volume swelling of UO₂ can also be calculated by porosity and solid fission products. The solid state swelling of UO₂ is described by:

$$\frac{\Delta V}{V_{solid}} = \left\{ (0.005 \times FIMA\% \times (1 - P_{before})) \times (1 - E_{fpd,particle}) \right\} \quad (5.4)$$

where FIMA% is the Fissioned Initial Metal Atoms, (Initial Metal Atom refers only to uranium), P_{before} is the fraction of porosity of the inclusion before neutron irradiation. The fraction of fission products remaining in the UO₂ inclusions is determined to be 0.871 (see paragraph 5.9.4). The factor 0.005 is the swelling of UO₂ without pores per FIMA%; the solid state swelling [Une et al. 2000]. The solid volume of the UO₂ inclusions before neutron irradiation becomes:

$$V_{solid,before} = \frac{V_{total,after} \times \{1 - P_{after}\}}{\left(1 + \frac{\Delta V}{V_{solid}}\right)} \quad (5.5)$$

where $V_{total,after}$ is the volume of the UO₂ inclusion and $\Delta V/V_{solid}$ as determined by equation 5.4. The total volume of the UO₂ inclusion before neutron irradiation is:

$$V_{total,before} = \frac{V_{solid,before}}{(1 - P_{before})} \quad (5.6)$$

A similar relation holds for after neutron irradiation. A combination of 5.5, 5.6 for before and after neutron irradiation results in the total increase in volume of the UO₂ inclusion:

$$\frac{\Delta V_{porosity+solid,fpd}}{V} = \frac{V_{total,after}}{V_{total,before}} - 1 = \left\{ \left(1 + \frac{\Delta V}{V_{solid}}\right) \times \left(\frac{1 - P_{before}}{1 - P_{after}}\right) \right\} - 1 \quad (5.7)$$

The porosity of the UO₂ inclusions before irradiation could only be determined for these inclusions embedded in MgO and Y₃Al₅O₁₂. This data is insufficient to determine the porosity of the UO₂ inclusions before irradiation. Table 5.16 shows the volume swelling of UO₂ using an identical porosity before irradiation of 5.5% ± 6.4% for all fuels.

Volume swelling of UO₂ inclusions after crack formation of matrix

The width of the cracks that surround the UO₂ inclusions can be used to determine the volume swelling of UO₂ after crack formation. This method is different than the previously two discussed methods of volume swelling of UO₂ since it requires a cracked matrix [Neeft 2003]. For example, if the matrix surrounding the UO₂ inclusion fractures at half of the total swelling of UO₂, then the UO₂ swelling determined using this method is 50% of the actual swelling of UO₂.

Comparison of swelling results

Table 5.16 shows that the volume swelling of UO₂ embedded in MgO, Y₂O₃ and CeO_{2-x} at a burn-up of 17.1% to 17.5% is about 40% to 50%. The volume swelling of UO₂ embedded in MgAl₂O₄ and Y₃Al₅O₁₂ at a burn-up of 19.3% to 19.7% is about 70% to 80%. Table 5.16 also shows that the volume swelling determined with dimensional measurements is similar to the volume swelling determined by porosity for UO₂ inclusions embedded in MgAl₂O₄.

Table 5.16 Swelling of the UO_2 inclusions using the three methods

UO ₂ inclusions in matrix	pin	swelling of UO ₂		swelling of UO ₂ after crack formation of matrix
		$\Delta V^{dim}/V_{dim}^{\sigma/\sqrt{N}}$	$\Delta V^{por.+fpd}/V^{\sigma}$	$\Delta V^{crack}/V_{dim}^{\sigma/\sqrt{N}}$
CeO _{2-x}	1		0.50 ± 0.21	
Y ₂ O ₃	18		0.40 ± 0.22	
MgO	5	0.47 ± 0.17		0.07 ± 0.17
MgAl ₂ O ₄	11	0.74 ± 0.22	0.68 ± 0.20	0.74 ± 0.23
Y ₃ Al ₅ O ₁₂	15		0.77 ± 0.17	

$$\sigma/\sqrt{N} \pm 1\sigma/\sqrt{N} \text{ with } N = \text{number of measurements, } \sigma \pm 1\sigma$$

The volume swelling of UO₂ determined after crack formation of the matrix ($\Delta V^{crack}/V_{dim}$) MgAl₂O₄ is equal to the volume swelling of UO₂ using dimensions of UO₂ ($\Delta V^{dim}/V_{dim}$). It suggests that a tiny swelling of UO₂ resulted in fracture of the matrix MgAl₂O₄; fracture of MgAl₂O₄ probably occurred just after BOI. The width of the cracks in the matrix MgO are so small that $\Delta V^{dim}/V_{dim} \gg \Delta V^{crack}/V_{dim}$. It suggests that the matrix MgO cracked later in the neutron irradiation period than the matrix MgAl₂O₄; probably near EOI.

5.10.2 Swelling of uranium free matrices

The swelling of uranium free matrices can also be determined from the experimental data. This swelling is an important parameter since it can facilitate the discussion to find a matrix without actinides that has similar dimensional stability upon fission product concentration as the matrix of ordinary reactor fuel: ²³⁸UO₂.

5.10.2.1 Micro dispersed fuel

For the micro dispersed fuel MgAl₂O₄+UO₂, all fission products are emitted into the matrix and neighbouring UO₂ inclusions. The fission product concentration for the pellet becomes $V_f \times U / cm^3 \times 2 \times FIMA = 2.34 \times 10^{20}$ fission products cm⁻³. The solid state swelling of MgAl₂O₄ becomes:

$$\left\{ \frac{\Delta V}{V} \right\}_{solid} = \left[\left(\left\{ \frac{\Delta V}{V} \right\}_{pellet} + 1 \right) \times \left(\frac{1 - P_{after}}{1 - P_{before}} \right) \right] - 1 \quad (5.8)$$

where $\left\{ \frac{\Delta V}{V} \right\}_{pellet}$ is the volume change of the pellet and P_{after} and P_{before} are the fraction in porosity after and before neutron irradiation. The derivation of this formula can be read in paragraph 5.10.1. The solid state swelling of MgAl₂O₄ (swelling of MgAl₂O₄ implanted with fission products without the contribution of pores) becomes 2.8 vol% ± 1.4 vol%. Such a low fission product concentration would result in a solid state swelling for UO₂ of 0.28 vol% using the solid state swelling of 0.005 per FIMA% in Une et al. [Une et al. 2000]. Thus, the solid state swelling of MgAl₂O₄ is about ten times larger than UO₂. Another irradiation experiment of

micro-dispersed UO_2 inclusions in MgAl_2O_4 is EFTTRA-T4ter [Klaassen et al. 2002]. This yields similar results for the solid state swelling as determined for EFTTRA-T3. Table 5.17 shows the experimental results of both experiments.

Table 5.17 Determination of solid state swelling of MgAl_2O_4

experiment	P_{before} [%]	P_{after} [%]	$\Delta V/V$ [%]	f.p. cm^{-3} $\times 10^{20}$ *	$\Delta V/V_{\text{solid}}$ solid	$\frac{\text{MgAl}_2\text{O}_4}{\text{UO}_2}$
EFTTRA-T3	7.6	4.3 ± 0.6	-0.83 ± 1.02	2.3	2.8 ± 1.4	11.6
EFTTRA-T4ter	8	0.2	10.9 ± 1.5	15.7	19.8 ± 2.0	12.4

* assuming 100% t.d., all values $\pm 1\sigma$.

5.10.2.2 Macro-dispersed fuel

For macro-dispersed fuel, it is difficult to estimate whether or not the uranium free matrix shows more swelling than UO_2 . It is likely that the concentration of fission products in the implantation zones larger is than in micro dispersed fuels and therefore that these implantation zones have a larger swelling. The calculated average fission product concentration in the implantation zones of the matrices is comparable to that in a UO_2 pellet with 3.94 FIMA% [Neeft 2003]. No fission gas bubbles are generated in the matrix MgAl_2O_4 (pin 9 and pin 11) at these irradiation conditions. For MgO , this cannot be deduced since outbreak occurred in the fission implanted zones of MgO during preparation of the ceramographic sections.

The zone implanted with fission products surrounding a UO_2 inclusion with a diameter of $193 \mu\text{m}$ (see paragraph 5.2.1) had a concentration of fission products of about 7 to 8 times larger than in the micro dispersed fuel of $\text{MgAl}_2\text{O}_4 + \text{UO}_2$ of EFTTRA-T3. Assuming a linear solid state swelling based on the data from micro-dispersed fuels, the swelling of the fission implanted zone of MgAl_2O_4 in the macro dispersed fuel becomes 19 vol% to 22 vol%.

Large fission-gas bubbles are created in the implantation zones of $\text{Y}_3\text{Al}_5\text{O}_{12}$. The swelling of these implantation zones becomes 179-228 vol% using the volume swelling of the pellet and swelling of the UO_2 inclusions [Neeft 2003].

5.10.3 Formation of cracks in matrices

The ceramic composites with MgO , MgAl_2O_4 and $\text{Y}_3\text{Al}_5\text{O}_{12}$ showed only cracks from UO_2 to UO_2 inclusion after neutron irradiation. These cracks do not run through the inclusions. The formation of cracks in the matrix is assumed to be due to swelling of the UO_2 inclusion during irradiation. This feature of swelling of inclusions in a matrix resulting in crack formation of the matrix, is described for ceramic composites [Lutz et al. 1991]. The formation of cracks in the matrix is favoured for ceramic composites with increasing radius of the particle, increasing volume fraction, increasing Young's moduli, decreasing Poisson's ratio and decreasing fracture toughness of the ceramic matrix. This theory is applied for the crack formation in the matrix upon neutron irradiation with a slight modification for the crack criteria.

The formation of cracks in a matrix containing single-sized spherical particles (radius

R_p , volume fraction V_p) of which the volume tends to strain with respect to the matrix is described in Lutz and Claussen [Lutz et al. 1991]. This volume strain can be a combination of two effects:

- 1) Increase of the volume due to swelling as observed in the present study.
- 2) A larger thermal expansion of the particle than that of the matrix upon heating.

The volumetric strain of the particle (ε_v) is defined by:

$$\varepsilon_v = \frac{\Delta V}{V} + 3 \times \Delta T (\alpha_p - \alpha_m) \quad (5.9)$$

where $(\Delta V / V)$ is the increase in volume of the particle by the swelling, α_p and α_m are the linearly thermally expansion coefficients of particle and matrix, respectively. ΔT is the temperature difference over which the complete ceramic composite is heated (or cooled), assuming that the temperature of the particles and the matrix is identical. The swelling of the particles causes stress at the interface between the matrix and the particle. Large annular cracks are formed in the matrix surrounding the particles when the stress is sufficiently. This means that the particles themselves remain intact. The condition for inter-particle fracture is:

$$\left[\frac{\beta R_p (\beta + 2)}{\pi (\beta + 1)} \right]^{1/2} \times \left[\left(\frac{1}{(\beta + 1)^2} + \frac{6\sqrt{2}}{\pi} V_p \right) c_4 \right] > K_{IC} \quad (5.10)$$

where $\beta = \frac{R_m}{R_p} - 1$, R_m (the effective half-distance between the particles) is defined as:

$$\sqrt[3]{\frac{\pi/3\sqrt{2}}{V_p} R_p^3}, \quad K_{IC} \text{ is the fracture toughness of the matrix material, } c_4 = \frac{c_1}{c_2 + c_3 (R_p/R_m)^3}$$

containing $c_1 = 2/3 E_p E_m \varepsilon_v$, $c_2 = 2E_m(1 - 2\nu_p) + E_p(1 + \nu_m)$ and $c_3 = 2[E_p(1 - 2\nu_m) - E_m(1 - 2\nu_p)]$ in which E_p and E_m are the Young's moduli of the particle and the matrix, ν_p and ν_m are the Poisson's ratios of the particle and the matrix.

Figure 5.26 shows the difference in temperature required to cause crack formation from inclusion to inclusion using the mechanical properties in Table 5.12, Table 5.13, Table 5.14 and the thermal expansion coefficients from Touloukian et al. [Touloukian et al. 1997]. Figure 5.26a shows that the difference in temperature should be at least 2000 K to cause inter-particle fracture in these ceramic composites during cooling down or heating up of the pellet by thermal expansion of matrix and UO_2 during the EFTTRA-T3 irradiation conditions. Figure 5.26b shows that ΔT significantly reduces for the formation of crack in the matrices for IMF-pellets with a four times larger volume fraction of UO_2 . It also clearly shows that crack formation of the matrix requires a larger difference in temperature when the radius of the inclusion decreases. Crack formation of the matrix by thermal expansion is ignored in the present study since the difference in temperature using a volume fraction of UO_2 of 0.025 is far smaller than at least 2000 K. Therefore, solely the swelling of the UO_2 inclusions is taken into account.

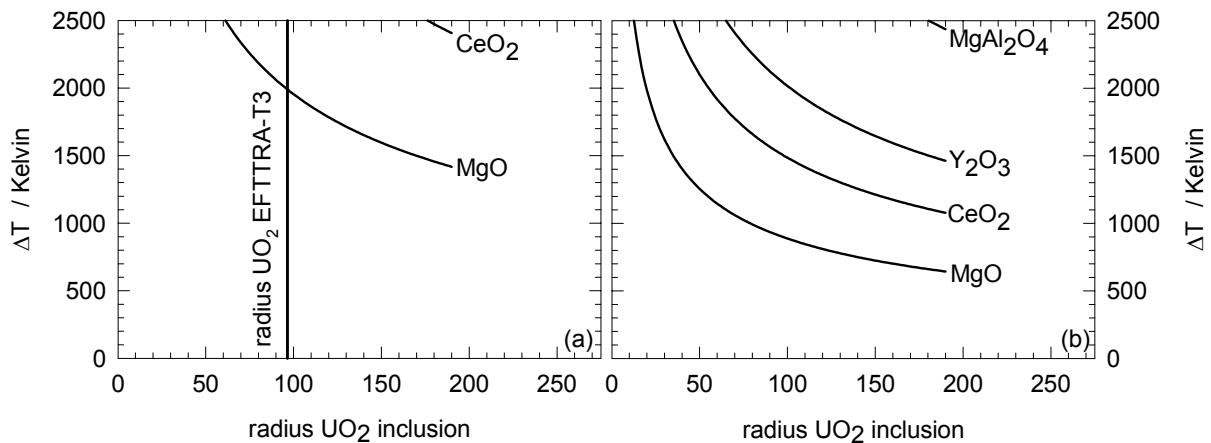


Figure 5.26 Difference in temperature in which the complete ceramic composite is heated versus radius of inclusion for (a) V_p of $UO_2 = 0.025$ (EFTTRA-T3 conditions) and (b) V_p of $UO_2 = 0.10$. The area above the curves indicates the criterion for cracks in a matrix from inclusion to inclusion.

The computed volume swelling of UO_2 to cause fracture of the matrix is 1.8 vol% to 2.6 vol% using a volume fraction of UO_2 of 0.025, a diameter of UO_2 of 193 μm and the mechanical properties described in paragraph 5.9.5.1. Note that this is very small in comparison with the volume change of the UO_2 inclusions in Table 5.16. The used mechanical properties are valid at room-temperature. Usually, the mechanical properties of ceramics change strongly at temperatures beyond half of the melting point. The irradiation temperature of EFTTRA-T3 is 700-1000 K, which is far below half of the melting point of all ceramic matrices. Temperature had probably a negligible impact on the mechanical properties for the present study.

5.11.4 Steady state creep of ceramics

The steady state creep of matrices is neglected in the model of Lutz and Claussen [Lutz et al. 1991]. Steady state creep is the stress-strain regime after the yielding point in which deformation takes place with a tiny increase in stress until the matrix cracks. Steady state creep of the matrix allows swelling of the UO_2 inclusions before crack formation of the matrix occurs. Before the yielding point, the linearly stress strain relation occurs and in the model of Lutz and Claussen solely this regime is assumed to be present.

The experimentally linearly deformation rate applied to bars of ceramics in order to:

- 1) determine the tangential strength or bending strength;
- 2) the presence of steady state creep;

is always hundreds till tens of thousands times larger than the required deformation rate of ceramics not to crack by swelling UO_2 inclusions in the present study. These literature data therefore have a smaller steady state creep regime than present during the EFTTRA-T3 irradiation conditions.

Little data about these creep regimes could be found by the author. From these literature data, it can be deduced that the linear deformation of MgO in the steady state creep regime is about 5 times larger than the regime with a linearly stress strain relation [Kingery et al. 1976];

temperature conditions and deformation rate of this experiment are unknown. But according to a deformation mechanism map of MgO for a grain size of 100 μm [Poirier 1990], this matrix should not have cracked at all. That MgO did crack in the present study may be due to embrittlement during neutron irradiation but literature data about brittleness upon neutron irradiation for MgO is unknown to the author. Nevertheless, the steady state creep regime of MgO may have caused that the swelling of UO_2 after inter-particle fracture is significantly smaller than the dimensional swelling of UO_2 in Table 5.16.

Only a linearly stress-strain relationship could be observed for MgAl_2O_4 [Viallard et al. 1997]; the temperature of this stress-strain curve is unknown. Yielding points and permanent deformation are clearly observed in the stress strain curves of single crystals of spinel at 1693-1903 K [Poirier 1990]. The absence of creep in the matrix MgAl_2O_4 at the temperature conditions of EFTTRA-T3 might explain the similar value obtained for the swelling of the UO_2 inclusions and the swelling of the UO_2 inclusions after inter-particle fracture in Table 5.16. The strain stress regimes for the other polycrystalline ceramics are unknown to the author.

5.10.5 Radial thermally induced stress gradient

The stress at the interface between UO_2 and the matrix is assumed to solely dependent on the swelling of inclusions. The radial thermally induced stress gradient, induced by the average low linear power (55 W/cm till 24 W/cm), is neglected for the determination of the crack formation of the matrix. This small thermally induced stress gradient is expected not to have an impact on the size of the fission-gas bubbles. This is true for the fission-gas bubbles in UO_2 since no difference could be observed between the porosity measured in the inclusions situated in the core or at the edge of the pellet. The stress profile induced by the thermal gradient results in a compressive stress in the centre of the pellet and an expansive stress at the edge of the pellet. The bubbles in the implantation zones of $\text{Y}_3\text{Al}_5\text{O}_{12}$ from half the radius to the edge of the pellet are significantly larger than the fission gas bubbles in these zones located more in the centre of the pellet. This small thermally induced stress gradient had an impact on the size of the fission-gas bubbles in $\text{Y}_3\text{Al}_5\text{O}_{12}$. It seems that the formation of bubbles in $\text{Y}_3\text{Al}_5\text{O}_{12}$ heavily depends on the hydrostatic pressure.

5.10.6 Impact of irradiation fission induced creep of the matrix

EPMA measurements show that UO_2 inclusions are surrounded by a shell of fission products in the matrices; the implantation zones of the matrices. Paragraph 5.9.2.1 showed that cracks are not always positioned at the interface between UO_2 inclusion and the ceramic matrices $\text{Y}_3\text{Al}_5\text{O}_{12}$, MgAl_2O_4 and MgO. The question is whether the implantation zone surrounding the UO_2 -inclusion can be regarded as a zone with high strain rates in which large creep occurs. This creep is caused by the highly local emission of fission products from fissile inclusions and stress introduced by swelling of the actinide inclusions. This creep probably prevented the formation of cracks in the implantation zones. Before the implanted fission product stops in the material, atoms are displaced from their position and frictional energy is released. Figure 5.27 shows the implantation profile of Figure 5.18 accompanied with the profile with displacements per atom (dpa) and average power frictional density. It is assumed

that all fission products are ^{95}Zr (98 MeV) and all atoms have a displacement energy of 20 eV for simplicity.

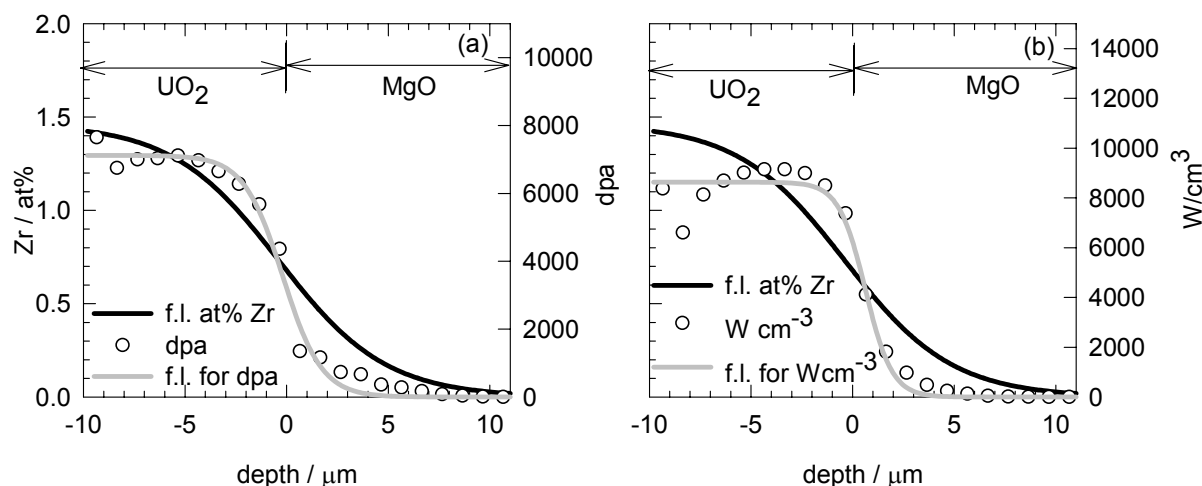


Figure 5.27 (a) Concentration of Zr and dpa and (b) concentration of Zr and power density by fission tracks, f.l. fitted line to guide the eye.

The dip in dpa from the UO_2 phase to the MgO phase is due to the 4.4 times on average larger mass of UO_2 in comparison with MgO , by which more displacements can be generated by recoil atoms. The number of displacements in the implantation zone of MgO created by fission tracks is about 100 times larger than in solely neutron irradiated zones. Insufficient statistics caused the larger scatter in the calculation. The combination of displacements and the power density created by the fission tracks may result in sufficient creep of the matrix by which also densification might occur.

Bleiburg, Berman and Lustman [Bleiburg et al. 1962] measured densification in a homogeneous-dispersed fuel of $\text{ZrO}_2 + \text{UO}_2$ after a tiny exposure of fission products. The volume decrease for these fuels after this tiny exposure of fission products was similar to the initial porosity. The rate of creep in ZrO_2 was about 5 times larger than that of UO_2 at the same rate of exposure of fission products. Densification of ZrO_2 can therefore take place at a lower rate of exposure of fission products than UO_2 .

For macro-dispersed fuels, densification of the matrices by fission-induced creep is limited to the implantation zones. The space obtained by reduction in volume of these zones can be used for swelling of the UO_2 inclusions preventing crack formation of the matrix. However, the porosity of the matrices MgO and MgAl_2O_4 are too small and the UO_2 inclusions are too large to prevent crack formation of the matrix due to swelling of the UO_2 inclusions by fission-induced creep of the matrix [Neeft 2003].

5.10.7 Solid solution with fissile phase

No solid solution could be detected in the fabricated targets between UO_2 and the matrices MgO , MgAl_2O_4 and $\text{Y}_3\text{Al}_5\text{O}_{12}$ by X-ray diffraction as well as the α -autoradiographs. The presence of a solid solution could clearly be observed between CeO_{2-x} and Y_2O_3 using X-

ray diffraction, α -autoradiograph and EPMA. The impact of such a solid solution is increasing the fission-induced creep zone in which swelling of the fissile inclusion can occur without crack formation of the matrix. The reduction in volume of the matrices CeO_{2-x} and Y_2O_3 by elimination of porosity by fission induced creep can accommodate a maximum swelling of UO_2 of about $10\times$ and $4\times$ times the swelling in Table 5.16, respectively [Neeft 2003]. The increase in hardness of both materials as measured after irradiation in Table 5.14 probably indicates densification of both matrices (polluted with uranium and fission products).

The shrinkage rate of the matrix by fission induced creep in order to prevent cracks in the matrices is a difficult parameter to control during irradiation. A very large porosity of the matrix and pollution of matrix with actinides to enhance densification in order to prevent cracks in the matrix may also result in an increase of the gap width between pellet and cladding resulting in a higher fuel temperature. Macro-dispersed fuel with pollution of actinides in the matrix with a large porosity is therefore not a suitable fuel concept.

5.10.8 Use of ellipsoidal fissile inclusions instead of spherical fissile inclusions

In the present study, the UO_2 particles were ellipsoidal instead of spherical. Cracks from fissile to fissile inclusion are aligned perpendicular to the height of the pellet, as can clearly be viewed in Figure 5.12. This shape and orientation of the UO_2 inclusions may have the advantage in comparison with spherical inclusions that after crack formation of the matrix, continuation of swelling of the fissile inclusion results in a change in height of the pellet and thereby pellet cladding interaction is prevented.

5.10.9 Fission-gas release

5.10.9.1 Determination of fission-gases in UO_2 inclusions

Paragraph 5.7.3 showed that the fission gas release of the macro dispersed fuels $\text{UO}_2+\text{MgAl}_2\text{O}_4$ and $\text{UO}_2+\text{Y}_3\text{Al}_5\text{O}_{12}$ was about 50%; this fission-gas release was determined by the number of gas atoms measured in the plenum and the number of calculated gas atoms that are generated during fission of actinides. Paragraph 5.9.3.1 showed that no thermal migration of Xenon took place in the matrices (outside the implantation zones). Paragraph 5.9.4 showed that most fission products were implanted in the UO_2 inclusions. In this paragraph, the amount of Xenon in the UO_2 inclusions is determined using ceramography and literature data of UO_2 in order to understand the high fission gas release of the two fuels.

The amount of Xenon and Krypton inside the UO_2 inclusions can be determined from the pore distribution and using the following relation that relates the size of the pores to the content of fission gases. The pressure of a fission gas bubble is described by [Koo et al. 2001]:

$$P_{\text{bubble}} = \frac{2\gamma}{R_{\text{bubble}}} + P_{\text{hydro}} + P_{\text{ex}} \quad (5.11)$$

where γ is the surface tension of the material, R_{bubble} is the radius of the bubble, P_{hydro} is the hydrostatic stress on the bubble and P_{ex} is the excessive pressure above equilibrium. These are pores with a radius between 0.1 and 1.0 μm . The surface tension of UO_2 is assumed to be 1.0 J m^{-2} [Koo et al. 2001]. For bubbles:

$$P_{ex} = \frac{Gb}{R_{bubble}} \quad (5.12)$$

where G is the shear modulus of UO_2 of 82 GPa and b is the Burgers vector with a value of 0.39 nm. The number of xenon atoms per pore is determined by [Koo et al. 2001]:

$$N_{Xe} = \left(\frac{4\pi R_{bubble}^3}{3} \right) \times \left(B + \frac{kT}{P_{bubble}} \right)^{-1} \quad (5.13)$$

where B for Xe is $85 \text{ \AA}^3/\text{atom}^{\text{EOS}}$.

The two-dimensional distribution of pores is determined using image analysis of ceramographic sections of UO_2 inclusions [Neeft 2003]. The number of pores per volume with a certain radius is determined using the Saltykov-method for the transformation of a two-dimensional distribution of pores into a three dimensional distribution of pores [ASM 1995].

The amount of Xe in the bubbles of UO_2 in the fuel is then determined by:

$$Xe_{fuel,bubble,UO_2} = \left\{ 1 + \frac{\Delta V}{V_{UO_2}} \right\} \times V_f \times V_{pellets} \times \sum_{D_{min}}^{D_{max}} N_{V,D_i} \times N_{Xe} \quad (5.14)$$

where $\Delta V/V_{UO_2}$ is the volume swelling of UO_2 , V_f is the initial volume fraction of UO_2 and $V_{pellets}$ is the initial volume of the pellets in the fission stack length, N_{V,D_i} is the number of pores per volume with diameter D_i determined by the Saltykov-method and N_{Xe} is the number of xenon atoms per pore. For UO_2 in pin 1, 5 and 18 the fractional volume swelling of UO_2 is taken as 0.5 and for UO_2 in pin 11 and 15 as 0.7. The amount of Xenon in the solid phase of UO_2 in the fuel is determined by:

$$Xe_{fuel,solid,UO_2} = \left\{ 1 + \frac{\Delta V}{V_{UO_2}} \right\} \times V_f \times V_{pellets} \times (1 - P_{UO_2}) \times Xe_{solid,UO_2} \quad (5.15)$$

where P_{UO_2} is the fraction in porosity of the UO_2 inclusions, Xe_{solid,UO_2} results from the experimental value of 0.25 wt% [Koo et al. 2001] at zero porosity of UO_2 .

Table 5.18 shows the amount of Xe in UO_2 in bubbles and solid phase using the distribution in size and number of fission gas bubbles and a temperature of 800 K. The term

$\frac{Xe_{bubble} + Xe_{matrix}}{Xe_{produced} \times \{1 - E_{UO_2,fp}\}}$ in Table 5.18 represents the amount of Xe determined using ceramography and using the previous described equations in UO_2 divided by the calculated amount of generated Xe in UO_2 . $1 - \frac{Xe_{bubble} + Xe_{matrix}}{Xe_{produced} \times \{1 - E_{UO_2,fp}\}}$ is the fractionally xenon release from UO_2 . E_{fp} is the emission of fission products by fission of actinides as determined in paragraph 5.9.4.

Pin 5 shows more Xenon in UO_2 than calculated by fission of actinides. This is probably due to the small area in which the porosity is measured and therefore the observation of areas with larger pores is missed as discussed in paragraph 5.9.2.

^{EOS} More Xenon is present in bubbles than the calculated generated amount of Xenon in Table 5.7 when using the equation of state for Xenon at 800 K by Schwarzblat [Schwarzblat 1981]. This equation of state of Xenon is therefore assumed to be incorrect.

The xenon release from UO₂ using ceramography is 6-10 times larger for nearly non-cracked matrices than the xenon release in Table 5.7. For the fuel with extensively cracked matrices, xenon release using ceramography is about 1.5-1.8 times larger than xenon release determined from the gas in the plenum and calculated burn-up.

Table 5.18 Xenon in UO₂ at 800 K

UO ₂ inclusions in matrix	I	Xe in bubbles of UO ₂ in all pellets ×10 ¹⁸	Xe in solid UO ₂ in all pellets ×10 ¹⁸	$\frac{Xe_{bubble} + Xe_{matrix}}{Xe_{produced} \times \{1 - E_{UO_2,fp}\}}$
CeO _{2-x}	C	6.2	4.8	0.36
CeO _{2-x}	E	6.7	5.4	0.40
Y ₂ O ₃	E	9.1	5.4	0.42
MgO	E	29.5	6.4	1.15
MgAl ₂ O ₄	C	2.7	4.9	0.21
Y ₃ Al ₅ O ₁₂	C	6.8	5.1	0.32

I = Image, C determined from ceramographic images, E determined from electron absorption images, $0.871 = 1 - E_{fp}$

Probably, xenon diffused into the implantation zones of the matrices instead of the plenum. It is difficult to confirm this hypothesis with the EPMA data in figure 5.19. Only fuels that do not form a solid solution with UO₂ can be compared. The wt% of Xe in the implantation zone of Y₃Al₅O₁₂ is about 3 times smaller than the wt% of Xe in the implantation zone of MgO. The range in which Xenon could be measured is about 10 μm in the implantation zone of MgO and about 7 μm in the implantation zones of Y₃Al₅O₁₂ and MgAl₂O₄. It is therefore questionable whether the high wt% of Xenon and large range in which Xenon could be measured in the implantation zone MgO, is only due to implantation of Xe. Possibly, this could also be due to Xenon release from the UO₂ inclusion.

5.10.9.2 Fission gas release from UO₂

Empirical data for the migration of fission gas in UO₂ are:

- 1) The migration energy (E_M) of Xe is measured to reduce almost linearly with burn-up from about 6 eV at 0 GWd/tU till 3 eV at 100 GWd/tU^a [Hiernaut et al. 2001];
- 2) The experimental migration energies for Xenon are measured to be 6.0±0.1 eV in UO_{2-x}, 3.9±0.4 eV in UO₂ and 1.7±0.4 eV in UO_{2+x} [Miekeley et al. 1972];

Atomistic calculations show that the empirical migration energy of xenon is similar to the cation migration of UO₂ for the three different stoichiometries of UO₂ indicating that the migration of xenon depends on the cation migration [Grimes 1990].

UO₂ becomes UO_{2+x} at higher burn-up due to the average lower oxidation state of fission products with respect to uranium. Not all oxygen atoms per fission U atom form

^a GWd/tU=GigaWattday per ton uranium = 10×0.95×FIMA%.

compounds with fission products; some fission products are inert like fission gases or form metal islands instead of oxides. The UO_2 inclusions embedded in MgAl_2O_4 for the present study are irradiated till 187 GWd/tU (pin 11). For the present study, it is therefore expected that UO_{2+x} is present after irradiation. A simple model is used to have an indication of the xenon release since there is too limited information about the characteristics of UO_2 of the present study. The pre-diffusion factor is assumed to be $0.5 \text{ cm}^2\text{s}^{-1}$ [Matzke 1991]. It is assumed that the migration energy for Xe linearly reduces with increasing burn-up till a value of 1.7 eV where it remains constant for higher burn-up. The generation rate of Xe at BOI is about 2.8 times larger than EOI (see Table 5.4). The time to diffuse out of a medium is described by [Atkins 1990]:

$$t = \frac{\langle x^2 \rangle}{2 \times D} \quad (5.16)$$

where x is the root mean square distance and D is the diffusion coefficient. x is taken here as the average radius of the UO_2 particle of $96.5 \text{ }\mu\text{m}$ and $D = D_0 e^{-\frac{E_M}{kT}}$ where T is 800 K. Figure 5.28 shows the Xe production rate, assumed migration properties of Xe in UO_2 and time for Xe to migrate out of UO_2 using equation 5.16. It shows that at about half the irradiation period, it takes about on average about 55 days for a Xe atom to diffuse the distance of $96.5 \text{ }\mu\text{m}$ that is the average radius of the sphere. At about half of the irradiation period 60% to 70% of xenon is generated by fission. Thus, this generated amount of 60% to 70% of xenon is released from the UO_2 inclusion at least before EOI since the root mean square distance is smaller than the radius of the particle. This corresponds to the low amount of xenon of UO_2 inclusions in Table 5.18. If a UO_2 inclusion is surrounded by cracks than fission gas release can also take place directly to the plenum. This case was present for UO_2 inclusions embedded in MgAl_2O_4 and $\text{Y}_3\text{Al}_5\text{O}_{12}$.

5.10.10 The origin of CO_2

Table 5.16 shows that 13 vol% CO_2 was measured in the plenum of capsule 7 with pellets of $\text{MgO}+\text{UY}_6\text{O}_x$ after neutron irradiation. This large amount of CO_2 cannot be introduced during the welding technique since this amount of CO_2 is too large to originate from air. The large amount of porosity near and in the UY_6O_x inclusions as observed in the ceramographic sections before neutron irradiation suggest that a gaseous phase was created during sintering. Therefore, the hypothesis that a carbonaceous mineral was created during the fabrication is evaluated. The metal stoichiometry was determined by ICP-AES and IDMS: wt% U = 22.45 ± 0.08 and wt% Y = 49.9 ± 0.2 . If this compound was a stoichiometric compound of U_3O_8 and $[\frac{5.94}{2}] \text{ Y}_2\text{O}_3$ than 90 wt% of this compound can be attributed to the uranium-and yttrium-compound. No additional precautions were taken to the gas atmosphere during fabrication. It is therefore assumed that the fabrication was performed in air. From a simulation of precipitation performed in air it can be deduced that yttrium-carbonates precipitated instead of yttrium-hydrates using the partial pressure of CO_2 in air. The precipitated compound after heating at 1073 K could be $\text{U}_3\text{O}_8\text{-}2.16\text{Y}_2\text{O}_3\text{-}0.81\text{Y}_2(\text{CO}_3)_3$, resulting in 100 wt%. Possibly, this compound was sintered in the pellet with matrix at 1873 K. The 13 vol% CO_2 in the plenum measured after irradiation is about 0.4% of the suggested amount of CO_2 in the previously described uranium-yttrium complex [Neeft 2003].

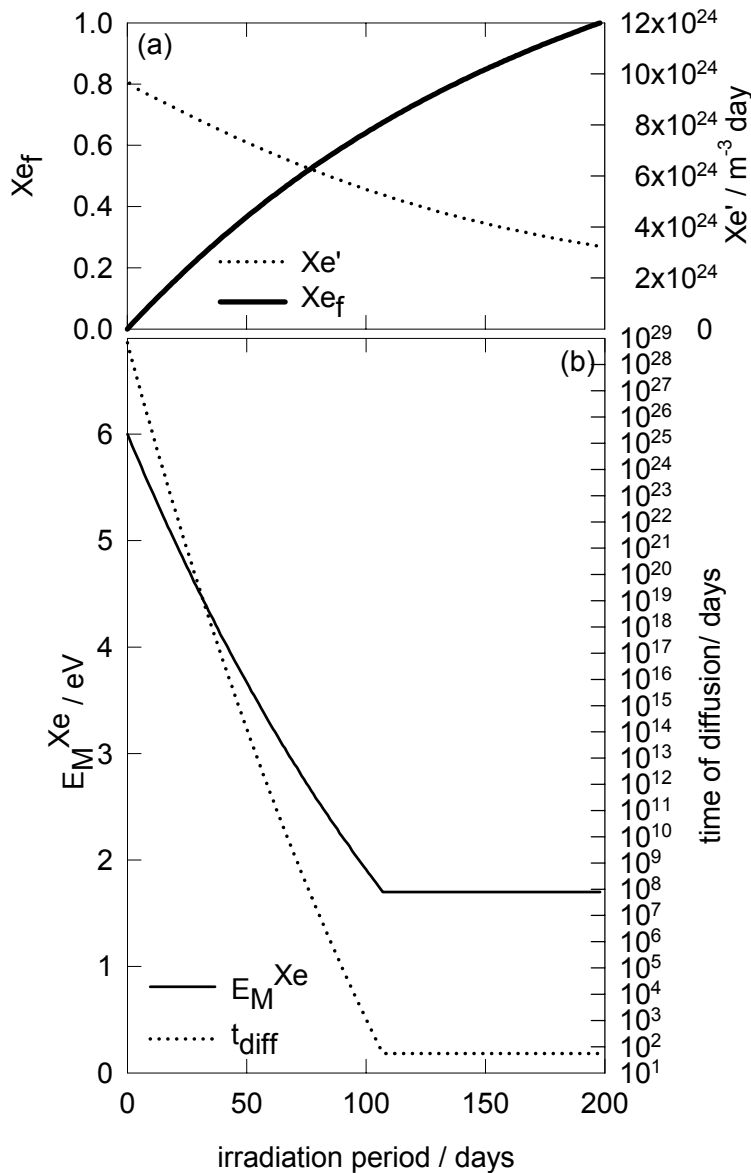


Figure 5.28. (a) Fraction generated Xe (Xe_f) and production rate of Xe (Xe') versus irradiation time and (b) assumed migration energy and time of diffusion at 800 K for a distance of $96.5 \mu\text{m}$ versus irradiation time.

5.11 Conclusions

Matrices without fissile phase

Pellets without fissile phase show a swelling less than +1 vol% after a neutron fluence of $6\text{-}7 \times 10^{25} \text{ m}^{-2}$ ($E > 0.1 \text{ MeV}$) and an irradiation temperature of 650-700 K, except BaZrO_3 . Only small fragments were left of the neutron irradiated BaZrO_3 . No change in microstructure could be observed in the bulk of other pellets.

Fission product distribution in matrices

The presence of fission products is limited to the implantation zone of fission products. No thermally induced migration of fission products in the

matrices outside the implantation zones took place in IMF at an irradiation temperature of 700-1000 K. The volume of matrix implanted with fission products is 5-10 vol% for macro dispersed IMF that did not form a solid solution with UO_2 after sintering. These fuels are UO_2 embedded in MgO , MgAl_2O_4 and $\text{Y}_3\text{Al}_5\text{O}_{12}$. About 50-100 vol% of matrix is implanted with fission products for the other macro-dispersed IMF. These are UO_2 embedded in Y_2O_3 and CeO_{2-x} and $(\text{U},\text{Y})\text{O}_x$ embedded in MgO and MgAl_2O_4 . For the micro-dispersed fuel $\text{UO}_2 + \text{MgAl}_2\text{O}_4$ 100 vol% of the matrix is implanted with fission products.

Fissile phases

The UO_2 inclusions in the matrices CeO_{2-x} , MgO and Y_2O_3 swelled about 50 vol% and in the matrices MgAl_2O_4 and $\text{Y}_3\text{Al}_5\text{O}_{12}$ about 75 vol%; the percentage of fissioned actinides was 17% and 20% respectively. The porosity of the irradiated UO_2 inclusions ranged from 30% to 40%. For the UY_6O_x inclusions, no swelling data is available except that the porosity in these

fissile inclusions reduced with about 40%. Fission gas bubbles could mainly be observed in the yttrium-aluminium phase for fuels made with powders of MgAl_2O_4 and UY_6O_x .

Cracks in matrices

The matrices MgO , MgAl_2O_4 and $\text{Y}_3\text{Al}_5\text{O}_{12}$ show cracks in the matrices from UO_2 inclusion to UO_2 inclusion; these cracks do not penetrate the inclusions and were not present before irradiation. These cracks are absent or rarely present in the matrices CeO_{2-x} and Y_2O_3 . Cracks from UY_6O_x inclusion to UY_6O_x inclusion were present before and after irradiation in MgO and only present after irradiation in MgAl_2O_4 .

Dimensional change of fuels and matrices

IMF with acceptable change in volume of pellets (-1.5 vol% till 1.5 vol%) are $\text{MgO}+\text{UO}_2$, $\text{MgO}+\text{UY}_6\text{O}_x$, $\text{MgAl}_2\text{O}_4+\text{UO}_2$ (micro-dispersed) and $\text{Y}_2\text{O}_3+\text{UO}_2$. $\text{CeO}_{2-x}+\text{UO}_2$ decreased 5 vol%. A decrease in volume is unwanted since the gap of the cladding can increase too much and thereby the fuel temperature increases too much. The swelling of $\text{MgAl}_2\text{O}_4+\text{UO}_2$ (7 vol%) and $\text{MgAl}_2\text{O}_4+\text{UY}_6\text{O}_x$ (3 vol%) are proportional to the width of the cracks in the matrices. By shape and orientation of the UO_2 inclusions, solely axial swelling of the pellet occurred due to swelling of the UO_2 inclusions for $\text{MgAl}_2\text{O}_4+\text{UO}_2$. $\text{Y}_3\text{Al}_5\text{O}_{12}+\text{UO}_2$ showed a swelling of 11 vol% and only this IMF deformed the cladding. The swelling is attributed to the zone of $\text{Y}_3\text{Al}_5\text{O}_{12}$ surrounding the UO_2 inclusions that is implanted with fission products. Only in these implantation zones of $\text{Y}_3\text{Al}_5\text{O}_{12}$, fission gas bubbles could be observed after irradiation. The solid state swelling of MgAl_2O_4 is at least ten times larger than UO_2 .

Fission gas and caesium release

Fission-gas release of IMF $\text{Y}_3\text{Al}_5\text{O}_{12}+\text{UO}_2$ and $\text{MgAl}_2\text{O}_4+\text{UO}_2$ is near 50%. The fission-gas release of IMF $\text{MgAl}_2\text{O}_4+\text{UO}_2$ (micro dispersed) is near 0%, the other IMF have fission-gas releases from 4% to 8%. Fission-gas release should be limited since it reduces the thermal conductivity of the helium filled gap and it also increases the pressure inside the cladding. An increase of the pressure inside the cladding may result in a larger pressure than the pressure of water against the cladding and thereby resulting in a larger gap width. Both effects caused by fission-gas release increase the temperature of the fuel. The fission gases in the present study are Xe and Kr.

The cesium release is for all IMF smaller than 2%, except for $\text{CeO}_{2-x}+\text{UO}_2$; this fuel showed a cesium release from 3% to 6%. Cesium release should be limited in order to prevent increase of the radiation dose for reactor employees in case of a crack in the cladding.

Hardness and fracture toughness

The hardness and fracture toughness of the matrices Y_2O_3 and CeO_{2-x} (polluted with uranium and fission products) increased after irradiation. The fracture toughness of MgAl_2O_4 and $\text{Y}_3\text{Al}_5\text{O}_{12}$ decreased.

Cause of inter-particle fracture in matrices and high fission gas release

With the mechanical properties of the matrices and UO_2 , average diameter of the UO_2 inclusions (193 μm) and volume fraction of UO_2 (0.025), it was deduced that a swelling of UO_2 of less than 3 vol% is required to obtain inter-particle fracture in the matrix when creep of the matrix is neglected. This is by far smaller than the measured swelling of UO_2 of 50-70%. That the matrices CeO_{2-x} and Y_2O_3 did nearly not show inter-particle fracture is probably due to reduction in volume of the matrix by (fission-induced) creep leaving room for the UO_2 inclusions to swell. UO_2 inclusions are in direct contact with the plenum after the formation of cracks in the matrices MgAl_2O_4 and $\text{Y}_3\text{Al}_5\text{O}_{12}$ resulting in a high fission gas release at high burn-up of UO_2 .

5.12 Final remarks

How can the present study be extrapolated for future research on inert matrix fuel? The irradiation temperature of the IMF in the present study is quite low (700-1000 K) and not comparable to irradiation temperature conditions in a reactor. Creep of the matrix may be larger during irradiation reactor conditions and may prevent cracks in the matrix induced by swelling of fissile inclusions. Nevertheless, since the cause for cracking of matrices in macro-dispersed fuels is understood, improvements, argued with the results and interpretations of the present study, can be given for these fuels.

Improvements for macro-dispersed fuels

In order to keep a steady-state volume of the pellet or prevent pellet cladding interaction during irradiation of macro dispersed fuels, it is probably best to:

- 1) induce a large porosity in the fissile inclusions during sintering in order to obtain the required space for swelling by fission products;
- 2) have a matrix that is polluted by actinides in order to increase the creep during irradiation conditions;
- 3) not to form a solid solution between fissile phase and matrix during sintering that is susceptible for swelling by implantation of fission products;
- 4) use of oriented ellipsoidal inclusions instead of spherical inclusions.

ad 1) The formation of porous inclusions in this study was performed by the formation of carbonaceous minerals during fabrication. During sintering, CO_2 dissociated and a large porosity was left after sintering.

ad 3) This study showed that fission gas bubbles were present in the yttrium-aluminium phase and not in the other phases present in the pellet. This phase is a solid solution between the fissile phase (uranium-yttrium oxides) and the matrix (MgAl_2O_4).

ad 4) If inter-particle fracture occurs in the macro-dispersed fuel, despite the three improvements, cracks in the matrices will be orientated parallel to the diameter of the pellet. The dimensional change of the fuel, induced by swelling of the fissile inclusions, will be axially and not diametrically. Diametrically dimensional change may cause deformation and cracking of the cladding. These ellipsoidal oriented inclusions embedded in matrix can be made by uni-

or opposite bi-directional pressing a mixture of spherical porous fissile microspheres and matrix powder into a pellet.

Micro-or macro-dispersed fuel?

For $\text{MgAl}_2\text{O}_4+\text{UO}_2$, the micro-dispersed fuel had, in this irradiation, a better performance than the macro-dispersed fuel concerning dimensional swelling, pellet integrity and fission gas release. However, the concentration of fissile atoms in the entire pellet is at least 6 times smaller than ordinary reactor fuels. The uranium free materials studied up till now show a larger swelling than UO_2 at similarly fission product concentration. The concept of macro-dispersed fuel is still a promising option since the concentration of fission products averaged over the entire matrix is smaller. The contribution in swelling of the pellet by swelling of fission products in the matrix can therefore be smaller than micro-dispersed fuels if swelling by fission products in the matrices is limited to solid state swelling.

Fissile phase diluted in actinides

The macro-dispersed fuel with diluted fissile inclusions in this irradiation perform well but it is unclear whether or not this is due to dilution of fissile atoms or the large porosity near and in these fissile inclusions generated during fabrication.

Discrimination of matrices

$\text{Y}_3\text{Al}_5\text{O}_{12}$ is not a suitable inert matrix since it shows extensive fission gas swelling when implanted with fission products.

CeO_{2-x} is less suitable as an inert matrix because after sintering in a reducing atmosphere pellets are fragile, it showed the highest Cs release of IMF and had a large shrinkage rate at these irradiation conditions. CeO_{2-x} could possibly be used to dilute the fissile phase to account for the excess of oxygen generated at higher burn-up of actinides.

The swelling by fission products by MgAl_2O_4 is till highly fission product concentrations limited to solid state swelling, no fission gas bubbles could be viewed in this matrix and the implantation zones show no outbreak. If this matrix is polluted in uranium than inter-particle fracture in the matrix may be prevented during irradiation.

MgO performed well during this irradiation programme but its hydrophilic behaviour puts an extra constraint on the fabrication of fuels and the outbreak observed after polishing of the irradiated matrix, especially in the implantation zones, may indicate amorphisation by fission products.

Y_2O_3 (polluted in uranium) seems to be the best inert matrix for the aspects tested in this irradiation programme: small Xe, Kr –and caesium release, absence of fission gas bubbles in the implantation zones, integrity of the implantation zones, dimensional stability, integrity of the pellets during irradiation possibly due to fission induced irradiation creep and remaining firm after sintering in a reducing atmosphere.

Appendix

Derivation of trapping rates

For the derivation of the trapping rate of helium for defects and intergranular pores, it is assumed that every imaginary cell contains one defect/intergranular pore. These imaginary cells are represented by a sphere/circle with radius R_V / R_A . The boundary conditions are:

-at the edge $c(R_V) / c(R_A) = c_s$;

-in the defect/intergranular pore: $c(r_i) / c(r_p) = 0$

General solutions of the stationary diffusion equations are required. For defects a 3-D approach is used and for intergranular pores a 2-D approach is used.

The 3-D approach requires the stationary diffusion equation for spheres. This is:

$$\frac{\partial c}{\partial r} \left(r^2 \frac{\partial c}{\partial r} \right) = 0 \quad (\text{A.1})$$

The general solution of this equation is:

$$c = \frac{A}{r} + B \quad (\text{A.2})$$

The boundary conditions are: $c(R_V) = \frac{A}{R_V} + B = c_s$ and $c(r_i) = \frac{A}{r_i} + B = 0$, where R_V and r_i are the radius of the imaginary cell and the radius of the defect, respectively. With these boundary conditions the constants A and B can be found. Differentiation of this equation results in $\left\{ \frac{\partial c}{\partial r} \right\}$. The trapping rate of helium for a single defect is:

$$K^{s_{r_i}} = -4\pi r_i^2 D \left\{ \frac{\partial c}{\partial r} \right\}_{r=r_i} = -4\pi D c_s \left(\frac{1}{\frac{1}{R_V} - \frac{1}{r_i}} \right) = 4\pi r_i D c_s \quad \text{if } R_V \rightarrow \infty \quad (\text{A.3})$$

Equation (A.3) times the concentration of defects ($N_t = \frac{1}{\frac{4}{3}\pi R_V^3}$) results in the trapping rate of

helium at defects in the bulk.

The 2-D approach requires the stationary diffusion equation for cylinders. This is:

$$\frac{\partial c}{\partial r} \left(r \frac{\partial c}{\partial r} \right) = 0 \quad (\text{A.4})$$

The general solution of this equation is:

$$c = A + B \ln r \quad (\text{A.5})$$

The boundary conditions are: $c(R_A) = A + B \ln R_A = c_s$ and $c(r_p) = A + B \ln r_p = 0$, where R_A and r_p are the radius of the imaginary cell and the radius of the intergranular pore, respectively. With these boundary conditions the constants A and B can be found. Differentiation of this equation results in $\left\{ \frac{\partial c}{\partial r} \right\}$. The trapping rate of helium for a single intergranular pore is:

$$K^s_{r_p} = 2\pi r_p D \left\{ \frac{\partial c}{\partial r} \right\}_{r=r_p} = \frac{2\pi D c_s}{\ln \left\{ \frac{R_A}{r_p} \right\}} \quad (\text{A.6})$$

Equation (A.6) times the concentration of intergranular pores ($N_p = \frac{1}{\pi R_A^2}$) results in the trapping rate of helium in the grainboundaries for intergranular pores.

For intragranular pores, the 3D approach for defects can be used.

- [Allen 1993] W.R. Allen, *J. Nucl. Mater.* 199 (1993) 121.
- [Ando et al. 1974] K. Ando, Y. Oishi, *J. Chem. Phys.* 61 (1974) 625.
- [ASM 1995] American Society for Metals, *Metallography and Microstructures*, vol.9, 6th Ed., (1995) USA, 123-134.
- [Atkins 1990] P.W. Atkins, *Physical Chemistry*, (Oxford University Press, Oxford, 1990) p. 785-793.
- [Beemsterboer 2001] B. Beemsterboer, research note K5041/01.42726 FAI/BB/JY.
- [Belvroy et al. 1998] R. Belvroy, G. Dassel, K.A. Duijves, M.G. Horsten, E.V. Osch, Specifications of post-irradiation examinations in the ECN Hot Cell Laboratory, ECN Nuclear Facilities 027/96-002 (1998).
- [van den Berg et al. 1999] F.A. van den Berg, K. Bakker, WDX-microanalyse aan radioactieve preparaten, project number 71069 (1991).
- [Bleiburg et al. 1962] M.L. Bleiburg, R.M. Berman, B. Lustman, *Symposium on Radiation damage in solids and reactor materials in Venice (1962)* by IAEA, 319
- [de Boer 1997] R. de Boer, A thermodynamic study on the zirconium-tellurium and the cesium-tellurium systems, University of Amsterdam, (1997) p. 15
- [Border et al. 1995] N. Bordes, K.E. Sickafus, E.A. Cooper, R.C. Ewing, *J. Nucl. Mater.* 225 (1995) 318.
- [Boshoven et al. 1997] J.G. Boshoven, E.A.C. Neeft, R.J.M. Konings, K. Bakker, H. Hein Fabrication of targets for heterogeneous transmutation {EFTTRA-T3, ARIM and EFTTRA-T4ter irradiation experiments}, ECN-I-97-025.
- [Bourgain et al. 1978] J.C. Bourgain, J.W. Courbett, *Radiation Effects* 36 (1978) 157.
- [Buckley 1986] S.N. Buckley *J. Nucl. Mater.* 141-143 (1986) 387.
- [van Bueren 1961] H.G. van Bueren, *Imperfections in crystals* (North-Holland Publishing, Amsterdam, (1961)
- [Busker et al. 2000] G. Busker, M.A. van Huis, R.W. Grimes, A. van Veen, *Nucl. Instr. and Meth. in Phys. Res. B* 171 (2000) 528.
- [Buurveld 1999] H.A. Buurveld, *Gamma-spectrometry profiles of pins*, only electronic files.
- [Carlslaw et al. 1959] H.S. Carlslaw, J.C. Jeager, *Heat conduction in Solids*, (Oxford University Press, Oxford, 1959).
- [Chauvin et al.2002] N. Chauvin, C. Thiriet-Dodane, J. Noirot, H.J. Matzke, R.J.M. Konings, T. Wiss, R.P.C. Schram, K. Bakker, E.A.C. Neeft, R. Conrad, A. van Veen, T. Yamashita, *Synthesis on MgAl₂O₄ irradiation results*, EC-JRC-ITU Report 1453, (2002) p. 8, 27 and 41.
- [Chen et al. 1996] S.P. Chen, M. Yan, J.D. Gale, R.W. Grimes, R. Devanathan, K.E. Sickafus, N. Yu, M. Nastasi, *Phil. Mag. Lett.*, 73 (1996) 51.
- [Cleave 2004] A. Cleave, correspondence by email in 2004.
- [Conrad 1997] R. Conrad, EFTTRA-T3, Irradiation of candidate inert matrices for the heterogeneous transmutation of fission products at the High Flux Reactor, HFR/97/4371, 11
- [Crank 2001] J. Crank, *The mathematics of diffusion*, (Oxford Science Publications, Oxford, 2001) p. 5.
- [Crawford et al. 1978] J.H. Crawford, K.H. Lee, G.S. White, *Bull. Amer. Phys. Soc.* 23 (1978) 253.
- [Damen 2003] P.M.G. Damen, Helium and fission gas behaviour in magnesium aluminate spinel and zirconia for actinide transmutation, Delft University of Technology (2003) p. 131.

- [Dassel et al. 1999] G. Dassel, H.A Buurveld, J. Minkema Gamma spectrometry of EFTTRA 280-T3, ECN-I—98-064.
- [Dassel 1999] G. Dassel, research note 20002/99.27378 IS/GD/NO.
- [Dienes et al. 1957] G.J. Dienes, G.H. Vineyard in Monographs in physics and astronomy 2 (1957) p. 150-152.
- [Downing et al. 1993] R.G. Downing, G.P. Lamaze, J.K. Langland, S.T. Hwang, J. Res. Natl. Inst. Stand. Technol. 98 (1993) 109.
- [Evans et al. 1983] J.H. Evans, A. van Veen, L.M. Caspers, Rad. Eff. 78 (1983) 105.
- [Fang et al. 2000] C.M. Fang, S.C. Parker, G. de With, J. Am. Ceram. Soc. 83 (2000) 2082.
- [Fedorov 2000] A.V. Fedorov, Evolution of point defect clusters during ion irradiation and thermal annealing, Delft University of Technology, (2000) p. 24-40.
- [Fink 1996] D. Fink, Neutron Depth Profiling, Hahn-Meitner-Institut, HMI-Berlin 539 (1996).
- [Freudenreich 1996] W.E. Freudenreich, Reactorfysica, Netherlands Energy Research Foundation, ECN-NUC-OPL-96-01, (1996).
- [Fromknecht et al. 2000] R. Fromknecht, J.-P. Hiernaut, Hj. Matzke, T. Wiss / Nucl. Instr. And Meth. In Phys. Res. B 166-167 (2000) 263.
- [Garner et al. 1994] F.A. Garner, G.W. Hollenberg, F.D. Hobbs, J.L. Ryan, J. Nucl. Mater. 212-215 (1994) 1087.
- [Gittus 1972] J.H. Gittus, Nuclear Eng. and Design 18 (1972) 69.
- [Grimes et al. 1990a] R.W. Grimes, C.R.A. Catlow, J. Am. Ceram. Soc. 73 (1990) 3251
- [Grimes et al. 1989] R.W. Grimes, C.R.A. Catlow, A.M. Stoneham, J. Phys.: Condens. Matter 1 (1989) 7367
- [Grimes et al. 1990b] R.W. Grimes, R.H. Miller, C.R.A. Catlow, J. Nucl. Mater. 172 (1990) 125.
- [Grimes 1972] N.W. Grimes, Philos. Mag. 25 (1972) 67.
- [Grimes 1990] R.W. Grimes, Simulating the behaviour of inert gases in UO₂, UKAEA, Harwell Laboratory Report, AEA-In-TEc-0195 (1990).
- [Grimes 1994] R.W. Grimes, J. Am. Ceram. Soc. 77 (1994) 378
- [Groot et al. 1988] P. Groot, F.A. van den Berg, Geavanceerde automatische dataverwerking bij de CAMECA elektronenmicrosonde, Netherlands Energy Research Foundation, ECN Report 88-106 (1988).
- [Gruppelaar et al. 1998] H. Gruppelaar, J.L. Kloosterman, R.J.M. Konings Advanced Technologies for the reduction of nuclear waste, Netherlands Energy Research Foundation, ECN-R—98-008, (1998).
- [Gritsyna et al. 2000] V.T. Gritsyna, I.V. Afanasyev-Charkin, V.A. Kobayakov, T.I. Voitsenya, K.E. Sickafus, Nucl. Instr. and Meth. in Phys. B166-167 (2000) 244.
- [Hahn 1993] T. Hahn, International Tables for Crystallography, (Kluwer Academic Publishers, Dordrecht, 1993).
- [Handbook of Chemistry and Physics 1992/2003] Handbook of Chemistry and Physics, CRC Press, Florida, 1992/2003
- [He et al. 2000] Z. He, P. Jung, Nucl. Instr. And Meth. In Phys. Res. B 166-167 (2000) 165.
- [Hiernaut et al. 2001] J.P. Hiernaut, C. Ronchi, J. Nucl. Mater. 294 (2001) 39.
- [Holbert] K.E. Holbert, <http://www.eas.asu.edu/~holbert/eee460/ReactorHeadProd.pdf>

- [Kingery et al. 1975] W.D. Kingery, H.K. Bowen, D.R. Uhlmann, Introduction to ceramics, (John Wiley&Sons, USA, 1975)
- [Klaassen et al. 2002] F.C. Klaassen, R.P.C. Schram, E.A.C. Neeft, R. Conrad, R.J.M. Konings, in Proc. of the Seventh information exchange meeting, Jeju 2002 Oct. 14-16 2002.
- [Klaassen et al. 2003] F.C. Klaassen, K. Bakker, R.P.C. Schram, R. Klein Meulekamp, R. Conrad, J. Somers, R.J.M. Konings, J. Nucl. Mater. 319 (2003) 108.
- [Konings et al 2000] R.J.M. Konings, R. Conrad, G. Dassel, B.J. Pijlgroms, J. Somers, E. Toscano, EUR 19138 (2000).
- [Koo et al. 2001] Y.-H. Koo, B.-H. Lee, J.-S. Cheon, D.-S. Sohn, J. Nucl. Mater. 295 (2001) 213.
- [Kuklja et al. 1999] M.M. Kuklja, R. Pandey, J. Am. Ceram. Soc. 82 (1999) 2881
- [Lambert Bates et al. 1981] J. Lambert Bates, J.E. Garnier, J.Am.Ceram.Soc. 64 (1981) C-138.
- [LSO 1997] NDO-PUNCT-AV/1, NDO-PUNCT-KV/1, NDO-PUNCT-AP/1, NDO-GAMMA-AV/1, NDO-GAMMA-AP/1, regulations for determination of pressure and volume of capsules and gammaspectrometry, Laboratory for Strong active Objects (LSO), department of Nuclear Research and Consultancy Group (1997).
- [Lutz et al. 1991] H.E. Lutz, N. Claussen, J. Europ. Cer. Soc. 83 (1991) 209.
- [Magill et al. 2003] J. Magill, V. Berthou, D. Haas, J. Galy, R. Schenkel, H.-W. Wiese, G. Heusener, J. Tomassi, G. Youinou, Nuclear Energy 42 (2003) 263.
- [Maschio et al.1990] S. Maschio, O. Sbaizero and S. Meriani, European Appl. Res. Rept-Nucl. Sci. Technol. 7 (1990) 1495.
- [Matzke et al. 2000] H.J. Matzke, P.G. Lucuta, T. Wiss, Nucl. Instr. Meth. in Phys. Res B 166-167 (2000) 920.
- [Matzke 1991] in S.E. Donnely, J.H. Evans (Eds.), Fundamental Aspects of Inert Gases in Solids, (Plenum Press, New York, 1991) p. 401-414
- [Miekeley et al. 1972] W. Miekeley, F.W. Felix, J. Nucl. Mater. 42 (1972) 297.
- [Mishra et al. 1977] R.K. Mishra, G. Thomas, J. Appl. Phys. 48 (1977) 4576
- [Morrell 1985] R. Morrel, Handbook of properties of technical & Engineering Ceramics, 1st, 1985, p. 128, 133
- [Munro et al. 1998] R.G. Munro, S.W. Freiman, T.L. Baker, Fracture toughness for brittle materials, 1998, NISTIR 6153
- [Navrotsky et al. 1967] A. Navrotsky, O.J. Kleppa, J. Inorg. nucl. Chem. (1967) 2715.
- [Neeft et al. 1999] E.A.C. Neeft, R.J.M. Konings, H. Schut, A.V. Fedorov, A. v. Veen in Advances in Science and Technology 24 (1999) 531.
- [Neeft et al. 2001] E.A.C. Neeft, K. Bakker, H.A. Buurveld, J. Minkema, A. Paardekooper, R.P.C. Schram, C. Sciolla, O. Zwaagstra, B. Beemsterboer, J.R.W. Woittiez, P. van Vlaanderen, W.J. Tams, H. Hein, R. Conrad, A. van Veen, Proc. 6th: Prog. Nucl. Energy 38 (2001) 427.
- [Neeft 2003] E.A.C. Neeft, Post Irradiation Examinations & additional characterization of EFTTRA-T3, NRG-report 21303/04.57381/I
- [Niihara et al. 1982] K. Niihara, R. Morena, D.P.H. Hasselman, J. Mater. Sci. Lett. 1 (1982) 13
- [Ohanian 1989] H.C. Ohanian, Physics, (W.W. Norton & Company, New York, 1989) p.1097.
- [Olander 1976] D.R. Olander, Fundamental aspects of nuclear reactor fuel elements, (TID-26711-P1, (1976) p.303.

- [Paardekooper 2000] A. Paardekooper, Neutron Metrology in experiment EFTTRA-T3 (R280-03), 20002/00.33777/P.
- [PCPDFWIN 1997] X-ray diffraction database, PCPDFWIN, version 1.30, 1997, ICDD.
- [Phase Equilibria Diagrams 1994] Phase Equilibria Diagrams Database, American Ceramic Society, NIST Standard Reference 31, 1994 (available on CD-rom)
- [Pirzada 2000] M. Pirzada, Note about Solution of MgO and Al₂O₃ in MgAl₂O₄ spinel, 04-2000.
- [Poirier 1990] J. P. Poirier, Creep of crystals, Cambridge University Press, (1990) p. 15, p. 233.
- [Pychlau 1994] C. Pychlau / Mikrostrukturelle Veränderungen und Schwellverhalten einiger ausgewählter keramischer Struktur- und Fensterwerkstoff unter niederenergetischem He-Ionenbeschuss, Kernforschungszentrum Karlsruhe, KfK 5428 (1994)
- [Roque et al. 2000] V. Roque, B. Cros, D. Baron, P. Dehault, J. Nucl. Mater. 277 (2000) 211
- [Samsonov 1982] G.V. Samsonov, The Oxide Handbook, 2nd, NY(1982) 183-187, 193-196
- [Sasajima et al. 2000] N. Sasajima, T. Matsui, S. Furono, T. Shiratori, K. Hojou / Nucl. Instr. And Meth. In Phys. Res. B 166-167 (2000) 250.
- [Schram et al. 2001] R.P.C. Schram, K. Bakker, H. Hein, J.G. Boshoven, R.R. van der Laan, C.M. Sciolla, T. Yamashita, Ch. Hellwig, F. Ingold, R. Conrad, S. Casalta, Prog. Nucl. Ener. 38 (2001) 259.
- [Schram et al. 1999] R.P.C. Schram, K. Bakker, J.G. Boshoven, E.A.C. Neeft, G. Dassel, H. Hein, R.R. van der Laan, R.J.M. Konings, R. Conrad in Proc. of the Int. Conf. on Future Nuclear Systems; Global '99, Wyoming, Aug.29-Sept. 3, 1999 (available on CD-rom, no page index)
- [Schwarzblat 1981] M. Schwarzblat, Nuclear Technology, 52 (1981) 426.
- [Sciolla 2000] C.M. Sciolla, Calculations of EFTTRA-T3 for burn-up, identity and quantity of fissioned atoms after irradiation till a year after irradiation, only electronic files.
- [Sciolla 2002] C.M. Sciolla, Calculations of EFTTRA-T3 for power, only electronic files.
- [Skoog et al. 1980] D.A. Skoog and J.J. Leary, Principles of Instrumental Analysis (Saunders College Publishing, USA, 1980) p.137.
- [Solomah 1990] A.G. Solomah, L. Esposito, European Appl. Res. Rept.-Nucl. Sci. Technol. 7 (1990) 1441.
- [Stevanovic et al. 1967] M. Stevanovic, J. Elston, Proc. Br. Ceram. Soc. 7 (1967) 423.
- [Stewart et al. 1980] R.L. Stewart, R.C. Bradt, J. Am. Ceram. Soc. 63 (1980) 619
- [Stewart et al. 1981] R.L. Stewart, M. Iwasa, R.C. Bradt, J. Am. Ceram. Soc. 64 (1981) C-22.
- [Suter et al. 2002] U.W. Suter, B.E. Eichinger, Polymer, 43 (2002) 575.
- [Touloukian et al. 1977] Y.S. Touloukian, R.K. Kirby, R.E. Taylor, T.Y.R. Lee, Thermophysical properties of Matter, 13 IFI/Plenum, New York, 1977
- [Une et al. 2000] K. Une, M. Hirai, K. Nogita, T. Hosokawa, Y. Suzawa, S. Shimizu, Y. Etoh, J. Nucl. Mater. 278 (2000) 54.
- [van Veen et al. 1979] A. van Veen, A. Warnaar, L.M. Caspers Vacuum 30 (1979) 109.
- [van Veen et al. 1999] A. van Veen, F. Labohm and K.T. Westerduin, Helium in materialen van een flat-panel display systeem; een TDS en NDP analyse, Interfaculty Reactor Institute, IRI-131-99-015 (1999).
- [van Veen 1991] A. van Veen in S.E. Donnelly, J.H. Evans (Eds.), Fundamental Aspects of Inert Gases in Solids, (Plenum Press, New York, 1991) p. 41-57

- [van Vlaanderen 1999/2000] P. van Vlaanderen, Research notes released on December 1999, and on February and May 2000.
- [Viallard et al. 1997] I. Viallard, J.M. Bonnerot, M. Bauer, in Proc. of the Int. Conf. on Future Nuclear Systems; Global '97, Japan, 1997, 1311.
- [Wachtman 1996] J.B. Wachtman, Mechanical properties of ceramics, (John Wiley & Sons, New York, 1996) 10th 24-32,410,411
- [Walker 1996] C.T. Walker, W. Goll, T. Matsumura, J. Nucl. Mater. 228 (1996) 8.
- [Weeks et al. 1980] R.A. Weeks, E. Sonder, J. Am. Ceram. Soc. 63 (1980) 92.
- [van Well 1992] A.A. van Well, Nuclear Science and Engineering 110 (1992) 10.
- [White et al. 1956] D.W. White, A.P. Beard, A.H. Willis, USAEC TID 7546 (1956) 717.
- [Wick 1967] O.J. Wick, Plutonium Handbook I (1967) New York.
- [Wiesenack et al. 2000] W. Wiesenack, T. Tverberg, Thermal performance of high burn-up fuel, Proc. 2000 Int. Topical Meeting on LWR Fuel Performance, Park City, Utah, April 10-13, 2000
- [WISE] <http://www.antenna.nl/wise/uranium/rdcu.html>
- [de With et al. 1985] G. de With, J.E.D. Parren, Solid State Ionics 16 (1985) 87.
- [Woittiez 1999/2000] J.R.W. Woittiez, Research notes released on September and November 1999 and on February and August 2000.
- [Wyckoff 1965] R.W.G. Wyckoff, Crystal Structures (John Wiley & Sons, 48-9169 USA, 1965)
- [Yano et al. 1994] T. Yano, Y. Fukushima, H. Sawada, M. Miyazaki, T. Iseki, J. Nucl. Mater. 212-215 (1994) 1046
- [Yano 1999] T. Yano, J. Am. Ceram. Soc. 82 (1999) 3355.
- [Yasuda et al. 2000] K. Yasuda, C. Kinoshita, K. Fukuda, F.A. Garner, J. Nucl. Mater. 283-287 (2000) 937.
- [Yasuda et al. 1997] K. Yasuda, R. Morisaki, C. Kinoshita, H. Abe, H. Naramoto Proc. of the 7th Int. Symp. on Advanced Nuclear Energy Research, (1997) 384.
- [Yehekel et al. 1999] O. Yehekel, O. Tevet, J. Am. Ceram. Soc. 99 [1] (1999) 136-144.
- [Zacate et al. 2000] M.O. Zacate, L. Minervini, D.J. Bradfield, R.W. Grimes, K.E. Sickafus, Solid State Ionics, 128 (2000) 243.
- [Ziegler et al. 2002] Ziegler and Biersack, Stopping and range of ions in matter, software downloaded from <http://www.SRIM.org>
- [Zinkle 1995] S.J. Zinkle, J. Nucl. Mater 219 (1995) 113.

Summary

Nuclear waste is more radiotoxic than uranium ore for a period of about 200.000 years. This long period is mainly caused by the actinides plutonium and americium. These actinides are formed during transmutation of ^{238}U . Theoretically, this long time of radiotoxicity can be reduced till about 250 years when a matrix without uranium is used in which these actinides are fissioned. The problem is finding a uranium free matrix that has similarly acceptable material degradation as the matrix $^{238}\text{UO}_2$ during irradiation conditions in a nuclear reactor. The inert matrix fuel should show as UO_2 during irradiation conditions a small fission gas release, almost absence of crack formation, no melting, limited swelling and no chemical interaction with the cladding.

During neutron irradiation of americium, a lot of helium can be generated. Research on He in MgAl_2O_4 is performed to simulate the behaviour of helium during irradiation conditions of americium in MgAl_2O_4 . Implantation of particles occurs during irradiation. Atoms are displaced from their lattice sites during implantation of particles, in this study helium. These displacements result in defects in materials. The diffusion of helium in materials without defects can be determined with the migration energy of helium. The dissociation energy of helium from a defect is required to determine the diffusion of helium in a solid material with defects. This dissociation energy is the sum of the binding energy of helium to the defect and migration energy of helium. The permeation energy of helium is required to allow diffusion of helium in a material with pores. The permeation energy is the sum of the solution energy and the migration energy.

Atomistic calculations show that the calculated migration energy of vacancies smaller is or comparable to the calculated migration energy of helium. This indicates that clustering of vacancies can occur before helium starts to migrate for samples with a high concentration of defects. The calculated self-diffusion energies for intrinsic defects are larger than the calculated permeation energy of helium. The diffusion of helium in MgAl_2O_4 therefore takes place by interstitial diffusion, dissociation from defects and permeation. Thermal helium redistribution of helium by vacancy-assisted diffusion is less likely due to the large formation energies of (partial) Schottky defects. The swelling by helium in the perfect lattice of MgAl_2O_4 is 0.5 vol% per helium atom per unit cell of MgAl_2O_4 .

Diffusion is generally viewed as the thermal redistribution of atoms or molecules dependent on the concentration of atoms or molecules in materials. In this thesis, new diffusion coefficients are proposed for diffusion of inert gas in implanted single crystals and poly crystal media. These diffusion coefficients are, besides the usual temperature-dependency, also determined by the concentration of vacancies or pores. This new theory is used to obtain the empirical parameters for diffusion of helium in MgAl_2O_4 .

For depth independent diffusion: the diffusion coefficient is constant in depth in materials without a temperature gradient. Depth independent diffusion can be interstitial diffusion, the migration energy of helium is required to calculate diffusion, or defect mediated

diffusion in case of a uniform concentration of defects in materials, the dissociation energy of helium from defects and the concentration of defects are required to calculate diffusion. The concentration of defects is almost always not uniform in implanted materials. For defect concentration mediated depth dependent diffusion: the diffusion coefficient varies in depth by the variation in concentration of defects. Both diffusion mechanisms ((defect) depth independent diffusion and defect depth dependent diffusion) show broadening of the helium concentration profile during heating of the samples. The difference between both diffusion mechanisms can be viewed in the displacement of the peak in concentration of helium of thermally evolved helium concentration profiles in implanted materials that can be assumed as semi-infinite media.

All thermally evolved helium concentration profiles in single crystals show defect concentration mediated depth dependent diffusion if no clustering of vacancies occurred. A uniform dissociation energy is used for the calculations of defect concentration mediated depth dependent diffusion in this thesis. The empirical activation energies for diffusion of helium in MgAl_2O_4 were determined with a temperature independent pre-factor of $2.30 \times 10^{-3} \text{ cm}^2\text{s}^{-1}$ and a concentration of vacancies of 10% of displaced atoms. These energies are: 1.59 eV for the migration energy of helium and 2.29 eV for the dissociation energy of helium from vacancies that were probably occupied by one helium atom. The empirical and calculated binding energy of helium atoms to (empty) vacancies are similar. The dissociation energies of helium from vacancies that are occupied by more than one helium atom are smaller.

For helium implanted polycrystalline samples, it is assumed that defect concentration mediated depth dependent diffusion takes place for helium within grains and that pore mediated depth independent diffusion takes place for helium at grainboundaries. The average grain size was a fourth of the helium implantation range and the porosity was 4%. Thermally evolved helium concentration profiles show broadening if the diffusion coefficient within the grain larger is than the diffusion coefficient at grainboundaries. Otherwise no broadening of the helium concentration profile takes place.

A migration energy of helium at grainboundaries of 0.45 eV and a temperature independent pre-factor of $3.45 \times 10^{-3} \text{ cm}^2\text{s}^{-1}$ are used for the simulation of thermally evolved helium concentration profiles. The empirical solution energy of helium in intergranular pores, at ideal gas conditions, is 1.75 eV when a difference in entropy of $-1 \times 10^{-3} \text{ eV K}^{-1}$ is used. The solution energy and differences in entropy are smaller for pressurised intergranular pores. The thermal evolution of helium concentration profiles, under the assumption of the presence of nano-sized bubbles, could be well modelled with a permeation energy of 2.89 eV of helium within grains. This is similar to the calculated permeation energy. The permeation energy of helium from intragranular pores (pores within grains) is probably larger than the permeation energy of helium from intergranular pores (pores between grains) because the migration energy of helium at grainboundaries smaller is than the migration energy of helium within the grain.

EFTTRA-T4 (MgAl_2O_4 immersed in an americium solution) does not have the properties of thermal diffusion of helium in MgAl_2O_4 . This is probably caused by the formation of a solid solution between MgAl_2O_4 and AmO_2 . Limited swelling in MgAl_2O_4 is expected by

the generated amount of defects and helium in MgAl_2O_4 during neutron irradiation of americium. In this perspective, MgAl_2O_4 seems to be an excellent uranium free matrix for the transmutation of americium.

In the EFTTRA-T3 irradiation experiment, five uranium free matrices were tested as potential candidates to replace the $^{238}\text{UO}_2$ matrix. These are CeO_{2-x} , MgO , MgAl_2O_4 , Y_2O_3 and $\text{Y}_3\text{Al}_5\text{O}_{12}$. Pellets contained 2.5-3 vol% UO_2 , determined from the weight percentage of UO_2 . Uranium was enriched in 20 at% ^{235}U . UO_2 was used as a phase of actinides to simulate the implantation of fission products that would also occur by neutron irradiation of PuO_2 and AmO_2 . Five series of pellets contained ellipsoidal UO_2 inclusions with an average diameter of 200 μm . Two series of pellets contained 19.5 vol% $\text{UY}_{5.94}\text{O}_x$ inclusions with a similar size as the UO_2 inclusions. These seven fuels are called macro-dispersed fuels. One micro-dispersed fuel contained submicron-sized UO_2 inclusions in MgAl_2O_4 . The diameter of the pellets was 5.1-5.4 mm. The formation of a solid solution between the fissile phase and the uranium free matrix occurred during sintering (and possibly continued during irradiation) between UO_2 , Y_2O_3 and CeO_{2-x} and between $\text{UY}_{5.94}\text{O}_x$ and MgAl_2O_4 .

Almost 20% of the initially present uranium was fissioned in 199 days. The irradiation temperature of these pellets was about 700 K to 1000 K. No thermally induced migration of fission products took place in the uranium free matrices (excluded the implantation zones). The swelling of the UO_2 inclusions was about 50-75 vol% due to the large amount of implanted fission products in these inclusions.

5-10 vol% of the matrix was implanted with fission products for the three macro-dispersed fuels with the uranium free matrices MgO , MgAl_2O_4 and $\text{Y}_3\text{Al}_5\text{O}_{12}$. These three macro-dispersed fuels show cracks from UO_2 inclusion to UO_2 inclusion after irradiation. This inter-particle fracture is caused by swelling of UO_2 and absence or insufficient creep of the matrices to accommodate the swelling of UO_2 . The swelling of the UO_2 inclusions after crack formation of the matrix resulted in displacement of the surrounding matrix by which the dimensional changes of the pellets can be significantly large. In the present study, the ellipsoidal shape and orientation of the UO_2 inclusions resulted mainly in a change in height of the pellets. Inter-particle fracture resulted in a significant reduction in diffusion length for (gaseous) fission products to the plenum. Fission gas releases till 50% were measured despite the low irradiation temperatures.

50-100 vol% of the matrix was implanted with fission products for the two macro-dispersed fuels with the uranium free matrices CeO_{2-x} and Y_2O_3 . This high percentage is caused by the formation of a solid solution between UO_2 and matrix. Inter-particle fracture was virtually absent in these two fuels after irradiation. This is probably due to the reduction in volume of the matrix by (fission-induced) creep leaving room for UO_2 to swell. This fission-induced creep was present in the majority of the matrix. These pellets shrank. The absence of inter-particle fracture resulted in low fission gas releases of 4-8%.

The swelling by fission products is excessive for $Y_3Al_5O_{12}$; at least 100 times larger than UO_2 for comparable fission product concentrations. Bubbles till a diameter of 75 μm were present in the implantation zones of $Y_3Al_5O_{12}$. Only this macro-dispersed fuel with $Y_3Al_5O_{12}$ deformed the cladding. $Y_3Al_5O_{12}$ is therefore a bad inert matrix. Fission gas bubbles could not be observed in the implantation zones of other macro-dispersed fuels.

No fission gases were released from the micro-dispersed fuel of $MgAl_2O_4$ and UO_2 . The pellets slightly shrank due to the initially high porosity before irradiation and low concentration of uranium. However, the solid state swelling by fission products in $MgAl_2O_4$ is about ten times larger than this solid state swelling in UO_2 . The use of $MgAl_2O_4$ as an inert matrix is therefore limited to macro-dispersed fuels with coated inclusions of actinides. This coating should be about 9 μm and show less swelling by implantation of fission products than $MgAl_2O_4$. This coating can also prevent the formation of a solid solution between AmO_2 and $MgAl_2O_4$. The limitations of the other inert matrices: MgO , CeO_{2-x} and Y_2O_3 cannot be deduced from this study. Their behaviour during neutron irradiation may be different if another actinide-oxide than UO_2 is used. The material degradation by implantation of fission products is probably worse for MgO than for CeO_{2-x} and Y_2O_3 .

The $UY_{5.94}O_x$ inclusions were, before sintering of the pellets, most probably composed of uranium-oxide and yttrium-carbonate. Dissociation of CO_2 during sintering of pellets with the uranium free matrices MgO or $MgAl_2O_4$ resulted in porous fissile inclusions. This generated porosity during sintering was an initial space for swelling by fission products.

No swelling of the pellet took place despite the numerous cracks that were present before irradiation in the fabricated fuel with $UY_{5.94}O_x$ inclusions in MgO . The initial porosity in the inclusions almost disappeared after neutron irradiation.

Fission gas bubbles were present in the yttrium aluminium phase in the fuel $UY_{5.94}O_x+MgAl_2O_4$. This yttrium aluminium phase is a solid solution between $MgAl_2O_4$ and $(U,Y)O_x$. Only after irradiation, cracks at almost each $(U,Y(Al))O_x$ inclusion were present in the matrix $MgAl_2O_4$. The pellets showed a dimensional enlargement.

The fission gas release of these macro-dispersed fuels is 3-4%. This low percentage in comparison with those macro-dispersed fuels with UO_2 , that also had an abundance of cracks in the matrix after irradiation, is due to the fabricated dilution in fissile atoms.

It is probably best to fabricate inert matrix fuels with porous fissile inclusions to have initial space for the swelling by fission products. Pollution of the matrices by actinides can enhance the creep of the matrices and thereby prevent inter-particle fracture if creep of the pure matrix is too small during irradiation conditions. Only those actinides that do not form that kind of solid solution with the matrix that shows excessive swelling during neutron irradiation of that actinide should be used for the pollution of matrices.

Samenvatting

Nucleair afval is meer radiotoxisch dan uranium erts voor een periode van ongeveer 200.000 jaar. Deze lange tijd wordt voornamelijk veroorzaakt door de actiniden: plutonium en americium. Deze actiniden ontstaan tijdens transmutatie van ^{238}U . Theoretisch kan deze lange tijd van radiotoxiciteit gereduceerd worden tot ongeveer 250 jaar wanneer een matrix zonder uranium wordt gebruikt waarin deze actiniden worden verspleten. Het probleem is het vinden van een matrix zonder uranium dat dezelfde degradatie van materiaaleigenschappen heeft als de matrix $^{238}\text{UO}_2$ tijdens de bestralingscondities in een kern reactor. De inerte matrix brandstof moet net als UO_2 tijdens neutronenbestraling een kleine splijtingsgasvrijzetting hebben, vrijwel geen breuken vormen, niet smelten, vrijwel niet zwellen en geen chemische interactie hebben met de cladding.

Tijdens neutronenbestraling van americium wordt er veel helium gegenereerd. Onderzoek aan helium in MgAl_2O_4 is gedaan om het gedrag van helium tijdens bestraling van americium in MgAl_2O_4 te simuleren. Tijdens bestraling worden deeltjes geïmplanteerd. Atomen worden van hun roosterpositie verplaatst door het implanteren van een deeltje, in dit geval helium. Deze verplaatsingen leiden tot defecten in materialen. Met de migratie energie van helium kan de diffusie van helium in een materiaal zonder defecten bepaald worden. Als helium getrap wordt in een vacature is de dissociatie energie van helium van een vacature nodig om de diffusie van helium te berekenen. Deze dissociatie energie is de som van de bindingsenergie van helium aan een vacature en de migratie energie van helium. De permeatie energie van helium is nodig om de diffusie van helium te berekenen als er poriën aanwezig zijn. De permeatie energie is de som van de oplosbaarheidsenergie en de migratie energie.

Atomaire berekeningen tonen aan dat de berekende migratie energie van vacatures kleiner of vergelijkbaar is met de berekende migratie energie van helium in MgAl_2O_4 . Dit toont aan dat vacatures kunnen clusteren voordat helium migreert in monsters met een grote concentratie van defecten. De berekende activeringsenergieën voor zelf-diffusie van intrinsieke defecten zijn groter dan de berekende permeatie energie van helium. De diffusie van helium in MgAl_2O_4 vindt daarom plaats door interstitiële diffusie, dissociatie van defecten en permeatie. Vacature-geassisteerde diffusie van helium vindt waarschijnlijk niet plaats door de grote vormingsenergieën van (partiële) Schottky defecten. De zwellen door helium in een perfect rooster van MgAl_2O_4 is 0.5 vol% per helium atoom per eenheidscel van MgAl_2O_4 .

Diffusie wordt in het algemeen gezien als een thermische redistributie van atomen of moleculen afhankelijk van de concentratie van atomen of moleculen in materialen. In dit proefschrift zijn nieuwe diffusiecoëfficiënten opgesteld voor diffusie van inert gas in geïmplanteerde eenkristallen en polykristallijne media. Deze diffusiecoëfficiënten zijn, naast de gebruikelijke temperatuur-afhankelijkheid, ook afhankelijk van de concentratie van vacatures of poriën. Deze nieuwe theorie is gebruikt om empirische parameters voor de diffusie van helium in MgAl_2O_4 te verkrijgen.

De diffusiecoëfficiënt is constant in materialen zonder temperatuurgradiënt waar diepte onafhankelijke diffusie plaatsvindt. Diepte onafhankelijke diffusie kan interstitiële diffusie zijn; dan is de migratie energie van helium nodig om helium concentratieprofielen te berekenen, of defect afhankelijke diffusie als de concentratie van defecten in materialen uniform is, hiervoor zijn de dissociatie energie van helium van defecten en concentratie van defecten nodig om helium concentratieprofielen te berekenen. In geïmplanteerde materialen is de concentratie van defecten vaak niet uniform in materialen. Voor defect diepte afhankelijke diffusie varieert de concentratie van defecten in diepte in materialen. Beide diffusiemechanismen ((defect) diepte onafhankelijke diffusie en defect diepte afhankelijke diffusie) laten een verbreding van het helium concentratieprofiel tijdens het verhitten van de geïmplanteerde monsters. Het verschil tussen deze twee diffusiemechanismen is te zien aan de verschuiving van de piek van het helium concentratieprofiel in helium geïmplanteerde materialen die kunnen worden beschouwd als semi-infinite media.

Alle helium geïmplanteerde eenkristallen lieten deze defect diepte afhankelijke diffusie zien wanneer clustering van vacatures afwezig was. Voor de berekeningen van defect diepte afhankelijke diffusie in dit proefschrift is de dissociatie energie van helium van defecten uniform. De empirische activeringsenergieën voor diffusie van helium in MgAl_2O_4 zijn bepaald met een temperatuur onafhankelijke voorfactor van $2.30 \times 10^{-3} \text{ cm}^2\text{s}^{-1}$ en een concentratie van vacatures van 10% van verplaatste atomen. Dit zijn: 1.59 eV voor de migratie energie van helium en 2.29 eV voor de dissociatie energie van helium van vacatures die waarschijnlijk 1 helium atoom bevatten. De empirische en berekende bindingsenergie van helium atomen aan lege vacatures is ongeveer hetzelfde. De bindingsenergie van helium atomen aan vacatures die meer dan 1 helium atoom bevatten is kleiner.

Voor helium geïmplanteerde polykristallijne materialen is aangenomen dat defect diepte afhankelijke diffusie plaatsvindt in de korrels en dat porie diepte onafhankelijke diffusie plaatsvindt in de korrelgrenzen. De gemiddelde korrelgrootte was een vierde van de helium implantatie range en de porositeit was 4%. Thermische geëvolueerde helium concentratieprofielen laten verbreding zien als de diffusiecoëfficiënt in de korrels groter is dan de diffusiecoëfficiënt in de korrelgrenzen. Andersom kan er geen verbreding van het helium concentratieprofiel plaatsvinden.

Een temperatuur onafhankelijke voorfactor van $3.45 \times 10^{-3} \text{ cm}^2\text{s}^{-1}$ en een migratie energie van helium in de korrelgrenzen van 0.45 eV zijn gebruikt voor de simulatie van de thermisch geëvolueerde helium concentratieprofielen in polykristallijne materialen. De empirische oplosbaarheidenergie van helium in intergranulaire poriën, onder ideale gas condities, is 1.75 eV wanneer een verschil in entropie van $-1 \times 10^{-3} \text{ eV K}^{-1}$ wordt gebruikt. Voor intergranulaire poriën met een hogere druk van helium zijn het verschil in entropie en oplosbaarheidenergie kleiner. De thermische geëvolueerde helium concentratieprofielen, onder de aanname van aanwezigheid van nano-grootte bubbles onder hoge druk in korrels, konden goed worden gesimuleerd met een permeatie energie van 2.89 eV van helium in korrels. Dit is vergelijkbaar met de berekende permeatie energie. De permeatie energie van helium van intragranulaire poriën (poriën in korrels) is waarschijnlijk groter dan de permeatie energie van helium van

intergranulaire poriën (poriën tussen korrels) omdat de migratie energie van helium aan de korrelgrenzen kleiner is dan de migratie energie van helium in de korrels.

EFTTRA-T4 (MgAl_2O_4 geïmpregneerd met een americium oplossing) heeft niet de eigenschappen van thermische diffusie van helium in MgAl_2O_4 waarschijnlijk door het vormen van een vaste oplossing tussen AmO_2 en MgAl_2O_4 . De gegenereerde hoeveelheid defecten in MgAl_2O_4 en helium door neutronenbestraling van americium veroorzaken vrijwel geen zwellen in MgAl_2O_4 . In dit perspectief lijkt MgAl_2O_4 een uitstekende uranium vrije matrix voor de transmutatie van americium.

In het bestralingsexperiment EFTTRA-T3 zijn vijf uranium-vrije matrices getest als potentiële kandidaten om $^{238}\text{UO}_2$ te vervangen. Dit zijn CeO_{2-x} , MgO , MgAl_2O_4 , Y_2O_3 en $\text{Y}_3\text{Al}_5\text{O}_{12}$. De pillen bevatten 2.5-3 vol% UO_2 , bepaald uit het gewichtspercentage van UO_2 . Uranium was verrijkt met 20 at% ^{235}U . UO_2 is gebruikt om de implantatie van splijtingsproducten tijdens neutronenbestraling van PuO_2 en AmO_2 te simuleren. Vijf series van pillen bevatten ellipsoïde inclusies van UO_2 met een gemiddelde diameter van 200 μm . Twee series van pillen bevatten 19.5 vol% $\text{UY}_{5.94}\text{O}_x$ inclusies met een vergelijkbare grootte als de UO_2 inclusies. Deze zeven brandstoffen worden heterogene brandstoffen genoemd. Een homogene brandstof bestond uit submicron grootte UO_2 inclusies in MgAl_2O_4 . De diameter van de pillen was 5.1-5.4 mm. Het vormen van een vaste oplossing van de uranium vrije matrix met de fase van splijstof was ontstaan na het sinteren (en mogelijk voortgegaan tijdens bestraling) tussen UO_2 , Y_2O_3 en CeO_{2-x} en tussen $\text{UY}_{5.94}\text{O}_x$ en MgAl_2O_4 .

Bijna 20% van het initieel aanwezige uranium was verspleten in 199 dagen en de bestralingstemperatuur van deze pillen was ongeveer 700 K tot 1000 K. In de matrices vond geen thermisch geïnduceerde migratie plaats van splijtingsproducten (exclusief de implantatiezones). Door de grote hoeveelheid geïmplanteerde splijtingsproducten waren de UO_2 inclusies 50-75 vol% gezwollen.

5-10 vol% van de matrix was geïmplanteerd met splijtingsproducten in drie van de heterogene brandstoffen met de uranium-vrije matrices MgO , MgAl_2O_4 en $\text{Y}_3\text{Al}_5\text{O}_{12}$. Breuken bij vrijwel iedere UO_2 inclusie waren aanwezig na bestraling van deze drie brandstoffen. Deze breuken zijn gevormd door het zwellen van UO_2 en afwezigheid of onvoldoende kruip van de matrices om de zwellen van UO_2 op te vangen. Het zwellen van UO_2 na breukvorming van de matrix resulteert in het verplaatsen van de matrix om de UO_2 inclusies. De dimensionele vergroting van de pillen kan hierdoor verschrikkelijk groot zijn. In de huidige studie was de dimensionele vergroting beperkt tot een toename in de hoogte van de pil door de ellipsoïde vorm en oriëntatie van de UO_2 inclusies. Het vormen van de breuken resulteert in een significante vermindering van de diffusielengte van splijtingsproducten naar het plenum. Vrijzettingen van splijtingsgas tot 50% werden gemeten ondanks de lage bestralingstemperatuur.

50-100 vol% van de matrix was geïmplanteerd met splijtingsproducten in de twee heterogene brandstoffen met de uranium-vrije matrices CeO_{2-x} en Y_2O_3 . Dit hoge percentage is

veroorzaakt door het vormen van een vaste oplossing tussen UO_2 en de matrix. Breuken van UO_2 inclusie naar UO_2 inclusie waren afwezig of zeldzaam na bestraling van deze twee brandstoffen. Dit is hoogstwaarschijnlijk veroorzaakt door reductie in volume van deze matrices door (splijting-geïnduceerde) kruip in vrijwel de gehele matrix door het grote vol% matrix waar implantatie van splijtingsproducten plaatsvond. Deze kruip gaf ruimte voor de UO_2 inclusie om te zwellen. Deze pillen waren gekrompen. Deze afwezigheid van breuken resulteerde in een lage vrijzetting van splijtingsgas van 4-8%.

De zwelling door splijtingsproducten in $\text{Y}_3\text{Al}_5\text{O}_{12}$ is excessief; meer dan 100 keer groter dan UO_2 bij vergelijkbare concentratie van splijtingsproducten. Bellen tot een diameter van 75 μm waren aanwezig in de implantatie zones van $\text{Y}_3\text{Al}_5\text{O}_{12}$. Alleen bij deze heterogene brandstof was het staal van de capsule gedeformeerd. $\text{Y}_3\text{Al}_5\text{O}_{12}$ is daarom een slechte inerte matrix. Er waren geen bellen te zien in de implantatie zones van matrices in de andere heterogene brandstoffen.

Bij de homogene brandstof UO_2 in MgAl_2O_4 waren geen splijtingsgassen vrijgekomen. De pillen vertonen een lichte krimp door de grote porositeit die aanwezig was voor bestraling en de lage concentratie UO_2 . Echter, de zwelling van het vaste materiaal door splijtingsproducten in MgAl_2O_4 is tien keer zo groot als deze vaste stof zwelling in UO_2 . Het gebruik van MgAl_2O_4 als inerte matrix is daarom waarschijnlijk gelimiteerd tot heterogene brandstoffen die gecoate actinideinclusies bevatten. De coating moet ongeveer 9 μm zijn en minder zwellen tijdens implantatie van splijtingsprodukten dan MgAl_2O_4 . Deze coating kan tevens het vormen van een vaste oplossing tussen AmO_2 en MgAl_2O_4 voorkomen. De beperkingen van de andere inerte matrices: MgO , CeO_{2-x} en Y_2O_3 kunnen niet worden gegeven door deze studie. Hun gedrag tijdens neutronenbestraling kan anders zijn als i.p.v. UO_2 een andere actinide-oxide wordt gebruikt. Degradatie van materiaaleigenschappen door implantatie van splijtingsproducten is waarschijnlijk groter voor MgO dan voor CeO_{2-x} en Y_2O_3 .

De $\text{UY}_{5,94}\text{O}_x$ inclusies bestonden, voor het sinteren van de pillen, hoogstwaarschijnlijk uit uranium-oxide en yttrium-carbonaat. Het dissociëren van CO_2 , tijdens het sinteren van de pillen met de uranium-vrije matrix MgO of MgAl_2O_4 , leidde tot poreuze splijstof inclusies. Deze, tijdens het sinteren gegeneerde porositeit, was een initiële ruimte voor zwelling door implantatie van splijtingsproducten.

Ondanks de talrijke aanwezigheid van breuken voor bestraling in de gefabriceerde brandstof van $\text{UY}_{5,94}\text{O}_x$ inclusies in MgO , vond er geen zwelling van de pil plaats. De initiële porositeit in deze inclusies was vrijwel verdwenen na bestraling.

Splijtingsgasbellen waren aanwezig in de yttrium-aluminium fase in de brandstof met MgAl_2O_4 . Deze yttrium-aluminium fase is een vaste stof oplossing tussen MgAl_2O_4 en $(\text{U},\text{Y})\text{O}_x$. Alleen na bestraling waren bij vrijwel iedere inclusie breuken aanwezig in de matrix. De pillen vertonen een dimensionele vergroting.

Het percentage van vrijgekomen splijtingsgas is 3-4%. Dit lage percentage in vergelijking met die heterogene brandstoffen met UO_2 , waar breuken in de matrix ook talrijk waren, is veroorzaakt de gefabriceerde verdunning in splijtbare atomen.

Het is waarschijnlijk het beste om inerte matrix brandstof te fabriceren met poreuze splijtstof inclusies om initiële ruimte te hebben voor de zwellings door implantatie van splijtstofproducten tijdens neutronenbestraling. Vervuiling van matrices met actiniden kan de kruip van de matrices doen toenemen en hiermee breuken in de matrix, door het zwellen van de actinidefase, voorkomen als de kruip van de pure matrix te klein is tijdens neutronenbestraling. Alleen die actiniden die niet zo'n vaste oplossing vormen met de matrix dat excessief zwelt tijdens neutronenbestraling van die actinide kunnen gebruikt worden voor de vervuiling van matrices.

list of publications

Results discussed in this thesis have been discussed in the literature:

Chapter 4

E.A.C. Neeft, R.J.M. Konings, A. van Veen, H. Schut, A.V. Fedorov, *Impact of neutron irradiation and helium implantation on ceramic support materials for uranium-free fuels*, Advances in Science and Technology 24 (1999) 531-539.

E.A.C. Neeft, R.P.C. Schram, A. van Veen, F. Labohm, A.V. Fedorov, *Helium irradiation effects in single crystals of $MgAl_2O_4$* , Nucl. Instr. and Meth. in Phys. Res. B 166-167 (2000) 238-243.

E.A.C. Neeft, A. van Veen, R.P.C. Schram, F. Labohm, *Annealing effects of helium implanted single crystals and polycrystalline magnesium aluminate spinel*, Progr. Nucl. Energy 38 (2001) 287-290.

articles related to this subject

H. Schut, A. van Veen, F. Labohm, A.V. Fedorov, E.A.C. Neeft, R.J.M. Konings, Nucl. Instr. and Meth. in Phys. Res. B 147 (1999) 212-215.

A. van Veen, H. Schut, A.V. Fedorov, E.A.C. Neeft, R.J.M. Konings, B.J. Kooi, J.Th.M. Hosson, Nucl. Instr. and Meth. in Phys. Res. B 147 (1999) 216-220.

A. van Veen, H. Schut, A.V. Fedorov, F. Labohm, E.A.C. Neeft, R.J.M. Konings, Nucl. Instr. and Meth. in Phys. Res. B 148 (1999) 768-772.

Chapter 5

J.C. Boshoven, E.A.C. Neeft, R.J.M. Konings, K. Bakker, H. Hein, Fabrication of targets for heterogeneous transmutation, Netherlands Energy Research Foundation ECN Report ECN-I-97-025 (1997).

R.P.C. Schram, K. Bakker, J.G. Boshoven, E.A.C. Neeft, G. Dassel, H. Hein, R.R. van der Laan, R.J.M. Konings, R. Conrad in Proc. of the Int. on Future Nuclear systems: Global'99, Wyoming, Aug. 29-Sept. 3, 1999 (on CD-rom, no page index).

K. Bakker, R.L. Belvroy, F.A. van den Berg, S. Casalta, R. Conrad, E.A.C. Neeft, R.P.C. Schram, W.J. Tams, *Progr. Nucl. Energy* 38 (2001) 313-316.

E.A.C. Neeft, K. Bakker, H.A. Buurveld, J. Minkema, A. Paardekooper, R.P.C. Schram, C. Sciolla, O. Zwaagstra, B. Beemsterboer, J.R.W. Woittiez, P. van Vlaanderen, W.J. Tams, H. Hein, R. Conrad, A. van Veen, *Post irradiation examination of uranium inclusions in inert matrices*, *Progr. Nucl. Energy* 38 (2001) 427-430.

N. Chauvin, C. Thiriet-Dodane, J. Noirot, Hj. Matzke, R.J.M. Konings, K. Bakker, E.A.C. Neeft, R. Conrad, A. van Veen, T. Yamashita, Synthesis on $MgAl_2O_4$ irradiation results, European Commission Joint Research Centre Report JRC-ITU-TN-2002/39 (2002).

F.C. Klaassen, R.P.C. Schram, K. Bakker, E.A.C. Neeft, R. Conrad, R.J.M. Konings, in Proc. of the Seventh information exchange meeting, Jeju 2002 Oct. 14-16 2002.

E.A.C. Neeft, K. Bakker, R.L. Belvroy, W.J. Tams, R.P.C. Schram, R. Conrad, A. van Veen, *Mechanical behaviour of macro-dispersed fuels*, *J. Nucl. Mater.* 317 (2003) 217.

E.A.C. Neeft, Post-irradiation examination & additional characterisation of EFTTRA-T3, NRG Report 21303/04.57381/I (2003).

E.A.C. Neeft, K. Bakker, R.P.C. Schram, R. Conrad, R.J.M. Konings, *The EFTTRA-T3 experiment on inert matrix fuels*, *J. Nucl. Mater.* 320 (2003) 106-116.

articles related to this subject:

E.A.C. Neeft, R.J.M. Konings, K. Bakker, J.G. Boshoven, H. Hein, R.P.C. Schram, A. van Veen, *Neutron irradiation of polycrystalline yttrium aluminate garnet, magnesium aluminate spinel and α -alumina*, *J. Nucl. Mater.* 274 (1999) 78-83.

Acknowledgements

I am gratefully thankful that prof. A. van Veen took me on a theoretically explorative journey with the rate diffusion theory described in this thesis as the outcome. I experienced this trip as performing enjoyable science at its highest level. This theory required his encyclopaedic knowledge, mathematical insight and open vision. I want to thank him for seriously thinking about my disagreements and questions. His criticism, not limited to negative criticism, made me enthusiastic for numerical analysis, made me feel more secure that I was on the right track for a thorough interpretation of results and gave me more reflecting properties.

I would like to thank prof. A.H.M. Verkooijen for being my supervisor when prof. A. van Veen suddenly no longer could. His practical suggestions helped me to improve my English writing.

I would like to thank H. Hein, J.C. Boshoven and R.J.M. Konings for the fabrication of EFTTRA-T3, P. van Vlaanderen, V. Smit-Groen, M.R. Roos and J.R.W. Woittiez for the measurements on fabricated fuels. These additional characteristics for the fabricated fuels were essential for the interpretation. These fuels were neutron irradiated in the HFR in Petten under the authority of R. Conrad. C. Sciolla and A. Paardekooper are thanked for their calculations concerning the power and burn-up of fuels and neutron metrology. Measurements concerning the (pre and) post irradiation of the fuels were performed by W.J. Tams, R.L. Belvroy, F.A. van den Berg, H.A. Buurveld, J. Minkema, D. d'Hulst, O. Zwaagstra and B. Beemsterboer. Thank you for answering my flow of questions. Thanks to you, I was able to understand how you obtained the results and that helped me to interpret them.

Besides extensive data and pictures, it is also nice if it can be understood what actually occurred with the fuels during irradiation. With K. Bakker I had intensive discussions because we both want to convince each other of our own interpretation of the data. Although emotions may have run high during these discussions, I think these discussions were essential for the interpretation of the data. I want to thank him for his critical review of Chapter 5 of this thesis and additional paragraphs. Performing such a task like the post-irradiation examination of EFTTRA-T3 in which so many people are involved requires a strict coordination. I want to thank R.P.C. Schram for performing this task as well as his ideas how to deal with geometrical features. Thanks to all the people working at FAI-NRG for the nice atmosphere.

During my PhD period, I also worked at IRI. I was allowed to perform experiments myself and I experienced that as a relief to be independent on so many other persons for results. I want to thank K. Westerduin and A.V. Fedorov for teaching me how to work with the THDS equipment and electrostatic accelerator, respectively. F. Labohm is thanked for the NDP measurements and H. Schut for the PBA measurements. G. Hamburg, C. Egmond and N.J. Kroone from ECN are thanked for additional measurements on the (implanted) samples.

I enjoyed settling down in pubs or a boat or go on a survival trip with also many other people I met during my PhD period at IRI. Dr. M. Blondiaux, S. Godey and Y. Tessier of CERI-CNRS in Orleans are thanked for the 900 keV implantations.

I worked for about a month of my PhD thesis at Imperial College in London. I enjoyed looking at materials on atomic level and the relaxed atmosphere. What looked like huge problems in modelling to me, that would take a lot of time to solve at first glance, were immediately solved since I was surrounded by many experts. I want to thank them all and especially R.W. Grimes for allowing me to work there and his critical review of the paragraphs about atomistic calculations.

I would like to thank my parents for the support that enabled me to work full-time on this thesis.

My computer crashed two days before this thesis was sent to the publisher. The work I performed for three days was not entirely lost. Maarten Sanders managed to retrieve essential documents of this thesis. I want to thank him for helping me in this stressful situation. His perseverance beyond midnight was extraordinary pleasant.

Curriculum vitea

1997-2004 PhD student at IRI Technical University Delft

1997-2001 junior researcher at NRG

1993-1998 Master Geochemistry University Utrecht

graduation thesis: *The morphology of analcime*

1997 apprentice at Hoogovens in IJmuiden

report: *The use of the ilmenite-magnetite thermometer after the pelletizing process*

relevant sidelines:

-student assistant for Petrology (twice) and Crystallography

-assistant for pupils in Chemistry at the private school Luzac

College in Utrecht

1992-1994 First year Chemistry University Utrecht

1986-1992 Secondary School Bonaventura College in Leiden

Date and place of birth 12th of March 1974 in Beverwijk